A Multiscale Finite Element Model for Damage Simulations in Fiber-Reinforced Composites

Vom Fachbereich Bau- und Umweltingenieurwissenschaften der Technischen Universität Darmstadt
zur Erlangung des akademischen Grades
eines Doktor-Ingenieurs (Dr.-Ing.) genehmigte

D i s s e r t a t i o n

vorgelegt von

Dipl.-Ing. Jan Grischa Maaß

aus Weilrod

Erstreferent:	Prof. Dr.-Ing. habil. F. Gruttmann
Korreferent:	Prof. Dr.-Ing. habil. D. Gross
Tag der Einreichung:	16.08.2016
Tag der mündlichen Prüfung:	20.10.2016

Darmstadt 2016
D42

Maaß, Jan Grischa
A Multiscale Finite Element Model for Damage Simulations in Fiber-Reinforced Composites
Forschungsberichte des Instituts für Mechanik der Technischen Universität Darmstadt
Band 42

Herausgeber der Reihe:
Studienbereich Mechanik, Technische Universität Darmstadt

Verfasser:
2016 Jan Grischa Maaß

Verlag:
Studienbereich Mechanik, Technische Universität Darmstadt
Franziska-Braun-Straße 7, 64287 Darmstadt

Druckerzeugung:
Lasertype GmbH, Darmstadt

Bibliografische Information der Deutschen Nationalbibliothek:
Die Deutsche Nationalbibliothek verzeichnet diese Publikation in der Deutschen Nationalbibliografie; detaillierte bibliografische Daten sind im Internet über http://dnb.d-nb.de abrufbar.

Creative Commons Lizenz (CC BY-NC-ND 3.0 DE), 2016.
Freies Vervielfältigen und Weiterverbreiten – Namensnennung – Nicht-kommerziell – Keine Bearbeitung

ISBN 978-3-935868-42-6

Acknowledgement

This thesis is a result of my research occupation at the chair of Solid Mechanics, Technische Universität Darmstadt. At this point I would like to thank everyone who has contributed towards finishing my thesis.
Firstly, I would like to express my sincere gratitude to my advisor Professor Dr.-Ing. Friedrich Gruttmann for the continuous support of my studies and related research, for his professional guidance, supervising and for giving me the opportunity to work in such a friendly working environment. Furthermore, I thank Professor Dr.-Ing. Dietmar Gross for his interest in co-supervising this thesis and for his helpful suggestions.
Additionally, I want to use this opportunity to thank all my colleagues for the scientific discussions and after work activities. I especially thank Florian Niederhöfer, Dominik Heller and Simon Klarmann for their support to finish this work.
Particulary I would like to extend my thanks to my parents, my sister and my girlfriend Karina, who always supported me in all my decisions and stages of life.

Contents

Nomenclature

Abbreviations and names

0	Zero (can be vector- or tensor-valued)
BVP	Boundary-value problem
CDM	Continuum damage mechanics
CFRP	Carbon-fiber-reinforced polymer
DOF	Degree of freedom
EMOC	Enhanced method of cells
FE2, FE^2	Multi-scale finite element model
FEAP	Research FEM code [74]
FEM	Finite element method
FF	Fiber failure
FM	Fiber mode
FMC	Failure mode concept
FRP	Fiber-reinforced plastics
GFRP	Glass-fiber-reinforced polymers
GMC	Generalized method of cells
HFGMC	High fidelity generalized method of cells
IFF	Inter fiber failure
IMPL-EX	Implicit-explicit integration scheme
MM	Multiscale method
MOC	Method of cells
RVE	Representative volume element
WWFE	World wide failure exercise

Greek letters

α, β	Indexes 1, 2
$\boldsymbol{\gamma}$	Euler-Almansi strain tensor
Γ	Boundary of a domain Ω
δ_{eq}	Equivalent displacement
δ	Variational operator

δ_{ij}	Kronecker symbol
ε	Longitudinal strain (1d)
$\tilde{\varepsilon}$	Effective longitudinal strain (1d)
$\boldsymbol{\varepsilon}$	Linearized strain tensor
$\tilde{\boldsymbol{\varepsilon}}$	Effective linearized strain tensor
λ	Load factor
ξ, η	Isoparametric coordinates
Π	Potential energy
Π_{ext}	External potential energy
Π_{int}	Internal potential energy
ρ	Mass density in current configuration
ρ_0	Mass density in reference configuration
σ	Normal stress (1d)
σ_{eq}	Equivalent stress
$\boldsymbol{\sigma}_i$	Vector of stresses in integration point i
$\boldsymbol{\sigma}$	Linearized stress tensor
$\tilde{\boldsymbol{\sigma}}$	Effective linearized stress tensor
$\tilde{\sigma}$	Effective normal stress (1d)
$\boldsymbol{\tau}$	Kirchhoff stress tensor
φ_t	Mapping from reference to current configuration
φ_t^{-1}	Mapping from current to reference configuration
$\hat{\varphi}$	Mapping from reference to current configuration
$\hat{\varphi}^{-1}$	Mapping from current to reference configuration
Ψ	Helmholtz free energy
Ω	Spatial domain
$\partial\Omega$	Boundary of a domain Ω

Roman letters

$\mathbf{A}$	Assembly matrix
$\tilde{\mathbf{A}}$	Effective area element
$\mathcal{B}$	Domain of a continuum body in Euclidean space
$\mathcal{B}_0$	Domain of a continuum body in the reference configuration
$\mathcal{B}_i$	Domain of a local continuum body in Euclidean space
$\mathcal{B}_t$	Domain of a continuum body in the current configuration
$\partial\mathcal{B}$	Boundary of a continuum body in Euclidean space
$\partial\mathcal{B}_0$	Boundary of a continuum body in the reference configuration
$\partial\mathcal{B}_i$	Boundary of a local continuum body
$\partial\mathcal{B}_t$	Boundary of a continuum body in the current configuration

$\mathbf{b}$	left Cauchy-Green tensor
$\mathbf{b}_0$	Outer volume force or body force
C^n	Space of n-times continuously differentiable functions
$\mathbb{C}$	Elasticity tensor or elasticity matrix
$\mathbb{C}^{tan}$	Tangential material stiffness in nonlinear calculations
$\mathbb{C}$	Elasticity tensor or tangential material stiffness
$\mathbf{C}$	Right Cauchy-Green tensor
d	Damage variable in isotropic material
D_i	Damage variable in anisotropic material
$\mathrm{d}\mathbf{a}$	Area element in current configuration
$\mathrm{d}\mathbf{A}$	Area element in reference configuration
D	Gâteaux directional derivative
$\mathcal{D}_{int}$	Internal dissipation or entropy production
$\mathrm{d}v$	Infinitesimal volume in current configuration
$\mathrm{d}V$	Infinitesimal volume in reference configuration
$\mathrm{d}\mathbf{X}$	Line element in reference configuration
$\mathrm{d}\mathbf{x}$	Line element in current configuration
e_0	Internal mechanical energy per unit volume
$\mathbf{e}_i$	Orthonormal base system in Euclidean space
$\mathcal{E}$	Internal energy
$\mathbf{E}$	Green-Lagrange strain tensor
$\mathbf{f}_e^L$	Element residual vector in a local scale boundary value problem
$\mathbf{f}_0$	Resultant of outer forces
$\mathbf{F}_i^L$	Global residual vector in a local scale boundary value problem
$\mathbf{F}$	Deformation gradient
G	Shear modulus
G_c	Critical energy release rate
h	Height (length in z-direction)
$\mathbf{H}$	Displacement gradient
$\mathbb{H}$	Damage compliance matrix
i, j	Indexes 1, 2, 3
$\mathbf{I}$	Identity matrix or tensor
J	Jacobian determinant of deformation gradient
$\mathbf{J}$	Jacobian matrix
$\dot{\mathbf{J}}$	Time derivative of angular momentum
$\mathbf{k}^G$	Global scale element tangential stiffness matrix
$\mathbf{k}_e^L$	Element tangential stiffness matrix in a local scale boundary value problem
$\mathcal{K}$	Kinetic energy

$\mathbf{K}_T$	Global tangential stiffness matrix
$\mathbf{K}_i^L$	Global tangential stiffness matrix in a local scale boundary value problem
l_x	Length in x-direction
l_y	Length in y-direction
l_c	Characteristic element length
L	Linearization of functional
$\dot{\mathbf{L}}$	Time derivative of linear momentum
$\mathbb{M}$	Damage effect tensor or matrix
n_{eq}	Number of equations
$\mathbf{n}$	Unit normal vector in current configuration
$\mathbf{n}_0$	Unit normal vector in reference configuration
N_I	Interpolation functions
$\mathbf{N}$	Unit normal vector
$\mathcal{P}_{ext}$	External mechanical power
$\mathcal{P}_{int}$	Internal mechanical stress power
$\mathbf{P}$	First Piola-Kirchhoff stress tensor
$\mathbf{q}_0$	Cauchy heat flow
$\mathcal{Q}$	Thermal power
$\tilde{\mathcal{Q}}$	Rate of ingoing entropy
$\mathbf{Q}$	Orthogonal tensor
r_0	Heat source
r	Damage threshold
$\mathbf{r}$	Position vector to reference point
$\mathbf{R}$	Rotation tensor
$\mathbf{s}$	Stress deviator
s_0	Local entropy per unit volume
$\mathcal{S}$	Entropy integrated over volume
$\mathbf{S}$	Second Piola-Kirchhoff stress tensor
$\mathbb{S}$	Compliance Tensor or compliance matrix
t	Time; thickness
$\bar{\mathbf{t}}$	Surface force
$\mathbf{t}_i$	Local base vectors
t_0	Initial time for reference configuration
$\mathbf{t}_0$	Outer boundary force vector
$\mathbf{t}$	Cauchy traction vector
$\mathbf{T}$	Cauchy stress tensor
u_x, u_y, u_z	Displacement components in spatial directions x, y, z
$\mathbf{u}$	Displacement vector

$\delta\mathbf{u}$	Virtual displacement field
$\Delta\mathbf{u}$	Increment of displacement field
$\mathbf{U}$	Right stretch tensor
$\mathbf{v}_0$	Velocity vector of control volume
$\mathbf{v}$	Left stretch tensor (Ch. 2); vector of nodal displacements (Ch. 5–7)
$\mathbf{V}_i^L$	Global displacement vector in a local scale boundary value problem
w	Displacement in z-direction
W	Mechanical work
δW	Virtual work
δW_{ext}	External virtual work
δW_{int}	Internal virtual work
X, Y, Z	Material coordinates
x, y, z	Spatial coordinates
$\mathbf{X}$	Position vector in reference configuration
$\mathbf{x}$	Position vector in current configuration

Kurzfassung

Faserverbundwerkstoffe gewinnen in den verschiedensten Ingenieurwissenschaften immer mehr an Bedeutung. Dieser Trend wird sich in den nächsten Jahren, gerade im Hinblick auf E-Mobilty und immer höheren Materialanforderungen, noch verstärken. Mit der zunehmenden Verwendung wird auch die Nachfrage nach geeigneten Berechnungsverfahren zur Beschreibung des komplexen mechanischen Verhaltens dieser Werkstoffe immer größer. Diese Arbeit leistet einen Beitrag zur theoretischen Entwicklung und Implementierung von Schädigungsmodellen. Mit Hilfe von Schädigungsmodellen kann der Beginn der Schädigung lokalisiert, der Verlauf durch die Struktur verfolgt sowie deren Traglast bestimmt werden. In der vorliegenden Arbeit werden verschiedene Modellansätze verfolgt, die auf einem sogenannten Smeared-Crack-Ansatz basieren. Dabei wird die Schädigung im Material als kontinuierlich verteilt angenommen. Vorgestellt wird ein auf makroskopischer Betrachtung basierendes anisotropes Schädigungsmodell, das wahlweise das Bruchkriterium nach Hashin oder das Failure Mode Concept nach Cuntze zur Bestimmung des Schädigungsbeginns verwendet. Der Verlauf der Schädigung wird durch ein lineares Degradationsmodell beschrieben, dessen Steigung von der kritischen Energiefreisetzungsrate bestimmt wird. Um die dissipierte Energie in Finite-Elemente-Modellen korrekt zu berechnen, wird die charakteristische Elementlänge als zusätzlicher Parameter eingeführt. Mit den gewonnenen Erkenntnissen wird dann ein zweiter Ansatz verfolgt, der auf einem zweiskaligen Finite-Elemente-Modell basiert, das aus einem Mikromodell und einem Makromodell besteht. Hierbei werden die Verzerrungen des Makromodells als Verschiebungsrandbedingungen auf das Mikromodell aufgebracht. In dem Mikromodell wird die Beschreibung der Schädigung separat auf den einzelnen Faser- und Matrixanteilen durchgeführt. Die endgültigen inneren Verschiebungen des Mikrosystems werden mit dem Newton-Raphson-Verfahren bestimmt und die homogenisierten Spannungen und die Materialtangente werden an das Makrosystem zurückgegeben. Die Schädigung im verwendeten Mikromodell wird durch ein exponentielles Degradationsgesetz ohne elastische Anfangsregion beschrieben, das sich als besonders robust erwiesen hat. Ein Gegenargument zur Verwendung von Mehrskalenmodellen ist die erhebliche Rechenzeit, da in jedem Integrationspunkt des globalen Systems ein komplettes Mikrosystem gelöst werden muss. Da sich aber Mehrskalenmodelle, aufgrund ihrer Struktur, besonders zur simultanen parallelen Berechnung eignen, ist zu ist zu erwarten, dass sie mittelfristig die makroskopischen Modelle ersetzen werden.

Abstract

Fiber-reinforced plastics are of increasing relevance in a broad variety of engineering applications. Developments in E-Mobility and ever-increasing demands on materials guarantee that this trend will continue. The increasing use and importance of FRP will in turn increase demand for appropriate methodologies for describing the complex mechanical properties of these materials. This thesis contributes to this end to the theoretical development and implementation of damage models. These models build on the so called smeared crack approach, whereby the damage in the material is assumed to have a continuous distribution. With the help of damage models, maximum bearing load computations can be performed and the damage initiation and propagation can be precisely followed. A variety of approaches are used in this thesis: firstly, a macroscopic view of anisotropic damage models is presented. The model utilizes either Hashin's failure criterion or Cuntze's failure mode concept to determine damage initiation. At the onset of damage, a linear degradation model is used, the path of which is determined by the critical energy release rate. In conjunction with the characteristic element length, an accurate calculation of the dissipated energy in the finite element model is assured. A second approach is based on a coupled multi-scaled finite element model. The model presented here is a two-scale model consisting of a micro scale and a macro scale. The distortions in the macro scale are mapped onto the micro scale using appropriate boundary conditions. In the micro scale, the modeling of the damage is carried out separately on the individual fiber and polymer components. The nonlinear micro model is solved by means of Newton-Raphson method before the homogenized stresses and material tangents are delivered to the macro system. This process is repeated until global equilibrium is achieved. The micro scale model utilizes an exponential degradation law, which lacks an elastic initial region and has proven to be especially robust. The multi scale model affects damage at locations where it actually occurs, giving it a significant advantage over macroscopic models. The use of costly failure criterion is spared in this approach. Furthermore, use of the multi scale approach allows detailed observations of the failure in the material, and failure modes such as fiber-polymer separation can easily be implemented. The counterargument to this approach is the significant computational cost, caused by the necessity of a complete iteration loop in the micro system for every integration point in the global system. However, the structure of the models makes them especially suitable for simultaneous parallel processing, so that it can be expected that they supersede macroscopic models in the mid term future.

Chapter 1

Introduction

1.1 Motivation and Objectives

Fiber-reinforced composite materials have gained recent popularity in high-performance products. In fact, global demand for carbon fiber has more than doubled over the last five years. The main reason for this is its impressive weight to stiffness ratio. A composite generally indicates a material class made of at least two different constituents. Subclasses include carbon fiber-reinforced polymers (CFRP), glass fiber-reinforced polymers (GFRP), aramid products (e.g. Kevlar), and biocomposites, which typically consist of one stiffness constituent (the reinforcement) and one binding constituent (the matrix). Classical applications of composite materials can be found in:

- Aircrafts
- Sports equipment
- Racing and automotive components
- Boats and marine
- Wind turbine plates

The Airbus A350, for example, uses more than 50% of composite materials in the fuselage and wing and saves roughly 25% in fuel as opposed to its aluminum competitors . In the automotive sector, carbon fiber composites have been used in race cars for years, where a conservation of mass is important. In automotive serial production, a rapid rise in the use of composite materials can also be observed. The BMW i8 and BMW i3, for example, have developed a passenger cabin made completely of a carbon fiber composites, which is not only much lighter, but also significantly stiffer and thus safer for passengers than metals. The automotive and transportation sectors are likely the main field where a rapid growth in the use of composite materials is expected in the coming years. Especially considering trends of E-Mobility, where the heavy weight of batteries must be conserved in other parts of the automobile to save energy and improve acceleration. Other applications of composite materials include wind turbine plates

(the less weight the plate has, the more energy it can produce), surfboards, mountain bikes, and snowboards. Besides weight savings, composites also have benefits in terms of design flexibility, low maintenance costs, and they have high stiffness, non-corrosive, and non-conductive properties. For this reason, and because of their flexibility in the choice of constituent, they are increasingly replacing metals in classical civil engineering applications, like prestressed concrete bridges, subsequent reinforcement of supporting frameworks, or even for constructional earthquake protections. The increasing use of composite materials makes it necessary to develop suitable methods which capture the complicated load deformation processes of such anisotropic material classes, especially, when nonlinear effects, such as damage, must be considered. One such approach is established on a macroscopic material level. Many macroscopic damage models have been developed for fiber-reinforced composites within the last decade, for instance, in [79, 84, 87–90]. In macroscopic damage models, different constituents are usually considered with their volume fraction and stiffness properties and then simple averaged. For further investigations, a material with homogeneous (averaged) properties is observed, instead taking into account the inhomogeneous nature of composites. For damage models, this means that failure or damage criteria must be established on the same macroscopic, averaged material level for each single damage mode, such as fiber failure, matrix failure, and delamination. Many such failure criteria have been developed, for instance, by the authors of [45, 65, 115]. One disadvantage of these models is the large number of material input parameters required. Besides averaged elastic properties, strength and fracture energy parameters are required for a physically accurate description of the damage process. These parameters are difficult to acquire and must often be determined in complicated experiments, which usually implies a shady quality.

Microscopic models are more accurate and convenient to describe complex damage processes. With such models, the damage process is described on a finer scale, where it actually occurs. Not only does the damage process, but also parameter identification, become easier to capture on a microscale. In micro models, different constituents are considered individually. This is particularly advantageous when considering each constituent as an isotropic material. Then, the various, more expensive failure modes discussed are no longer necessary, and instead, an easy to handle isotropic failure mode can be used for each constituent. Often when using finite element methods, and within this study, a microscopic model is used in conjunction with a macroscopic model, leading to the concept of multiscale models. Multiscale models also have computational advantageous because of their good parallel computing ability.

When using multiscale models, effective quantities of the micro model are returned to the macro model for further calculations. These effective quantities are obtained from a homogenization procedure. Several such procedures have been developed which can be subdivided into analytical, semi-analytical, and computational homogenization procedures. Classical homogenization methods assume that the homogenized effective properties of the micro model remain constant. Such an assumption is obviously infringed in damage simulations.

Contrary to classical homogenization methods, coupled macro-micro models or more general global-local models are used for nonlinear damage simulations in which the effective properties of the micro model change during the calculation. In such coupled finite element calculations, each integration point of the global system is connected to one local scale model such that every element is homogenized individually, dependent on its current load state. This means that the local model is assessed for each integration point of each iteration in each load step. Using this coupled approach results in expensive computational calculations, but unlike full scale models, the global model can be partitioned in much larger parts.

This thesis aims to predict the maximum bearing load of fiber-reinforced composite structures. Therefore, several varying approaches for the simulation of damage in fiber-reinforced composite are introduced. First, an isotropic and anisotropic one-scale model are introduced. Special attention is given to the numerical implementation. The anisotropic model is developed based on the works of [79, 87, 89, 92]. To improve Newton convergence issues, an Implicit-Explicit integration scheme, first proposed by Oliver [109], is adapted from an isotropic model for use in anisotropic damage models. Additionally, the crack band theory [13] is applied to weaken the effect of mesh dependent solutions and localization phenomenon. The full scale model uses eight noded, finite continuum elements with linear shape functions for the discretization. Because full scale damage models have limits, and damage itself is better described on a microscale, another approach, namely a multiscale damage model for fiber-reinforced composite structures is suggested. Therefore, a general multiscale procedure [62] is introduced, followed by an introduction to micromechanical concepts and homogenization procedures. Some important aspects obtained from the anisotropic full scale damage model are inherited to improve numerical robustness. The multiscale model is used with eight noded, finite continuum elements with linear shape functions on a macroscale. The microscale is approximated using an enhancement of the method of cells (EMOC) which is also developed in section 7.3.2 of this thesis. Again, particular attention is given to the numerical implementation of the model. Both models are verified and tested on several examples with experimental test data and plausibility controls.

1.2 State of Research

In this study, several different models for damage simulations are introduced based on continuum damage mechanics (CDM). Continuum damage mechanics is a common engineering approach to model the complex mechanisms of damage on a macroscopic scale. Damage mechanics is a field of applied mechanics based on continuum mechanics. The chief aim of CDM is the prediction of damage initiation, its progress in structures, and how the overall stiffness is affected.

The development of CDM began in the 1970s and 1980s when a wide variety of research in the field of damage mechanics was completed by [24, 25, 76, 80, 97, 98, 124, 125]. It is during this time that CDM was invented. The damage process highly depends on the investigated material and the type of load that causes it (static or dynamic). One can distinguish, among others,

between ductile, brittle, and creep damage, as well as damage initiated by fatigue. Composite materials, investigated in the current study, belong to the class of brittle damage. Moreover, the current study considers only static loads. Since the pioneering work of [73], who defined damage as the decrease of the load carrying area, several other approaches have been proposed. For instance, [25] uses fourth and eighth-order tensors to represent damage in terms of the variation of the elastic modulus. A more general definition of effective stresses has been proposed by [25, 42, 123], where a so called damage effect tensor, a fourth-order tensor, is used to transform the Cauchy stresses σ into the corresponding, fictitious effective stresses. This approach results in a general and non-symmetric stress tensor. Therefore, several symmetrization schemes have been proposed by the authors of [25, 42, 99, 101, 123]. Since these schemes are developed purely in a mathematical sense, [42] introduced a form of mechanical equivalence which satisfies the condition of symmetry. This is called the hypotheses of complementary strain energy equivalence. From this, several other equivalence principles and approaches have been developed. For further information, and a fundamental historical background of the development of damage mechanics, the more recent works of [81, 100, 138] are recommended.

Another topic which belongs to CDM is the use of cohesive laws, commonly used in interface models for the propagation of delamination in layered structures. Several such laws are based on a universal relationship between binding energies of materials, first introduced, among others, in [21, 102, 111, 118]. Since their introduction, they have been implemented in finite element software by many authors, for example, in [103, 119, 120, 131, 132], or more recently in [5, 61, 134, 135].

The finite element method is often used to solve problems in structural mechanics. It has been established, among a variety of numerical methods, as a standard method in engineering mechanics. The finite element method has had practical relevance since the 1950s and was first used at Boeing for structural computations on aircraft wings. The works [140, 141] are well known and have been established as standard references since the 1960s. More recent works concerning nonlinear finite element methods include, for instance, [11, 46, 71, 116, 122, 137]. A more mathematically grounded approach is given in, for example, [17, 106], whereas [127] focuses on implementation techniques.

The theory of cohesive laws and its application in finite elements has been a basis for many studies concerning CDM. For instance, [63, 79, 94], are based on the theory proposed by Camanho et al. in [22]. This study introduced the concept of equivalent displacements within the theory of delamination. It enhances and modifies the theory for use in continuum damage models, as is completed in the implemented macroscopic anisotropic damage model in the current study. The damage evolution law of this model considers the energy released during a damage process according to the works of [13, 107].

The heterogeneous nature of fiber-reinforced composites and the complex behavior of damage have inspired researchers to develop more accurate and convenient models than macroscopic models. The latter are limited due to the averaged nature of quantities, such as Youngs moduli

and strength parameter. Not only are averaged elastic parameters a disadvantage of macro models, but also the mechanism of damage itself is difficult to capture. To overcome these difficulties, multiscale models have been developed. In multiscale formulations, at least two different scales are used for the description of a problem: a global or macro scale and a local or micro scale. The expressions of global and local scales are more general and often used in the current study because the multiscale approach is not limited to micro-macro systems, as can be seen in [62, 66].

A global scale is used to discretize an arbitrary geometry of interest, whereas a local scale is used to capture the behavior of complex materials within a so called representative volume element (RVE). Of interest for the macro model are the effective quantities from the RVE which are obtained by applying homogenization methods.

Homogenization methods can be divided into analytical, semi-analytical, and computational techniques. Classic analytical methods relate to Eshelby's theory [52], who used an analytical approximation of the micromechanical material. The microscopic structure is decomposed into a homogeneous infinite matrix material with isolated elliptical inclusions. The Eshelby solution is a fundamental principal for the development of analytical homogenization methods. Without a claim of completeness, examples include the derivation of the differential scheme [93] and the double inclusion method [104] have been derived. Moreover, so called mean field theories, [39, 40, 64, 68] have been developed, and in the context of interacting adjacent particles, the Mori-Tanaka method [96] was introduced and later extended.

Due to its limitations in practical use, semi-analytical methods have been developed. Such methods attempt to use the advantages of numerical homogenization techniques by maintaining the efficiency of analytical techniques. For a detailed overview of analytical and semi-analytical homogenization methods, please refer to [4, 38, 49, 56, 59, 142].

Of special interest for the current study are coupled homogenization techniques in association with the MOC , originally introduced by [1]. The MOC was later extended by the same author [2, 113] to the generalized method of cells (GMC), which has itself been further developed into the high fidelity generalized method of cells (HFGMC) [3].

In this study, both scales are discretized with finite elements, leading to the application of computational homogenization techniques. This technique becomes increasingly important because of the increase in computational power. Unlike semi-analytical models, the micro problem is also described with numerical solution techniques, such as finite elements.

By using finite elements for the description of the micro scale, any arbitrary geometry can easily be discretized. When addressing strongly nonlinear problems like damage, an iterative coupling between the scales is inevitable. Here, coupling implies that the local model is executed in each integration point of the global model. This can be enabled either by hard-coding the local FEM routine into the material law of the integration point of the global system or by using an FE^2

approach such as in [126] and [53], where the FE program is accessed a second time at the integration point. Recent contributions concerning the FE^2 method are given in [121] or [62] in the context of layered shells. For use of the FE^2 method within the topic of damage simulations, the reader is referred to [114, 133].

Many different types of materials and composites, such as fiber-reinforced materials and polycristallines, have been investigated by means of multiscale methods (MM) [53, 57, 58, 74, 75, 95]. A rapid rise of research in this area is based on increases in computational power. Within the last decade, numerous articles and textbooks on the subject have been published. Most publications focus on general approaches, the determination of material properties, or damage modeling. A reliable overview of publications concerning MM and the handled topics is given in [4]. The authors of [77] and [54], for example, focus on general simulation techniques. In [14] and [32] specific aspects of composite materials are discussed and in [12], the topic of modeling damage is treated.

1.3 Outline

Chapter 2 presents the important and relevant foundations of continuum mechanics. The kinematic equations of a continuum body are introduced by means of the deformation gradient from which different strains tensors are derived. To analyze how a continuum behaves under the impact of external loads, the concept of stress is discussed and several traction vectors and stress tensor are introduced. For further mechanical investigations, it is important to know which strain and stress tensors can be used together, thus work conjugated tensor pairs are suggested. After naming important mechanical and thermo-mechanical balance laws, important principles of virtual work are derived by means of a one field variational principle for numerical implementation. Having defined some general valid relations, constitutive laws for hyperelastic, transversely isotropic materials, and materials classes with internal variables are discussed to describe mechanical coherences. The elasticity tensor $\mathbb{C}$ and its inverse, the stiffness tensor $\mathbb{S}$ are explicitly derived for several material classes because they are applied in the description of damage processes in the following chapter.

Chapter 3 extends definitions of continuum mechanics to capture the process of damage, included within the scope of CDM . General principles of CDM, as well as a short historical overview of the description of three dimensional damage states, are followed by a presentation of different equivalence principles. A thermo-mechanically consistent damage model is derived with a special focus on Kuhn-Tucker conditions which enforce a correct response of the model in terms of loading, unloading, and reloading conditions. After introducing varying damage effect tensors and suggesting a damage compliance matrix for transversely isotropic materials, the topic of damage initiation in particular is discussed. Therefore, different failure criteria which serve as a starting point for damage evolution are presented for isotropic and anisotropic composite materials. The evolution law, then discussed, relates internal variables to the damage

variable and is necessary to fully define the constitutive equations of damage models. Evolution laws are based on energy dissipation during the damage process which can be challenging to correctly determine in numerical approximation methods, such as the finite element method. The chapter concludes with a universal relationship between binding energies of materials, used for interface damage modes in chapter 7.

Chapter 4 presents an isotropic and an anisotropic damage model. The isotropic damage model is based on work by [108]. The model begins with a definition of a Helmholtz free energy from which the required quantities, such as stresses and constitutive equations, are derived by incorporating the concept of effective stresses, as given in chapter 3. The crack band theory is applied to ensure the correct computation of the energy dissipated during a damage process and to reduce mesh dependency in finite element calculations. Because the modeling of brittle material failure suffers from a lack of numerical robustness, an implicit-explicit integration scheme (IMPL-EX), first proposed in [110], is presented, with which highly robust solutions are obtained. Furthermore, an anisotropic model is suggested for damage simulations in fiber-reinforced composites. The developed damage model uses the concept of equivalent displacements, first proposed by [22], and a bilinear damage evolution law in conjunction with the characteristic element length to ensure correct damage dissipation. The damage compliance matrix $\mathbb{H}$ is dependent on the different damage mode and is derived from a complementary free energy function (Gibbs energy). The number of damage modes differs depending on whether Hashin's damage criterion or Cuntze's failure mode concept is applied. For the same reason as in the isotropic damage model, the IMPL-EX scheme is adapted and modified such that it can be used for the anisotropic damage model.

Both damage models are implemented into the finite-element software Feap using eight noded continuum elements with linear interpolation functions, introduced in **chapter 5**. The nonlinear finite-element description begins with the linearized, weak form of equilibrium, followed by a presentation of the isoparametric concept and derivation of the approximated Green-Lagrange strain tensor. Using the variation, linearization, and variation of linearization, the consistent linearized variational functional is derived, from which the element stiffness matrix and element residual vector are obtained. By means of standard assembly procedures, the global load vector and global stiffness matrix are obtained. With these definitions, the damage models are fully described and can be used in finite element calculations.

Chapter 6 is one of two chapters containing numerical examples. The isotropic and anisotropic damage models are validated and tested on several different models. After demonstrating some general aspects of damage models, the implemented isotropic damage model is tested in terms of convergence studies. Furthermore, damage behavior under displacement driven simulations is observed in greater detail. Various implemented damage models, as well as the effects of different regularization schemes, are tested with the anisotropic damage model before results from the IMPL-EX scheme are compared to results from the standard implicit schemes. The damage behavior and load displacement paths are discussed after the model is validated with

simple damage mode examples and experimental test data.

Chapter 7 presents a coupled multiscale model for damage simulation. First, the formulation of the principle of virtual work and its linearization are extended to incorporate the characterization of a micro model. The equations obtained are then used for the finite element formulation of a two-scale model, whereby the general procedure introduced in [62] is used. The required input quantities for this formulation are obtained from the section discussing micromechanics and homogenization. After a short introduction of micro-macro concepts, the MOC, introduced in [1] is presented. This method is the basis for EMOC, introduced in section 7.3.2. The EMOC is enhanced such that damage can be simulated in interface elements positioned between the original subcell elements. Furthermore, to capture longitudinal fiber damage, the MOC is extended to a third periodic direction. The EMOC is fully described with special attention given to boundary conditions because they serve as the connection between the scales. After deriving the kinetic equations and the finite element quantities, such as local residual vector $\mathbf{f}$ and local stiffness matrix $\mathbf{k}$, potential damage modes are discussed in greater detail. Each damage mode is based on the universal atomistic binding energy, introduced in chapter 3. In addition to classical damage modes, such as fiber damage and matrix damage, debonding damage modes, known as a driving quantity of delamination, are incorporated within the model.

Chapter 8 is the second chapter to employ numerical examples. The multiscale damage model is first elastically verified through a comparison between analytical results of the MOC and experimental test data from the world wide failure exercise (WWFE). Once the elastic behavior is proven, the damage modes are activated and the model is contrasted, using single damage mode examples, with experimental tests from WWFE and numerical data provided by [51]. Finally, the damage behavior of specific problems is investigated in greater detail.

Finally, the results are summarized in **chapter 9**, where future perspectives and suggestions regarding damage modeling are also provided.

Chapter 2

Basics of Continuum Mechanics

For the purpose of modeling solid mechanics using the finite element method, it is essential to introduce the basic concepts of kinematics, deformations, stresses, constitutive equations and thermodynamics within the context of continuum mechanics. Continuum mechanics is a branch of mechanics, which deals with continuous distributed quantities rather than discrete particles. Following this approach, physical phenomena are modeled on a macroscopic level, without detailed consideration of the microscopic circumstances, which tend to be sufficiently accurate for certain engineering problems. Concerning some specific mechanical problems, such as damage mechanics, microscopic material behavior can be considered in the macroscopic model in a statistical averaged sense by introducing and plugging in so called internal variables.

In this chapter, the basic equations of continuum mechanics are discussed. Starting with a general description of motion, deformation and perspectives from which the required tensor quantities are derived. The concept of stress is subsequently introduced, followed by work conjugated tensor pairs and the crucial balance laws of continuum mechanics. Considering some thermodynamic aspects, the chapter ends with an exploration of variational principles and their linearization, subsequently leading to the most important and in this work extensively used constitutive equations.

For a more comprehensive and detailed introduction to continuum mechanics, the reader is referred to the fundamental works on this subject, such as [6, 15, 31, 70, 91]. The textbooks of [6, 70] have been indispensable to this study, and are highly recommended for prospective researchers in the field of continuum mechanics. Further works, such as [9, 72, 78] are also used in specific issues. For a brief conclusion to the most important aspects of continuum mechanics, the works of [16, 60, 137] should be mentioned.

In the following descriptions, it is assumed that the indexes of Roman letters $i, j, ...$ range from 1-3, the Greek indexes $\alpha, \beta, ...$ range from 1-2, and the Einstein summation convention is used, which implies summation of a set of index terms.

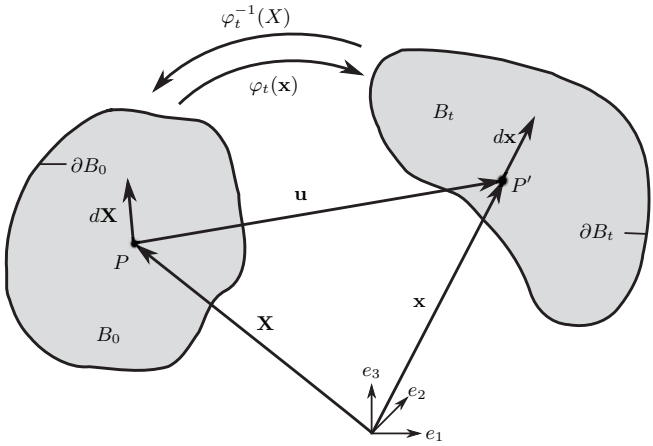

Figure 2.1: Reference configuration and current configuration of a continuum body.

2.1 Kinematics of a Continuum

When considering a continuum body $\mathcal{B}$ as a bulk of material points (particles) with its boundary surface $\partial\mathcal{B}$ and its Volume V. The continuum body is described in the Euclidean space $\mathbb{E}^3$, and consists, at any time t, of the same particles. It is important to note that a particle refers to a body and is defined in a mathematical sense; a single particle does not have any mass nor is it associated with a point mass in Newton's mechanics. The motion of a continuum body is described through the motion of its material points. Therefore, it is necessary to identify each and every material point on the continuum body with a position vector $\mathbf{X}$.

2.1.1 Configurations and Perspectives

In order to describe motion or a deformation process, the change of a continuum body is observed from one state to another, which is generally called the reference configuration at time $t = t_0$, or the current (deformed) configuration at an arbitrary time $t = t_0 + \Delta t$. The body will generally change in shape, position and orientation from one state to another. A notational distinction between the two configurations is made by identifying the continuum body and its surface in the reference configuration with $\mathcal{B}_0$ and $\partial\mathcal{B}_0$, and in the current configuration with $\mathcal{B}_t$ and $\partial\mathcal{B}_t$, respectively.

A material point $P \in \mathcal{B}_0$ in the reference configuration can be described by a position vector $\mathbf{X}$ relative to the origin at an arbitrary chosen orthonormal base system $\{\mathbf{e}_i\}$ with $i = 1, 2, 3$.

The same material point $P' \in \mathcal{B}_t$ in the current configuration is described by a position vector $\mathbf{x}$ relative to the same base system, as illustrated in figure 2.1. In general, the base systems of two different configurations do not necessarily have to coincide, however, for the purpose of this study, it is assumed that they do.

A one-to-one (bijective) and in general nonlinear function of the position vector $\mathbf{X}$

$$\hat{\varphi}(\mathbf{X}, t) : \mathcal{B}_0 \mapsto B_t \tag{2.1}$$

is introduced, which maps material points from the reference configurations into material points in the current configurations. Since the transformation is bijective, an inverse function

$$\hat{\varphi}^{-1}(\mathbf{x}, t) : \mathcal{B}_t \mapsto B_0 \tag{2.2}$$

exists, which then maps material points from the current configuration into material points in the reference configuration. A bijective function signifies that each material point of one configuration is paired with exactly one material point of the second configuration. It is spread widely to label the functions $\hat{\varphi}(\mathbf{X}, t)$ and $\hat{\varphi}^{-1}(\mathbf{x}, t)$ in a shortened notation as $\hat{\varphi}_t(\mathbf{X})$ and $\hat{\varphi}_t^{-1}(\mathbf{x})$.

Furthermore, in continuum mechanics, there are at least two different perspectives which affect, among others, the time derivatives of motion. In the Lagrangian (or material, or referential) description, a viewer is related to a material point and observes, with respect to the material coordinates (X_1, X_2, X_3), what happens to the particle when it moves. In the Eulerian (or spatial) description, a viewer is related to a fixed position and observes the change of a point space (field functions) at a specific location, with respect to the spatial coordinates (x_1, x_2, x_3). Once the equations of motion from a material point are known, the perspective can be switched by means of equations (2.1) and (2.2). Generally, in solid continuum mechanics, Lagrangian coordinates and the reference description are used. However, in fluid mechanics, due to large displacements and complex deformations, it is usually necessary and most practical to use Eulerian coordinates and the spatial description.

Having discussed some basic aspects of continuum mechanics, it is now necessary to define more specific quantities that help to describe the deformation process of a continuum body. These quantities are either defined with respect to the reference configuration in Lagrangian coordinates or with respect to the current configuration in Eulerian coordinates. To denote scalar, vector and tensor quantities, uppercase letters are used when they are evaluated in the reference configuration, whereas lowercase letters are used for quantities evaluated in the current configuration. Sometimes quantities in the reference configuration are also identified by a subscripted 0, and in the current configuration by a subscripted t (e.g. $\mathcal{B}_0$, $\mathcal{B}_t$, $\partial\mathcal{B}_0$ and $\partial\mathcal{B}_t$). All vector and tensor quantities that are declared in this study refer to an orthonormal base system $\{\mathbf{e}_i\}$.

2.1.2 Deformation and Deformation Gradient

For the purpose of relating line, area and volume elements from the reference to the current configuration, the deformation gradient $\mathbf{F}$ is introduced. The deformation gradient is in general an non-symmetric, two-point tensor field of second order, which refers to both the reference and the current configuration. Even though the deformation gradient is not suitable for strain measurement, as is discussed in the next chapters, it still serves as a basis for such suitable quantities.

Assuming a linear mapping, as represented in

$$\mathbf{x} = \mathbf{x}(\mathbf{X}, t) \quad \text{or} \quad x_i = x_i(X_j, t) \quad , \tag{2.3}$$

the deformation gradient from the reference to the current configuration is defined by the following equation:

$$\mathbf{F} = \operatorname{Grad} \mathbf{x}(\mathbf{X}, t) := \frac{\partial \mathbf{x}}{\partial \mathbf{X}} \quad \text{or} \quad [F_{ij}] = \left[\frac{\partial x_i}{\partial X_j}\right] \quad . \tag{2.4}$$

Here, the components of equation (2.4) are the partial derivatives of the coordinates x_i with respect to the coordinates X_i. $\mathbf{F}$ causes a transformation of a (infinitesimal) material line element $d\mathbf{X}$ in the reference configuration to a material line element $d\mathbf{x}$ in the current configuration

$$\mathrm{d}\mathbf{x} = \mathbf{F}(\mathbf{X}, t)\, \mathrm{d}\mathbf{X} \quad \text{or} \quad \mathrm{d}x_i = F_{ij} \mathrm{d}X_j \quad . \tag{2.5}$$

Since equation (2.3) represents a bijective mapping, $\mathbf{F}$ is also bijective and a singularity can be debarred. Furthermore, to exclude self-penetration as well, the Jacobian determinant has to be greater than zero. These last conditions can be expressed as

$$J = \det \mathbf{F} = \det \left[\frac{\partial x_i}{\partial X_j}\right] > 0 \quad . \tag{2.6}$$

Due to the positive determinant ($J > 0$), an inverse mapping $\mathbf{F}^{-1}$ exists at all times t. The inverse mapping maps a deformed line element $\mathrm{d}\mathbf{x}$ in the current configuration back to a material line element $d\mathbf{X}$ in the reference configuration:

$$\mathrm{d}\mathbf{X} = \mathbf{F}^{-1}(\mathbf{x}, t)\, \mathrm{d}\mathbf{x} \quad \text{or} \quad \mathrm{d}X_i = F_{ij}^{-1} \mathrm{d}x_j \quad . \tag{2.7}$$

The inverse deformation gradient is defined by

$$\mathbf{F}^{-1}(\mathbf{x}, t) = \operatorname{grad} \mathbf{X}(\mathbf{x}, t) := \frac{\partial \mathbf{X}}{\partial \mathbf{x}} \quad \text{or} \quad \left[F_{ij}^{-1}\right] = \left[\frac{\partial X_i}{\partial x_j}\right] \quad . \tag{2.8}$$

In addition, the deformation gradient not only transforms line elements, but also area and volume elements from one configuration to another. By describing the area element in the

reference configuration d$\mathbf{A}$ by its vectors in the following equation:

$$d\mathbf{A} = \mathrm{d}\mathbf{X} \times \mathrm{d}\mathbf{X} \quad , \tag{2.9}$$

using relation (2.5), and some further calculations, the following transformation for area elements can be obtained:

$$\mathrm{d}\mathbf{a} = J\mathbf{F}^{-T} d\mathbf{A} \quad . \tag{2.10}$$

An infinitesimal volume element dV is mapped by the Jacobian determinant J into the deformed volume dv with

$$\mathrm{d}v = J\mathrm{d}V \quad . \tag{2.11}$$

The Jacobian determinant J is thus a measure for the relative change in volume during a deformation.

2.1.3 Displacement and Displacement Gradient

In some cases, as is examined later in this study, it is advantageous to define kinematic quantities with respect to the displacement gradient $\mathbf{H}$ or the displacement vector $\mathbf{u}$. Similar to the deformation gradient, the displacement gradient explains how material line elements transform from the reference to the current configuration.

As illustrated in figure 2.1, the displacement vector of a particle P in a continuum, identified by its material coordinate $\mathbf{X}$, from the reference position $\mathbf{X}$ to the current position $\mathbf{x}$ is given by the vector

$$\mathbf{u}(\mathbf{X}, t) = \mathbf{x}(\mathbf{X}, t) - \mathbf{X} \quad . \tag{2.12}$$

Since the displacement field is a function of the reference position $\mathbf{X}$ at time $t = t_0$, equation (2.12) shows its Lagrangian description. The Eulerian description leads to the following expression of the displacement vector:

$$\mathbf{u}(\mathbf{x}, t) = \mathbf{x} - \mathbf{X}(\mathbf{x}, t) \quad . \tag{2.13}$$

Following the preceding equation one can conclude that whenever the path lines of a continuum are known, its displacement field is also known. Note that the displacement field in the Eulerian description has the same values as in the Lagrangian description, but represents different functions in its arguments. For rigid body motions, the displacement field is independent of $\mathbf{X}$, which signifies that all particles of the continuum move identically.

Moreover, the second-order displacement gradient tensor is defined by the partial derivative of the displacement field, and therefore depends on whether the displacements are defined in Lagrangian coordinates or in Eulerian coordinates. In the Lagrangian description, the derivative

leads to the following displacement gradient tensor:

$$\mathbf{H} = \operatorname{Grad} \mathbf{u} = \frac{\partial \mathbf{u}}{\partial \mathbf{X}} \quad \text{or} \quad [H_{ij}] = \left[\frac{\partial u_i}{\partial X_j}\right] \tag{2.14}$$

By substituting relation (2.12) into equation (2.14), the displacement gradient $\mathbf{H}$ can also be represented by means of the deformation gradient:

$$\mathbf{H} = \mathbf{F}(\mathbf{X}, t) - \mathbf{I} \quad \text{or} \quad [H_{ij}] = F_{ij} - \delta_{ij} \quad . \tag{2.15}$$

2.1.4 Polar Decomposition

The deformation gradient $\mathbf{F}$ was introduced as a non-singular ($\det \mathbf{F} > 0$) second-order tensor, describing transformations of line elements. These transformations, in general, include rigid body rotations as well as stretching. Due to the rigid body rotation, it is not suitable to measure strains. For any tensor $\mathbf{T}$ with a non-zero determinant, an equivalent decomposition into a product of an orthogonal tensor and a symmetric tensor exists. In terms of the deformation gradient, a unique polar decomposition in the form of

$$\mathbf{F} = \mathbf{R}\,\mathbf{U} = \mathbf{v}\,\mathbf{R} \tag{2.16}$$

can be conducted. In the preceding equation, $\mathbf{U}$ and $\mathbf{v}$ are known as the right stretch tensor and the left stretch tensor, respectively, where $\mathbf{R}$ is an orthogonal rotation tensor ($\mathbf{R}^{-1} = \mathbf{R}^T$). A physical interpretation can be executed by applying the decomposition to an infinitesimal line element:

$$\mathrm{d}\mathbf{x} = \mathbf{F}\,\mathrm{d}\mathbf{X} = \mathbf{R}\mathbf{U}\mathrm{d}\mathbf{X} \quad . \tag{2.17}$$

The Tensor $\mathbf{U}$ describes a pure stretch along its eigenvectors, followed by a rigid body rotation $\mathbf{R}$. Similarly, a deformation can be expressed as a rigid body rotation $\mathbf{R}$, followed by pure stretching $\mathbf{v}$. It is clear that there is no geomectrical difference between these two expressions, even though the stretch tensors $\mathbf{U}$ and $\mathbf{v}$ do differ, and their components have a different geometric significance. The relation of the two stretch tensors are defined as:

$$\begin{aligned} \mathbf{U} &= \mathbf{R}^T \mathbf{v} \mathbf{R} \\ \mathbf{v} &= \mathbf{R}\mathbf{U}\mathbf{R}^T \quad . \end{aligned} \tag{2.18}$$

2.1.5 Measurement of Strain

Having defined the deformation gradient $\mathbf{F}$ in the preceding sections, and keeping in mind that it is not a suitable quantity for strain measures, the aim of this chapter is to introduce the most common strain tensors related to either the material or the spatial description used in the field of nonlinear solid continuum mechanics. According to whether the strain is based on the reference configuration $\mathrm{d}\mathbf{X}^2$ or on the current configuration $\mathrm{d}\mathbf{x}^2$, two symmetric and positive

definite strain tensors can be introduced:

$$\begin{aligned} \mathbf{C} &= \mathbf{U}^2 = \mathbf{F}^T \mathbf{F} \quad , \\ \mathbf{b} &= \mathbf{v}^2 = \mathbf{F} \mathbf{F}^T \quad . \end{aligned} \tag{2.19}$$

They are known as the right Cauchy-Green tensor $\mathbf{C}$, and the left Cauchy-Green tensor $\mathbf{b}$, present in the reference configuration and in the current configuration, respectively.

The geometrical interpretation of another, and probably one of the most important, strain measure has its interpretation in the change of the square lengths $\mathrm{d}\mathbf{x}^2 - \mathrm{d}\mathbf{X}^2$. Using relation (2.5), and the identity tensor $\mathbf{I}$, one can define the so-called Green-Lagrange strain tensor as

$$\mathbf{E} = \frac{1}{2} \left(\mathbf{F}^T \mathbf{F} - \mathbf{I} \right) = \frac{1}{2} \left(\mathbf{C} - \mathbf{I} \right) \quad . \tag{2.20}$$

Since the tensors $\mathbf{C}$ and $\mathbf{I}$ are both symmetric and related to the reference configuration, $\mathbf{E} = \mathbf{E}^T$ is also valid. The analogue strain tensor to $\mathbf{E}$, associated to the current configuration, is known as the Euler-Almansi strain tensor and is defined by

$$\boldsymbol{\gamma} = \frac{1}{2} \left(\mathbf{I} - \mathbf{F}^{-T} \mathbf{F}^{-1} \right) = \frac{1}{2} \left(\mathbf{I} - \mathbf{b}^{-1} \right) \quad . \tag{2.21}$$

An alternative description of the Green-Lagrange tensor can be obtained by using the displacement gradient (2.14):

$$\mathbf{E} = \frac{1}{2} \left(\mathbf{H}^T + \mathbf{H} + \mathbf{H}^T \mathbf{H} \right) \quad . \tag{2.22}$$

The preceding defined vector or tensor quantities belong either to the reference configuration or the current configuration. An exception is the two-field deformation gradient tensor $\mathbf{F}$, which is associated to both configurations. The transformation of quantities between these two configurations is typically called a push-forward or a pull-back operation. In this context, a push-forward operation transforms vector or tensor quantities based on the reference configuration into the current configuration, whereas a pull-back operation transforms vector or tensor quantities based on the current configuration (back) to the reference configuration. Specifically, this leads to the following transformation equations for the Green-Lagrange tensor and the Euler-Almansi tensor:

$$\begin{aligned} \boldsymbol{\gamma} &= \mathbf{F}^{-T} \mathbf{E} \mathbf{F}^{-1} \quad , \\ \mathbf{E} &= \mathbf{F}^T \boldsymbol{\gamma} \mathbf{F} \quad . \end{aligned} \tag{2.23}$$

In terms of the so called linear theory ($\mathbf{H} \ll 1$), the nonlinear terms in equation (2.22) can be neglected, and the Green-Lagrange strain tensor $\mathbf{E}$ and the Euler-Almansi strain tensor $\boldsymbol{\gamma}$ coincide, and can then be expressed as the widely used linearized strain tensor (engineering strain tensor)

$$\begin{aligned} \boldsymbol{\varepsilon} = \mathbf{E} = \boldsymbol{\gamma} &= \frac{1}{2} \left(\mathbf{H}^T + \mathbf{H} \right) \\ \varepsilon_{ij} &= \frac{1}{2} \left(\frac{\partial u_i}{\partial x_j} + \frac{\partial u_j}{\partial x_i} \right) = \frac{1}{2} \left(u_{i,j} + u_{j,i} \right) \quad . \end{aligned} \tag{2.24}$$

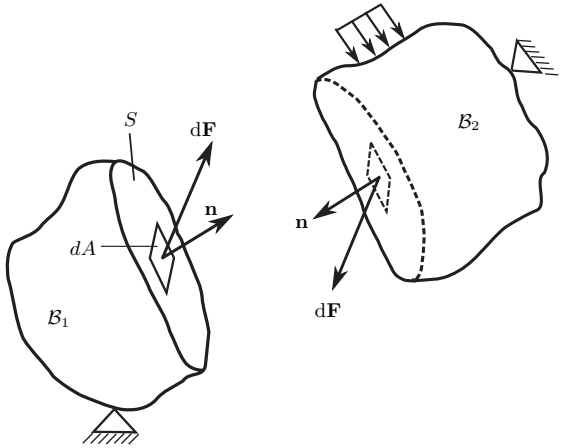

Figure 2.2: Visualization of Cauchy stresses.

Throughout this study, the expression $u_{i,j}$ generally signifies the partial derivative of the component u_i with respect to the component of $\mathbf{x}_j$.

2.2 The Concept of Stress - Kinetic Equations

Purely kinematic equations have been shown without any consideration of external loads that act on the continuum and cause these deformations. According to the kinematic descriptions of motion, elaborated in the previous section, kinetic equations are derived in this section, which are also independent of specific material properties. Therefore, in order to analyze how a continuum body behaves under external loads, the concept of stress is introduced. The term external load contains two different types of forces that can act on a body, body forces $\bar{\mathbf{g}}$ acting throughout a volume (e.g. gravity), and surface forces $\bar{\mathbf{t}}$ acting on the surface of a body. In classical continuum mechanics the volume of a material point is close to zero ($\mathrm{d}V \to 0$), and therefore, the existence of momentum-stress vectors are debarred. In addition, by imagining an arbitrary chosen virtual cut along a plane surface S that subdivides the body $\mathcal{B}$ into two sub-bodies $\mathcal{B}_1$ and $\mathcal{B}_2$, the concept of internal forces $\mathbf{t}$ is introduced, describing the reaction at this resulting surface, caused by the impact of external loads.

With regard to picture 2.2 the Cauchy traction vector is defined as

$$\mathbf{t} = \mathbf{t}(\mathbf{x}, \mathbf{n}) = \lim_{\Delta A \to 0} \frac{\Delta \mathbf{F}}{\Delta A} = \frac{\mathrm{d}\mathbf{F}}{\mathrm{d}A} \quad , \tag{2.25}$$

with $\Delta \mathbf{F}$ being the resultant force acting on a small area ΔA, and $\mathbf{n}$ being the unit normal vector with respect to the surface S.

2.2.1 Stress Tensors

The Cauchy traction vector $\mathbf{t}$, acting within a given spatial point $\mathbf{x}$, depends on the orientation of the unit vector $\mathbf{n}$. The Cauchy theorem implies that a linear mapping exists:

$$\mathbf{t} = \mathbf{T}\mathbf{n} \quad \text{or} \quad t_i = T_{ij} n_j \quad . \tag{2.26}$$

Here $\mathbf{T}$ denotes a symmetrical ($\mathbf{T} = \mathbf{T}^T$) tensor field, called the Cauchy stress tensor, which is no longer dependent on the orientation of $\mathbf{n}$. In addition, $\mathbf{T}$ and $\mathbf{t}$ are related to the current configuration, thus they are also known as the true stress vector and true stress tensor, respectively. Another stress tensor acting in the current configuration is the Kirchhoff stress tensor given by

$$\boldsymbol{\tau} = J\,\mathbf{T} \quad . \tag{2.27}$$

In numerical simulations of solid bodies, it is useful to define stress tensors acting in the reference configuration rather than in the current configuration. Following a similar procedure as has been declared above in this section, or by simply deriving it from the Cauchy stress tensor by transformation relations, another stress tensor known as the first Piola-Kirchhoff stress tensor, can be defined:

$$\mathbf{P} = J\,\mathbf{T}\,\mathbf{F}^{-T} \quad . \tag{2.28}$$

The first Piola-Kirchhoff tensor $\mathbf{P}$ is also known as a nominal-stress tensor related, like the deformation gradient, to both the current and the reference configuration. However, since $\mathbf{P}$ is generally non-symmetric and not completely related to the reference configuration, the second Piola-Kirchhoff tensor $\mathbf{S}$ is introduced:

$$\mathbf{S} = \mathbf{F}^{-1}\mathbf{P} = J\,\mathbf{F}^{-1}\,\mathbf{T}\,\mathbf{F}^{-T} \quad . \tag{2.29}$$

The second Piola-Kirchhoff tensor is symmetric ($\mathbf{S} = \mathbf{S}^T$), and is, in contrast to the previously defined stress tensors, completely related to the reference configuration. Even though its components do not have a descriptive interpretation, $\mathbf{S}$ is the most important tensor in the branch of finite element methods and, as is discussed in section 2.2.3, is work conjugated to the Green-Lagrange strain tensor $\mathbf{E}$.

2.2.2 Time Derivatives and Strain Rates

The aim of this section is to derive the time derivatives of vector or tensor quantities with respect to different configurations. The material description provides a value φ at time t for a material point $\mathbf{X}$; in contrast, the spatial description provides a value φ at time t for a fixed location $\mathbf{x}$. Thus, it is apparent that there are different time derivatives depending on which theory is underlying.

In a material description, considering that $\mathbf{X}$ is independent of t, the local derivative is given as

$$\frac{\mathrm{D}\,\varphi(\mathbf{X},t)}{\mathrm{D}\,t} = \frac{\partial\varphi}{\partial t} \quad . \tag{2.30}$$

The material derivative for a spatially-described field function, considering that the coordinates $\mathbf{x}$ are no longer independent of t, is calculated as

$$\begin{aligned}\frac{\mathrm{D}\,\varphi\left(\mathbf{x}(\mathbf{X},t),t\right)}{\mathrm{D}\,t} &= \frac{\partial\varphi}{\partial t} + \frac{\partial\varphi}{\partial\mathbf{x}}\cdot\frac{\partial\mathbf{x}}{\partial t} \\ &= \frac{\partial\varphi}{\partial t} + \mathbf{v}\cdot\operatorname{grad}\varphi \quad .\end{aligned} \tag{2.31}$$

Using the preceding declarations, one can derive the material derivative of a spatially-described acceleration field with

$$\mathbf{a} = \frac{\mathrm{D}\,\mathbf{v}(\mathbf{x},t)}{\mathrm{D}\,t} = \frac{\partial\mathbf{v}}{\partial t} + \frac{\partial\mathbf{v}}{\partial\mathbf{x}}\cdot\frac{\partial\mathbf{x}}{\partial\mathbf{t}} \quad . \tag{2.32}$$

The derivative of $\mathbf{v}$ with respect to $\mathbf{x}$ is known as the velocity gradient; it holds for velocities a similar interpretation as the deformation gradient holds for coordinates. Again, it is necessary to consider whether working with quantities acting in the material or in the spatial description. The derivative of a spatial velocity $\mathbf{v}(\mathbf{x},t)$ field with respect to the spatial coordinates is defined by

$$\operatorname{grad}\mathbf{v}(\mathbf{x},t) = \frac{\partial\mathbf{v}(\mathbf{x},t)}{\partial\mathbf{x}} = \mathbf{l}(\mathbf{x},t) = \dot{\mathbf{F}}\mathbf{F}^{-1} \quad , \tag{2.33}$$

with $\mathbf{l}$ being a non-symmetric second-order tensor. The derivative of a velocity field with respect to a material description is defined by

$$\operatorname{Grad}\mathbf{V}(\mathbf{X},t) = \frac{\partial\mathbf{V}(\mathbf{X},t)}{\partial\mathbf{X}} = \dot{\mathbf{F}}(\mathbf{X},t) \quad . \tag{2.34}$$

It can be shown that the spatial velocity gradient $\mathbf{l}$ can be decomposed into a symmetric part and an asymmetric part of the spatial velocity gradient $\mathbf{l}$, denoted with $\mathbf{d}$ and $\mathbf{w}$, respectively:

$$\mathbf{l}(\mathbf{x},t) = \mathbf{d}(\mathbf{x},t) + \mathbf{w}(\mathbf{x},t) \quad . \tag{2.35}$$

Both $\mathbf{d}$ and $\mathbf{w}$ are purely spatial fields, defined as

$$\begin{aligned}\mathbf{d} &= \frac{1}{2}\left(\mathbf{l}+\mathbf{l}^T\right) = \frac{1}{2}\left(\operatorname{grad}\mathbf{v} + \operatorname{grad}^T\mathbf{v}\right) = \mathbf{d}^T \quad , \\ \mathbf{w} &= \frac{1}{2}\left(\mathbf{l}-\mathbf{l}^T\right) = \frac{1}{2}\left(\operatorname{grad}\mathbf{v} - \operatorname{grad}^T\mathbf{v}\right) = -\mathbf{w}^T \quad .\end{aligned} \tag{2.36}$$

Finally, for the purpose of defining an energetic conjugated tensor pair in the next section, and without further elaborating the time derivative of the Green-Lagrange strain tensor, the following equation is constructed:

$$\dot{\mathbf{E}} = \frac{1}{2}\left(\mathbf{F}^T\dot{\mathbf{F}} + \dot{\mathbf{E}}^T\mathbf{F}\right) = \mathbf{F}^T\frac{1}{2}\left(\mathbf{l}^T+\mathbf{l}\right)\mathbf{F} = \mathbf{F}^T\mathbf{d}\mathbf{F} \quad . \tag{2.37}$$

2.2.3 Energetic Conjugated Stresses and Strains

For mechanical calculations, it is often necessary to calculate work or energy in terms of stresses and strains. As is elaborated further in this paper, the internal virtual work, calculated by infinitesimal stresses and strains, must equal the external infinitesimal work, executed by corresponding virtual displacements and loads. The aim of this section is to derive the energetic conjugated stress and strain relations. They must be selected in a way that their product, the internal stress power (internal energy density), accurately reflects the internally stored strain energy in an observed system.

In a spatial description, the internal stress power is given by means of the Cauchy stress tensor $\mathbf{T}$ and the spatial velocity gradient $\mathbf{l}$:

$$\mathcal{P}_{int} = \int_{\mathcal{B}_t} \mathbf{T} : \mathbf{l} \, \mathrm{d}v \quad . \tag{2.38}$$

Using equation (2.11) and (2.27), the internal work can be reformulated related to the Kirchhoff stress tensor integrated over the initial volume:

$$\mathcal{P}_{int} = \int_{\mathcal{B}_t} \mathbf{T} : \mathbf{l} \, \mathrm{d}v = \int_{\mathcal{B}_0} J\mathbf{T} : \mathbf{l} \, \mathrm{d}V = \int_{\mathcal{B}_0} \tau : \mathbf{l} \, \mathrm{d}V \quad . \tag{2.39}$$

Similarly, and additionally using equations (2.28) and (2.37), another energetic conjugated pair is given with

$$\begin{aligned} \mathcal{P}_{int} &= \int_{\mathcal{B}_t} \mathbf{T} : \mathbf{l} \, \mathrm{d}v = \int_{\mathcal{B}_0} J \, tr\left(\mathbf{T}\mathbf{l}^T\right) \, \mathrm{d}V \\ &= \int_{\mathcal{B}_0} Jtr\left(\mathbf{T}\mathbf{F}^{-T}\mathbf{F}^T\mathbf{l}^T\right) \, \mathrm{d}V = \int_{\mathcal{B}_0} J \, tr\left(\mathbf{T}\mathbf{F}^{-T}(\mathbf{l}\mathbf{F})^T\right) \, \mathrm{d}V \\ &= \int_{\mathcal{B}_0} \left(J\mathbf{T}\mathbf{F}^{-T} : (\mathbf{l}\mathbf{F})\right) \, \mathrm{d}V \\ &= \int_{\mathcal{B}_0} \mathbf{P} : \dot{\mathbf{F}} \, \mathrm{d}V \qquad , \end{aligned} \tag{2.40}$$

where the scalar product of two second-order tensors is expressed by

$$\mathbf{A} : \mathbf{B} = tr\left[\mathbf{B}^T\mathbf{A}\right] = tr\left[\mathbf{A}\mathbf{B}^T\right] = tr\left[\mathbf{B}\mathbf{A}^T\right] = tr\left[\mathbf{A}^T\mathbf{B}\right] \quad . \tag{2.41}$$

Following a similar procedure, using equations (2.28) and (2.37) and replacing $\mathbf{l}$ with $\mathbf{d}$, a last

energetic conjugated pair can be derived:

$$\begin{aligned}\mathcal{P}_{int} &= \int_{\mathcal{B}} \mathbf{T} : \mathbf{d}\, \mathrm{d}v = \int_{\mathcal{B}_0} \left(\frac{1}{J}\mathbf{P}\mathbf{F}^T\right) : \left(\mathbf{F}^{-T}\dot{\mathbf{E}}\mathbf{F}^{-1}\right) J\, \mathrm{d}V \\ &= \int_{\mathcal{B}_0} tr\, \left(\mathbf{F}\mathbf{P}^T\mathbf{F}^{-T}\dot{\mathbf{E}}\mathbf{F}^{-1}\right) \mathrm{d}V \\ &= \int_{\mathcal{B}_0} \mathbf{S} : \dot{\mathbf{E}}\, \mathrm{d}V \quad .\end{aligned} \tag{2.42}$$

In conclusion, whenever the internal virtual work has to be calculated, one has to choose one of the four pairs $(\mathbf{T}, \mathbf{l})$, $(\boldsymbol{\tau}, \mathbf{l})$, $(\mathbf{P}, \dot{\mathbf{F}})$ and $(\mathbf{S}, \dot{\mathbf{E}})$. All other combinations are physically wrong and consequently invalid.

2.3 Balance Laws

Balance laws describe the general principles or laws of nature. They are valid for all kinds of materials and have an axiomatic character. They can be established in a global integral form, acting on the whole body, as well as in a differential local form, acting in every point of the body. Balance laws are used to connect the external loads on a body with its internal quantities. They are called conservation laws if these quantities are constant during a process. In this section, the mechanical conservation laws are derived, which are the conservation of mass, linear momentum, angular momentum, and energy, and by means of the first and second law of thermodynamics, the entropy inequality is derived. These defined formulations are used as a basis for describing deformation processes in solid mechanics. They are applicable to any particular material and must be satisfied at all times. According to the preceding sections, it is important to know that the balance laws can be described in the reference and the current configurations. The description is performed in both configurations depending on which is easier to describe or which quantity is required later in this work. The introduced notation clarifies which of both descriptions is intended. By means of transformation relations, as defined earlier, one can switch from one configuration to another.

Conservation laws have a general pattern. For the current configuration, the following equation is applicable:

$$\frac{\mathrm{D}}{\mathrm{D}\,t} \int_{\Omega_t} \Psi(\mathbf{x}, t) \mathrm{d}v = \int_{\Omega_t} \Xi(\mathbf{x}, t) \mathrm{d}v + \int_{\partial\Omega_t} \mathbf{n}(\mathbf{x}, t) \cdot \Phi(\mathbf{x}, t)\, \mathrm{d}a \quad . \tag{2.43}$$

At the same time, the following equation applies to the reference configuration:

$$\frac{\mathrm{D}}{\mathrm{D}\,t} \int_{\Omega_0} \Psi_0(\mathbf{X}, t) \mathrm{d}V = \int_{\Omega_0} \Xi_0(\mathbf{X}, t) \mathrm{d}V + \int_{\partial\Omega_0} \mathbf{n}_0(\mathbf{X}, t) \cdot \Phi_0(\mathbf{X}, t)\, \mathrm{d}A \quad . \tag{2.44}$$

The preceding equations describe the rate of change of an overall quantity, expressed by $\Psi(\mathbf{x}, t)$

and $\Psi_0(\mathbf{X}, t)$. Here $\Xi_0(\mathbf{X}, t)$ and $\Xi(\mathbf{x}, t)$ signify the volume densities representing sources and sinks inside the body Ω, and $\Phi(\mathbf{x}, t)$ and $\Phi_0(\mathbf{X}, t)$ being surface densities of external impact, representing flow across the bodies surface $\partial\Omega$.

In summary, the rate of change of a balance quantity Ψ equals the sum of inflow and outflow Φ across the body's surface A, and the increase or loss Ξ of the balance quantity Ψ inside the body $\mathcal{B}$.

2.3.1 Balance of Mass

Every continuum body $\mathcal{B}$ possesses mass, denoted by m, used to measure the amount of material inside that body. It is assumed that the mass is uniformly distributed over the body $\mathcal{B}$, and is further invariant during motion. As such, body mass can be calculated with

$$m = \int_{\mathcal{B}_0} \rho_0(\mathbf{X}) \, \mathrm{d}V = \int_{\mathcal{B}_t} \rho(\mathbf{x}, t) \, \mathrm{d}v = \text{const} \quad . \tag{2.45}$$

Here $\rho_0(\mathbf{X})$ and $\rho(\mathbf{x}, t)$ describe the mass density of an infinitesimal volume $\mathrm{d}V$ and $\mathrm{d}v$ in the reference and the current configurations.

Considering the continuity of mass (2.45), and using equation (2.11), the Jacobian determinant not only is a measure of change in volume, but also a measure of change in mass density during a deformation process, if the mass remains unchanged:

$$J = \frac{\rho_0}{\rho} \quad . \tag{2.46}$$

Following equations (2.43) or (2.44) and under the condition that the mass m is a scalar field, no production occurs inside the body, and no mass is exchanged over the surface, the global conservation of mass can be defined by

$$\dot{m} = \frac{\mathrm{D}}{\mathrm{D}\,t} \int_{\mathcal{B}_t} \rho(\mathbf{x}, t) \mathrm{d}v = \int_{\mathcal{B}_t} \left(\frac{\partial}{\partial t} \rho(\mathbf{x}, t) + \operatorname{grad} \cdot [\rho(\mathbf{x}, t) \mathbf{v}] \right) \mathrm{d}v = 0 \quad . \tag{2.47}$$

From this follows the local form of conservation of mass in the Eulerian description:

$$\frac{\partial}{\partial t} \rho(\mathbf{x}, t) + \operatorname{grad} \cdot [\rho(\mathbf{x}, t) \mathbf{v}] = 0 \quad . \tag{2.48}$$

2.3.2 Balance of Linear Momentum

The conservation of linear momentum is a generalization of Newton's second law applied to a continuum body. As such, it is also known as the first Eulerian equation of motion and states, that the change of linear momentum in time is equal to the sum of all external volume and

surface force. In material description, and considering a closed system it reads

$$\frac{\mathrm{D}}{\mathrm{D}\,t}\int\limits_{\mathcal{B}_0}\rho_0\mathbf{v}(\mathbf{X},t)\,\mathrm{d}V=\int\limits_{\mathcal{B}_0}\mathbf{b}_0(\mathbf{X},t)\rho_0\,\mathrm{d}V+\int\limits_{\partial\mathcal{B}_0}\mathbf{t}_0(\mathbf{X},t)\,\mathrm{d}A\quad . \tag{2.49}$$

Here, $\mathbf{v}$ is the velocity of the observed continuum, $\mathbf{b}_0$ is an external body force (e.g. gravity) and $\mathbf{t}_0$ is an external traction vector acting on the bodies surface:

$$\int\limits_{\mathcal{B}_0}(\mathbf{b}_0-\rho_0\dot{\mathbf{v}})\,\mathrm{d}V+\int\limits_{\partial\mathcal{B}_0}\mathbf{t}_0\,\mathrm{d}A=\mathbf{0}\quad . \tag{2.50}$$

Using the divergence theorem and $\mathbf{t}_0=\mathbf{P}\mathbf{n}$, which states that

$$\int\limits_{\partial\mathcal{B}_0}\mathbf{t}_0\,\mathrm{d}A=\int\limits_{\partial\mathcal{B}_0}\mathbf{P}\mathbf{n}\,\mathrm{d}A=\int\limits_{\partial\mathcal{B}_0}\mathrm{Div}[\mathbf{P}]\,\mathrm{d}V\quad , \tag{2.51}$$

equation (2.50) can be written as

$$\int\limits_{\mathcal{B}_0}(\mathrm{Div}\,\mathbf{P}+\rho_0\mathbf{b}_0-\rho_0\dot{\mathbf{v}})\;\mathrm{d}V=\mathbf{0} \tag{2.52}$$

or, in its local form as

$$\mathrm{Div}\,\mathbf{P}+\rho_0\mathbf{b}_0-\rho_0\dot{\mathbf{v}}=\mathbf{0}\quad . \tag{2.53}$$

At the same time, in a static case, the acceleration is zero ($\dot{\mathbf{v}}=0$), the time derivative vanishes, and the equation reduces to

$$\mathrm{Div}\,\mathbf{P}+\rho_0\mathbf{b}_0=\mathbf{0}\quad . \tag{2.54}$$

2.3.3 Balance of Angular Momentum

The Angular momentum is the rotational analog of the linear momentum; it is an important quantity in mechanics. If there is no external torque on the continuum, it is subject to the fundamental constraints of the conservation of angular momentum. According to the linear momentum, the conservation law is obtained by differentiating the angular momentum with respect to time t:

$$\begin{aligned}\frac{\mathrm{D}}{\mathrm{D}\,t}\int\limits_{\mathcal{B}_0}\mathbf{r}\times\rho_0\mathbf{v}(\mathbf{X},t)\,\mathrm{d}V&=\int\limits_{\mathcal{B}_0}\mathbf{r}\times\mathbf{b}(\mathbf{X},t)\,\mathrm{d}V+\int\limits_{\partial\mathcal{B}_0}\mathbf{r}\times\mathbf{t}_0(\mathbf{X},t)\,\mathrm{d}A\\ \text{or}\quad \dot{\mathbf{J}}&=\mathbf{m}_0\quad .\end{aligned} \tag{2.55}$$

Here, the vector $\mathbf{r}$ denotes the position vector $\mathbf{r}=\mathbf{x}-\mathbf{x}_0$ with respect to a fixed point $\mathbf{x}_0$. The symmetry of the Cauchy stress tensor is ensured using equation (2.55) by inserting current quantities for $\mathbf{v}$, $\mathbf{b}$ and $\mathbf{t}$. By using the Cauchy stress theorem (2.26), the divergence theorem,

equation (2.55), and further calculations, the following equation is yielded:

$$\sigma_{32} - \sigma_{23} = 0 \quad , \qquad \sigma_{13} - \sigma_{31} = 0 \quad , \qquad \sigma_{21} - \sigma_{12} = 0 \quad . \tag{2.56}$$

This relation is only satisfied if the Cauchy stress tensor σ is symmetric $\sigma = \sigma^T$

2.3.4 Balance of Mechanical Energy

In this section, only mechanical energy is considered. Other types of energy, such as thermal energy, are neglected, as they are considered in the following section. The conservation of energy is a consequence of the conservation of linear momentum and implies that in a closed system, the rate of change of kinetic energy $\mathcal{K}$, plus the internal stress power $\mathcal{P}_{int}$ of a system equals the external mechanical power $\mathcal{P}_{ext}$ created by the impact of external loads:

$$\frac{\mathrm{D}}{\mathrm{D}\,t}\mathcal{K} + \mathcal{P}_{int} = \mathcal{P}_{\mathrm{ext}} \quad . \tag{2.57}$$

In the preceding equation the following definitions are used:

$$\begin{aligned} \mathcal{K} &= \int_{\mathcal{B}_0} \frac{1}{2}\rho_0 \mathbf{v}(\mathbf{X},t)\cdot\mathbf{v}(\mathbf{X},t)\,\mathrm{d}V \quad , \\ \mathcal{P}_{int} &= \int_{\mathcal{B}_0} \mathbf{P} : \dot{\mathbf{F}}\,\mathrm{d}V = \int_{\mathcal{B}_0} \mathbf{S} : \dot{\mathbf{E}}\,\mathrm{d}V \quad , \\ \mathcal{P}_{\mathrm{ext}} &= \int_{\mathcal{B}_0} \left(\mathbf{b}_0(\mathbf{X},t)\cdot\mathbf{v}(\mathbf{X},t) + r_0\right)\,\mathrm{d}V + \int_{\partial\mathcal{B}_0} \mathbf{t}_0(\mathbf{X},t)\cdot\mathbf{v}(\mathbf{X},t)\,\mathrm{d}A \quad . \end{aligned} \tag{2.58}$$

Inserting the preceding definitions in (2.57), the conservation of mechanical energy in an isothermal process in the material description can finally be expressed by

$$\frac{\mathrm{D}}{\mathrm{D}\,t}\int_{\mathcal{B}_0} \frac{1}{2}\rho_0 \mathbf{v}\cdot\mathbf{v}\,\mathrm{d}V + \int_{\mathcal{B}_0} \mathbf{S} : \dot{\mathbf{E}}\,\mathrm{d}V = \int_{\mathcal{B}_0} \mathbf{b}_0\cdot\mathbf{v}\,\mathrm{d}V + \int_{\partial\mathcal{B}_0} \mathbf{t}_0\cdot\mathbf{v}\,\mathrm{d}A \quad . \tag{2.59}$$

Here the external loads are defined in equation (2.58) and refer to the reference configuration.

In order to involve more general forms of energy in the next section, equation (2.57) can be reformulated as

$$\frac{\mathrm{D}}{\mathrm{D}\,t}(\mathcal{K} + \mathcal{U}) = \mathcal{P}_{\mathrm{ext}} \quad , \tag{2.60}$$

Here $\mathcal{U}$ signifies the internal energy of a continuum, while u describes a thermodynamic state variable, including all kinds of microscopic internal energy per unit volume:

$$\mathcal{U} = \int_{\mathcal{B}_0} u(\mathbf{X},t)\rho\,\mathrm{d}V \quad , \tag{2.61}$$

or, in an explicit form according to equation (2.59):

$$\frac{\mathrm{D}}{\mathrm{D}\,t}\int\limits_{\mathcal{B}_0}\left(\frac{1}{2}\rho_0\mathbf{v}\cdot\mathbf{v}+u\rho_0\right)\mathrm{d}V=\int\limits_{\mathcal{B}_0}\mathbf{b}_0\cdot\mathbf{v}\,\mathrm{d}V+\int\limits_{\partial\mathcal{B}_0}\mathbf{t}_0\cdot\mathbf{v}\,\mathrm{d}A \quad . \tag{2.62}$$

Where the left hand side describes the total energy of a system, as a sum of the kinetic energy and all internal energies caused by the external power $\mathcal{P}_{\mathrm{ext}}$. When only mechanical energy is considered, the time derivative of $\mathcal{U}$ equals the internal stress power $\mathcal{P}_{int}$:

$$\frac{\mathrm{D}}{\mathrm{D}\,t}\mathcal{U}=\mathcal{P}_{int} \quad . \tag{2.63}$$

2.3.5 Balance of Energy - The First Law of Thermodynamics

A thermodynamic continuum is known as a continuum which possesses both mechanical and thermal energy. In order to extend equation (2.60) to include a thermodynamic part, a new quantity is defined as

$$\mathcal{Q}(t)=\int\limits_{\mathcal{B}_0}R\rho_0\,\mathrm{d}V-\int\limits_{\partial\mathcal{B}_0}\mathbf{Q}\cdot\mathbf{n}_0\,\mathrm{d}A \quad . \tag{2.64}$$

Here, $\mathcal{Q}$ is defined as the thermal power, which is a sum of heat flux vector $\mathbf{Q}$ per unit time and unit surface, and a heat source R per unit time and unit volume inside the continuum. With this equation, the definition of the rate of internal energy $\mathcal{U}$ in equation (2.63) has to be expanded, and now equals the sum of internal mechanical stress power $\mathcal{P}_{int}$ plus the rate of thermal work $\mathcal{Q}$:

$$\mathcal{P}_{int}+\mathcal{Q}=\frac{\mathrm{D}}{\mathrm{D}\,t}\mathcal{U} \quad . \tag{2.65}$$

The preceding equation is known as the balance of thermal energy.

Plugging in equation (2.65) in the equation of balance of mechanical energy (2.57) the important equation of balance of energy is obtained:

$$\frac{\mathrm{D}}{\mathrm{D}\,t}\mathcal{K}+\frac{\mathrm{D}}{\mathrm{D}\,t}\mathcal{U}=\mathcal{P}_{ext}+\mathcal{Q} \quad . \tag{2.66}$$

Inserting the defined expressions (2.58),(2.64) and (2.61), using Stokes heat flux theorem and the divergence theorem, the reduced first law of thermodynamics in material description can be written in a global (integrated) form as

$$\frac{\mathrm{D}}{\mathrm{D}\,t}\int\limits_{\mathcal{B}_0}u\rho_0\,\mathrm{d}V=\int\limits_{\mathcal{B}_0}\left(\mathbf{S}:\dot{\mathbf{E}}-\mathrm{Div}\,\mathbf{Q}+R\rho_0\right)\mathrm{d}V \quad . \tag{2.67}$$

Since the volume V is independent of time t, the local form of the reduced first law of thermodynamics can be expressed as

$$\rho_0\dot{u}=\mathbf{S}:\dot{\mathbf{E}}-\mathrm{Div}\,\mathbf{Q}+R\rho_0 \quad . \tag{2.68}$$

Equation (2.67) and (2.68) can be transferred to the spatial description, yielding

$$\begin{aligned} \frac{\mathrm{D}}{\mathrm{D}\,t}\int\limits_{\mathcal{B}} u\rho\,\mathrm{d}v &= \int\limits_{\mathcal{B}} \Big(\mathbf{T} : \dot{\mathbf{d}} - \operatorname{div}\mathbf{q} + r\rho\Big)\,\mathrm{d}v \\ \rho\dot{u} &= \mathbf{T} : \dot{\mathbf{d}} - \operatorname{div}\mathbf{q} + r\rho \quad . \end{aligned} \tag{2.69}$$

In summary, it has been shown that the first law of thermodynamics states that the rate of change of total energy (kinetic and internal) of a system equals the total energy input into that system, conducted by mechanical and thermal energy.

2.3.6 Entropy Inequality - The Second Law of Thermodynamics

The second law of thermodynamics is based on the concept of entropy and provides directional information of energy transformations. It specifies, for instance, that heat is always transferred from a warmer to a colder region inside a continuum. Entropy is an important quantity in the field of irreversible continuum mechanics, such as damage mechanics. Conservation of entropy implies a reversible process, whereas an entropy production always implies an irreversible process. Decreasing entropy is physically impossible, e.g. heat produced during a friction process can never be transferred back into mechanical energy.

Defining the entropy with

$$\mathcal{S} = \int\limits_{\mathcal{B}_0} \rho_0 s\,\mathrm{d}V \tag{2.70}$$

the second law of thermodynamics can be defined as

$$\Gamma = \dot{\mathcal{S}} - \tilde{\mathcal{Q}} \geq 0 \quad . \tag{2.71}$$

This states, that the total production of entropy Γ per unit time equals the difference between the rate of change of entropy $\dot{\mathcal{S}}$ and the rate of entropy input $\tilde{\mathcal{Q}}$ in a system. In addition, it postulates that entropy production is always greater than zero in all thermodynamic processes. By introducing more relations to the second law of thermodynamics, it can be defined more explicitly with

$$\Gamma = \frac{\mathrm{D}}{\mathrm{D}\,t}\int\limits_{\mathcal{B}_0} \rho_0 s\,\mathrm{d}V + \int\limits_{\partial\mathcal{B}_0} \frac{\mathbf{Q}}{\Theta}\cdot\mathbf{n}_0\,\mathrm{d}A - \int\limits_{\mathcal{B}_0} \frac{R}{\Theta}\rho_0\,\mathrm{d}V \geq 0 \quad . \tag{2.72}$$

This is known as the Clausius-Duhem inequality, here presented in the material description. The local form can be obtained by converting the surface integral into a volume integral and back substituting the result in equation (2.72), yielding

$$\rho_0\Theta\dot{s} - \rho_0 R + \operatorname{Div}\mathbf{Q} - \frac{1}{\Theta}\mathbf{Q}\cdot\operatorname{Grad}\Theta \geq 0 \quad . \tag{2.73}$$

An alternative version of the local form is given by

$$\rho_0 \Theta \dot{s} - \rho_0 \dot{u} + \mathbf{S} : \dot{\mathbf{E}} - \frac{1}{\Theta} \mathbf{Q} \cdot \operatorname{Grad} \Theta \geq 0 \quad . \tag{2.74}$$

Since heat flows from warmer to colder regions, entropy production by conduction of heat must be non-negative. Assuming the temperature gradient to vanish, implies that there is no heat flux. According to these restrictions, the Clausius-Duhem inequality can be redefined in a stronger form as

$$\mathcal{D}_{int} := \mathbf{S} : \dot{\mathbf{E}} - \rho_0 \dot{u} + \Theta \dot{s} \quad . \tag{2.75}$$

This is known as the Clausius-Planck inequality, or also as the dissipation inequality.

Moreover, a function which is equal to the difference of inner energy and entropy can be defined by

$$\Psi = u - \Theta s \quad . \tag{2.76}$$

This is known as a free energy function or as Helmholtz free energy. It further suggests an adiabatic process, meaning that thermal energy cannot cross of the boundary nor can it be produced inside the continuum. This is presented in the reduced equation

$$\begin{aligned} \mathcal{D}_{int} &= \mathbf{P} : \dot{\mathbf{F}} - \dot{\Psi}_0 \geq 0 \quad , \\ \mathcal{D}_{int} &= \mathbf{T} : \dot{\mathbf{d}} - \dot{\Psi} \geq 0 \quad , \end{aligned} \tag{2.77}$$

in the material and spatial descriptions, respectively. Note that for a reversible process, the rate of internal mechanical work (stress power) coincides with the time derivative of the defined energy function Ψ.

In any equation within the chapters on the first and second laws of thermodynamics, the expression $\mathbf{P} : \dot{\mathbf{F}}$ can be replaced by its analogous internally conjugated work pair $\mathbf{S} : \dot{\mathbf{E}}$. Throughout this study, these different expressions are used according to which problem is under scrutiny and which is most convenient.

2.4 Variational Principles and Linearization

In discretization techniques, such as the well-known and widely used finite element method, variational principles based on weak formulations often serve as a starting point to derive the governing equations. Within the scope of this work, variational principles only depend on a displacement vector $\mathbf{u}$, and thus are also termed one-field variational principles.

The finite element method requires the weak formulation (variational form) of the balance laws. To begin the variation, the static first equation of motion (2.54) is multiplied by an arbitrary

test function $\delta\mathbf{u}$ and integrated over the observed volume:

$$g(\mathbf{u}, \delta\mathbf{u}) := \int_{\mathcal{B}_0} (-\operatorname{Div}\mathbf{P} - \mathbf{b}_0) \cdot \delta\mathbf{u}\, \mathrm{d}V = 0 \quad . \tag{2.78}$$

The test function can be chosen as an virtual displacement field $\delta\mathbf{u}$, which is supposed to be infinitesimal, independent of the actual displacement $\mathbf{u}$, and which must meet the kinematic boundary conditions. The so-called variational operator δ is linear and can be treated likewise as a differential operator. Since the test function $\delta\mathbf{u}$ can be chosen arbitrarily, the weak form of equation (2.78) coincides with the strong form (2.54).

Using the divergence theorem and applying integration by parts to the weak form of equilibrium, equation (2.78), the principal of virtual work is yielded:

$$g(\mathbf{u}, \delta\mathbf{u}) = \int_{\mathcal{B}_0} (\mathbf{P} : \operatorname{grad}\delta\mathbf{u} - \mathbf{b}_0 \cdot \delta\mathbf{u})\, \mathrm{d}V - \int_{\partial\mathcal{B}_{0\sigma}} \bar{\mathbf{t}}_0 \cdot \delta\mathbf{u}\, \mathrm{d}A = 0 \quad . \tag{2.79}$$

Here, $\partial\mathcal{B}_{0\sigma}$ describes a Neumann boundary condition, where the vector $\mathbf{t}_0 = \mathbf{P}\mathbf{N} = \bar{\mathbf{t}}_0$ is acting on. The displacements $\delta\mathbf{u}$ vanish at the boundary $\partial\mathcal{B}_{0\sigma}$, and thus no additional terms emerge out of the integration by parts along the boundary. Under the condition of

$$\delta\mathbf{F} = \delta(\operatorname{grad}\mathbf{u} + \mathbf{I}) = \delta(\operatorname{grad}\mathbf{u}) = \operatorname{grad}\delta\mathbf{u} \qquad , \tag{2.80}$$

equation (2.79) and (2.81) describe the principle of virtual work composed of internal and external virtual work:

$$g(\mathbf{u}, \delta\mathbf{u}) := \int_{\mathcal{B}_0} (\mathbf{P} : \delta\mathbf{F} - \mathbf{b}_0 \cdot \delta\mathbf{u})\, \mathrm{d}V - \int_{\partial\mathcal{B}_{0\sigma}} \bar{\mathbf{t}}_0 \cdot \delta\mathbf{u}\, \mathrm{d}A = 0 \quad . \tag{2.81}$$

The first term in (2.81) describes the internal virtual work

$$\delta W_{\mathrm{int}} = \int_{\mathcal{B}_0} \mathbf{P} : \delta\mathbf{F}\, \mathrm{d}V = \int_{\mathcal{B}_0} \mathbf{S} : \delta\mathbf{E}\, \mathrm{d}V \quad . \tag{2.82}$$

At the same time, the second term refers to external virtual work:

$$\delta W_{\mathrm{ext}} = \int_{\mathcal{B}_0} \mathbf{b}_0 \cdot \delta\mathbf{u}\, \mathrm{d}V + \int_{\partial\mathcal{B}_{0\sigma}} \bar{\mathbf{t}}_0 \cdot \delta\mathbf{u}\, \mathrm{d}A \quad . \tag{2.83}$$

In the static case, the internal virtual and external virtual work must be in equilibrium, meaning that the condition of

$$g(\mathbf{u}, \delta\mathbf{u}) = \delta W_{\mathrm{int}} - \delta W_{\mathrm{ext}} = 0 \tag{2.84}$$

must be fulfilled.

In many fields of solid mechanics, a conservative mechanical system is assumed, meaning that loads do not change in direction or value (conservative or dead loads) during the deformation

process. These loads always possess an energy potential Π when using hyperelastic materials. A formulation based on energy potentials has proven very useful in terms of developing robust numerical algorithms. The existence of potential functions are not necessary to meet the principle of virtual work (2.81), which holds for all materials, yet has benefits for finding solutions of variational formulations.

In case of hyperelastic materials the energy potential Π is given as the sum of the internal potential energy Π_{int} and the external potential energy Π_{ext}:

$$\Pi_{\text{int}} = \int_{\mathcal{B}_0} \Psi \, \mathrm{d}V \quad , \tag{2.85}$$

$$\Pi_{\text{ext}} = -\int_{\mathcal{B}_0} \mathbf{b}_0 \cdot \mathbf{u} \, \mathrm{d}V - \int_{\partial\mathcal{B}_{0\sigma}} \bar{\mathbf{t}}_0 \cdot \mathbf{u} \, \mathrm{d}A \quad . \tag{2.86}$$

Here Ψ is the so-called Helmholtz free energy, which is discussed in detail in section 2.5. The state during which the internal and external potential is in equilibrium is called the stationary state and is equivalent to the state in which the potential has a minimum. It can be achieved by requiring the directional derivative of Π with respect to the displacements $\mathbf{u}$ to vanish in all directions δu. As such, the principle of stationary potential energy can be stated as

$$\delta\Pi(\mathbf{u}, \delta\mathbf{u}) = \mathrm{D}\left[\Pi(\mathbf{u})\right] \cdot \delta\mathbf{u} = \frac{\mathrm{d}}{\mathrm{d}\varepsilon}\Pi\left(\mathbf{u} + \varepsilon\delta\mathbf{u}\right)\big|_{\varepsilon=0} = 0 \quad , \tag{2.87}$$

which is also known as the first variation of Π.

In equation (2.87), ε is a scalar parameter and D is a directional derivation operator, known as the Gateaux operator. It can be shown that the potential energy Π is stationary for any variation $\delta\mathbf{u}$ by applying equation (2.87) to the principal of virtual work (2.81):

$$\delta\Pi(\mathbf{u}, \delta\mathbf{u}) = \delta\Pi_{\text{int}} + \delta\Pi_{\text{ext}} = \delta W_{\text{int}} - \delta W_{\text{ext}} = 0 \quad . \tag{2.88}$$

The variational formulation presented in the preceding equations is usually nonlinear with respect to the displacements $\mathbf{u}$. A consistent linearization of equation (2.81) has to be provided to find solutions when using iterative procedures, such as the Newton-Raphson method. The fundamental relationship for the linearization of g is based on a first-order Taylor expansion, specified as:

$$L[g(\mathbf{u}, \delta\mathbf{u}), \Delta\mathbf{u}] := g(\mathbf{u}, \delta\mathbf{u}) + \mathrm{D}\left[\, g(\mathbf{u}, \delta\mathbf{u}) \,\right] \cdot \Delta\mathbf{u} \quad . \tag{2.89}$$

Here $\Delta\mathbf{u}$ and $\delta\mathbf{u}$ both represent an imaginary infinitesimal displacement field. Using prescribed conservative external loads, the linearization of the external loads vanishes, and thus only the linearization of the internal virtual work needs to be considered. Expressing the internal virtual work by means of the second Piola-Kirchhoff stress tensor and the Green-Lagrange strain tensor and considering that $\delta\mathbf{u}$ is independent of $\mathbf{u}$ leads to the following definition of the second term

in (2.89):

$$\mathrm{D}\,[\,g(\mathbf{u},\delta\mathbf{u})\,]\cdot\Delta\mathbf{u} = \mathrm{D}[\,\delta W_{\mathrm{int}}(\mathbf{u},\delta\mathbf{u})\,]\cdot\Delta\mathbf{u} = \int_{\mathcal{B}_0} [\,\mathbf{S}:\Delta\delta\mathbf{E} + \delta\mathbf{E}:\mathbb{C}:\Delta\mathbf{E}\,]\,\mathrm{d}V \quad . \tag{2.90}$$

Here, $\mathbb{C} = \dfrac{\partial \mathbf{S}}{\partial \mathbf{E}}$ denotes the tangential material stiffness introduced and derived in equation 2.120. Equation (2.89) can be and is often used as a starting point for implementation in finite element methods. The term $g(\mathbf{u},\delta\mathbf{u})$ describes the residuum caused by the incremental displacements $\Delta\mathbf{u}$, calculated in each iteration as long as it vanishes, implying that a final solution of $\mathbf{u}$ has been found.

In equation 2.90, the Green-Lagrange strain tensor $\mathbf{E}$ is present in its variation $\delta\mathbf{E}$, linearization $\Delta\mathbf{E}$, and linearization of the variation $\Delta\delta\mathbf{E}$. The variation δ and the linearization Δ are mathematically equivalent and both can be treated as the Gateaux derivative. The order of differentiations in the linearized variation is arbitrary and can be exchanged.

$$\begin{aligned}
\delta\mathbf{E} &= \delta E_{ij}\,\mathbf{e}_i\otimes\mathbf{e}_j \quad , & \delta E_{ij} &= \frac{1}{2}(\delta\mathbf{x}_{,i}\cdot\mathbf{x}_{,j} + \delta\mathbf{x}_{,j}\cdot\mathbf{x}_{,i}) \quad , \\
\Delta\mathbf{E} &= \Delta E_{ij}\,\mathbf{e}_i\otimes\mathbf{e}_j \quad , & \Delta E_{ij} &= \frac{1}{2}(\Delta\mathbf{x}_{,i}\cdot\mathbf{x}_{,j} + \Delta\mathbf{x}_{,j}\cdot\mathbf{x}_{,i}) \quad , \\
\Delta\delta\mathbf{E} &= \Delta\delta E_{ij}\,\mathbf{e}_i\otimes\mathbf{e}_j \quad , & \Delta\delta E_{ij} &= \frac{1}{2}(\delta\mathbf{x}_{,i}\cdot\Delta\mathbf{x}_{,j} + \delta\mathbf{x}_{,j}\cdot\Delta\mathbf{x}_{,i}) \quad .
\end{aligned} \tag{2.91}$$

2.5 Constitutive Equations

In the previous chapters, the governing equations of stresses and strains have been discussed. They hold for any macroscopic continuum and can be calculated using the fundamental laws of physics. Even though they remain valid for any arbitrary continuum, they do not distinguish between different materials. In the academic literature, authors often term them material independent equations. In general, constitutive material dependent equations involve a functional relationship to specify stress in terms of other field functions, such as strain and temperature. Unlike the governing equations, they cannot generally be deduced from the fundamental laws of physics; instead, they are yielded from experimental data. Material laws can be developed with or without considering a dissipative process.

In general, when establishing constitutive equations for stress-strain relations they have to satisfy the laws of thermodynamics (equations (2.77), (2.68), (2.69)), they must satisfy objectivity conditions (which ensures that the tensor transforms correct under a change of basis system), and in addition, it is recommended that the Drucker stability criterion is proven.

2.5.1 Hyperelastic Materials

If the material response of a continuum can be derived from a strain-energy-density function, the material is called hyperelastic. Hyperelastic materials cover a wide range of material classes, including isotropic and transversely isotropic, compressible and incompressible, rubber-like and even some classes of inelastic materials. Hyperelastic materials account for both physical nonlinear materials and geometric nonlinear behaviors. In physically nonlinear materials, stresses are nonlinear with respect to strains, whereas in geometric nonlinearity, strains are nonlinear with respect to the displacements.

Using the strain tensors defined in section 2.1.5, the Helmholtz free energy can be defined in homogeneous materials as a function solely depending on strains. According to the definitions specified in chapter 2.1.5, the strain-energy function in particular can be expressed with respect to the deformation gradient $\Psi(\mathbf{F})$, the Green-Lagrange strain tensor $\Psi(\mathbf{E})$, or the right Cauchy-Green tensor $\Psi(\mathbf{C})$. As is expounded later on in this chapter, the last two descriptions are advantageous because of symmetry in $\mathbf{E}$ and $\mathbf{C}$.

For convenience, the strain-energy function is assumed to fulfill certain requirements throughout this work, which will be discussed below.

The first assumption is known as the normalized condition, stating that the strain-energy vanishes in the undeformed state where $\mathbf{F} = \mathbf{I}$:

$$\Psi = \Psi(\mathbf{F}) = \Psi(\mathbf{I}) = 0 \quad . \tag{2.92}$$

Following the fact that during a deformation, the strain energy must increase, the requirement

$$\Psi = \Psi(\mathbf{F}) \geq 0 \tag{2.93}$$

has to be fulfilled. Equations (2.92) and (2.93) ascertain that the stress in the (undeformed) reference configuration is equal to zero. In addition, the so-called growth condition has to be satisfied:

$$\Psi \to \infty \quad \text{for } J \to 0 \text{ or } J \to \infty \quad . \tag{2.94}$$

This signifies that for any infinitesimal expansion or compression of a continuum, the required strain energy has to be infinitesimal as well.

In homogeneous materials, it is assumed that the Helmholtz free energy Ψ is solely a function of strains, and the material behaves the same in all spatial locations. In contrast, the behavior of heterogeneous materials, such as composite materials made up with fibers and matrix material, additionally depend on a specific point inside the observed continuum, and the material behavior differs at each point. As such, the strain energy takes the form of

$$\Psi(\mathbf{F}) = \Psi(\mathbf{F}) \quad \text{or} \quad \Psi(\mathbf{X}, \mathbf{F}) = \Psi(\mathbf{X}, \mathbf{F}) \tag{2.95}$$

for homogeneous and heterogeneous materials, respectively.

Moreover, in order to fulfill the objectivity condition, the strain energy, or the constitutive equations, must be invariant when the continuum is subjected to rigid body motions. By defining $\mathbf{Q}$ as an orthogonal transformation tensor, describing an arbitrary rigid body motion, the following statement can be made:

$$\Psi(\mathbf{F}^*) = \Psi(\mathbf{QF}) \quad \text{or} \quad \Psi(\mathbf{X}, \mathbf{F}^*) = \Psi(\mathbf{X}, \mathbf{QF}) \quad . \tag{2.96}$$

With the choice of a special transformation tensor $\mathbf{Q}$, namely the transposition of the rotational tensor $\mathbf{R}^T$, defined in section 2.1.4, and by applying the polar decomposition (2.16) to $\mathbf{F}$, equation (2.96) leads to

$$\Psi(\mathbf{F}) = \Psi(\mathbf{U}) \quad \text{or} \quad \Psi(\mathbf{X}, \mathbf{F}) = \Psi(\mathbf{X}, \mathbf{U}) \quad . \tag{2.97}$$

This implies that hyperelastic materials only depend on the pure stretch tensor $\mathbf{U}$, and thus are independent of rigid body rotations $\mathbf{R}$. Since the right Cauchy-Green tensor $\mathbf{C}$ and the Green-Lagrange tensor $\mathbf{E}$ can be related to the right stretch tensor $\mathbf{U}$ using equations (2.18) and (2.19), the following expression is yielded:

$$\Psi(\mathbf{F}) = \Psi(\mathbf{C}) = \Psi(\mathbf{E}) \quad \text{or} \quad \Psi(\mathbf{X}, \mathbf{F}) = \Psi(\mathbf{X}, \mathbf{C}) = \Psi(\mathbf{X}, \mathbf{E}) \quad . \tag{2.98}$$

As the definition of hyperelastic materials implies, the response of a material caused by a deformation process is given as the derivative of the strain-energy function with respect to the preferred quantity. This can be obtained by using the Clausius-Plank inequality (2.77) from the second law of thermodynamics, related to the first Piola-Kirchhoff tensor $\mathbf{P}$, and due to the fact that in perfect elastic materials, the internal dissipation (entropy production) is equal to zero:

$$\mathcal{D}_{int} = \mathbf{P} : \dot{\mathbf{F}} - \dot{\Psi}_0 = \left(\mathbf{P} - \frac{\partial \Psi(\mathbf{F})}{\partial \mathbf{F}} \right) : \dot{\mathbf{F}} = 0 \quad . \tag{2.99}$$

Since $\dot{\mathbf{F}}$ can be chosen arbitrarily, the expression in parentheses must be zero, and the first Piola-Kirchhoff stress tensor $\mathbf{P}$ can be deduced, in homogeneous materials, as a function of the deformation gradient. On the other hand, in heterogeneous materials, the stress tensor $\mathbf{P}$ is given as a function of the deformation gradient and the position vector $\mathbf{X}$

$$\mathbf{P}(\mathbf{F}) = \frac{\partial \Psi(\mathbf{F})}{\partial \mathbf{F}} \quad \text{or} \quad \mathbf{P}(\mathbf{X}, \mathbf{F}) = \frac{\partial \Psi(\mathbf{X}, \mathbf{F})}{\partial \mathbf{F}} \quad . \tag{2.100}$$

In the case of homogeneous materials, stress tensors, with respect to differently defined strain-energy functions, can be derived. For instance, equation (2.100) can alternatively be written by defining the strain-energy function with respect to the Cauchy-Green tensor $\mathbf{C}$:

$$\mathbf{P} = 2\,\mathbf{F}\,\frac{\partial \Psi(\mathbf{C})}{\partial \mathbf{C}} \tag{2.101}$$

Using the Green-Lagrange tensor in the Helmholtz energy function one obtains the second Piola-

Kirchhoff tensor in the form of

$$\mathbf{S} = 2\,\frac{\partial \Psi(\mathbf{C})}{\partial \mathbf{C}} = \frac{\partial \Psi(\mathbf{E})}{\partial \mathbf{E}} \qquad , \tag{2.102}$$

and the analogue Cauchy stress tensor in the spatial description as

$$\mathbf{T} = J^{-1}\,\mathbf{F}\,\left(\frac{\partial \Psi(\mathbf{F})}{\partial \mathbf{F}}\right)^{T} = 2\,J^{-1}\,\mathbf{F}\,\left(\frac{\partial \Psi(\mathbf{C})}{\partial \mathbf{C}}\right)\mathbf{F}^{T} \qquad . \tag{2.103}$$

Further distinctions of material behaviors can be made by observing the material responses in different spatial directions. When a material behavior is the same in each of its spatial directions, it is called isotropic, whereas a different behavior along its directions refers, in general, to an anisotropic material. Further subdivisions of anisotropic materials can be made, leading to other classifications, such as transversely isotropic materials. An alternative definition of isotropic materials can be made based on the strain-energy function. Similar to, but not to be confused with definition (2.96), an isotropic material is present, when

$$\Psi(\mathbf{F}) = \Psi(\mathbf{F}^{*}) = \Psi(\mathbf{F}\mathbf{Q}^{\mathbf{T}}) \quad \text{or} \quad \Psi(\mathbf{C}) = \Psi(\mathbf{Q}\mathbf{C}\mathbf{Q}^{\mathbf{T}}) \tag{2.104}$$

holds. This signifies that a superimposed rigid body motion on the reference configuration does not change the strain-energy function when an isotropic material is present. Otherwise, if the strain energy changes, it would be a proof for the presence of an anisotropic material. It is noteworthy that the orthogonal transformation $\mathbf{Q}$ in (2.104) acts on the reference configuration, whereas the transformation tensor defined for the objectivity condition in equation (2.96) refers to the current configuration.

If an isotropic material is present, the strain-energy function and therefore the constitutive equations can, in addition, be expressed in terms of the independent strain invariants of the right Cauchy-Green tensor $\mathbf{C}$:

$$\Psi = \Psi\left(I_1(\mathbf{C}), I_2(\mathbf{C}), I_3(\mathbf{C})\right) \quad . \tag{2.105}$$

Here I is defined as

$$I_1 = \operatorname{tr}\mathbf{C}\,, \quad I_2 = \frac{1}{2}\left((\operatorname{tr}\mathbf{C})^2 - \operatorname{tr}\mathbf{C}^2)\right)\,, \quad I_3 = \det\mathbf{C} \quad . \tag{2.106}$$

Applying the latest definitions to equation (2.102) and by means of the chain rule of differentiation, the following equation is yielded:

$$\frac{\partial \Psi(\mathbf{C})}{\partial \mathbf{C}} = \frac{\partial \Psi}{\partial I_1}\frac{\partial I_1}{\partial \mathbf{C}} + \frac{\partial \Psi}{\partial I_2}\frac{\partial I_2}{\partial \mathbf{C}} + \frac{\partial \Psi}{\partial I_3}\frac{\partial I_3}{\partial \mathbf{C}} \qquad , \tag{2.107}$$

The second Piola-Kirchhoff tensor is then finally defined with respect to the Helmholtz free energy, depending exclusively on the invariants of $\mathbf{C}$:

$$\mathbf{S} = 2\,\left[\left(\frac{\partial \Psi}{\partial I_1} + I_1\,\frac{\partial \Psi}{\partial I_2}\right)\mathbf{I} - \frac{\partial \Psi}{\partial I_2}\mathbf{C} + I_3\frac{\partial \Psi}{\partial I_3}\mathbf{C}^{-1}\right] \quad . \tag{2.108}$$

2.5.2 Transversely Isotropy - Composite Materials

A composite material or fiber-reinforced composite is known to be a material composed of a matrix material and fibers. Such materials have strong directional properties and as a consequence of these different types of materials, a composite becomes heterogeneous. An important requirement for transverse isotropy is that the fibers are continuously arranged; otherwise, the material would be (completely) anisotropic. Composite materials are extensively used in industrial engineering applications where the structures' weights matter, as in aircrafts or new automobiles, for example. It has an unrivalled weight to stiffness ratio compared to classically used materials; the costs are consequently also much higher. A wide field of research on the different types of fibers and matrix material that can be used is going on. Furthermore, the combination of those materials referred to the direction and amount of plies, in order to become a highly efficient problem specific stack sequence, is also a huge topic. The aim of this section is to derive the constitutive equations solely according to a continuum approach. Following the assumption that the fibers are continuously distributed throughout the observed material. In directions orthogonal to the preferred direction, the material is assumed to behave transversely isotropic.

Analogous to the isotropic strain energy density defined in equation (2.96), a strain energy for transversely isotropic materials is used as a starting point for further discussions. This strain energy can be constructed as a function of the deformation gradient $\mathbf{F}$, and the base vector $\mathbf{a}_0(\mathbf{X})$. The base vector is defined as the unit vector in the referential configurations in the direction of the fiber. By introducing a pure stretch measure λ, along the fiber direction $\mathbf{a}_0$, the square of the stretch can be found:

$$\lambda^2 = \mathbf{a}_0 \cdot \mathbf{F}^T \mathbf{F} \mathbf{a}_0 = \mathbf{a}_0 \cdot \mathbf{C}\, \mathbf{a}_0 \tag{2.109}$$

Assuming the transversely isotropic material to be hyperelastic, the strain energy can be established using the Helmholtz free energy function Ψ per unit volume, defined as a function of $\mathbf{C}$ and $\mathbf{a_0}$:

$$\Psi = \Psi(\mathbf{C}, \mathbf{a}_0 \otimes \mathbf{a}_0) \qquad . \tag{2.110}$$

According to the objectivity condition, equation (2.104), the free energy of transversely isotropic materials must also be independent under the observer's perspective. This is automatically fulfilled if the requirement of

$$\Psi(\mathbf{C}, \mathbf{a}_0 \otimes \mathbf{a}_0) = \Psi\left(\mathbf{Q}\,\mathbf{C}\,\mathbf{Q}^T, \mathbf{Q}\,\mathbf{a}_0 \otimes \mathbf{a}_0\,\mathbf{Q}^T\right) \tag{2.111}$$

holds true. In order to fulfill equation (2.111), in addition to the three invariants defined in (2.106), two further invariants of $\mathbf{C}$ (or $\mathbf{b}$) have to be specified as

$$I_4 = \mathbf{a}_0 \cdot \mathbf{C}\, \mathbf{a}_0 \qquad \text{and} \qquad I_5 = \mathbf{a}_0 \cdot \mathbf{C}^2\, \mathbf{a}_0 \quad . \tag{2.112}$$

These are called pseudo invariants of $\mathbf{C}$ (or $\mathbf{b}$) and $\mathbf{a}_0$ and arise directly from the anisotropy.

For a transversely isotropic material, the strain-energy function can finally be written, by means of the three invariants of equation (2.106) and the two pseudo invariants (2.112) as

$$\Psi = \Psi\left(I_1(\mathbf{C}), I_2(\mathbf{C}), I_3(\mathbf{C}), I_4(\mathbf{C}, \mathbf{a}_0), I_5(\mathbf{C}, \mathbf{a}_0) \right) \quad . \tag{2.113}$$

According to equation (2.107) and (2.108), the derivative for transversely isotropic materials in terms of the invariants of the strain-energy function Ψ is calculated by employing the chain rule

$$\frac{\partial \Psi(\mathbf{C}, \mathbf{a}_0 \otimes \mathbf{a}_0)}{\partial \mathbf{C}} = \sum_{i=1}^{5} \frac{\partial \Psi(\mathbf{C}, \mathbf{a}_0 \otimes \mathbf{a}_0)}{\partial I_n} \frac{\partial I_n}{\partial \mathbf{C}} \quad . \tag{2.114}$$

With this, the constitutive law yields the second Piola-Kirchhoff stress for transversely isotropic materials:

$$\mathbf{S} = 2\left(\left(\frac{\partial \Psi}{\partial I_1} + I_1 \frac{\partial \Psi}{\partial I_2} \right) \mathbf{I} - \frac{\partial \Psi}{\partial I_2} \mathbf{C} + I_3 \frac{\partial \Psi}{\partial I_3} \mathbf{C}^{-1} + \frac{\partial \Psi}{\partial I_4} \mathbf{a}_0 \otimes \mathbf{a}_0 + \frac{\partial \Psi}{\partial I_5} (\mathbf{a}_0 \otimes \mathbf{C}\mathbf{a}_0 + \mathbf{a}_0 \mathbf{C} \otimes \mathbf{a}_0) \right) \tag{2.115}$$

2.5.3 Constitutive Equations with Internal Variables

In many engineering problems, the material behavior is no longer reversible and therefore, in addition to the hitherto discussed concepts, dissipative processes must be heeded. Dissipative processes occur in many different material models, such as plasticity and viscoelasticity models, and, more importantly for the scope of this study, in damage models. Thus, the aim of this section is to discuss the basic concepts of deriving constitutive equations undergoing such dissipative processes. To extend the concepts developed so far, internal variables are introduced as a basis for the derivation of the constitutive equations. Internal variables are constructed mathematically, as they can in general not be measured or observed. They are also called thermodynamic state variables, and describe aspects of internal material behavior within a macroscopic model. Internal variables have to be defined in such a way that they characterize the microscopic material behavior within a macroscopic calculation.

Considering an isothermal process, the Helmholtz free energy function of isotropic materials (2.98) extends to a function additionally depending on internal variables $\boldsymbol{\xi}_i$:

$$\Psi = \Psi(\mathbf{F}, \boldsymbol{\xi}_i) \quad . \tag{2.116}$$

The amount of internal variables $\boldsymbol{\xi}_i$ depends on the underlying material model, the numerical conditions, and the physical circumstances (e.g. porosity, damage, plasticity, anisotropy, etc.); they have to be adjusted in each specific problem class in a way that they represent the microscopic material behavior properly. For further examination, the time derivative of Ψ is

needed:

$$\dot{\Psi}(\mathbf{F}, \boldsymbol{\xi}_1, ..., \boldsymbol{\xi}_m) = \frac{\partial \Psi}{\partial \mathbf{F}} : \dot{\mathbf{F}} + \sum_{\alpha=1}^{m} \frac{\partial \Psi}{\partial \boldsymbol{\xi}}_{\alpha} : \dot{\boldsymbol{\xi}}_{\alpha} \quad . \tag{2.117}$$

With this, the Clausius-Plank inequality for dissipative processes, equation (2.77), becomes:

$$\mathcal{D}_{int} = \left(\mathbf{P} - \frac{\partial \Psi(\mathbf{F}, \boldsymbol{\xi}_1, ..., \boldsymbol{\xi}_m)}{\partial \mathbf{F}} \right) : \dot{\mathbf{F}} - \sum_{\alpha=1}^{m} \frac{\partial \Psi(\mathbf{F}, \boldsymbol{\xi}_1, ..., \boldsymbol{\xi}_m)}{\partial \boldsymbol{\xi}_{\alpha}} : \dot{\boldsymbol{\xi}}_{\alpha} \geq 0 \tag{2.118}$$

when using the stress power in form of $\mathbf{P} : \dot{\mathbf{F}}$. To accomplish the requirement $\mathcal{D}_{int} \geq 0$ in equation (2.118) for arbitrary time derivatives of deformation states $\dot{\mathbf{F}}$, the second law of thermodynamics yields definitions for the first Piola-Kirchhoff tensor and the dissipative variable:

$$\mathbf{P} = \frac{\partial \Psi(\mathbf{F}, \boldsymbol{\xi}_1, ..., \boldsymbol{\xi}_m)}{\partial \mathbf{F}} \qquad \text{and} \qquad \mathcal{D}_{int} = \sum_{\alpha=1}^{m} -\frac{\partial \Psi(\mathbf{F}, \boldsymbol{\xi}_1, ..., \boldsymbol{\xi}_m)}{\partial \boldsymbol{\xi}_{\alpha}} : \dot{\boldsymbol{\xi}}_{\alpha} \geq 0 \quad . \tag{2.119}$$

This equation must hold for any arbitrary point inside the continuum.

In summary, when internal variables are used within a material model, the free energy function Ψ has to be extended with further variables, which justifies the additional constitutive equations in equation (2.119). A more specific and detailed derivation of damage materials is conducted in chapter 3.

2.5.4 The Elasticity Tensor

In nonlinear finite element calculations iterative solution techniques, for instance, Newton-Raphson method, are applied to solve a sequence of linear problems. The linearization procedure was discussed in more detail in chapter 2.4. By measuring the change in stress resulting from a change in strain, which can be characterized as a derivative of $\mathbf{S}$ with respect to $\mathbf{C}$, a quantity $\mathbb{C}$, known as the elasticity tensor in the referential description, can be derived:

$$\mathbb{C} = 2 \frac{\partial \mathbf{S}(\mathbf{C})}{\partial \mathbf{C}} = \frac{\partial \mathbf{S}(\mathbf{C})}{\partial \mathbf{E}} \quad . \tag{2.120}$$

The elasticity tensor is a tensor of rank four $\mathbb{C} = \mathbb{C}_{ijkl}$ and therefore has in general $3^4 = 81$ scalar components. Due to the symmetry of the second Piola-Kirchhoff tensor $\mathbf{S}$, and the Green-Lagrange strain tensor $\mathbf{C}$, the elasticity tensor has symmetry conditions in the first and second, and third and fourth columns, respectively:

$$\mathbb{C}_{ijkl} = \mathbb{C}_{jikl} = \mathbb{C}_{ijlk} \quad . \tag{2.121}$$

This reduces the independent components from 81 to 36. If an existence of a scalar valued function (hyperelasticity) is assumed, one can further derive the material elasticity tensor $\mathbb{C}$

directly from the Helmholtz free energy, as the second derivative of that function:

$$\mathbb{C} = 4\,\frac{\partial^2 \Psi(\mathbf{C})}{(\partial \mathbf{C})^2} \quad . \tag{2.122}$$

According to the Schwartz theorem, which implies that the order of differentiation in equation (2.122) is arbitrary, another symmetry can be obtained:

$$\mathbb{C} = \mathbb{C}^T \quad \text{or} \quad \mathbb{C}_{ijkl} = \mathbb{C}_{klij} \quad . \tag{2.123}$$

This further reduces the independent components of $\mathbb{C}$ from 36 to 21 for the most general (anisotropic) elastic material. With the symmetry conditions of (2.121) and (2.123), the fourth order elasticity tensor is reduced to a more manageable second-order matrix and can be written in a more contracted form as:

$$\mathbb{C} = \begin{bmatrix} \mathbb{C}_{11} & \mathbb{C}_{12} & \mathbb{C}_{13} & \mathbb{C}_{14} & \mathbb{C}_{15} & \mathbb{C}_{16} \\ \mathbb{C}_{12} & \mathbb{C}_{22} & \mathbb{C}_{23} & \mathbb{C}_{24} & \mathbb{C}_{25} & \mathbb{C}_{26} \\ \mathbb{C}_{13} & \mathbb{C}_{23} & \mathbb{C}_{33} & \mathbb{C}_{34} & \mathbb{C}_{35} & \mathbb{C}_{36} \\ \mathbb{C}_{14} & \mathbb{C}_{24} & \mathbb{C}_{34} & \mathbb{C}_{44} & \mathbb{C}_{45} & \mathbb{C}_{46} \\ \mathbb{C}_{15} & \mathbb{C}_{25} & \mathbb{C}_{35} & \mathbb{C}_{45} & \mathbb{C}_{55} & \mathbb{C}_{56} \\ \mathbb{C}_{16} & \mathbb{C}_{26} & \mathbb{C}_{36} & \mathbb{C}_{46} & \mathbb{C}_{56} & \mathbb{C}_{66} \end{bmatrix} \quad . \tag{2.124}$$

In equation (2.124) and from now on, there is no notational distinction between the tensor and matrix form of quantities such as $\mathbb{C}, \mathbf{S}$ and $\mathbf{E}$. The single subscript notation is called the engineering notation. It should thus be noted that the elasticity matrix as well as the stress and strain vectors in this notation do not transform in the same way as a tensor. When using the matrix form of $\mathbb{C}$, it is obvious that the second order stress tensor $\mathbf{S}$, and the second order strain tensor $\mathbf{E}$ have to be rearranged to a first order vector matching the order given in $\mathbb{C}$:

$$\begin{aligned} \mathbf{S} &= (S_{11}, S_{22}, S_{33}, S_{12}, S_{13}, S_{23})^T \quad , \\ \mathbf{E} &= (E_{11}, E_{22}, E_{33}, 2E_{12}, 2E_{13}, 2E_{23})^T \quad . \end{aligned} \tag{2.125}$$

Here, and from now on, the strain vector is used with its double shear components.

In linear elastic calculations, the stresses can be calculated using the linear relation

$$\mathbf{S} = \mathbb{C}\,\mathbf{E} \quad . \tag{2.126}$$

The preceding equation is valid as long as moderate strains are present, it can also be used within a iterative solution technique in incremental form. Another important relation is the inverse of equation (2.126) using the anisotropic stiffness tensor $\mathbb{S}$, defined as the inverse of the

second-order elasticity matrix $\mathbb{C}$ (not as the inverse of the fourth order tensor $\mathbb{C}_{ijkl}$):

$$\mathbf{E} = \mathbb{C}^{-1}\,\mathbf{S} = \mathbb{S}\,\mathbf{S} \quad . \tag{2.127}$$

Here, $\mathbb{S}$ is also called the compliance matrix. Both forms $\mathbb{S}$ and $\mathbb{C}$ are required in the scope of this work. Anisotropic material features direction dependent elasticity properties. Fully anisotropic materials have no symmetry planes. Besides transverse and normal strain couplings, they reveal couplings between normal strains and shear strains.

The independent material constants in equation (2.124) can be further reduced using material symmetries. If a material coordinate system x_1, x_2, x_3, which should not be confused with a coordinate system in material description, in which the elastic parameters at a specific point have an equivalent mirror image of themselves with respect to any arbitrary plane inside the material, then the reflective plane is called a material plane of symmetry. However, these symmetry planes describe unexceptional directional property conditions, not positional ones.

If one material plane of symmetry, for instance, a mirror image regarding the $x_2{-}x_3$ plane, can be found, the material is called monoclinic. Considering the discussed symmetry, the independent constants in the elasticity matrix (2.124) are reduced to $21 - 8 = 13$. This suggests that a monoclinic material is invariant under one specific reflection, exemplarily chosen for a reflection described by the following transformation:

$$x_1' = x_1, \qquad x_2' = x_2, \qquad x_3' = -x_3 \quad . \tag{2.128}$$

As such, the principal axes of stress do not coincide with the principal axis of strain, or in other words, shear strain can produce normal stress.

Furthermore, another special case of anisotropic material is known as orthotropic material. An orthotropic material is defined as a material being invariant in the case of three mutual material planes of symmetry, which further reduces the independent material constants from 13 to 9. Orthotropic materials indeed have directional elasticity properties, but there are no couplings between strains and shear strains with reference to one specific coordinate system. In other words, once a rectangular orthotropic material is loaded along its symmetry planes, no coupling between strains and shear strains arises, whereas when it is loaded outside its symmetry plane, shear strains appear and the rectangular will deform into a parallelogram. As the orthotropic elasticity matrix $\mathbb{C}$, is extensively used in this study, or its inverse $\mathbb{S}$, they are written down

using the same abstract coefficients as used in equation (2.124):

$$\mathbb{C} = \begin{bmatrix} \mathbb{C}_{11} & \mathbb{C}_{12} & \mathbb{C}_{13} & 0 & 0 & 0 \\ \mathbb{C}_{12} & \mathbb{C}_{22} & \mathbb{C}_{23} & 0 & 0 & 0 \\ \mathbb{C}_{13} & \mathbb{C}_{23} & \mathbb{C}_{33} & 0 & 0 & 0 \\ 0 & 0 & 0 & \mathbb{C}_{44} & 0 & 0 \\ 0 & 0 & 0 & 0 & \mathbb{C}_{55} & 0 \\ 0 & 0 & 0 & 0 & 0 & \mathbb{C}_{66} \end{bmatrix} \quad . \tag{2.129}$$

In order to construct a more practical form of equation (2.129) when solving specific problems, the material constants are determined in experiments and are expressed by means of the well known engineering constants, which are the Young's modulus E_i, the shear modulus G_i and the Poisson's ratio ν_{ij}, instead of their more abstract form $\mathbb{C}_{ij}$. These constants have obvious physical meanings and are measured within standard tests (e.g. simple tension and pure shear tests). For the sake of convenience, only the compliance matrix $\mathbb{S}$ is expressed in matrix form by means of the engineering constants:

$$\mathbb{S} = \begin{bmatrix} \frac{1}{E_1} & -\frac{\nu_{12}}{E_1} & -\frac{\nu_{13}}{E_1} & 0 & 0 & 0 \\ -\frac{\nu_{12}}{E_1} & \frac{1}{E_2} & -\frac{\nu_{23}}{E_2} & 0 & 0 & 0 \\ -\frac{\nu_{13}}{E_1} & -\frac{\nu_{23}}{E_2} & \frac{1}{E_3} & 0 & 0 & 0 \\ 0 & 0 & 0 & \frac{1}{G_{12}} & 0 & 0 \\ 0 & 0 & 0 & 0 & \frac{1}{G_{13}} & 0 \\ 0 & 0 & 0 & 0 & 0 & \frac{1}{G_{23}} \end{bmatrix} \quad . \tag{2.130}$$

Here, the symmetry of the compliance matrix $\mathbb{S}$ is already enforced, by using the following reciprocal relations:

$$\frac{\nu_{ij}}{E_i} = \frac{\nu_{ji}}{E_j} \quad \text{(no sum on i,j)} \quad . \tag{2.131}$$

This describes the ratio of transverse strain in the j^{th} direction to the axial strain in the i^{th} direction, according to an axial load in direction i.

In conclusion, the nine independent engineering constants are:

$$E_1,\, E_2,\, E_3, \qquad G_{12},\, G_{13},\, G_{23}, \qquad \nu_{12},\, \nu_{13},\, \nu_{23} \quad . \tag{2.132}$$

The components of the orthotropic elasticity matrix $\mathbb{C}_{ij}$, defined as the inverse of the compliance

matrix, can be written by means of the engineering constants as

$$\begin{aligned}
C_{11} &= \frac{1-\nu_{23}\,\nu_{32}}{E_2\,E_3\,\Delta} \quad , & C_{22} &= \frac{1-\nu_{13}\,\nu_{31}}{E_1\,E_3\,\Delta} \quad , & C_{33} &= \frac{1-\nu_{12}\,\nu_{21}}{E_1\,E_2\,\Delta} \quad , \\
C_{12} &= \frac{\nu_{12}+\nu_{32}\,\nu_{13}}{E_1\,E_3\,\Delta} \quad , & C_{13} &= \frac{\nu_{31}+\nu_{21}\,\nu_{32}}{E_2\,E_3\,\Delta} \quad , & C_{23} &= \frac{\nu_{23}+\nu_{21}\,\nu_{13}}{E_1\,E_2\,\Delta} \quad , \\
C_{44} &= G_{12} \quad , & C_{55} &= G_{13} \quad , & C_{66} &= G_{23} \quad ,
\end{aligned} \tag{2.133}$$

whereby

$$\Delta = \frac{1-\nu_{12}\,\nu_{21}-\nu_{23}\,\nu_{32}-\nu_{31}\,\nu_{13}-2\,\nu_{21}\,\nu_{32}\,\nu_{13}}{E_1\;E_2\,E_3} \quad . \tag{2.134}$$

For the purpose of modeling fiber-reinforced composites, in addition to the specified orthotropic material, another symmetry can be found. If there is an additional invariance regarding an arbitrary chosen rotation around one axis, for instance, around the x_1-axis, the material is defined as transversely isotropic. As such, the amount of independent constants is reduced from 9 to 5. It thus follows that

$$E_2 = E_3 \quad , \qquad \nu_{12} = \nu_{13} \quad , \qquad G_{12} = G_{13} \quad . \tag{2.135}$$

Furthermore, the relation

$$G_{23} = \frac{E_2}{2(1+\nu_{23})} \qquad \text{or} \qquad \nu_{23} = \frac{E_2}{2\,G_{23}} - 1 \tag{2.136}$$

holds. Following these definitions, the remaining five independent material parameters of transversely isotropic materials are

$$E_1,\, E_2,\, G_{12},\, G_{23},\, \nu_{12} \quad . \tag{2.137}$$

Accordingly, the compliance matrix S takes the following form:

$$\mathbb{S} = \begin{bmatrix}
\frac{1}{E_1} & -\frac{\nu_{12}}{E_1} & -\frac{\nu_{12}}{E_1} & 0 & 0 & 0 \\
-\frac{\nu_{12}}{E_1} & \frac{1}{E_2} & -\frac{\nu_{23}}{E_2} & 0 & 0 & 0 \\
-\frac{\nu_{12}}{E_1} & -\frac{\nu_{23}}{E_2} & \frac{1}{E_2} & 0 & 0 & 0 \\
0 & 0 & 0 & \frac{1}{G_{12}} & 0 & 0 \\
0 & 0 & 0 & 0 & \frac{1}{G_{13}} & 0 \\
0 & 0 & 0 & 0 & 0 & \frac{E_2}{2(1+\nu_{23})}
\end{bmatrix} \quad . \tag{2.138}$$

The components of the analogue elasticity matrix $\mathbb{C}_{ij}$ are defined as

$$\begin{aligned}
C_{11} &= \frac{1-\nu_{23}\,\nu_{32}}{E_2\,E_3\,\Delta} \quad , & C_{22} &= \frac{1-\nu_{13}\,\nu_{31}}{E_1\,E_3\,\Delta} \quad , & C_{33} &= \frac{1-\nu_{12}\,\nu_{21}}{E_1\,E_2\,\Delta} \quad , \\
C_{12} &= \frac{\nu_{12}+\nu_{32}\,\nu_{13}}{E_1\,E_3\,\Delta} \quad , & C_{13} &= \frac{\nu_{31}+\nu_{21}\,\nu_{32}}{E_2\,E_3\,\Delta} \quad , & C_{23} &= \frac{\nu_{23}+\nu_{21}\,\nu_{13}}{E_1\,E_2\,\Delta} \quad , \\
C_{44} &= G_{12} \quad , & C_{55} &= G_{13} \quad , & C_{66} &= \frac{2(1+\nu_{23})}{E_2} \quad ,
\end{aligned} \tag{2.139}$$

by means of the engineering constants, with Δ being defined in equation (2.134).

The last definition of a material class, namely isotropic materials, involves a material which behaves identically in each direction. As such, the last two remaining material constants are:

$$E, \nu \quad . \tag{2.140}$$

Furthermore, the isotropic compliance matrix of the three-dimensional, generalized Hook's law takes the form of:

$$\mathbb{S} = \frac{1}{E}\begin{bmatrix} 1 & -\nu & -\nu & 0 & 0 & 0 \\ -\nu & 1 & -\nu & 0 & 0 & 0 \\ -\nu & -\nu & 1 & 0 & 0 & 0 \\ 0 & 0 & 0 & 2(1+\nu) & 0 & 0 \\ 0 & 0 & 0 & 0 & 2(1+\nu) & 0 \\ 0 & 0 & 0 & 0 & 0 & 2(1+\nu) \end{bmatrix} \quad . \tag{2.141}$$

At the same time, its analogues inverse counterpart, the isotropic elasticity matrix, is given as:

$$\mathbb{C} = \frac{E}{(1+\nu)(1-2\nu)}\begin{bmatrix} 1-\nu & \nu & \nu & 0 & 0 & 0 \\ \nu & 1-\nu & \nu & 0 & 0 & 0 \\ \nu & \nu & 1-\nu & 0 & 0 & 0 \\ 0 & 0 & 0 & \frac{1-2\nu}{2} & 0 & 0 \\ 0 & 0 & 0 & 0 & \frac{1-2\nu}{2} & 0 \\ 0 & 0 & 0 & 0 & 0 & \frac{1-2\nu}{2} \end{bmatrix} \quad . \tag{2.142}$$

The strain matrix $\mathbf{E}$ in the two preceding equations is sorted in the form of double shear terms, as defined in equation (2.125).

Chapter 3

Continuum Damage Mechanics - Basic Concepts

Continuum damage mechanics (CDM) is a field of mechanics which considers damage and fracture processes in materials based on classical continuum mechanical theory. The key of damage mechanics in engineering problems is the prediction of how structure's stiffness will decrease with damage, and how much further load the damaging structure can bear until its maximum bearing load is reached. Furthermore the developing direction of damage is on interest.

Damage mechanics examines material failure on a microscopic level that is triggered by micro cracks and micro cavities that emerge from broken bonds between atoms. Macroscopic fractures originate from the culmination and extension of these microscopic ruptures. To capture the effect of microscopic discontinuities as a continuous field within a macroscopic material model, a damage variable d is introduced, serving as a connection between micro and macro scales. The damage variable d depends on microscopic quantities and is adopted as a so-called representative volume element (RVE), representing the statistical average of the mechanical behavior of a material, and can be obtained through a homogenization procedure. In other words, the homogenized material in the RVE must represent the actual material's behavior in the sense of a statistical average. The use of RVE's within the context of internal damage variables is illustrated in figure 3.1.

In this study a Saint-Venant-Kichhoff Material is assumed, which implies that the material undergoes only small strains even in case of nonlinear displacements. Thus, a distinction of the different introduced strain and stress quantities is redundant in this section and stresses are generally denoted with σ and strains with ε.

3.1 General Principles of Continuum Damage Mechanics

In 1958, Kachanov [73] was the first who introduced a (scalar) damage variable d, with $d = 0$ representing an undamaged state and $d = 1$ a fully damaged material. The parameter d is defined as the ratio between the damaged and undamaged initial area:

$$d = \frac{A_d}{A_0} \qquad \text{with} \qquad d \in [0, 1] \quad . \tag{3.1}$$

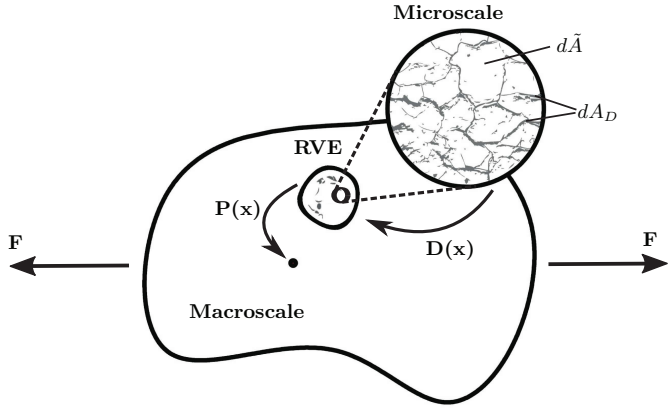

Figure 3.1: Visual depiction of the damage variable D.

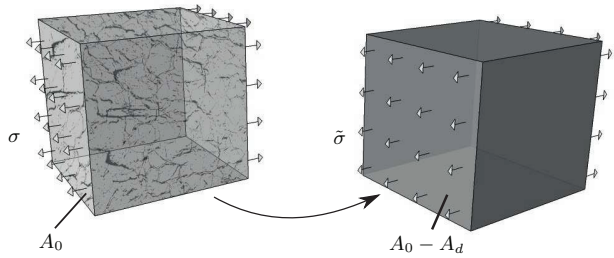

Figure 3.2: Stress suspended continuum with micro defects (left) and homogenized continuum with effective stresses (right).

In 1968, Robotnov [117] used the damage variable and introduced the concept of effective stresses, figure 3.2.

The concept of effective stresses implies that the mechanical behavior of a body with a damaged material can be investigated on a fictitious body with an undamaged (homogenized) material. Both bodies are assumed to have a mechanical equivalence. A first approach is to assume the bodies in a so called strain equivalence, where the strain in the actual body equals the strain in the fictitious body. From this theory the following equation can be derived:

$$\tilde{\boldsymbol{\sigma}}(A_0 - A_d) = \boldsymbol{\sigma} A_0 \qquad \text{or} \qquad \tilde{\boldsymbol{\sigma}} = \frac{\boldsymbol{\sigma}}{1-d} \quad . \tag{3.2}$$

Here, $\tilde{\sigma}$ is called the effective stress tensor. Other approaches for mechanical equivalence principles are discussed in detail in section 3.2.1. In equation (3.2) the damage state is described with a scalar damage variable, referring to an isotropic damage model. For anisotropic damage, the damage variable has to be defined as a higher order tensor $\mathbf{D}$ to consider directional dependent material properties.

Based on the pioneering work of [73], which defined damage as the decrease of the load carrying area, several approaches have been proposed. In the next section, some of these approaches are introduced and concepts of CDM which have been introduced are extended to capture the complex behavior of damage in composite materials.

3.2 Three Dimensional Damage State

As previously discussed, the defined scalar damage variable d is unable to take into account the diverse directional damage behavior of anisotropic materials. Thus, the concepts presented in equations (3.1) and (3.2) must be extended into a general three-dimensional anisotropic damage model. Based on effective area reduction, the scalar damage variable d in equation (3.1), becomes in general, a symmetric second order tensor

$$\mathbf{D} = \sum_{i=1}^{3} = D_i \, \mathbf{n}_i \otimes \mathbf{n}_i \quad , \tag{3.3}$$

where D_i and $\mathbf{n}_i$ refer to the principal directions of $\mathbf{D}$. In an infinitesimal cross section, the area vector $A\,\mathbf{n}$ of an arbitrarily chosen cutting surface can be written in terms of its three principal directions:

$$A\,\mathbf{n} = A_1\,\mathbf{n}_1 + A_2\,\mathbf{n}_2 + A_3\,\mathbf{n}_3 \quad . \tag{3.4}$$

Applying the concept proposed in equation (3.1), the effective load carrying subareas can be calculated as

$$\mathrm{d}\tilde{A}_i = (1 - D_i)\mathrm{d}A_i \quad . \tag{3.5}$$

Due to the symmetry and principal directions in $\mathbf{D}$, the damage tensor can not represent damage in more complex materials than those that are orthotropic as long as it is based on area reduction. If the damage tensor is not given in the principal directions, it has to be transformed using eigenvalues and eigenvectors. However, the simplest way is to define three principal damage variables in their three corresponding principal directions $\mathbf{n}_i$.

To develop a basic model for anisotropic damage, an infinitesimal orthogonal cube, as illustrated in figure 3.2, is examined. Assuming the resulting internal forces, acting on the (principal) damaged surface of the cube, to coincide with the resulting internal forces, acting on a fictitious undamaged surface area from the homogenized cube, the following relationship can be obtained

by using the principles defined in (3.1) and (3.2):

$$\begin{bmatrix} \tilde{\sigma}_{11} & \tilde{\sigma}_{12} & \tilde{\sigma}_{13} \\ \tilde{\sigma}_{21} & \tilde{\sigma}_{22} & \tilde{\sigma}_{23} \\ \tilde{\sigma}_{31} & \tilde{\sigma}_{32} & \tilde{\sigma}_{33} \end{bmatrix} = \begin{bmatrix} \frac{\sigma_{11}}{1-D_1} & \frac{\sigma_{12}}{1-D_2} & \frac{\sigma_{13}}{1-D_3} \\ \frac{\sigma_{21}}{1-D_1} & \frac{\sigma_{22}}{1-D_2} & \frac{\sigma_{23}}{1-D_3} \\ \frac{\sigma_{31}}{1-D_1} & \frac{\sigma_{32}}{1-D_2} & \frac{\sigma_{33}}{1-D_3} \end{bmatrix} \quad . \tag{3.6}$$

It is apparent that the damaged Cauchy stress tensor is in general a non-symmetric tensor of second order. Since a non-symmetric stress tensor complicates numerical analysis and disagrees with the fundamental definition of the Cauchy stress tensor, introduced in equation (2.26), several symmetrization schemes have been proposed by the authors of [25, 42, 99, 101, 123]. These symmetrization schemes are developed purely in a mathematical sense and do not have a physical basis. For this reason, such schemes have to be used carefully as they falsify the natural anisotropic damage behavior. The differences between various symmetrization schemes with regard to the resulting constitutive equations are presented in section 3.4. In observing equation (3.6) and recalling that the undamaged Cauchy stress is by definition symmetric, one can conclude that symmetry in the effective stress tensor $\tilde{\sigma}$ can be forced by setting the shear terms to

$$\tilde{\sigma}_{ij}(1-D_j) = \tilde{\sigma}_{ji}(1-D_i) \quad . \tag{3.7}$$

Such an approach can be helpful because this statement is fulfilled when $D_i = D_j$ is true. For further studies on the effect of different symmetrization schemes, the work of [138] is recommended.

As discussed in the previous section, a variety of damage variables and effective stresses have been defined. For instance, [25] uses fourth-, and eighth-order tensors to represent damage in terms of the variation of elastic modulus. A more general definition of effective stresses has been proposed by [25, 42, 123], where a so called damage effect tensor $\mathbb{M}(\boldsymbol{D})$, a fourth-order tensor, is used to transform the Cauchy stresses σ into the corresponding fictitious effective stresses:

$$\tilde{\boldsymbol{\sigma}} = \mathbb{M}(\boldsymbol{D}) : \boldsymbol{\sigma} \quad . \tag{3.8}$$

Depending on the underlying theory, the components of $\mathbb{M}(\boldsymbol{D})$ differ. In the isotropic case defined by equation (3.2), the damage effect tensor $\mathbb{M}(\boldsymbol{D})$ becomes a scalar

$$M(\boldsymbol{D}) = \frac{1}{1-d} \quad . \tag{3.9}$$

3.2.1 Equivalence Principles

In isotropic materials, the hypothesis of strain equivalence is introduced within the effective stress concept shown by equation (3.2). This states that strains in the damaged material coincide with strains in a fictitious undamaged material, as illustrated in figure 3.3. This hypothesis

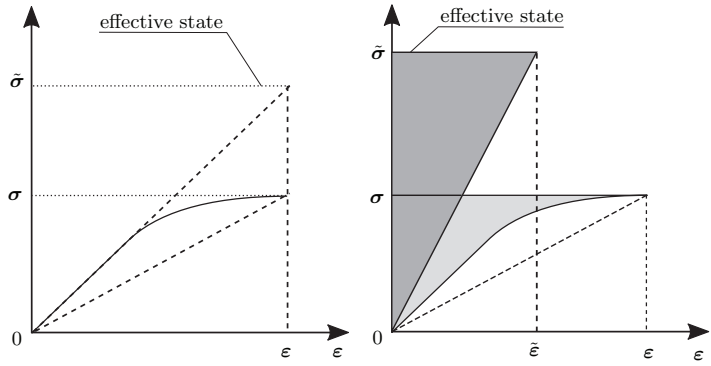

Figure 3.3: Strain equivalence (left) and complementary strain energy equivalence (right).

remains valid in isotropic materials and is approximately valid in more complex materials when a simple damage state is present. However, if the damage process in an anisotropic material is observed, the directional dependent behavior and the oriented definition of damage variables can force the material into a deformation state in which this hypothesis is no longer valid. Therefore, other definitions of mechanical energy must be introduced. This is accomplished in the following section.

Hypotheses of Strain Equivalence

A generalization of equation (3.2) for inelastic deformation is proposed by Chaboche [24, 26]. In the case of elastic deformation, the stress strain relation in a three-dimensional damaged and undamaged material is defined as

$$\begin{aligned} \tilde{\boldsymbol{\varepsilon}} &= \mathbb{S} : \tilde{\boldsymbol{\sigma}} \quad , \\ \boldsymbol{\varepsilon} &= \mathbb{S}(\boldsymbol{D}) : \boldsymbol{\sigma} \quad , \end{aligned} \tag{3.10}$$

where $\mathbb{S}$ is the undamaged compliance tensor defined in equation (2.127). According to the hypotheses of strain equivalence, the following relation between the fictitious (undamaged) and the damaged material must be:

$$\begin{aligned} \boldsymbol{\varepsilon} = \mathbb{S} : \tilde{\boldsymbol{\sigma}} = [\mathbb{S}\,\mathbb{M}(\boldsymbol{D})] : \boldsymbol{\sigma} = \mathbb{S}(\boldsymbol{D}) : \boldsymbol{\sigma} \\ \mathbb{S}(\boldsymbol{D}) = \mathbb{S}\,\mathbb{M}(\boldsymbol{D}) \quad . \end{aligned} \tag{3.11}$$

The resulting damage compliance tensor is in general non-symmetric, but by defining the damage variable $\mathbf{D}$ differently, labeled $\bar{\mathbf{D}}$, this problem was solved in [19, 29] by introducing another definition of the compliance tensor:

$$\bar{\mathbb{S}}(\boldsymbol{D}) = \frac{1}{2}\left[\mathbb{S}\,\mathbb{M}(\bar{\boldsymbol{D}}) + \mathbb{M}^T(\bar{\boldsymbol{D}})\,\mathbb{S}\right] \quad , \tag{3.12}$$

where $\bar{\mathbb{S}}(\boldsymbol{D})$ is now a symmetric tensor.

Hypotheses of Complementary Strain Energy Equivalence

As has been discussed in the previous section, the hypothesis of strain equivalence generally leads to a non-symmetric compliance tensor on which a symmetrization procedure must be applied. For this reason, [42] introduced another form of mechanical equivalence which satisfies the condition of symmetry by itself. This is called the hypotheses of complementary strain energy equivalence, stating that the stored energy $V(\boldsymbol{\sigma}, \boldsymbol{D})$ in a stress suspended damaged body coincides with the stored energy $\overset{*}{V}(\tilde{\boldsymbol{\sigma}})$ in a fictitious undamaged body:

$$\overset{*}{V}(\tilde{\boldsymbol{\sigma}}) = V(\boldsymbol{\sigma}, \boldsymbol{D}) \quad . \tag{3.13}$$

Using tensor quantities for the derivation, the energy in equation (3.13) can be expressed as

$$\begin{aligned} \frac{1}{2}\tilde{\boldsymbol{\sigma}}^T : \mathbb{S} : \tilde{\boldsymbol{\sigma}} &= \frac{1}{2}\boldsymbol{\sigma}^T : \mathbb{S}(\boldsymbol{D}) : \boldsymbol{\sigma} \\ \frac{1}{2}\boldsymbol{\sigma}^T : \left[\mathbb{M}^T(\boldsymbol{D})\,\mathbb{S}\,\mathbb{M}(\boldsymbol{D})\right] : \boldsymbol{\sigma} &= \frac{1}{2}\boldsymbol{\sigma}^T : \mathbb{S}(\boldsymbol{D}) : \boldsymbol{\sigma} \quad , \end{aligned} \tag{3.14}$$

leading to a definition of the damaged compliance tensor:

$$\mathbb{S}(\boldsymbol{D}) = \mathbb{M}^T(\boldsymbol{D})\,\mathbb{S}\,\mathbb{M}(\boldsymbol{D}) \quad , \tag{3.15}$$

with which strains in a damaged body can be related to stresses as

$$\boldsymbol{\varepsilon} = \mathbb{S}(\boldsymbol{D}) : \boldsymbol{\sigma} \quad . \tag{3.16}$$

Using the effective stress definition in equation (3.8), a correlating effective strain definition can be observed:

$$\tilde{\boldsymbol{\varepsilon}} = \mathbb{M}^{-T}(\boldsymbol{D}) : \boldsymbol{\varepsilon} \quad . \tag{3.17}$$

Hypotheses of Strain Energy Equivalence

Alongside a definition of a complementary strain energy equivalence, it is apparent to define another hypothesis based on a strain energy function in a similar way. According to the previous section, the strain energy $W(\boldsymbol{\varepsilon}, \boldsymbol{D})$ stored in a strain suspended elastic (damaged) body has to coincide with the energy $\overset{*}{W}(\tilde{\boldsymbol{\varepsilon}})$ stored in a fictitious (undamaged) body:

$$\overset{*}{W}(\tilde{\boldsymbol{\varepsilon}}) = W(\boldsymbol{\varepsilon}, \boldsymbol{D}) \quad . \tag{3.18}$$

Again, using tensor quantities for the derivation and using equation (3.17), the energy in equation (3.18) can be expressed as

$$\begin{aligned} \frac{1}{2}\tilde{\boldsymbol{\varepsilon}}^T : \mathbb{C} : \tilde{\boldsymbol{\varepsilon}} &= \frac{1}{2}\boldsymbol{\varepsilon}^T : \mathbb{C}(\boldsymbol{D}) : \boldsymbol{\varepsilon} \\ \frac{1}{2}\boldsymbol{\varepsilon}^T : \left[\mathbb{M}^{-1}(\boldsymbol{D})\,\mathbb{C}\,\mathbb{M}^{-T}(\boldsymbol{D})\right] : \boldsymbol{\varepsilon} &= \frac{1}{2}\boldsymbol{\varepsilon}^T : \mathbb{C}(\boldsymbol{D}) : \boldsymbol{\varepsilon} \quad , \end{aligned} \tag{3.19}$$

leading to a definition of the damage elasticity tensor:

$$\mathbb{C}(\boldsymbol{D}) = \mathbb{M}^{-1}(\boldsymbol{D})\,\mathbb{C}\;\mathbb{M}^{-T}(\boldsymbol{D}) \quad . \tag{3.20}$$

The same result, as defined above, can be obtained by inverting equation (3.15).

3.3 Thermodynamic Derivation and Damage Activation

Having defined the general laws of thermodynamics in section 2.3, and aspects of constitutive equations with internal variables in section 2.5, the aim of this section is to derive a thermodynamically consistent damage material. In considering an isothermal process in elastic damage materials, the Helmholtz free energy is solely a function of strains and of damage variables, defined as

$$\Psi = \Psi(\boldsymbol{\varepsilon}, \boldsymbol{D}) \quad , \tag{3.21}$$

where $\boldsymbol{\varepsilon}$ represents elastic strains. Using equation (3.21) and substituting in the generally derived second law of thermodynamics (2.77) together with equation (2.118) yields

$$\left(\boldsymbol{\sigma} - \frac{\partial \Psi}{\partial \boldsymbol{\varepsilon}}\right) : \dot{\boldsymbol{\varepsilon}} - \frac{\partial \Psi}{\partial \boldsymbol{D}} : \dot{\boldsymbol{D}} \geq 0 \quad . \tag{3.22}$$

By introducing a new variable $\mathbf{Y}$ and considering the indications and relations made in (2.119), the two quantities

$$\boldsymbol{\sigma} = \frac{\partial \Psi}{\partial \boldsymbol{\varepsilon}} \quad \text{and} \quad \mathbf{Y} = \frac{\partial \Psi}{\partial \boldsymbol{D}} \tag{3.23}$$

are obtained. In this situation, $\mathbf{Y}$ is defined as the damage strain energy release rate and represents the derived thermodynamic force. By inserting the last two definitions of equation (3.23) into equation (3.22), the Clausius-Duhem inequality simplifies to

$$\mathcal{D}_{int} = \mathbf{Y}\,\dot{\boldsymbol{D}} \leq 0 \quad . \tag{3.24}$$

This states that the dissipated energy is defined by the product of the thermodynamic force $\mathbf{Y}$ and the rate of the damage variable $\dot{\mathbf{D}}$. Most materials typically have a virgin elastic domain in which no damage occurs under the impact of loading, but once the elastic domain is exceeded, damage, and with it the elastic domain, increases. The elastic domain, representing the damage threshold, can be described either in a strain or in a stress state and can be defined by the

damage activation function as

$$f(\mathbf{Y}, \mathbf{D}) = \hat{f}(\mathbf{Y}) - \hat{g} \leq 0 \quad , \tag{3.25}$$

where $\hat{f}(\mathbf{Y})$ is a positive monotonic function dependent on the thermodynamic variable $\mathbf{Y}$, whereas $\hat{g}$ is an updated damage threshold, considering an initial damage threshold g_0, and a positive monotonic softening function that depends on the damage driving quantity δ:

$$\hat{g} = g_0 + g(\delta) \quad . \tag{3.26}$$

The authors of [125] have shown that the damage criterion (3.25) and the second law of thermodynamics (3.22) leads to an optimization problem in cases of using a maximum condition on $\mathcal{D}_{int}$. As a result, by introducing the Lagrangian multiplier $\dot{\lambda} \geq 0$, the evolution of damage can be described by

$$\dot{\mathbf{D}} = \dot{\lambda} \frac{\partial f}{\partial \mathbf{Y}} = \dot{\lambda} \frac{\partial \hat{f}(\mathbf{Y})}{\partial \mathbf{Y}} \quad . \tag{3.27}$$

Furthermore, the Lagrangian multiplier $\dot{\lambda}$, together with the damage activation function f, allows to distinguish between different loading/unloading instances according to the Kuhn-Tucker conditions explained, for example, in [122]:

$$f \leq 0 \quad , \qquad \dot{\lambda} \geq 0 \quad , \qquad \dot{\lambda} f = 0 \quad . \tag{3.28}$$

Using these conditions, the following instances can be distinguished:

1. $f < 0 \rightarrow$ unloading or elastic loading (no damage)
2. $f = 0 \rightarrow$ damage loading

In instances of unloading, or during (re)loading in the elastic domain, the damage activation function (3.25) is smaller than zero. Considering the definition in equation (3.28) yields $\dot{\lambda} = 0$, and thus $\dot{\mathbf{D}} = 0$, according to equation (3.27). In contrast, if $f = 0$ damage occurs and $\dot{\lambda} > 0$, implying that $\dot{\mathbf{D}} > 0$. An illustration of these different instances is presented in figure 3.4.

In the equations described above, a number of internal variables, such as $\mathbf{D}$ and δ, are needed to sufficiently describe a damage process, concerning the damage surface, damage evolution, or softening functions. However, these variables are not easily obtained with standard tests. Therefore, it is necessary for a user to evaluate multiple experiments under specific or previously observed conditions, with which parameters can be properly fitted.

This section concludes with an analogue definition of equation (3.21), a complementary energy function related to stresses and the damage variable:

$$\chi = \chi(\boldsymbol{\sigma}, \boldsymbol{D}) \quad . \tag{3.29}$$

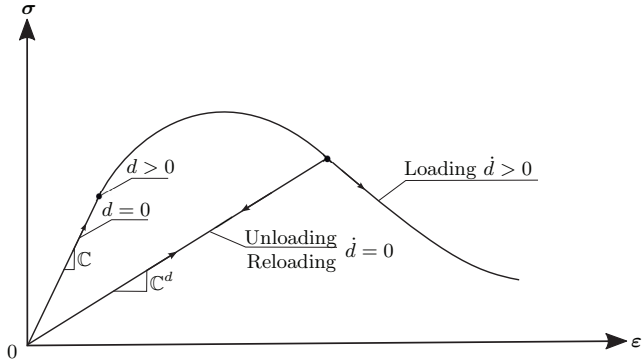

Figure 3.4: Stress-strain curve under loading and reloading.

This type of energy function is called the Gibbs free energy, from which the following relations can be obtained:

$$\boldsymbol{\varepsilon} = \frac{\partial \chi}{\partial \boldsymbol{\sigma}} \quad \text{and} \quad \mathbf{Y} = \frac{\partial \chi}{\partial \boldsymbol{D}} \quad , \tag{3.30}$$

and

$$\mathbb{H} = \frac{\partial^2 \chi}{\partial \boldsymbol{\sigma}^2} \quad . \tag{3.31}$$

3.4 Damage Effect Tensor and Constitutive Equations

To define the constitutive equations of elastic damage materials, a brief introduction of the damage effect tensor $\mathbb{M}$, introduced in equation (3.8), using previously discussed symmetrization schemes, is necessary. The definition of different effect tensors produces varying forms of constitutive equations. A more detailed study, employed in this section, can be found in [100].

3.4.1 Damage Effect Tensor

This section aims to show different forms of damage effect tensors $\mathbb{M}^i$ resulting from the theories introduced in section 3.2.1. To this end, attention is paid to the final components of $\mathbb{M}$. For the purpose of simplicity, the tensor $\mathbb{M}$ is expressed in matrix form $\bar{\mathbf{M}}$ of its components, using the sorting defined in equation (2.125). Furthermore, in this section, an orthonormal basis $\mathbf{n}_i$, with its principal directions $\mathbf{n}_i$ of the symmetric second-order damage tensor $\boldsymbol{D}$ is assumed. Applying transformation relations on $\bar{\mathbf{M}}$ leads to a new matrix $\mathbf{M}$ with which the vector matrix relation for effective stresses can be defined as

$$\tilde{\boldsymbol{\sigma}} = \mathbf{M}\,\boldsymbol{\sigma} \quad . \tag{3.32}$$

Here $\mathbf{M}$ is a 6x6 matrix which comprises entries without exception on the principal diagonal, implying an orthonormal base system in the principal directions:

$$\mathbf{M} = \begin{bmatrix} M_1 & 0 & 0 & 0 & 0 & 0 \\ 0 & M_2 & 0 & 0 & 0 & 0 \\ 0 & 0 & M_3 & 0 & 0 & 0 \\ 0 & 0 & 0 & M_{12} & 0 & 0 \\ 0 & 0 & 0 & 0 & M_{13} & 0 \\ 0 & 0 & 0 & 0 & 0 & M_{23} \end{bmatrix} . \tag{3.33}$$

In the anisotropic damage model proposed in chapter 4, a user can switch between different definitions of $\mathbf{M}$ resulting from different symmetrization schemes. The first damage effect tensor $\mathbf{M}^1$ is proposed by authors Chow and Lu [35, 36], using the symmetrization scheme of Murakami et al. shown in the works [99, 101]. Its components are

$$\begin{aligned} M_1^1 = \frac{1}{1-D_1} \quad ,..., \quad M_3^1 = \frac{1}{1-D_3} \\ M_{12}^1 = \frac{1}{2}\left(\frac{1}{1-D_1} + \frac{1}{1-D_2}\right) \quad ,..., \quad M_{23}^1 = \frac{1}{2}\left(\frac{1}{1-D_2} + \frac{1}{1-D_3}\right) \end{aligned} . \tag{3.34}$$

Notice that the damage effect tensor $\mathbf{M}^i$ in the previous and following equations is no longer a tensor, but nevertheless is named so, dependent on its original definition. The second, and at the same time, when using the above mentioned orthonormal basis system, fourth damage effect tensor $\mathbf{M}^{2,4}$ are proposed in [30, 37] and [34], where the authors use the symmetrization scheme shown in [41, 42] and [34, 36], respectively. Its components are

$$\begin{aligned} M_1^{2,4} = \frac{1}{1-D_1} \quad ,..., \quad M_3^{2,4} = \frac{1}{1-D_3} \\ M_{12}^{2,4} = \frac{1}{\sqrt{(1-D_1)(1-D_2)}} \quad ,..., \quad M_{23}^{2,4} = \frac{1}{\sqrt{(1-D_2)(1-D_3)}} \end{aligned} . \tag{3.35}$$

The third damage effect tensor $\mathbf{M}^3$ is proposed in [139] using the symmetrization scheme from [20]. Its components are defined as

$$\begin{aligned} M_1^3 = \frac{1}{(1-D_1)(1-D_1)} \quad ,..., \quad M_3^3 = \frac{1}{(1-D_3)(1-D_3)} \\ M_{12}^3 = \frac{1}{(1-D_1)(1-D_2)} \quad ,..., \quad M_{23}^3 = \frac{1}{(1-D_2)(1-D_3)} \end{aligned} . \tag{3.36}$$

The fifth and last definition of the components of a damage effect tensor $\mathbf{M}^5$ is accomplished by [34] using a symmetrization scheme that the study developed:

$$M_1^5 = \frac{1}{(1-D_1)} \quad ,..., \quad M_3^5 = \frac{1}{(1-D_3)}$$
$$M_{12}^5 = \frac{1}{\left(1-\frac{D_1+D_2}{2}\right)} \quad ,..., \quad M_{23}^5 = \frac{1}{\left(1-\frac{D_2+D_3}{2}\right)} \quad . \tag{3.37}$$

A study on the effects of the different forms of the previously defined damage effect tensors is completed in section 6.2.6.

3.4.2 Damage Compliance Matrix

In section 3.4.1 various types of damage effect tensors $\mathbf{M}$ are defined, whereas in section 3.2.1 different equivalent principles are introduced. With that, several diverse versions of damage compliance matrices $\mathbb{S}(\mathbf{D})$ (or damage elasticity matrices $\mathbb{C}(\mathbf{D})$) can be defined by using equations (3.11),(3.12),(3.15) or (3.20). It's general form is given as

$$\mathbb{S}(\mathbf{D}) = \mathbb{H} = \begin{bmatrix} \mathbb{H}_{11} & \mathbb{H}_{12} & \mathbb{H}_{13} & 0 & 0 & 0 \\ \mathbb{H}_{21} & \mathbb{H}_{22} & \mathbb{H}_{23} & 0 & 0 & 0 \\ \mathbb{H}_{31} & \mathbb{H}_{32} & \mathbb{H}_{33} & 0 & 0 & 0 \\ 0 & 0 & 0 & \mathbb{H}_{44} & 0 & 0 \\ 0 & 0 & 0 & 0 & \mathbb{H}_{55} & 0 \\ 0 & 0 & 0 & 0 & 0 & \mathbb{H}_{66} \end{bmatrix} \quad , \tag{3.38}$$

having renamed the tensor $\mathbb{S}(\mathbf{D})$ to $\mathbb{H}$ for the purpose of simplification. With this definition, a damaged elasticity matrix can finally be calculated as

$$\mathbb{C}(\mathbf{D}) = \mathbb{H}^{-1} \quad . \tag{3.39}$$

When using the definitions created by equation (3.11), without the reciprocal condition (2.131) and through inserting one of the defined damage effect tensors $\mathbf{M}^i$, $\mathbb{H}$ can take on several different forms. Its components besides the main diagonal in matrix (3.38) become

$$\mathbb{H}_{ij} = -\frac{\nu_{ji}}{(1-D_j)E_j} \quad . \tag{3.40}$$

Because D_i and D_j are obviously not equal, $\mathbb{H}$ becomes non-symmetric. To overcome such a problem, either a symmetrization procedure according to equation (3.12) is used or the damage values entering the positions beside the main diagonal have to be modified. A simple relation

can be obtained by enforcing the symmetry and setting $\mathbb{H}_{12} = \mathbb{H}_{21}$.

Symmetric Compliance Tensor

Even though the strain equivalence is from its theory not the best choice for anisotropic damage materials, it is yet widely used in numerical calculations. In the current study, based on more recent studies [33, 48, 79, 85], the following form is used as default in the anisotropic macro model, proposed in chapter 4.2. This is done because the strain equivalence has been shown to create reliable results and are effective in a numerical point of view:

$$\mathbb{H} = \begin{bmatrix} \frac{1}{(1-D_1)E_1} & -\frac{\nu_{12}}{E_1} & -\frac{\nu_{13}}{E_1} & 0 & 0 & 0 \\ -\frac{\nu_{12}}{E_1} & \frac{1}{(1-D_2)E_2} & -\frac{\nu_{23}}{E_2} & 0 & 0 & 0 \\ -\frac{\nu_{13}}{E_1} & -\frac{\nu_{23}}{E_2} & \frac{1}{(1-D_3)E_2} & 0 & 0 & 0 \\ 0 & 0 & 0 & \frac{1}{(1-D_{12})G_{12}} & 0 & 0 \\ 0 & 0 & 0 & 0 & \frac{1}{(1-D_{13})G_{13}} & 0 \\ 0 & 0 & 0 & 0 & 0 & \frac{1}{(1-D_{23})G_{23}} \end{bmatrix} . \quad (3.41)$$

The authors of [23, 92, 105] have shown that damage does not significantly affect the minor Poisson ratio. Therefore, the components besides the main diagonal from equation (3.41), can be roughly assumed to remain elastic and continue to deliver reliable results.

3.5 Damage Models - General Aspects

Continuum damage models, using finite element methods, follow a general pattern as illustrated by figure 3.5. This figure shows the general procedure of damage materials. According to chapter 5, the material routine is performed in each Gauss point until convergence is reached.

The continued investigation of damage materials requires supplementary definitions of material quantities. First, as shown in equation (3.26), an initial damage threshold g_0 is used to find the load state where damage first occurs. As long as this initial threshold remains unreached, the material response stays elastic. Once the threshold is exceeded, the material starts to degrade (damage) and the response becomes inelastic. It is important to note that the damage threshold $g(\delta)$ amplifies in relation to the present load state after damage first occurs, but holds its maximum value and can never decrease, creating an elastic reloading region, shown in figure 3.4. Upon reaching the threshold, a damage evolution law must be defined, describing the development of the damage variable $\mathbf{D}$ in relation to the present load state, as well as other quantities that enforce a physically valid material behavior. Both aspects are discussed in more detail below.

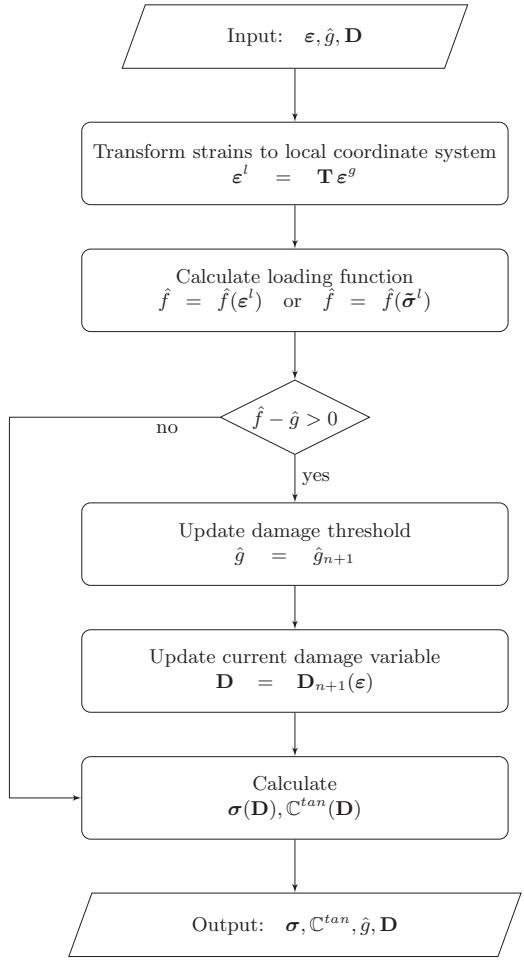

Figure 3.5: General flowchart of damage analysis.

3.5.1 Damage Initiation

This section introduces the basics of failure criteria. Initially, a short overview of classical isotropic failure criteria is provided, followed by the more complex criteria of fiber-reinforced composites. This section does not aim to provide an extensive study of the different concepts, but rather to show some general aspects and give a short overview of the present criteria. For more, [7, 8, 50] are recommended and a short overview is also given in [59]. Over the last decades,

several failure criteria have been developed, although some of them use a simple theory, they still have practical importance.

Classical Failure Criteria - Isotropic Damage

Classical failure criteria have the general form

$$F(\boldsymbol{\sigma}) = 0 \quad \text{or} \quad \hat{F}(\boldsymbol{\varepsilon}) = 0 \tag{3.42}$$

and are often formulated using principal stresses or strains. This holds a number of advantages because principal stresses arise from invariants and are therefore independent of the chosen base system. Without any claim to completeness, the following main failure criteria can be distinguished:

- Principal stress hypothesis (Rankine, Lame, Navier): Failure is postulated if the highest principal stress reaches the tension strength or the lowest principal stress reaches the compressive strength. The associated failure plane for a three-dimensional stress state is the surface of a cube. This hypothesis is often used within brittle materials but is limited when more than one principal stress state is present.

- Principal strain hypothesis (Saint-Venant, Bach): Similarly to the principle stress hypothesis, failure is postulated when the main principal strain reaches its critical value. Experiments have shown that this hypothesis rarely matches actual behavior and thus is not widely used in practical applications.

- Strain energy hypothesis (Beltrami): Failure is postulated when the strain energy density $U = U_v + U_G$ reaches a critical value U_c. The corresponding failure surface is an ellipsoid around its hydrostatic axis. According to this theory, a hydrostatic pressure state causes the same failure as a hydrostatic tension state, which has proved incorrect.

- Von Mises yield criterion: The von Mises criterion is obtained by omitting the volumetric part U_V in the strain energy hypothesis proposed by Beltrami. This theory suggests that yielding begins once the (scalar) von Mises stresses σ_V reaches a critical value σ_y, known as the yield strength. The von Mises criterion can also be related to the second deviatoric stress invariant J_2, from which J_2 plasticity arises. This hypothesis creates a smooth failure surface around its hydrostatic axis, as with the Beltrami surface. This hypothesis produces reliable agreement with experiments when ductile materials are used.

- Other failure criteria, are among others, the yield condition of Tresca, which is similar to the von Mises criteria, but more difficult to implement because of its discontinuity. There are also the Coloumb-Mohr and Drucker-Prager hypotheses which are widely used in the field of geological and granular materials.

Failure Criteria in Composite Materials

The failure criteria which have been examined so far are not suited to predict failure in anisotropic materials correctly. This is because in a material with intensely directionally dependent strengths, failure does not, in general, occur at the highest stress or strain state. Therefore, to predict the onset of damage, other failure criteria have to be considered. To specify the different criteria used in anisotropic materials, definitions of unidirectional single ply strengths are introduced:

- the longitudinal or axial tension strength X_t,
- the longitudinal or axial compression strength X_c,
- the transversely tension strength Y_t,
- the transversely compression strength Y_c,
- the shear strength S_{12} and S_{23}.

Diverse classes of failure criteria can be distinguished by differing between mode dependent and mode independent criteria. In an abbreviated fashion, the most well-known criteria are introduced below. For a mode independent class, the following criteria are introduced:

- The maximum stress criterion (2-D): Similar to the Rankine criteria, single ply failure is postulated if one of the following stress conditions is reached:

$$\begin{aligned} -X_c < \quad \sigma_1 \quad &< X_t \\ -Y_c < \quad \sigma_2 \quad &< Y_t \\ |\tau_{12}| \quad &< S_{12} \end{aligned} \tag{3.43}$$

  These criterion is easy to employ but not reliable, in part because they do not consider an interaction between the stresses. A similar form, with the same advantages and disadvantages, can be obtained by using the maximum strain criteria.

- Tsai-Hill criteria (2-D): In reference to the yield criterion of plasticity theory, the Tsai-Hill criterion postulate a failure surface based on a quadratic function of the stress components, given with maximum stess criterion.

$$\frac{\sigma_1^2}{X^2} - \frac{\sigma_1 \sigma_2}{X^2} + \frac{\sigma_2^2}{Y^2} + \frac{\tau_{12}^2}{S^2} = 1 \tag{3.44}$$

  This criterion is advantageous because it presents a single formula with a smooth damage surface and considers interactions between different stresses. The correspondence with experiments is better than that of the maximum stress criterion. However, the criterion lack a distinction between tension and compression, and between different damage modes.

- Tsai-Wu criterion (2D): This criterion advance the Tsai-Hill criterion and distinguishes

between tension and compression impact. The damage surface has the shape of an ellipsoid in the $(\sigma_1, \sigma_2, \tau_{12})$-stress space. Even though this criterion does not distinguish between different damage modes, it is well-recognized and often used:

$$\frac{\sigma_1^2}{X_t\, X_c} - \frac{\sigma_1\, \sigma_2}{\sqrt{X_t\, X_c\, Y_t\, Y_c}} + \frac{\sigma_2^2}{Y_t\, Y_c} + \frac{\tau_{12}^2}{S^2} + \sigma_1 \left(\frac{1}{X_t} - \frac{1}{X_c}\right) + \sigma_2 \left(\frac{1}{Y_t} - \frac{1}{Y_c}\right) = 1 \quad (3.45)$$

Because the failure criterion introduced so far have limited accuracy, other approaches of failure criteria were necessarily developed. These new criteria distinguish between different failure modes and are explained below. One such criterion distinguishes between two different partial failure criteria, fiber failure and inter-fiber failure. For the damage mode of inter-fiber failure, the criterion of Tsai-Wu is used in a modified form. Whereas, for the damage mode of fiber failure, a simple quadratic stress criterion is used. The resulting damage surface is an ellipsoid (Tsai-Wu) with cutting-planes at its ends, called Puck's cigar. Puck further developed his own criterion, considering 2-4 different damage modes, depending on whether considering a two- or three-dimensional space. In addition, to distinguish between different damage modes, Puck suggests and inevitably determines the corresponding fracture angle. Puck's criterion is widely accepted for physically based predictions of failure. In fact, during the world-wide failure exercise (WWFE), the criterion emerged as one of the best available failure criteria. Unfortunately, the theory is comparably complex and requires extensive training.

In addition to Puck's criterion, two other mode dependent failure criteria are introduced. These are used in modified forms in the developed and implemented damage model introduced in Chapter 4.2:

- The criterion of Hashin [65]: This criterion was developed in the 1980s. It is deduced, like Puck's criterion, from the Mohr-Coloumb theory, but does not consider a fracture plane. Hashin's failure criterion is mode dependent and distinguishes between two types of failure, fiber fracture and matrix fracture. Each type can be further subdivided into tension and compression states, leading to the following four different damage modes:

  - Fiber failure in tension ($\sigma_{11} > 0$):

$$F_1^t = \left(\frac{\sigma_{11}}{X_T}\right)^2 + \frac{\alpha\sigma_{12}^2 + \alpha\sigma_{13}^2}{S_{12}^2} = 1 \quad (3.46)$$

  - Fiber failure in compression ($\sigma_{11} < 0$):

$$F_1^c = \frac{\sigma_{11}}{X_C} = 1 \quad (3.47)$$

– Matrix failure in tension ($(\sigma_{22}+\sigma_{33})>0$):

$$F_2^t=\left(\frac{\sigma_{22}+\sigma_{33}}{Y_T}\right)^2+\frac{\sigma_{23}^2-\sigma_{22}\sigma_{33}}{S_{23}^2}+\frac{\sigma_{12}^2+\sigma_{13}^2}{S_{12}^2}=1 \tag{3.48}$$

– Matrix failure in compression ($(\sigma_{22}+\sigma_{33})<0$):

$$\begin{aligned}F_2^c=&\left[\left(\frac{Y_C}{2S_{23}}\right)^2-1\right]\left(\frac{\sigma_{22}+\sigma_{33}}{Y_C}\right)+\left(\frac{\sigma_{22}+\sigma_{33}}{2S_{23}}\right)^2+....\\&....+\frac{\sigma_{23}^2-\sigma_{22}\sigma_{33}}{S_{23}^2}+\frac{\sigma_{12}^2+\sigma_{13}^2}{S_{12}^2}=1\end{aligned} \tag{3.49}$$

The Hashin criterion for orthotropic materials is based on seven material strength parameters which can be obtained under investigation of standard tests.

- Cuntze's failure mode concept (FMC): The FMC is a recently developed failure criterion, introduced in [43–45], that delivers a reliable correspondence to experimental data. In fact, the FMA has been shown in the WWFE to be, overall, one of the best currently available damage criterion. Cuntze suggests that a change in one specific failure mode does not affect another failure mode, leading to the conclusion that the same number of conditions as the number of failure modes must be established, whereby each failure mode is considered in particular. Moreover, Cuntze considers that the number of independent elasticity constants equals the number of independent material strengths. Furthermore, it is postulated that the number of independent failure modes equals the number of independent material strengths. Because of its simple structure, the FMC is easy to implement. It differs between fiber failure (FF) and inter-fiber failure (IFF) and is further subdivided into the five following damage modes, according to the five independent elasticity constants in anisotropic materials:

  – Fiber failure in tension ($\sigma_{11}>0$):

$$\mathrm{FF1}=\frac{\sigma_{11}}{X_T}=1 \tag{3.50}$$

  – Fiber failure in compression ($\sigma_{11}<0$):

$$\mathrm{FF2}=\frac{-\sigma_{11}}{X_C}=1 \tag{3.51}$$

  – Matrix failure in tension ($(\sigma_{22}+\sigma_{33})>0$):

$$\mathrm{IFF1}=\frac{(\sigma_{22}+\sigma_{33})+\sqrt{(\sigma_{22}-\sigma_{33})^2+4\sigma_{23}^2}}{2Y_t}=1 \tag{3.52}$$

– Matrix failure in compression ($(\sigma_{22}+\sigma_{33})<0$):

$$\text{IFF2} = \frac{(b_{sp}-1)\cdot(\sigma_{22}+\sigma_{33}) + b_{ss}\sqrt{(\sigma_{22}-\sigma_{33})^2+4\sigma_{23}^2}}{Y_c} = 1 \tag{3.53}$$

– Shear failure:

$$\text{IFF3} = \left[\frac{b_{sp}\cdot I_{23-5} + \sqrt{b_{sp}^2\cdot I_{23-5}^2 + 4S_{12}^2\cdot(\sigma_{31}^2+\sigma_{21}^2)^2}}{2S_{12}^3}\right]^{0.5} = 1 \tag{3.54}$$

where

$$I_{23-5} = 2\sigma_{22}\cdot\sigma_{21}^2 + 2\sigma_{33}\cdot\sigma_{31}^2 + 4\sigma_{23}\sigma_{31}\sigma_{21} \tag{3.55}$$

and

$$b_{sp} = \nu_{sp} \qquad \text{and} \qquad b_{ss} = \frac{1}{1-\nu_{ss}} \quad . \tag{3.56}$$

Here, ν are the friction parameters typically ranging from

$$0.05 < \nu_{sp} < 0.3 \qquad \text{and} \qquad 0.05 < \nu_{ss} < 0.2 \quad , \tag{3.57}$$

Cuntze recommends values of $\nu_{sp} = 0.1$ and $\nu_{ss} = 0.1$ for a first approximation when no further information is present.

The FMC, described by equations (3.50) to (3.54) are based on the local ply coordinate system. It can also be defined using principal stresses, or even by stresses resulting from an arbitrarily chosen cutting-plane. Different damage modes of the FMC are illustrated in figure 3.6.

A closed solution of the multi-dimensional failure surface is obtained by superimposing five single independent failure modes:

$$\text{F}_{\text{Inter}} = (\text{FF1})^m + (\text{FF2})^m + (\text{IFF1})^m + (\text{FF2})^m + (\text{FF3})^m \quad , \tag{3.58}$$

in which the mode interaction parameter, $2.5 < m < 3.1$, is fitted from test data and differs in its specified range. A recommended value for pre-design is $m = 2.6$.
Overall, Cuntze's FMC is a simple method to formulate damage and is highly robust in a numerical point of view. Furthermore, it is based on the physical world and reliably agrees with experimental test data, as shown in the WWFE. Thus, this failure mode concept is used, in addition to Hashin's criterion, in section 4.2.

Aside from the criteria that have been introduced, several other failure criteria have been developed. The goal of this research is not to examine the advantages and disadvantages of these criteria. This work is not a study of different failure criteria. Rather, these criteria are employed as a starting point for damage. The events that occur after initial damage, including, and in particular focusing on numerical implementation, are of interest. Difficulties that arise during implementation are discussed in greater detail in section 6, alongside a presentation of

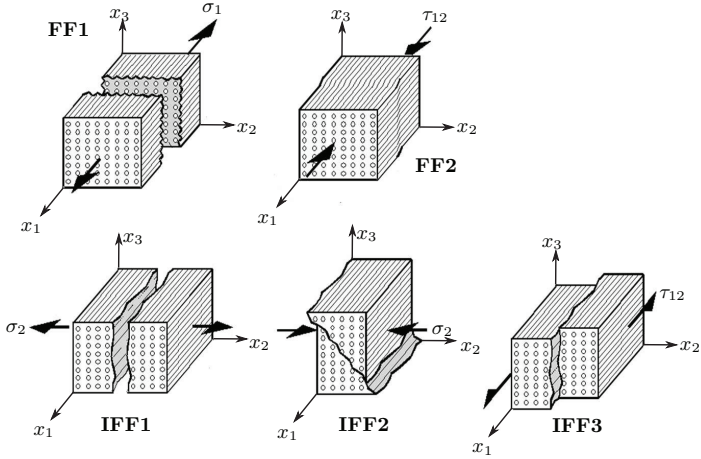

Figure 3.6: Visualization of the FMC damage modes.

the developed model.

3.5.2 Damage Evolution and Energy Release Rate

To fully define the constitutive equations of a damage model, a damage evolution law is introduced. The evolution law relates internal variables to the damage variable, resulting in a softened (degraded) material response. Several forms of evolution laws have been defined with different material responses. Assuming a one-dimensional model, the material response in a softening regime can be observed as linear, bilinear, exponential, and so on. In section 4.2, linear and exponential softening laws according to figure 3.8 are applied. The linear softening law is widely used and is advantageous because of its simple structure and closed analytical form. However, both softening laws can have numerical problems at the discontinuous peak when it switches from a linear, elastic increasing region to a decreasing region. The work done in [85] is recommended for those interested in a more detailed study of softening laws. The proposed evolution law is a generalization of the approach proposed by [22] for delamination models and is based on energy dissipation during a damage process.

In figure 3.7, the parameter G_c^i is known as the critical strain energy release rate. It is a material parameter that additionally depends on the investigated fracture mode i and has the unit of energy per unit area. The definition of δ is given in equation (4.33). In literature, three basic fracture modes, as shown in figure 3.8, are distinguished:

- Mode I is an opening mode, triggered by a tensile stress normal to the plane of the crack.

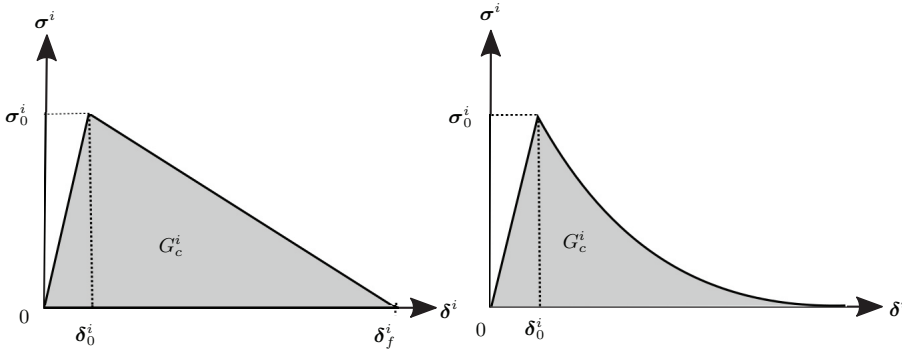

Figure 3.7: Linear (left) and exponential (right) damage evolution.

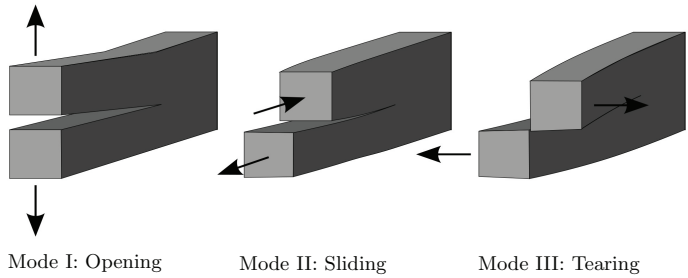

Figure 3.8: Visualization of basic fracture modes.

- Mode II is a plane shearing mode (sliding mode), triggered by a shear stress acting parallel to the plane of crack and perpendicular to the front of the crack.
- Mode III is an out of plane shearing mode (tearing mode), triggered by a shear stress acting parallel to the plane of the crack and parallel to the front of the crack.

The area under the stress-strain curve, depicted in figure 3.7, is the mode dependent associated fracture toughness. It is defined by the displacement δ_f^i, where a complete separation (damage)

is present according to equation:

$$\int_0^{\delta_f^i} \sigma^i d\delta = G_c^i \quad . \tag{3.59}$$

In light of equation (3.59), the critical energy release rate (fracture toughness) G_c^i has to be specified in each single damage mode. Such a process can be challenging because the rates are not easily measured or often available in literature. Fracture toughness greatly influences the pathway of an load-displacement curve in the decreasing region. As shown in figure 3.7, the degreasing path is flatter when G_c is a higher value and describes the ductility of a material.

Mixed mode damage behavior

For practical applications of composite structures, the complex damage process cannot often be reduced to one of the three single fracture modes introduced in section 3.5.2. Therefore, to allow for more complex loading and fracture modes, a more general formula, addressing mixed-mode fracture propagation, was introduced by [22]. If mode I, II, or III is considered, the onset of damage can be determined by comparing single stresses with corresponding material strengths. However, under mixed-mode loading, a simple maximum stress criterion has been shown to be inappropriate. Therefore, a mixed-mode criterion has been established which considers the interaction of different stress components. Thus, a total mixed mode relative strain δ_m, containing all single strains of the currently discussed damage modes, must be introduced. When using this mixed mode strain, a mixed mode energy release rate G_c^m has to be defined as well. The most widely used criterion for mixed-mode loading is the power law criterion, defined as:

$$\left(\frac{G_I}{G_{Ic}}\right)^{\alpha} + \left(\frac{G_{II}}{G_{IIc}}\right)^{a} = 1 \quad . \tag{3.60}$$

Suggestions concerning the parameters of α can be found in [22]. Recent studies have shown some disadvantages of this criterion, as a large range of mode ratios have been shown to yield inaccurate results. To accurately account for differences in fracture toughness, the criterion proposed by [18] is recommended, named the B-K criterion. This criterion is based on the fracture modes I and II and on a parameter η, which can be obtained from mixed mode bending tests. The criterion is defined as:

$$G_{Ic} + (G_{IIc} - G_{Ic}) \left(\frac{G_{II}}{G_T}\right)^{\eta} = G_c \quad , \tag{3.61}$$

where $G_T = G_I + G_{II}$. If mode III loading occurs, the term G_{II} in equation (3.61) can be replaced with its corresponding value G_{shear}. Suggestions concerning the parameter η can also be found in [22]. The mixed mode softening law can be illustrated by a three dimensional cube, as shown in figure 3.9. In [87–90] a detailed study on the determination of the critical energy release rates, related to the five different damage modes used in the FMC (shown in section 3.5.1), is completed.

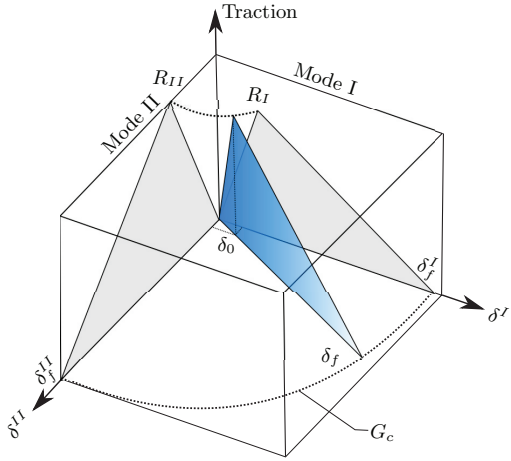

Figure 3.9: Critical energy release rate in mixed mode material softening.

3.6 Cohesive Interface Elements

Cohesive laws are commonly used in interface models for the propagation of delamination in layered structures. They are based on a universal relationship between binding energies of materials and have been used or introduced into finite element software by many authors, e.g. in [10, 62, 103, 131, 132, 134, 135]. Though cohesive laws are often used to model delamination, they are not restricted to this task. They can also be used for other separation modes, such as fiber damage, matrix damage, and debonding, among others.

For the description of an irreversible cohesive law, the existence of a free energy function

$$\phi = \phi(\mathbf{u}, \mathbf{q}) \tag{3.62}$$

is postulated. In equation (3.62), $\mathbf{u}$ denotes an opening displacement vector and $\mathbf{q}$ a vector of internal variables. Furthermore an isothermal process is assumed. In the current study, the cohesive law is defined through the widely used universal energy relation

$$\phi(\delta) = G_c \left[1 - \left(1 + \frac{\delta}{\delta_c} \right) e^{-\frac{\delta}{\delta_c}} \right] \quad , \tag{3.63}$$

suggested in [118]. In equation (3.63), G_c is the critical energy release rate, $\delta_c = G_c / e\,\sigma_c$ corresponds to the critical displacement, and σ_c is the critical traction. Furthermore, δ denotes

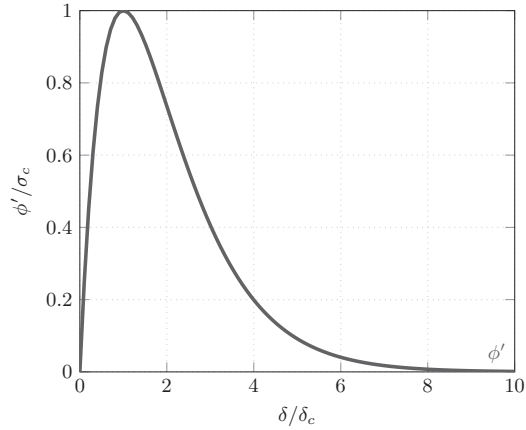

Figure 3.10: Atomistic separation law.

an effective opening vector, defined as

$$\delta = \sqrt{\beta^2(u_1^2 + u_2^2) + u_3^2} = \sqrt{\mathbf{u}^T\,\bar{\mathbf{C}}\,\mathbf{u}} \quad \text{with} \quad \mathbf{C} = \begin{bmatrix} \beta^2 & 0 & 0 \\ 0 & \beta^2 & 0 \\ 0 & 0 & 1 \end{bmatrix} \quad , \tag{3.64}$$

according to [112]. In equation (3.64), the parameter β describes the ratio of the shear to the normal critical tractions. The unloading/reloading conditions, according to equation (3.28), are considered by including the maximum displacement δ_{max} as an internal variable $\delta = \delta(\delta_{max})$. The resulting graph is a smooth, exponential function, shown in figure 3.10. When using this separation law, the main difference from the damage law illustrated in figure 3.4 is the absence of an elastic regime. Damage (or separation) is present from the beginning of the calculation.

Following the explanations given in chapter 2 and 3, the traction vector $\mathbf{t}$ and the tangential material stiffness $\mathbb{C}^{tan}$ are given with the first and second derivative of equation (3.62) with respect to the displacements $\mathbf{u}$. Applying the chain rule on δ yields

$$\begin{aligned} \mathbf{t} &= \frac{\partial \phi}{\partial \delta}\frac{\partial \delta}{\partial \mathbf{u}} = \frac{\phi'}{\delta}\,\bar{\mathbf{C}}\,\mathbf{u} \qquad \text{for loading} \quad , \\ \mathbf{t} &= \frac{\phi'(\delta_{max})}{\delta_{max}}\,\bar{\mathbf{C}}\,\mathbf{u} \qquad \text{for unloading} \quad , \end{aligned} \tag{3.65}$$

where ϕ' is defined as the derivative of ϕ with respect to δ:

$$\phi' = \frac{\partial \phi}{\partial \delta} = \sigma_{\mathbf{c}}\, e\, \frac{\delta}{\delta_c}\, e^{-\frac{\delta}{\delta_c}} \quad . \tag{3.66}$$

The second derivative of δ with respect to the displacements $\mathbf{u}$ reads

$$\begin{aligned} \frac{\partial \mathbf{t}}{\partial \mathbf{u}} &= \frac{\phi'}{\delta}\,\bar{\mathbf{C}} + \left[\phi'' - \frac{\phi'}{\delta}\right]\,(\bar{\mathbf{C}}\,\mathbf{u})\,(\bar{\mathbf{C}}\,\mathbf{u})^T \qquad \text{for loading} \quad , \\ \frac{\partial \mathbf{t}}{\partial \mathbf{u}} &= \frac{\phi'(\delta_{max})}{\delta_{max}}\,\bar{\mathbf{C}}\mathbf{u} \qquad\qquad\qquad\qquad\quad \text{for unloading} \quad , \end{aligned} \tag{3.67}$$

in which the second derivative of ϕ with respect to δ is defined as

$$\phi'' = e\frac{\sigma_c}{\delta_c}\left(1 - \frac{\delta}{\delta_c}\right)\,e^{-\dfrac{\delta}{\delta_c}} \quad . \tag{3.68}$$

Finally, by using relation

$$\sigma_{\mathbf{c}}\,e\,\frac{\delta}{\delta_c}\,e^{-\frac{\delta}{\delta_c}} = (1-D)\,\mathbb{C}_0\,\delta \tag{3.69}$$

the damage parameter D can be calculated:

$$D = 1 - \frac{\sigma_c}{\delta_c\,\mathbb{C}_0}\,e^{\,1-\dfrac{\delta}{\delta_c}} \quad . \tag{3.70}$$

This section introduced core notions related to damage evolution based on cohesive material laws using the critical energy release rate. The specific and resulting damage evolution laws that are implemented and introduced throughout the current study are further examined as necessary.

Chapter 4

Macroscopic Damage Models

This chapter presents two different damage models, an isotropic and an anisotropic damage model. The isotropic model presented in section 4.1 was originally proposed by Oliver et al. in [108] and expanded in [110] by the same authors to improve the numerical convergence. The anisotropic damage model is more complex and discussed in detail in section 4.2, using, among others, concepts introduced in chapter 3. The implicit-explicit integration scheme (IMPL-EX), first proposed by Oliver et al. in [110], is adapted and implemented for the developed anisotropic damage model to improve convergence issues in the anisotropic damage model.

4.1 The Isotropic Damage Model

As noted in the introduction, this model is based on work by Oliver et al. [108] (originally developed for concrete materials) which uses concepts developed by Simo et al. in [124, 125]. These basic concepts are also summarized in [27, 28]. An isotropic damage model is the simplest case of damage. A single damage variable represents the nonlinear material behavior. In the implemented model, there is no general distinction between damage caused by pressure and damage caused by tension.

The beginning of the derivation is the Helmholtz free energy, generally defined in equation (3.21) and for an (elastic) isotropic and isothermal process defined as

$$\Psi = (1-d)\,\Psi^e \qquad \text{with} \qquad \Psi^e = \frac{1}{2}\,\boldsymbol{\varepsilon} : \tilde{\boldsymbol{\sigma}} = \frac{1}{2}\,\boldsymbol{\varepsilon} : \mathbb{C} : \boldsymbol{\varepsilon} \quad , \tag{4.1}$$

where Ψ^e is the undamaged, elastic free Helmholtz energy. The stresses can either directly be obtained by using relation (3.23), or by using the basic constitutive equation (2.126) together with the effective stress concept introduced in equations (3.1), (3.2) and (3.8). Both paths yield a final constitutive equation for the isotropic damage model:

$$\boldsymbol{\sigma} = \frac{\partial \psi}{\partial \varepsilon} = (1-d)\,\tilde{\boldsymbol{\sigma}} = (1-d)\,\mathbb{C}^0\,\boldsymbol{\varepsilon} \quad . \tag{4.2}$$

Here, $\boldsymbol{\sigma}$ and $\boldsymbol{\varepsilon}$ are the stress and strain tensors, respectively; d is the damage variable, and $\mathbb{C}^0$

is the undamaged stiffness matrix. The model, as defined in equation (4.2) is fully described if the damage variable d is known.

Based on the flowchart shown in figure 4.1, the following, and for this model necessary, steps are discussed in greater detail:

- loading function
- damage criterion
- damage evolution

4.1.1 Loading Functions - Norm in Strain Space

It is necessary to introduce the concept of equivalent strains in relation to the damage initiation criterion. An equivalent strain is a scalar strain measurement dependent on the single strains within the damage criterion being used. An equivalent strain is used as a norm to compare different states of deformation, as introduced in section 3.3 and depicted in figure 3.4. The implemented model, and in turn the norm, does not distinguish between degradation caused by tension or compression. The norm can alternatively be defined in an undamaged effective stress state $\boldsymbol{\sigma}$. Both forms are defined as follows:

$$\tau = \sqrt{\tilde{\boldsymbol{\sigma}} : \mathbb{S}_0 : \tilde{\boldsymbol{\sigma}}} \qquad \text{or} \qquad \tau = \sqrt{\boldsymbol{\varepsilon} : \mathbb{C}_0 : \boldsymbol{\varepsilon}} \quad . \tag{4.3}$$

Together with the definition of the free elastic Helmholtz energy given by equation 4.1, the norm can equivalently be defined in the effective stress state as

$$\tau^2 = 2\,\Psi \quad , \tag{4.4}$$

where τ is the energy norm of the strain tensor. It represents an ellipsoid surface centered at the origin of the space of principal stresses. If Poisson's ratio is zero, the ellipsoid becomes a sphere.

4.1.2 Isotropic Damage Criterion

The damage criterion is formulated in the undamaged stress or strain space according to equation (3.25). Damage occurs if

$$F(\tau, r^t) = \tau - r^t \geq 0 \tag{4.5}$$

holds true. Here, r^t is the damage threshold, generally defined in equation (3.26). It includes an initial damage value and a load dependent value represented by the norm according to

$$r^t = \max[r_0, \tau] \qquad \text{with} \qquad r_0 = \frac{\sigma_u}{\sqrt{E}} \quad , \tag{4.6}$$

where σ_u is a material tensile strength parameter and E is Young's modulus. Once the norm τ exceeds the initial threshold r_0, the material begins to degrade ($d > 0$) and the damage threshold increases according to the load state, but holds its maximum value and can never decrease.

4.1.3 Damage evolution

Once the initial threshold is reached, a damage evolution law $d(r^t)$ must be defined which relates the internal variable r^t with the damage variable. When $d = 0$, the internal variable takes the initial value $r^t = 1$. When the material is completely damaged, a fracture plane is created. Oliver et al. [108] propose the following evolution law in

$$d = 1 - \frac{r^0}{r_t} e^{A\left(1 - \frac{r^t}{r_0}\right)} \quad . \tag{4.7}$$

Parameter A in equation (4.7) is obtained by following the crack band theory proposed by Bazant [13]. This ensures the correct computation of the dissipated energy during a damage process and reduces the mesh dependency in finite-element calculations. Using the rate of energy dissipated during damage according to [125], the total specific energy within a uniaxial tension test can be described as

$$g = \int_0^\infty \Psi^e \, \dot{d} = \int_0^\infty \Psi^e \, \frac{\partial d}{\partial r} \, \mathrm{d}\dot{r} = \frac{G_c}{l_c} \quad , \tag{4.8}$$

where G_c is the critical fracture energy introduced in section 3.5.2, $\Psi^e = \frac{\sigma_u^2}{2E}$ is the free elastic energy, and l_c is a mesh dependent parameter used in smeared crack models, known as the characteristic element length according to [107]. Energy dissipated during damage, g, is exemplary shown in figure 3.7. Using (4.4) and (4.7), setting $\tau = r^t$ and computing the derivative yields

$$\begin{aligned} g &= \int_0^\infty \underbrace{\frac{1}{2} \, e^{A\left(1 - \frac{r^t}{r_0}\right)} \, (r_0 + A r^t)}_{\frac{\partial \bar{G}}{\partial r}} \, \frac{\partial r}{\partial t} \, dt \Rightarrow \\ g &= \int_0^\infty \frac{\bar{G}}{\partial t} \, dt \; = \bar{G} \, \big|_0^\infty \quad . \end{aligned} \tag{4.9}$$

Here, the derivative of $\bar{G}$ defines a function, marked with the curly bracket in equation (4.9). Integrating the expression yields

$$\bar{G} = \int_0^\infty \frac{\partial \bar{G}}{\partial r}\, dr = -\frac{1}{2\,A} e^{A\left(1-\frac{r^t}{r_0}\right)} \left(2\,r_0 + A r^t\right)\big|_0^\infty \quad . \tag{4.10}$$

Through a limit value consideration of equation (4.10), the two following expressions are obtained:

$$\begin{aligned} \lim_{r^t \to \infty} \bar{G} &= 0 \\ \lim_{r^t \to 0} \bar{G} &= -r_0^2 \left(\frac{1}{A} + \frac{1}{2}\right) \quad . \end{aligned} \tag{4.11}$$

The parameter A can finally be calculated using equations (4.8) and (4.6) as:

$$A = \left(\frac{G_c\, E_0}{l_c\, \sigma_u^2} - \frac{1}{2}\right)^{-1} \quad . \tag{4.12}$$

This completes the definition of the damage evolution law.

The tangential material stiffness in the case of damage can be analytically calculated as

$$\mathbb{C}^{tan} = \frac{\partial \boldsymbol{\sigma}}{\partial \boldsymbol{\varepsilon}} = (1-d)\,\mathbb{C}^0 - \frac{\partial d}{\partial r}\frac{1}{\tau}\,\tilde{\boldsymbol{\sigma}}\,\tilde{\boldsymbol{\sigma}}^T \tag{4.13}$$

with

$$\frac{\partial d}{\partial r} = \frac{r_0 + A\,\tau}{\tau^2}\, e^{A\left(1-\frac{r}{r_0}\right)} \quad , \tag{4.14}$$

in which the undamaged constitutive equation $\mathbb{C}^0$ and the effective stress $\tilde{\boldsymbol{\sigma}}$ are values from the present load step, inserted in matrix and vector forms, respectively. In cases of elastic un- or reloading, the tangential material matrix remains constant within each load step and is given as

$$\mathbb{C}^{tan} = (1-d)\,\mathbb{C}^0 \quad . \tag{4.15}$$

4.1.4 Flowchart of the Isotropic Damage Model

The previously described isotropic damage model is implemented into the finite element software FEAP. The implementation can be summarized in a flowchart shown in figure 4.1. In this diagram, the subscript $(_{n+1})$ means the present (trial) load step, whereas the subscript $(_n)$ represents values from the last converged load step. The flowchart is made up with vector and matrix forms of the quantities. Once a converged solution is found, the values are stored in a history array for the next time step.

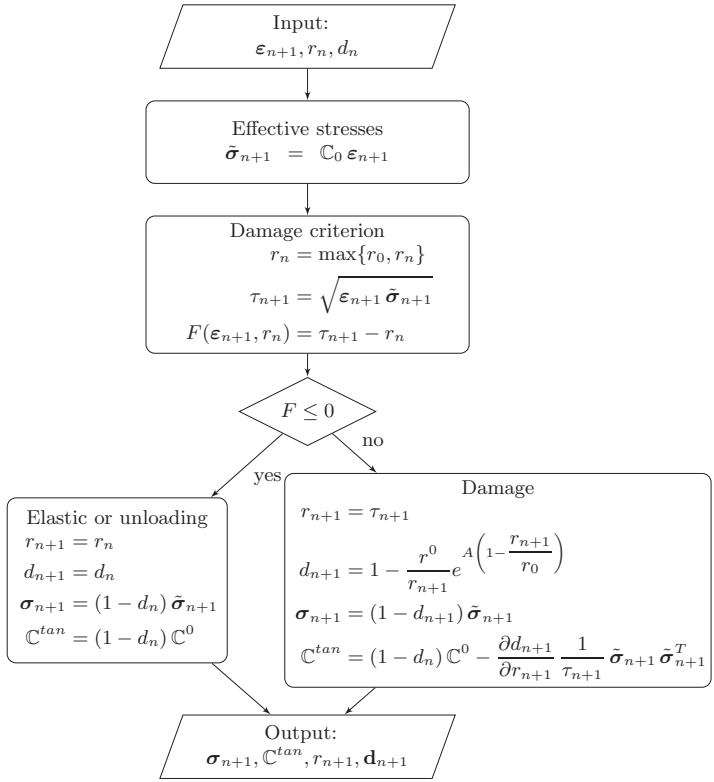

Figure 4.1: Flowchart of the isotropic damage analysis.

4.1.5 Isotropic Damage Model Using the Implex Scheme

Finite element formulations for modeling brittle material failure suffer from a lack of numerical robustness. Therefore, many authors [79, 85, 108] use a viscous stabilization procedure to dampen degradation on the stresses. In the implemented isotropic damage model, such a regularization could be used but it leads to incorrect results in attempts to force convergence within the Newton iteration scheme. Alternatively, the IMPL-EX scheme first proposed by Oliver et al. [109, 110] can be used. In this case, a slight modification of the inner variable r_{n+1} is necessary, affecting the r_{n+1} dependent quantities. The flowchart presented in figure 4.1 can still be used

though, only with the following modification of the quantities defined in the damage node:

$$\begin{aligned}
\hat{r}_{n+1} &= \tau_n + \Delta\tau \quad , \\
\hat{d}_{n+1} &= 1 - \frac{r^0}{\hat{r}_{n+1}} e^{A\left(1-\frac{\hat{r}_{n+1}}{r_0}\right)} \quad , \\
\boldsymbol{\sigma}_{n+1} &= (1-\hat{d}_{n+1})\,\tilde{\boldsymbol{\sigma}}_{n+1} \quad , \\
\mathbb{C}^{tan} &= (1-\hat{d}_n)\,\mathbb{C}^0 \quad .
\end{aligned} \tag{4.16}$$

Here, the $\hat{\cdot}$ identifies values that are extrapolated according to the IMPL-EX scheme. The inner variable is extrapolated by means of the expression

$$\Delta\tau = (\tau_n - \tau_{n-1})\,\frac{\Delta t^{n+1}}{\Delta t^n} \quad , \tag{4.17}$$

allowing for a change in the time step value. Because the inner variable $\hat{r}_{n+1}$ in equation (4.16) depends exclusively on values from the last two converged time steps, it remains constant during the Newton iteration from the present time step, as they are independent of the current strain state. This delivers considerable numerical improvements because the derivatives vanish or simplify throughout the damage model. Consequently, this yields a so-called step linear problem where the algorithmic tangent operator becomes constant within each time step. This is likely the principal reason for the improvement of the robustness. On the other hand, due to the implicit calculation of τ_{n+1}, stored in a history field for the next two time steps, the error arises by extrapolating the inner variable is solely the error of the actual time step. It does not amplify throughout the calculation. The evaluation of the inner variable and the corresponding error using the IMPL-EX scheme is illustrated in figure 4.2.

4.2 The Anisotropic Damage Model

Many studies from different authors, such as [63, 79, 94], are based on the theory proposed by Camanho et al. in [22]. This study introduced the concept of equivalent displacements within the theory of delamination. It enhances and modifies the theory for use in continuum damage models. The presented and implemented anisotropic damage model is used together with Hashin's failure criteria [65] or Cuntze's FMC [43–45]. The operator can also decide which of the equivalent principles, introduced in 3.2.1, should be used. By default, the principle of strain equivalence is used because it has been shown to be far more robust than others. When it is not used during this study, it is clearly clarified. Furthermore, for simplicity but still yielding viable results, a linear damage evolution law is implemented. The evolution law considers the energy released during a damage process according to the works of [13, 107]. The lack of numerical robustness is improved by incorporating the IMPL-EX scheme for isotropic damage models from Oliver et al. [109, 110] and adapting it for use in anisotropic damage models.

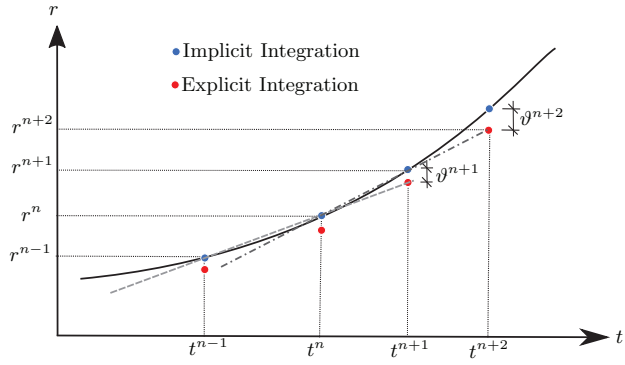

Figure 4.2: Extrapolation of the inner variable using the implicit explicit integration scheme.

4.2.1 Constitutive Equations of the Anisotropic Damage Model

The components of the global strain vector are sorted as $\boldsymbol{\varepsilon}^g = \{\varepsilon^g_{11}, \varepsilon^g_{22}, \varepsilon^g_{33}, 2\varepsilon^g_{12}, 2\varepsilon^g_{13}, 2\varepsilon^g_{23}\}$. Additionally, a transversely isotropic material is described locally through a set of orthonormal vectors $\{\mathbf{e}_1, \mathbf{e}_2, \mathbf{e}_3\}$, where $\mathbf{e}_1$ is parallel to the fiber direction. The relation between the global and the local strain vector (where ε_{11} is the strain in fiber direction $\mathbf{e_1}$) is then given as

$$\boldsymbol{\varepsilon} = \mathbf{T}\,\boldsymbol{\varepsilon}^g \quad . \tag{4.18}$$

The transformation matrix $\mathbf{T}$ transforms the strains from a global to a local coordinate system. Without a loss of generality, it is assumed that the third direction (stacking direction) coincides in both coordinate systems. Thus, the transformation matrix yields

$$\mathbf{T} = \begin{bmatrix} \cos^2\theta & \sin^2\theta & 0 & \sin\theta\cos\theta & 0 & 0 \\ \sin^2\theta & \cos^2\theta & 0 & -\sin\theta\cos\theta & 0 & 0 \\ 0 & 0 & 1 & 0 & 0 & 0 \\ -2\sin\theta\cos\theta & 2\sin\theta\cos\theta & 0 & \cos^2\theta - \sin^2\theta & 0 & 0 \\ 0 & 0 & 0 & 0 & \cos\theta & \sin\theta \\ 0 & 0 & 0 & 0 & -\sin\theta & \cos\theta \end{bmatrix} \quad . \tag{4.19}$$

Having defined the coordinate system and the transformation rules, it is now necessary to define a suitable energy norm from which the constitutive equations can be derived. In the works of [79, 83, 86–90] a similar form of energy density, were used as a starting point. With a slight modification for the specific damage model, the complementary free energy (Gibbs energy) per unit volume is proposed as

$$\begin{aligned} W =& \frac{1}{2}\left(\frac{\sigma_{11}^2}{E_1^0(1-D_1)} + \frac{\sigma_{22}^2}{E_2^0(1-D_2)} + \frac{\sigma_{33}^2}{E_3^0(1-D_3)} - 2\frac{\sigma_{11}\sigma_{22}\nu_{12}}{E_1^0} - 2\frac{\sigma_{11}\sigma_{33}\nu_{13}}{E_1^0} - \ldots \right. \\ & \left. \ldots - 2\frac{\sigma_{22}\sigma_{33}\nu_{23}}{E_2^0} + \frac{\sigma_{12}^2}{G_{12}^0(1-D_{12})} + \frac{\sigma_{13}^2}{G_{13}^0(1-D_{13})} + \frac{\sigma_{23}^2}{G_{23}^0(1-D_{23})}\right) \end{aligned} \tag{4.20}$$

where the superscript 0 defines the initial undamaged state and the stresses are the undamaged effective stresses ($\sigma = \tilde{\sigma}$). According to equations (3.30) and (3.31), the strains are calculated as

$$\boldsymbol{\varepsilon} = \frac{\partial W}{\partial \boldsymbol{\sigma}} = \mathbb{H} : \boldsymbol{\sigma} \quad \text{with} \quad \mathbb{H} = \frac{\partial^2 W}{\partial \boldsymbol{\sigma}^2} \quad . \tag{4.21}$$

The damage compliance tensor $\mathbb{H}$, relates the strains with the effective stresses and depends on the damage variables which, as before, depend on the damage criterion chosen. If Cuntze's criterion is used, the compliance damage tensor from equation (3.41) is defined as

$$\mathbb{H} = \begin{bmatrix} \frac{1}{(1-D_1)E_1} & -\frac{\nu_{12}}{E_1} & -\frac{\nu_{13}}{E_1} & 0 & 0 & 0 \\ -\frac{\nu_{12}}{E_1} & \frac{1}{(1-D_2)E_2} & -\frac{\nu_{23}}{E_2} & 0 & 0 & 0 \\ -\frac{\nu_{13}}{E_1} & -\frac{\nu_{23}}{E_2} & \frac{1}{(1-D_3)E_2} & 0 & 0 & 0 \\ 0 & 0 & 0 & \frac{1}{(1-D_6)G_{12}} & 0 & 0 \\ 0 & 0 & 0 & 0 & \frac{1}{(1-D_6)G_{13}} & 0 \\ 0 & 0 & 0 & 0 & 0 & \frac{1}{(1-D_6)G_{23}} \end{bmatrix} . \tag{4.22}$$

Here, D_6 represents the shear damage mode IFF3 from the FMC introduced in section 3.5.1. The damage variables can be assigned to the FMC-modes as follows:

$$\begin{aligned} D_1 &\rightarrow \text{FF1, FF2} \\ D_2 &\rightarrow \text{IFF1, IFF2} \\ D_3 &= D_2 \\ D_6 &=\rightarrow \text{IFF3} \end{aligned} \tag{4.23}$$

Note that $D_2 = D_3$. Both damage variables are defined by matrix failure modes. Assuming a smeared crack model, this assumption holds true, as the damaged material is not assigned to any direction. For example, when an infinitesimal cube is damaged because of an impact on σ_2, the material is assumed to have been damaged in a statistically distributed average over the volume. Therefore, the material is damaged for all other directions as well. However, Maimi [90] has shown a more sophisticated evolution law where the damage variables D_2 and D_3 differ according to a factor related to σ_2 and σ_3, respectively.

On the other hand, if Hashin's failure criteria is used, which delivers a non-specific shear damage mode, equation (3.41) can be used and the damage variables concerning the shear terms have to be defined according to one of the damage effect tensors $\mathbb{M}$. The implemented model uses by default the zero marked damage effect tensor $\mathbb{M}^0$ and yields the following damage variables for shear damage modes:

$$\begin{aligned} D_{12} &= D_1 + D_2 - D_1 \cdot D_2 \\ D_{13} &= D_1 + D_3 - D_1 \cdot D_3 \\ D_{23} &= D_2 + D_3 - D_2 \cdot D_3 \end{aligned} \tag{4.24}$$

With the definition of the damage compliance tensor $\mathbb{H}$, the damage constitutive matrix is also defined by the inverse relation (3.39). The local stresses are defined with equation 3.8, or through the following relation:

$$\boldsymbol{\sigma} = \mathbb{C}(\mathbf{D})\,\boldsymbol{\varepsilon} \quad . \tag{4.25}$$

Because global quantities are necessary for continued calculations, the stresses have to be transformed back into a global coordinate system according to

$$\boldsymbol{\sigma}^g = \mathbf{T}^T\,\boldsymbol{\sigma} \quad . \tag{4.26}$$

When using the IMPL-EX scheme the tangential material stiffness stays constant within each time step and therefore equals the damage compliance tensor, $\mathbb{C}(\mathbf{D})^{tan} = \mathbb{C}(\mathbf{D})$. The general matrix transformation from a local to a global coordinate system is defined by

$$\mathbb{C}^g = \mathbf{T}^T\,\mathbb{C}\,\mathbf{T} \quad . \tag{4.27}$$

If the damage model is used without the IMPL-EX scheme, the global tangential material stiffness can be directly calculated according to

$$\mathbb{C}^{tan} = \frac{\partial \boldsymbol{\sigma}^g}{\partial \boldsymbol{\varepsilon}^g} \quad . \tag{4.28}$$

The derivatives of the energy function W with respect to the damage variables are known as the thermodynamic forces Y_M, M being the observed damage mode. In case of Cuntze's failure criterion, they are calculated as

$$\begin{aligned} Y_1 &= \frac{\partial \Psi}{\partial D_1} = \frac{\sigma_{11}^2}{2(1-D_1)^2\,E_1} \quad , \quad Y_2 = \frac{\partial \Psi}{\partial D_2} = \frac{\sigma_{22}^2}{2(1-D_2)^2\,E_2} \quad , \\ Y_3 &= \frac{\partial \Psi}{\partial D_3} = \frac{\sigma_{33}^2}{2(1-D_3)^2\,E_2} \quad , \quad Y_6 = \frac{\partial \Psi}{\partial D_6} = \frac{\sigma_{12}^2+\sigma_{13}^2+\sigma_{23}^2}{2(1-D_6)^2\,G_{12}} \quad . \end{aligned} \tag{4.29}$$

The rate of dissipation is determined by means of the thermodynamic forces as

$$\Xi = Y_1\,\dot{D}_1 + Y_2\,\dot{D}_2 + Y_3\,\dot{D}_3 + Y_6\,\dot{D}_6 \quad . \tag{4.30}$$

4.2.2 Anisotropic Damage Criterion

The damage criterion is, much like the isotropic damage model, formulated in an undamaged stress space according to equation (3.25). The actual loading functions depend on the use of either Hashin's or Cuntze's theory. There are as many independent loading functions as independent damage modes present. The procedure has to pass through each single damage mode. If the subscript $\cdot_I$ is a number which identifies the damage mode and counts from one to four (Hashin) or five (Cuntze), then the criterion can be summarized in a single equation as

$$F^I(\mathrm{FM}^I, r_t^I) = \mathrm{FM}^I(\tilde{\sigma}) - r_t^I \geq 0 \quad . \tag{4.31}$$

Here, r^t is the damage threshold generally defined in equation (3.26), including an initial damage value and a load dependent value analogous to equation (4.6). The second term, FM, represents the loading function related to the present failure mode, they are obtained by inserting the effective stresses $\tilde{\sigma}$ into the correlated damage criterion, as is shown for Cuntze's FMC:

$$\begin{aligned}
\mathrm{FM}^{\mathrm{FF1}} &= \frac{\tilde{\sigma}_{11}}{X_T} \quad , \\
\mathrm{FM}^{\mathrm{FF2}} &= \frac{-\tilde{\sigma}_{11}}{X_C} \quad , \\
\mathrm{FM}^{\mathrm{IFF1}} &= \frac{(\tilde{\sigma}_{22}+\tilde{\sigma}_{33}) + \sqrt{(\tilde{\sigma}_{22}-\tilde{\sigma}_{33})^2 + 4\tilde{\sigma}_{23}^2}}{2Y_t} \quad , \\
\mathrm{FM}^{\mathrm{IFF2}} &= \frac{(b_{sp}-1)\cdot(\tilde{\sigma}_{22}+\tilde{\sigma}_{33}) + b_{ss}\sqrt{(\tilde{\sigma}_{22}-\tilde{\sigma}_{33})^2 + 4\tilde{\sigma}_{23}^2}}{Y_c} \quad , \\
\mathrm{FM}^{\mathrm{IFF3}} &= \left[\frac{b_{sp}\cdot I_{23-5} + (\sqrt{b_{sp}^2\cdot I_{23-5}^2 + 4S_{12}^2\cdot(\tilde{\sigma}_{31}^2+\tilde{\sigma}_{21}^2)^2}}{2S_{12}^3}\right]^{0.5} \quad .
\end{aligned} \tag{4.32}$$

All other terms in equation (4.32) are introduced in section 3.5.1.

4.2.3 Equivalent Displacements and Stresses

The anisotropic damage model works with equivalent displacements and stresses corresponding to each individual damage mode. This results in four or five different equivalent displacements with associated stresses from using Hashin's criterion or Cuntze's FMC, respectively. This principle can be easily extended or applied to other failure criteria. In general, the number of independent failure criteria reflects the number of independent equivalent displacements and stresses. The principle of equivalent displacements was developed by Camanho et al. in [22], among others. Furthermore, the crack band model (characteristic element length) [13] is directly included in the concept of equivalent displacements. The equivalent quantities are defined below for both Hashin's and Cuntze's damage initiation criteria. In both formulations, the equivalent

displacements are generally defined as

$$\delta_{ij} = l_c \, \varepsilon_{ij} \quad \text{with} \quad l_c = \sqrt[3]{V_{GP}} \quad . \tag{4.33}$$

Here, l_c describes the characteristic element length and is defined as the third root of the Gauss point volume when working with continuum elements within finite element calculations. This is an approximation because it holds true only if the crack surface is normal to the crack direction and the edges of the element are equal in length. As soon as the crack surface appears under an angle to any direction, which is definitely expected in shear damage modes, the characteristic element length is typically modified according to this angle. This fact is neglected in the implemented damage model, but other definitions of l_c could be easily incorporated into the proposed damage model. In fact, if the crack angle must be considered, Puck's failure theory could be applied as it delivers the crack angle during calculations of the damage criterion. The calculation of l_c according to the mesh discretization does not, in general, completely eliminate the mesh dependency, but rather minimizes the degree of error of the result to an acceptable amount. Another definition, the so called Macauley brackets are defined:

$$\langle x \rangle = \frac{x + |x|}{2} \quad . \tag{4.34}$$

With this definition, the equivalent displacements and stresses can be declared. The superscript $ft, ..., mc$ serves as a shortened, general declaration of fiber failure tension (or FF1),...,up to matrix failure compression (or IFF2) . Additionally, and only in the case of Cuntze's criterion, the superscript ms represents the shear failure mode.

Equivalent Displacements Using Hashin's Criterion

$$\begin{aligned}
\delta_{eq}^{ft} &= \sqrt{\langle \delta_{11}^2 \rangle + (\alpha \delta_{12})^2 + (\alpha \delta_{13})^2} \quad , \\
\delta_{eq}^{fc} &= \langle -\delta_{11}^2 \rangle \quad , \\
\delta_{eq}^{mt} &= \sqrt{\langle \delta_{22}^2 \rangle + \langle \delta_{33}^2 \rangle + \delta_{23}^2} \quad , \\
\delta_{eq}^{mc} &= \sqrt{\langle -\delta_{22}^2 \rangle + \langle -\delta_{33}^2 \rangle + \delta_{12}^2 + \delta_{13}^2 + \delta_{23}^2} \quad .
\end{aligned} \tag{4.35}$$

The parameter α is a user input by ranging from 0 to 1 depending on the degree to which the shear terms should be involved in the fiber tension damage.

Equivalent Stresses Using Hashin's Criterion

$$
\begin{aligned}
\sigma_{eq}^{ft} &= \frac{\sqrt{\langle\delta_{11}\rangle\langle\sigma_{11}\rangle + \alpha\delta_{12}\langle\sigma_{12}\rangle + \alpha\delta_{13}\langle\sigma_{13}\rangle}}{\delta_{eq}^{ft}} \quad , \\
\sigma_{eq}^{fc} &= \frac{\sqrt{\langle\delta_{11}\rangle}}{\delta_{eq}^{fc}} \quad , \\
\sigma_{eq}^{mt} &= \frac{\sqrt{\langle\delta_{22}\rangle\langle\sigma_{22}\rangle + \langle\delta_{33}\rangle\langle\sigma_{33}\rangle + \delta_{23}\langle\sigma_{23}\rangle}}{\delta_{eq}^{mt}} \quad , \\
\sigma_{eq}^{mc} &= \frac{\sqrt{\langle\delta_{22}\rangle\langle\sigma_{22}\rangle + \langle\delta_{33}\rangle\langle\sigma_{33}\rangle + \delta_{23}\langle\sigma_{23}\rangle}}{\delta_{eq}^{mc}} \quad .
\end{aligned}
\tag{4.36}
$$

Equivalent Displacements Using Cuntze's Criterion

$$
\begin{aligned}
\delta_{eq}^{ft} &= \langle\delta_{11}\rangle \quad , \\
\delta_{eq}^{fc} &= \langle-\delta_{11}\rangle \quad , \\
\delta_{eq}^{mt} &= \sqrt{\langle\delta_{22}^2\rangle + \langle\delta_{33}^2\rangle + \delta_{23}^2} \quad , \\
\delta_{eq}^{mc} &= \sqrt{\langle-\delta_{22}^2\rangle + \langle-\delta_{33}^2\rangle + \delta_{23}^2} \quad , \\
\delta_{eq}^{ms} &= \sqrt{\langle-\delta_{22}^2\rangle + \langle-\delta_{33}^2\rangle + \delta_{12}^2 + \delta_{13}^2 + \delta_{23}^2} \quad .
\end{aligned}
\tag{4.37}
$$

Equivalent Stresses Using Cuntze's Criterion

$$
\begin{aligned}
\sigma_{eq}^{ft} &= \frac{\sqrt{\langle\delta_{11}\rangle\langle\sigma_{11}\rangle}}{\delta_{eq}^{ft}} \quad , \\
\sigma_{eq}^{fc} &= \frac{\sqrt{\langle\delta_{11}\rangle\langle\sigma_{11}\rangle}}{\delta_{eq}^{fc}} \quad , \\
\sigma_{eq}^{mt} &= \frac{\sqrt{\langle\delta_{22}\rangle\langle\sigma_{22}\rangle + \delta_{33}\langle\sigma_{33}\rangle + \delta_{23}\langle\sigma_{23}\rangle}}{\delta_{eq}^{mt}} \quad , \\
\sigma_{eq}^{mc} &= \frac{\sqrt{\langle\delta_{22}\rangle\langle\sigma_{22}\rangle + \delta_{33}\langle\sigma_{33}\rangle + \delta_{23}\langle\sigma_{23}\rangle}}{\delta_{eq}^{mc}} \quad , \\
\sigma_{eq}^{ms} &= \frac{\sqrt{\langle\delta_{22}\rangle\langle\sigma_{22}\rangle + \delta_{33}\langle\sigma_{33}\rangle + \delta_{12}\langle\sigma_{12}\rangle + \delta_{13}\langle\sigma_{13}\rangle + \delta_{23}\langle\sigma_{23}\rangle}}{\delta_{eq}^{ms}} \quad ,
\end{aligned}
\tag{4.38}
$$

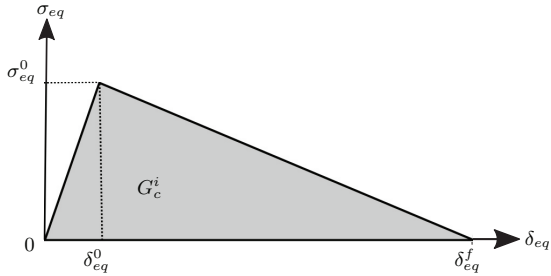

Figure 4.3: Linear damage evolution law using equivalent displacements.

4.2.4 Anisotropic Damage Evolution

The implemented macroscopic anisotropic damage model works with a linear degradation law. As discussed while examining the isotropic damage model, the evolution law relates the internal variables with the damage variables while the condition for positive dissipation is automatically fulfilled. The damage evolution law is defined independently for each equivalent displacement, in other words for each damage mode. In figure 4.3, the term δ^f_{eq} represents the scalar value where full damage ($d = 1$) is expected. The scalar value δ^0_{eq} belongs to the equivalent displacement at which the initiation criterion is initially satisfied, while σ^0_{eq} is the corresponding stress at this position. In the following equation, the subscript $\cdot_I$ represents the specific damage mode. Using linear degradation, the equivalent displacement at full damage can be defined, considering equations (3.59) and (4.8), in each damage mode as

$$\delta^f_{eq,I} = \frac{2G_{f,I}}{\sigma^0_{eq,I}} \quad , \tag{4.39}$$

in which $G_{f,I}$ is the mixed mode critical fracture energy according to figure 3.9. The equivalent displacements and stresses at the onset of damage can be computed as follows:

$$\delta^0_{eq,I} = \delta_{eq,I} \frac{1}{\sqrt{F^I}} \tag{4.40}$$

where F^I represents the value of the damage initiation criterion corresponding to the equivalent displacements at the onset of damage. This value is independent of the load state and is calculated once and then stored for additional calculations. The corresponding stress at the onset of damage is defined by

$$\sigma^0_{eq,I} = \sigma_{eq,I} \frac{1}{\sqrt{F^I}} \quad . \tag{4.41}$$

Through these definitions, the damage variable is obtained as

$$D^I = \frac{\delta^f_{eq,I}(\delta_{eq,I} - \delta^0_{eq,I})}{\delta_{eq,I}(\delta^f_{eq,I} - \delta^0_{eq,I})} \quad . \tag{4.42}$$

Here, $\delta_{eq,I}$ is the equivalent displacement from the present load step and belongs to the associated damage mode. The critical fracture energies $G_{f,I}$ must be in place for each failure mode. However, as there is no standard test to measure them, this may be challenging. Conversely, the actual value has not been shown to be important compared to the correct calculation of the dissipated energy during the damage process. Maimi et al. [85] discuss methods to measure and calculate the fracture energies in the specific damage modes.

4.2.5 The Anisotropic Damage Model Using the IMPL-EX Scheme

The IMPL-EX scheme introduced in section 4.1.5 from Oliver et al. [109, 110] is modified such that it can be used for the current anisotropic damage model. Because the introduced damage model does not have a strain like variable r, explicit extrapolation is done on the equivalent displacements, which are the damage driving forces in this model. While the model is described sequentially in section 4.2.6, a few additional quantities are necessary to declare. The first is the increment $\Delta\delta_I^n$, it is used to calculate the extrapolated equivalent displacement and is stored in the history array. At the beginning of the material routine, this value is multiplied by the current time step Δt^{n+1} and holds information from the last two time steps:

$$\Delta\delta_I^n = (\delta_{\mathrm{imp,I}}^n - \delta_{\mathrm{imp,I}}^{n-1}) \frac{\Delta t^{n+1}}{\Delta t^n} \quad . \tag{4.43}$$

It is updated at the end of the routine with the current values and divided through the same (current) time step as above. The subscript I stands for the damage mode. It ranges from one to four or five according to the failure criterion that is used, either Hashin's or Cuntze's. With this definition, the damage criterion, equation (4.5), can alternatively be checked with

$$\Delta\delta_I^n \geq 0 \quad . \tag{4.44}$$

If equation (4.44) is true, damage occurs. Otherwise, the model is in an unloading or reloading state. The initial or the load dependent damage threshold of each damage mode is considered by the equivalent displacements.

Again, it is necessary to note that when using the IMPL-EX scheme, the tangential material stiffness remains constant during the Newton iteration scheme and does not depend on the actual strains. Therefore, the expression

$$\mathbb{C}^{tan} = \mathbb{C}(\mathbf{D}) \tag{4.45}$$

holds true. Note that the fulfillment of momentum balance within the finite element calculation is imposed in terms of the stresses related to the extrapolated variables and not the implicit variables. The complete procedure, using the anisotropic damage model together with the IMPL-EX scheme, is shown in the next section.

4.2.6 Flowchart of the Anisotropic Damage Model

The previously deduced anisotropic damage model is implemented in the finite element software FEAP. The procedure followed for implementation is summarized in the flowchart in figure 4.4. The model is implemented using the IMPL-EX scheme introduced in the isotropic damage model, seen in section 4.1. Within the flowchart, the subscripts $(n-1)$,(n) and $(n+1)$ declare values from the second last, previous, and actual time step, respectively. Furthermore, the subscript (exp) declares values that are explicitly extrapolated and the subscript (imp) declares implicitly evaluated quantities. The counter, I runs from one to four in the case of Hashin's criterion and from one to five in the case of Cuntze's criterion. The values

$$\delta^0_{eq,I},\ \sigma^0_{eq,I},\ \delta^f_{eq,I} \tag{4.46}$$

are the only values that have to be computed once and then stored for further calculations. These values do not depend on the actual load state.

The material routine is called within the finite element calculation as explained in chapter 5.

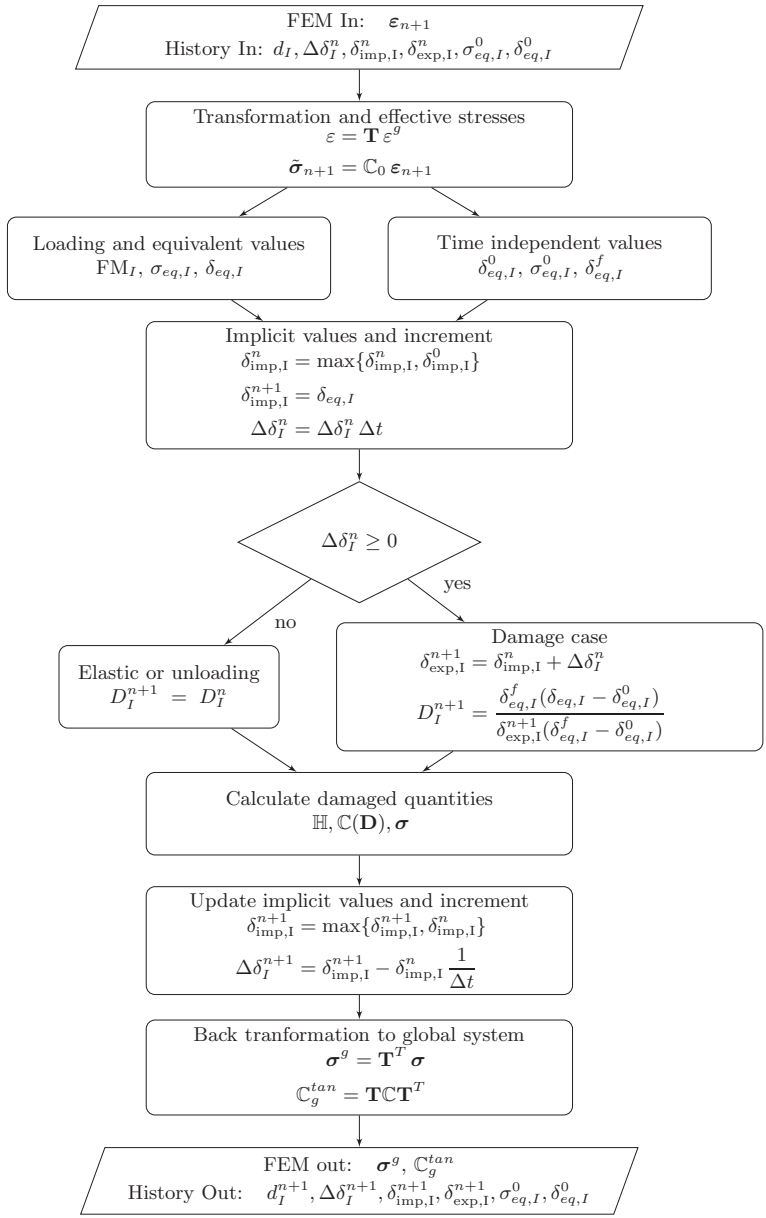

Figure 4.4: Flowchart of the anisotropic damage model.

Chapter 5

Finite Element Formulation of a Nonlinear Continuum Element

Even though many engineering problems can be sufficiently approximated linearly, nonlinear effects in the material and/or in the geometry have to be considered in a variety of applications. Concrete or fiber reinforced composites, for example, behave in a highly nonlinear fashion due to micro cracks or damage even under small strains. Other examples are crash simulations or deep-drawing techniques, where large deformations occur in the geometry that cause additional nonlinear material behaviors such as plasticity. The field of nonlinear applications is large and makes it necessary to derive suitable numerical procedures.

5.1 Basic Equations

As discussed in section 2.4, the linearization of the weak form of equilibrium (2.89)

$$L[g(\mathbf{u}^h, \delta\mathbf{u}^h)] := g(\mathbf{u}^h, \delta\mathbf{u}^h) + \mathrm{D}\left[\, g(\mathbf{u}^h, \delta\mathbf{u}^h)\right] \cdot \Delta\mathbf{u}^h \quad , \tag{5.1}$$

based on a first order Taylor approximation, is often used as a starting point for nonlinear numerical simulations. The superscript h in equation (5.1) indicates the finite element approximation of the correlated quantity. Analogous to equation (2.90), the second term in equation (5.1) refers to the linearized internal virtual work of the approximated quantity and is given as

$$\mathrm{D}\left[\, g(\mathbf{u}^h, \delta\mathbf{u}^h)\right] \cdot \Delta\mathbf{u}^h = \int_{\mathcal{B}_0} \left[\, \mathbf{S}^h : \Delta\delta\mathbf{E}^h + \delta\mathbf{E}^h : \mathbb{C}^{tan} : \Delta\mathbf{E}^h \right] \mathrm{d}V \quad . \tag{5.2}$$

The (nonlinear) tangential material stiffness $\mathbb{C}^{tan}$ in the preceding equation is decoupled from the consideration of geometrical nonlinear effects. It is already derived in chapter 4 and given in equation (4.13), (4.16), (4.28) or (4.45) depending on whether the isotropic or the anisotropic damage model is used in standard or IMPL-EX form.

To wholly define the boundary value problem the geometric boundary conditions must be fulfilled.

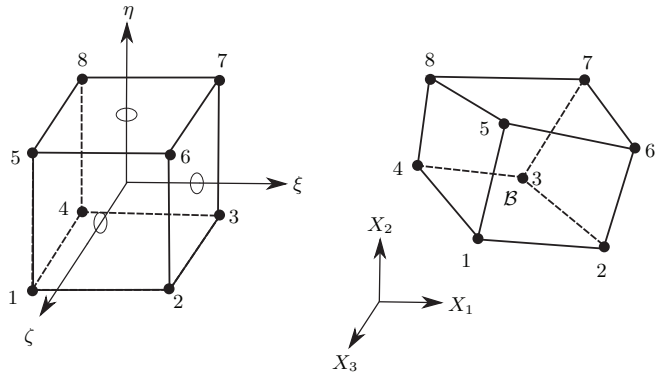

Figure 5.1: Isoparametric continuum element in parameter space and reference configuration.

5.2 Isoparametric Formulation

Within finite element formulations, interpolation functions have to be chosen to approximate the geometry and field variables. The isoparametric formulation indicates that the same ansatz functions are used for both the geometry and displacement. A reference element and its shape functions are defined in a parameter space with a local orthogonal coordinate system (ξ, η, ζ) according to figure 5.1. In the following section, a continuum element with eight nodes and linear shape functions is presented. The local numbering of the element is illustrated in figure 5.1. The element has three degrees of freedom at each node. The geometry in the reference configuration is approximated with tri-linear shape functions acting on the cube in the parameter space according to:

$$\mathbf{X}^h = \sum_{I=1}^{8} N_I(\xi, \eta, \zeta)\mathbf{X}_I \qquad -1 \leq \{\xi, \eta, \zeta\} \leq 1 \quad . \tag{5.3}$$

The index I in equation (5.3) represents the number of nodes per element and runs from one to eight. The shape functions are defined as

$$\begin{aligned}
N_1 &= \frac{1}{8}(1-\xi)(1-\eta)(1-\zeta) \quad , & N_5 &= \frac{1}{8}(1-\xi)(1-\eta)(1+\zeta) \quad , \\
N_2 &= \frac{1}{8}(1+\xi)(1-\eta)(1-\zeta) \quad , & N_6 &= \frac{1}{8}(1+\xi)(1-\eta)(1+\zeta) \quad , \\
N_3 &= \frac{1}{8}(1+\xi)(1+\eta)(1-\zeta) \quad , & N_7 &= \frac{1}{8}(1+\xi)(1+\eta)(1+\zeta) \quad , \\
N_4 &= \frac{1}{8}(1-\xi)(1+\eta)(1-\zeta) \quad , & N_8 &= \frac{1}{8}(1-\xi)(1+\eta)(1+\zeta) \quad .
\end{aligned} \tag{5.4}$$

From the weak form of equilibrium in equation (2.81), it follows that the ansatz functions for the displacements and virtual displacements must show at least C^0 continuity. Choosing the

same ansatz functions for both, the displacements can be approximated as

$$\mathbf{u}^h = \sum_{I=1}^{8} N_I \mathbf{v}_I \qquad \delta\mathbf{u}^h = \sum_{I=1}^{8} N_I \delta\mathbf{v}_I \quad , \tag{5.5}$$

where $\mathbf{u}$ and $\delta\mathbf{u}$ hold the nodal displacements and virtual displacements, respectively.

For an approximation of the Green-Lagrange strain tensor, defined in equation (2.20), the approximation of the deformation gradient $\mathbf{F}$ in equation (2.4) is necessary. Using equation (2.12) together with (5.5) yields

$$\begin{aligned} \mathbf{x}^h &= \sum_{I=1}^{8} N_I \mathbf{x}_I &&= \sum_{I=1}^{8} N_I (\mathbf{X}_I + \mathbf{v}_I) \quad , \\ \delta\mathbf{x}^h &= \sum_{I=1}^{8} N_I \, \delta\mathbf{x}_I &&= \sum_{I=1}^{8} N_I \, \delta\mathbf{v}_I \quad , \end{aligned} \tag{5.6}$$

from which the tangent vectors can be obtained using the derivatives of N_I with respect to the coordinates from the reference (or current) configuration:

$$\begin{aligned} \mathbf{x}^h_{,j} &= \sum_{I=1}^{8} N_{I,j} \, \mathbf{x}_I &&= \sum_{I=1}^{8} N_{I,j} (\mathbf{X}_I + \mathbf{v}_I) \quad , \\ \delta\mathbf{x}^h_{,j} &= \sum_{I=1}^{8} N_{I,j} \, \delta\mathbf{x}_I &&= \sum_{I=1}^{8} N_{I,j} \, \delta\mathbf{v}_I \quad . \end{aligned} \tag{5.7}$$

The derivatives $N_{I,j}$ in equation (5.7) to the coordinates (i, j, k) are independent of whether the transformation is performed from the parameter element (ξ, η, ζ) to the current or reference configuration. Using coordinates from the reference configuration, exemplary denoted with $(1, 2, 3)$, the following derivatives are obtained:

$$\begin{bmatrix} N_{I,1} \\ N_{I,2} \\ N_{I,3} \end{bmatrix} = \mathbf{J}^{-1} \begin{bmatrix} N_{I,\xi} \\ N_{I,\eta} \\ N_{I,\zeta} \end{bmatrix} \quad . \tag{5.8}$$

Here, $\mathbf{J}^{-1}$ denotes the inverse of the Jacobian matrix $\mathbf{J}$, which holds the derivatives of X_I with respect to the parameter coordinates (ξ, η, ζ) and is defined as

$$\begin{bmatrix} N_{I,\xi} \\ N_{I,\eta} \\ N_{I,\zeta} \end{bmatrix} = \underbrace{\begin{bmatrix} X^h_{1,\xi} & X^h_{2,\xi} & X^h_{3,\xi} \\ X^h_{1,\eta} & X^h_{2,\eta} & X^h_{3,\eta} \\ X^h_{1,\zeta} & X^h_{2,\zeta} & X^h_{3,\zeta} \end{bmatrix}}_{\mathbf{J}} \begin{bmatrix} N_{I,1} \\ N_{I,2} \\ N_{I,3} \end{bmatrix} \quad . \tag{5.9}$$

5.3 Approximated Green Lagrange Strains

In this section the Green-Lagrange strain tensor, defined in equation (2.20), is approximated in its finite element formulation and then variated and linearized for use it in equation (5.2). The Green-Lagrange strains are approximated with equation (5.6) and depicted in vector form as

$$\mathbf{E}^h = \begin{bmatrix} E^h_{11} \\ E^h_{22} \\ E^h_{33} \\ 2E^h_{12} \\ 2E^h_{13} \\ 2E^h_{23} \end{bmatrix} = \begin{bmatrix} \frac{1}{2}\left(\mathbf{x}^h{}_{,1} \cdot \mathbf{x}^h{}_{,1} - 1\right) \\ \frac{1}{2}\left(\mathbf{x}^h{}_{,2} \cdot \mathbf{x}^h{}_{,2} - 1\right) \\ \frac{1}{2}\left(\mathbf{x}^h{}_{,3} \cdot \mathbf{x}^h{}_{,3} - 1\right) \\ \mathbf{x}^h{}_{,1} \cdot \mathbf{x}^h{}_{,2} \\ \mathbf{x}^h{}_{,1} \cdot \mathbf{x}^h{}_{,3} \\ \mathbf{x}^h{}_{,2} \cdot \mathbf{x}^h{}_{,3} \end{bmatrix} \quad . \tag{5.10}$$

Using equation (2.91) together with (5.7) yields the approximated virtual strains

$$\delta\mathbf{E}^h = \begin{bmatrix} \delta E^h_{11} \\ \delta E^h_{22} \\ \delta E^h_{33} \\ 2\delta E^h_{12} \\ 2\delta E^h_{13} \\ 2\delta E^h_{23} \end{bmatrix} = \begin{bmatrix} \mathbf{x}^h{}_{,1} \cdot \delta\mathbf{x}^h{}_{,1} \\ \mathbf{x}^h{}_{,2} \cdot \delta\mathbf{x}^h{}_{,2} \\ \mathbf{x}^h{}_{,3} \cdot \delta\mathbf{x}^h{}_{,3} \\ \mathbf{x}^h{}_{,2} \cdot \delta\mathbf{x}^h{}_{,1} + \mathbf{x}^h{}_{,1} \cdot \delta\mathbf{x}^h{}_{,2} \\ \mathbf{x}^h{}_{,3} \cdot \delta\mathbf{x}^h{}_{,1} + \mathbf{x}^h{}_{,1} \cdot \delta\mathbf{x}^h{}_{,3} \\ \mathbf{x}^h{}_{,3} \cdot \delta\mathbf{x}^h{}_{,2} + \mathbf{x}^h{}_{,2} \cdot \delta\mathbf{x}^h{}_{,3} \end{bmatrix} = \sum_{I=1}^{8} \begin{bmatrix} N_{I,1}\, \mathbf{x}^h{}_{,1} \\ N_{I,2}\, \mathbf{x}^h{}_{,2} \\ N_{I,3}\, \mathbf{x}^h{}_{,3} \\ N_{I,1}\, \mathbf{x}^h{}_{,1} + N_{I,2}\, \mathbf{x}^h{}_{,2} \\ N_{I,1}\, \mathbf{x}^h{}_{,1} + N_{I,3}\, \mathbf{x}^h{}_{,3} \\ N_{I,2}\, \mathbf{x}^h{}_{,2} + N_{I,3}\, \mathbf{x}^h{}_{,3} \end{bmatrix} \delta\mathbf{v}_I \quad , \tag{5.11}$$

which can generally be defined as

$$\delta\mathbf{E}^h = \sum_{I=1}^{8} \mathbf{B}_I\, \delta\mathbf{v}_I \quad . \tag{5.12}$$

As discussed, there is no difference in the operations between variations and linearizations. It follows that the linearized Green-Lagrange strains can be obtained by replacing the δ in equation (5.10) with Δ, yielding the general formulation

$$\Delta\mathbf{E}^h = \sum_{I=1}^{8} \mathbf{B}_I\, \Delta\mathbf{v}_I \quad . \tag{5.13}$$

In equations (5.12) and (5.13), the $\mathbf{B}_I$ matrix is a fully staffed 6x3 matrix, which is calculated for each node I. Later in this section, a numerical more convenient form is derived.

To fully describe equation (5.2), the linearized variation of the Green-Lagrange strains are

needed:

$$\Delta\delta\mathbf{E}^h = \begin{bmatrix} \Delta\delta E^h_{11} \\ \Delta\delta E^h_{22} \\ \Delta\delta E^h_{33} \\ 2\Delta\delta E^h_{12} \\ 2\Delta\delta E^h_{13} \\ 2\Delta\delta E^h_{23} \end{bmatrix} = \begin{bmatrix} \delta\mathbf{x}^h{}_{,1} \cdot \Delta\mathbf{x}^h{}_{,1} \\ \delta\mathbf{x}^h{}_{,2} \cdot \Delta\mathbf{x}^h{}_{,2} \\ \delta\mathbf{x}^h{}_{,3} \cdot \Delta\mathbf{x}^h{}_{,3} \\ \delta\mathbf{x}^h{}_{,1} \cdot \Delta\mathbf{x}^h{}_{,2} + \delta\mathbf{x}^h{}_{,2} \cdot \Delta\mathbf{x}^h{}_{,1} \\ \delta\mathbf{x}^h{}_{,1} \cdot \Delta\mathbf{x}^h{}_{,3} + \delta\mathbf{x}^h{}_{,3} \cdot \Delta\mathbf{x}^h{}_{,1} \\ \delta\mathbf{x}^h{}_{,2} \cdot \Delta\mathbf{x}^h{}_{,3} + \delta\mathbf{x}^h{}_{,3} \cdot \Delta\mathbf{x}^h{}_{,2} \end{bmatrix} \quad . \tag{5.14}$$

With the preceding definitions, the linearized weak form of equilibrium (5.1) is fully defined.

5.4 Consistent Linearized Variational Functional

In this section, definitions from the previous sections are used to express the approximated linearized variational functional given with equation (5.1). First, the term $\mathbf{S} : \Delta\delta\mathbf{E}^h$ is calculated using the approaches provided by equations (2.91), (5.7) and (5.14):

$$\begin{aligned} \mathbf{S} : \Delta\delta\mathbf{E}^h &= S_{ij}\Delta\delta E_{ij} = S_{ij}\frac{1}{2}(\delta\mathbf{x}^h_{,i} \cdot \Delta\mathbf{x}^h_{,i} + \delta\mathbf{x}^h_{,i} \cdot \Delta\mathbf{x}^h_{,i}) \\ &= \sum_{I=1}^{8}\sum_{K=1}^{8} \delta\mathbf{v}_I^T\, S_{ij}\frac{1}{2}\left(N_{I,i}\, N_{K,j} + N_{I,j}\, N_{K,i}\right)\Delta\mathbf{v}_K \\ &= \sum_{I=1}^{8}\sum_{K=1}^{8} \delta\mathbf{v}_I^T\, \mathbf{G}_{IK}\Delta\mathbf{v}_K \quad . \end{aligned} \tag{5.15}$$

In equation (5.15), a switch from tensor to vector quantities has been completed which retained for all quantities until the end of this section.

Using equations (5.12), (5.13) and (5.5) together with the principle of virtual work in equation (2.81) yields

$$\begin{aligned} g(\mathbf{u}^h, \delta\mathbf{u}^h) &= \sum_{I=1}^{8}\int_{\mathcal{B}_0}\left(\delta\mathbf{v}_I^T\mathbf{B}_I^T\mathbf{S} - \delta\mathbf{v}_I^T N_I\rho\mathbf{b}\right)\mathrm{d}V - \sum_{I=1}^{8}\int_{\partial\mathcal{B}_0}\delta\mathbf{v}_I^T N_I\mathbf{t}_0\,\mathrm{d}A \\ &= \sum_{I=1}^{8}\delta\mathbf{v}_I^T\left[\int_{\mathcal{B}_0}\left(\mathbf{B}_I^T\,\mathbf{S} - N_I\rho\mathbf{b}\right)\mathrm{d}V - \int_{\partial\mathcal{B}_0} N_I\mathbf{t}_0\,\mathrm{d}A\right] \quad . \end{aligned} \tag{5.16}$$

By inserting equations (5.15), (5.12) and (5.13) into the definition of the Gateaux derivative, equation (5.2), the following form is obtained:

$$\mathrm{D}\left[g(\mathbf{u}^h, \delta\mathbf{u}^h)\right] \cdot \Delta\mathbf{u}^h = \sum_{I=1}^{8}\sum_{K=1}^{8}\int_{\mathcal{B}_0}\delta\mathbf{v}_I^T\left(\mathbf{B}_I^T\ \mathbb{C}\,\mathbf{B}_K + \mathbf{G}_{IK}\right)\mathrm{d}V \quad . \tag{5.17}$$

Here, $\mathbb{C} = \mathbb{C}^{tan}$ is the tangential material stiffness. With the following definitions,

$$\begin{aligned}
\mathbf{f}_I^i &= \int_{\mathcal{B}_0} \mathbf{B}_I^T \, \mathbf{S} \, \mathrm{d}V \quad , \\
\mathbf{f}_I^a &= \int_{\mathcal{B}_0} N_I \rho \mathbf{b} \, \mathrm{d}V + \int_{\partial\mathcal{B}_0} \delta \mathbf{v}_I^T \, N_I \mathbf{t}_0 \, \mathrm{d}A \quad , \\
\mathbf{f}_I^e &= \mathbf{f}_I^i - \mathbf{f}_I^a \quad , \\
\mathbf{k}_{TIK}^e &= \int_{\mathcal{B}_0} \left(\mathbf{B}_I^T \, \mathbb{C} \, \mathbf{B}_K + \mathbf{G}_{IK} \right) \mathrm{d}V \quad ,
\end{aligned} \tag{5.18}$$

the linearized weak form of equilibrium can be rewritten as

$$\begin{aligned}
L[g(\mathbf{u}^h, \delta\mathbf{u}^h)] :&= \sum_{e=1}^{nelem} \left[\sum_{I=1}^{8} \sum_{K=1}^{8} \delta \mathbf{v}_I^T (\mathbf{f}_I^e + \mathbf{k}_{TIK}^e \Delta\mathbf{v}) \right] \\
&= \sum_{e=1}^{nelem} \delta \mathbf{v}^T (\mathbf{f}^e + \mathbf{k}_T^e \Delta\mathbf{v}) \\
&= \delta \mathbf{V}^T (\hat{\mathbf{F}} + \mathbf{K}_T \Delta\mathbf{V}) = 0 \quad .
\end{aligned} \tag{5.19}$$

Here, $\mathbf{f}^e$ represents the element residual vector and $\mathbf{k}_T^e$ the tangential element stiffness matrix. Equation (5.19) must hold for any arbitrary $\delta\mathbf{V}^T$ not equal to zero. Using standard assembly operations, the global load vector $\hat{\mathbf{F}}$ and the global tangential stiffness matrix $\mathbf{K}_T$ are obtained. Considering geometrical boundary conditions the linear system

$$\mathbf{K}_T \, \Delta\mathbf{V} = -\hat{\mathbf{F}} \tag{5.20}$$

is solved.

To improve numerical calculation time, it is advantageous to establish the quantities from the virtual inner work, equation (5.15), and the linearization, equation (5.17), with respect to the current configuration instead of the reference configuration. By transforming the derivatives of N_I from the reference configuration to the current configuration

$$\begin{bmatrix} N_{I,x} \\ N_{I,y} \\ N_{I,z} \end{bmatrix} = \mathbf{F}^{-T} \begin{bmatrix} N_{I,1} \\ N_{I,2} \\ N_{I,3} \end{bmatrix} \quad , \tag{5.21}$$

the $\mathbf{B}$ matrix becomes sparse with half of the entries being zero, and thus the calculation becomes more efficient. Using the transformation

$$\boldsymbol{\tau} = \mathbf{T} \, \mathbf{S} \qquad \text{with} \qquad T_{ij} = F_{ik} \, F_{jl} \tag{5.22}$$

together with the internal virtual work in equation (5.16), yields

$$\delta\mathbf{E} = \mathbf{T}^T\,\delta\boldsymbol{\varepsilon} \qquad \text{and} \qquad \Delta\mathbf{E} = \mathbf{T}^T\,\Delta\boldsymbol{\varepsilon} \quad , \tag{5.23}$$

such that the definition

$$\delta\mathbf{E}^T\,\mathbb{C}\,\Delta\mathbf{E} = \delta\boldsymbol{\varepsilon}^T\,(\mathbf{T}\mathbb{C}\mathbf{T}^T)\,\Delta\boldsymbol{\varepsilon} \tag{5.24}$$

is obtained. By inserting the preceding equations into the linearized weak form of equilibrium in equation (5.1) and following the same procedure as completed with (5.16), the load vector $\mathbf{f}_I^i$ and the tangential stiffness matrix $\mathbf{k}_{TIK}^e$ defined in equation (5.18) can alternatively be written with quantities from the current configuration as

$$\begin{aligned} \mathbf{f}_I^i &= \int_{\mathcal{B}_0} \check{\mathbf{B}}_I^T\,\boldsymbol{\tau}\,\mathrm{d}V \quad , \\ \mathbf{k}_{TIK}^e &= \int_{\mathcal{B}_0} \left(\check{\mathbf{B}}_I^T\mathbf{c}\check{\mathbf{B}}_K + \mathbf{G}_{IK}\right)\mathrm{d}V \quad , \\ \mathbf{c} &= \mathbf{T}\,\mathbb{C}\,\mathbf{T}^T \quad , \end{aligned} \tag{5.25}$$

but still integrated over the reference volume $\mathcal{B}_0$.

For the computation of the linearized weak form in equation (5.19), an integration over the body $\mathcal{B}_0$ of each element is necessary. The integration is performed numerically within the parameter element, thus the integrals have to be transformed from the initial (or current) configuration to the parameter space according to

$$\begin{aligned} \int_{\mathcal{B}_0} g(\mathbf{X})\,dV &= \int_{-1}^{+1}\int_{-1}^{+1}\int_{-1}^{+1} g(\xi,\eta,\zeta)\,det\mathbf{J}\,\mathrm{d}\xi\,\mathrm{d}\eta\,\mathrm{d}\zeta \\ &\approx \sum_{I=1}^{8} g(\xi_P,\eta_P,\zeta_P)\,det\mathbf{J}(\xi_P,\eta_P,\zeta_P)\,W_P \quad . \end{aligned} \tag{5.26}$$

Here, W_P are the weighting factors of the Gauss integration points P, which has been chosen within the finite element method due to its accuracy and efficiency.

Chapter 6

Numerical Examples - Macroscopic Models

In this section, numerical experiments are investigated which relate to the macroscopic damage theory described in the previous sections. Problems used in both the isotropic and the anisotropic examples can be seen in figures 6.1 and 6.2. The tension rod seen in figure 6.1 has a symmetric geometry and is tapered at the center. The cross section has a length $l = 1$ m and a width and height of $b = 0.2$ m and $h = 0.2$ m at section B-B, and $l = 1$ m, $b_1 = 0.1897$ m and $h_1 = 0.1897$ m at section A-A, respectively. It is displacement-loaded at its end surfaces in horizontal direction. To reduce calculation time, symmetry conditions are utilized, which are explained at each specific example. The plate with an open hole in figure 6.2 has an equal length and width of $l = 10$ mm, a depth of $t = 0.1667$ mm and an open hole at the center with a diameter $d = 2$ mm. If the layup allows, symmetry conditions are utilized, otherwise a full model is calculated. The numerical examples are ordered similarly to the development of the damage model. This section first shows general aspects of damage mechanics using the isotropic damage model, followed by an investigation of convergence, regularization, and damage evolution and behavior. Particular attention is paid to the load displacement curves and damage initiation.

The anisotropic damage model is tested and validated in greater detail with various examples and material sets. In the first examples, special attention is given to numerical stabilization. The results of classical regularization and the IMPL-EX scheme are contrasted with results without regularization schemes. The damage model is then validated with single damage mode examples and compared to experimental test data. Then, the effects of different theories, defined in chapter 3, are illustrated. The chapter concludes with a detailed investigation of examples concerning damage initiation and evolution, load displacement behavior, and convergence issues.

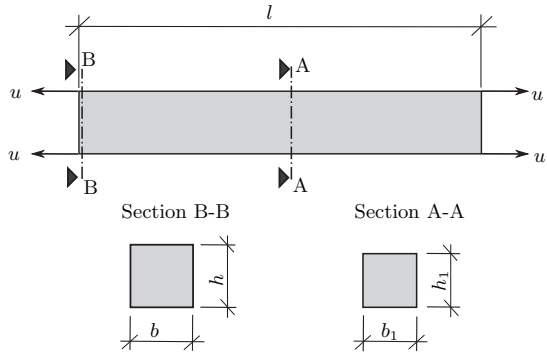

Figure 6.1: Geometry of a tension rod example.

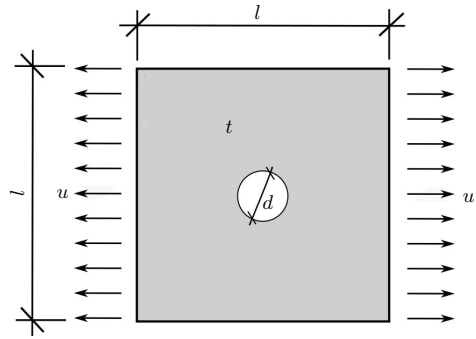

Figure 6.2: Geometry of a plate with an open hole example.

6.1 Isotropic Damage Model

In this section, the isotropic damage model is investigated. Some general aspects of damage behavior, as well as a mesh convergence study of the introduced tension rod and the plate with an open hole, are examined. Finally, the plate with an open hole is investigated in greater detail with an elaboration on the load displacement behavior and the evolution of damage in the structure during loading. The examples use concrete as a material with the following specifications:

Table 6.1: Material properties in [N/mm^2] or stated otherwise.

Label	E	G	y_0	ν [-]	G_c [N/mm]
Concrete	28800	12000	2.2	0.20	0.085

Here, E and G are the Young's and shear modulus, y_0 is the tensile strength, ν the Poisson's ratio and G_c the critical energy release rate given in energy per unit area.

6.1.1 Behavior of Isotropic Elastic Damage Models

The first example discussed is a rod under cyclic loading and shows the damage behavior of an elastic isotropic damage model with no distinction between damage caused by tension or compression. For illustration reasons, a user defined material is used with Young's modulus and a tension strength of E=G=1. Other parameters are not of interest for this example. The numerical results are illustrated in figure 6.3. With the explanations provided in section 4.1 in mind, a number of interesting aspects can be observed. The material shows elastic behavior until its initial damage threshold ($r = 1$) is reached (A-B). At point B, the degradation begins if the load impact is continuous (B-C). At point C, the load switches its direction (unloading). The new damage threshold is stored and the material behaves elastic during unloading. Within the degradation, the load displacement curve must meet the origin (C-A). In the negative regime (pressure), the process is also linear until its updated damage threshold is reached (A-D), then damage growth is continuous (D-E). A second load switch causes another unloading (E-A). After passing the origin again, reloading (A-F) is applied until the damage threshold value is reached in point F. Finally, further tensional loading with a small unloading/reloading domain is hinted at.

On the right side of figure 6.3 the internal variables of the damage model are illustrated. Here, d_{n+1} and dd_{n+1} are the damage variable and its derivative. r_{n+1} is a strain energy variable holding the current damage threshold, whereas Ψ is the strain energy function. The results as illustrated in figure 6.3 correspond to a user defined material under pure tensile loading. The workings of the model can be easily seen. The strain energy is given as a quadratic function, whereas the current damage threshold holds its initial value until damage first occurs and then grows under further loading. At the same time, upon reaching the initial threshold, the damage process immediately begins, and its derivative can be calculated.

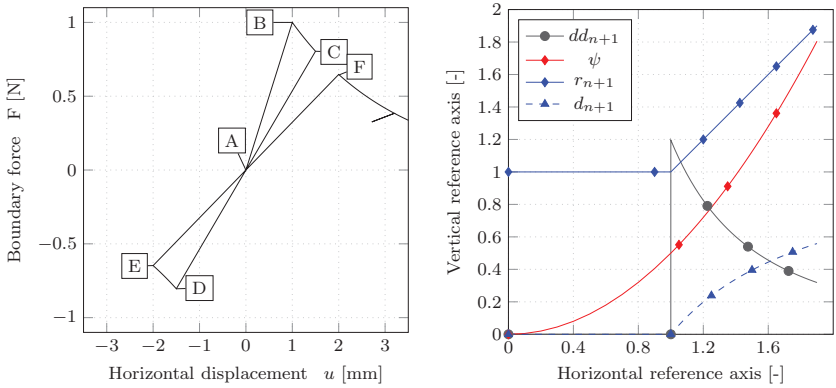

Figure 6.3: Behavior of an isotropic damage material (left) with corresponding internal variables (right).

6.1.2 Localization and Mesh Dependency

The example discussed in this section shows the effect of localization and the problem of mesh dependent solutions within the simulation of damage models when using the finite element method. The introduced example tension rod is modeled as one-eighth of the full model, using symmetry conditions on three of its faces. A discretization of 5x1x1 and 20x4x4 elements is chosen, as illustrated in figure 6.4 a.) and b.), respectively. Imagine the model in an idealized real world: The fracture of the rod at full damage would be expected on the tapered right side, in a tiny area. This is because at one specific damage level the continuous distribution of micro-cracks can no longer be observed. Instead, one crack dominates the others and grows until full separation is reached. This phenomenon is known as localization. It can be observed in most materials, but is especially challenging in those that are brittle. Another issue arises within the finite element model: During the damage process in the real world, a specific amount of energy dissipates, depending on the specific critical energy release rate and the area of the crack plane. Since the finite element method is formulated in an integral form (weak form), the dissipated energy changes, dependent on the mesh size, as can be seen by comparing figure 6.4 a.) and b.). In both scenarios, damage occurs to the first two elements, but the difference is that the volume, over which is integrated, is roughly five times higher in case a.) than in case b.). Without regularization, the total dissipated energy would than appear to be much higher as well, even though the same problem is modeled. With further mesh refinement, the damage would localize to an increasingly smaller region and the effect would intensify. Therefore, regularization must be employed in such a way that the dissipated energy per unit volume increases for smaller mesh sizes. It should be noted that localization is a real world problem that can be observed in experiments and not a problem present solely in numerical modeling. Still, localization presents less difficulties in the real world than in numerical modeling. After decades of research, the numerical modeling of localization remains a challenging problem which has yet

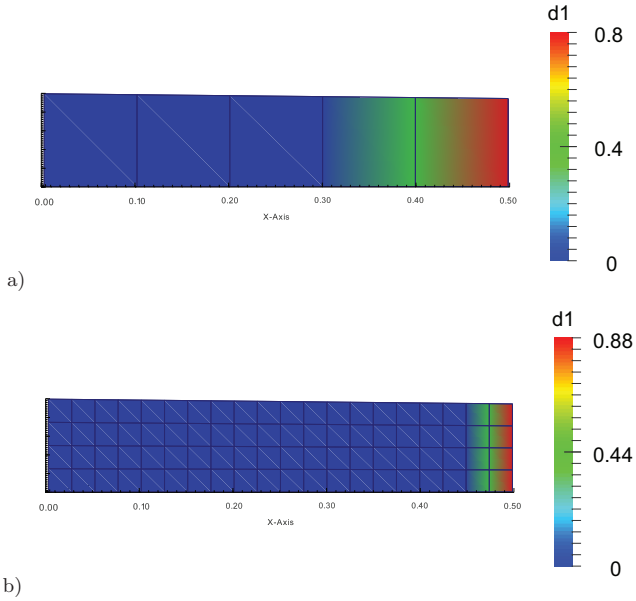

Figure 6.4: Damage variable d_1 in the tension rod example with a.) 5x1x1 and b.) 20x4x4 elements.

to be satisfactorily solved. Nevertheless, Bazant [13] provides suggestions which dramatically reduce the effect of mesh dependent results. This issue is revisited in a convergence study in section 6.1.3

6.1.3 Tension Rod and Plate with Open Hole

In this section, both examples (tension rod and plate with an open hole) are investigated in terms of mesh dependency and the evolution of damage. In figure 6.5, the numerical results of several different discretizations are plotted. The upper graphs show the results of the IMPL-EX scheme, investigated in more detail in section 6.2.3.

The upper graphs show that the degradation in the stiffness of a structure increases for finer meshes. The first two discretizations agree well, but the mesh is too coarse to properly simulate the complex behavior of damage. With further mesh refinement, a non-negligible difference in the resulting boundary force can be observed between each discretization step. Even though the effect of mesh dependent solutions is weakened, a net convergence cannot be seen. The statements hold true in the bottom plots, where the results from a standard implicit scheme are shown. With the standard integration scheme and a higher mesh purity, it is challenging

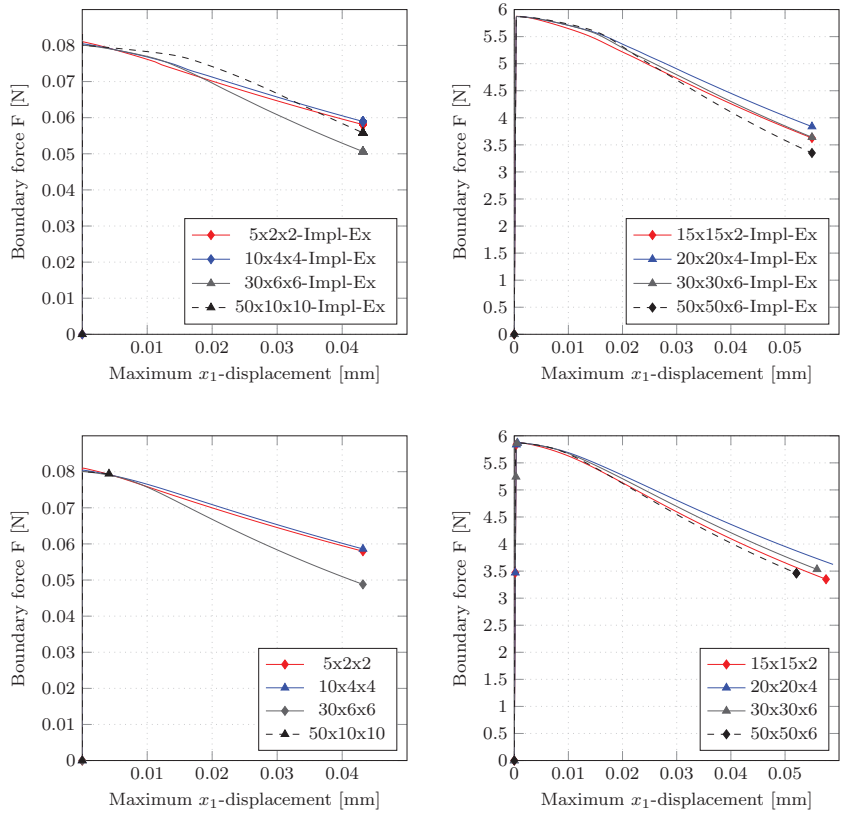

Figure 6.5: Convergence study for tension rod (left) and plate with open hole (right).

to reach numerical convergence. This is well demonstrated by the lower left picture with a discretization of 50x10x10 elements where the computation aborts at around 0.003 mm. The regularization in this model is performed using the characteristic element length l_c defined in equation (4.12). For the implemented model, and as long as continuum elements are used, l_c is defined as the cubic root of the Gauss point volume:

$$l_c = \sqrt[3]{V_{GP}} \quad . \tag{6.1}$$

This approximation requires the assumption that the element is cubic, with equal edge lengths, and the crack area is sufficiently smooth and perpendicular to one edge. Otherwise, it is an approximation delivering more or less sufficient results. In a more sophisticated model, the characteristic element length would be calculated depending on the crack angle and the actual shape of the element.

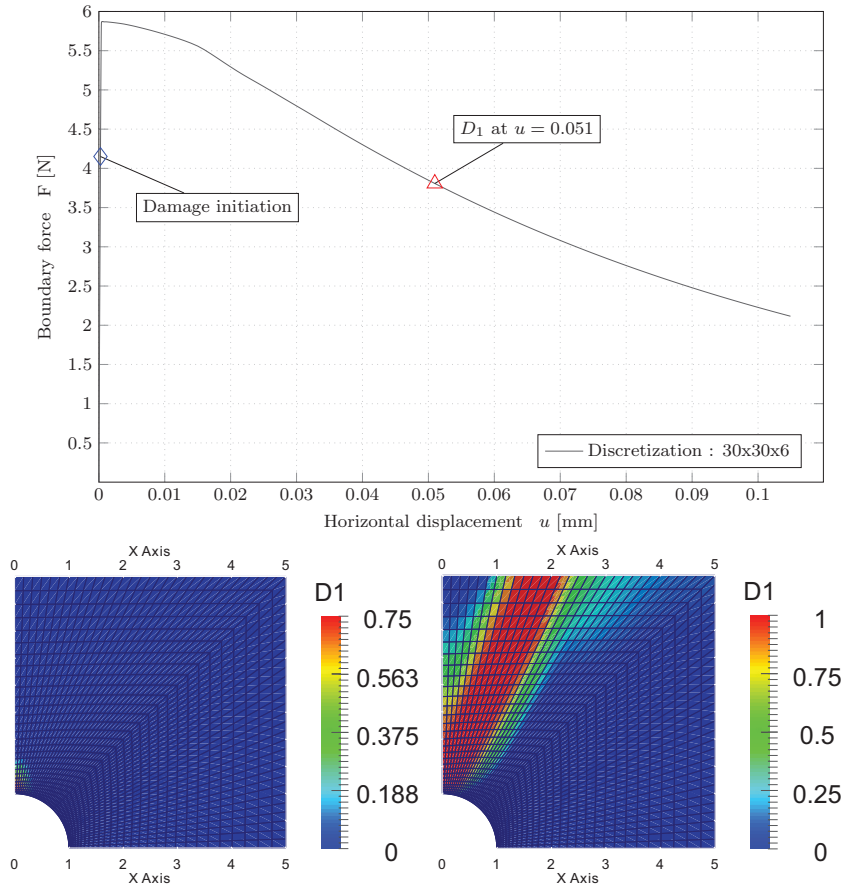

Figure 6.6: Plate with an open hole: Load-displacement path (top), D_1 damage initiation (bottom left), damage variable D_1 at $u = 0.051$ mm (bottom right).

In figure 6.6, the load displacement curve and the corresponding damage evolution of the plate with an open hole with a discretization of 30x30x6 is discussed. The finite element model utilizes symmetry conditions and the calculation is performed as one-eighth of the full model. The horizontal displacement corresponds to an arbitrary node on the right edge. The boundary force is the horizontal sum of all supported edge nodes. The computation is executed displacement controlled with a horizontal displacement on the right edge. The load displacement curve proceeds relatively flat, indicating a ductile material, and two further points of interest are marked. The first corresponds to the damage initiation and the second serves as a reference for illustrating

damage evolution at $u = 0.051$ mm, highlighted in the lower left and lower right picture, respectively. It is remarkable that the structure can take 28% more loading after damage initiation until its maximum bearable load is reached. The structure can activate a number of reserves and shows a good ability for load redistribution. Damage first occurs at the stress concentration position at the upper hole edge, as is expected. It develops under a specific angle through the structure, as has been observed in [47, 94].

In this section, important and general aspects of isotropic damage models have been discussed. With this background in mind, an anisotropic macroscopic damage model is investigated in the following section.

6.2 Anisotropic Damage Model

An anisotropic damage model was developed and implemented in the finite element software Feap. This section details the important steps in the development of the model, difficulties that were encountered, and attempted solutions. In this section, several numerical examples with different geometries and material data sets are discussed. For the sake of clarity, the material sets are defined once and identified by a number according to table 6.2. The material data is considered in terms of elasticity, strength, and damage driving properties. Some values must had been chosen reasonable, as it is difficult to find complete material data sets in the literature. The geometry of the first examples has already been introduced for the isotropic damage model. New geometries are also defined to verify numerical results with experimental data.

Table 6.2: Elastic properties in [N/mm^2].

No.	Label	E_1	E_2	G_{12}	ν_{12} [-]	ν_{23} [-]
1	T300/1034-C	146800	11400	6100	0.30	*0.38*
2	Glass Epoxy	52000	8000	3000	0.28	0.34
3	CE1007-310-37	80000	5000	3100	0.35	0.50
4	Tenax E HTS40	145000	7000	3100	0.29	0.37

Note: Values written in italic are approximately chosen

Table 6.3: Unidirectional strengths in [N/mm^2].

No.	Label	X_t	X_c	Y_t	Y_c	S_l
1	T300/1034-C	1730	1379	66.5	268.2	58.7
2	Glass Epoxy	1840	1580	44	172	39
3	CE1007-310-37	2400	400	40	100	130
4	Tenax E HTS40	2240	1200	50	300	108

Table 6.4: Critical energy release rate in [Nm/mm^2].

No.	Label	G_{l+}	G_{l-}	G_{t+}	G_{t-}	G_S
1	T300/1034-C	89.83	78.27	0.23	0.76	0.46
2	Glass Epoxy	*8.0*	*8.0*	*1.5*	*1.5*	*1.5*
3	CE1007-310-37	280	40	0.8	1.5	*1.0*
4	Tenax E HTS40	240	20	0.6	1.5	*1.0*

Note: Values written in italic are approximately chosen

6.2.1 Investigation of Different Implemented Anisotropic Damage Models

The first example depicts the result of different implemented damage models applied to the plate with an open hole with one single zero degree layer. The models were implemented in the finite element program Feap. For the calculation, material number 2 from table 6.2 is used. The results are shown in figure 6.7. In the legend, model $1, 2$, and 3 correspond to the models introduced in [82, 83, 136], respectively, whereas model 4 is an earlier version of the developed damage model introduced in section 4.2.

All models clearly show that the Newton iteration fails at a point before the final maximum bearable load was reached. The calculation was driven displacement controlled without any further stabilizations. It should be noted that the statements made are valid for the implementation in the finite element software Feap, with no doubts that the authors made it work in other software. Without any stabilization procedure, it is impossible to obtain results in most numerixal examples, except for numerically simple examples, such as the cantilever beam. Examples where the overall stiffness in one load step does not decrease by a large amount are not numerically challenging. On the other hand, the simple tension rod is one of the most challenging numerical examples, the decrease in stiffness concerns the whole cross section and is drastic. This supports localization and the effect increases. Therefore, in order to satisfy requirements

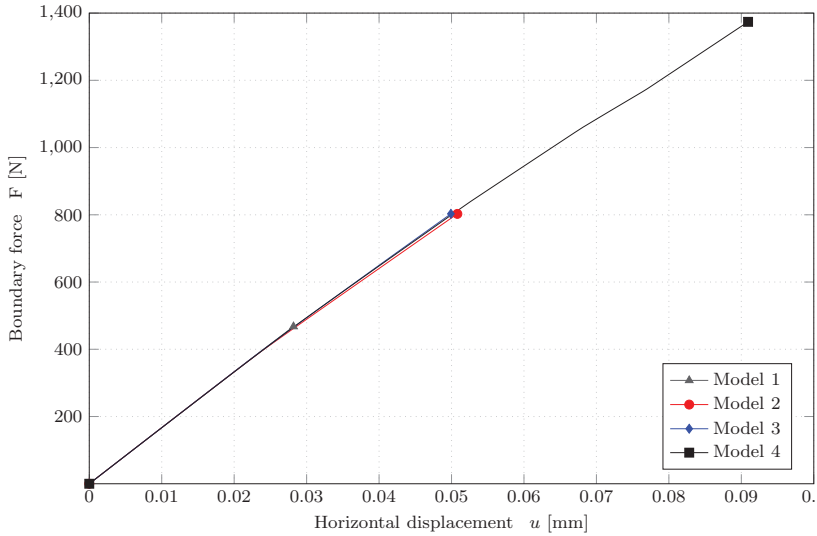

Figure 6.7: Comparison of different implemented anisotropic damage models.

in a damage model, stabilization procedures are introduced in the next section.

6.2.2 Effects of Classical Regularization

The first attempt to improve numerical convergence is a generalization of the Duvaut-Lions regularization, which is widely used in CDM. The stabilization is performed for each damage mode. The updated damage variable at time $t + \Delta t$ reads

$$D^v_{t+\Delta t} = \frac{\Delta t}{\eta + \Delta t} D_{t+\Delta t} + \frac{\eta}{\eta + \Delta t} D^v_t \quad . \tag{6.2}$$

Here, D is the kinematic damage variable depending on the strain-like variable r, and D^v is the regularized damage variable. The viscous damping factor η specifies the rate of change in D^v according to

$$\dot{D}^v = \frac{1}{\eta}(D - D^v) \quad . \tag{6.3}$$

This regularized damage variable D^v is then used instead of D in equation (4.25) and (4.28) to calculate the stresses $\boldsymbol{\sigma}$ and the tangential material stiffness $\mathbb{C}^{tan}$. Figure 6.8 shows the results of the two examples, the tension rod (left) and plate with open hole (right). The endpoints of the curves are the points where the simulation breaks because of convergence issues. The behavior of the examples concerning three to four different damping parameters η are investigated. It can be seen that an increasing parameter η does improve the convergence issue, but falsifies the results until they are no longer useful. On the other hand, a relatively small parameter η keeps the results close to those without damping but the convergence issue is still significant. The improvement in convergence of the tension rod (left) is better than that of the plate with open hole (right). Overall, the utilization of a viscous damping scheme does result in a slightly more stable computation, but with a simultaneous deterioration of results. In the next section, an alternative stabilization scheme is introduced.

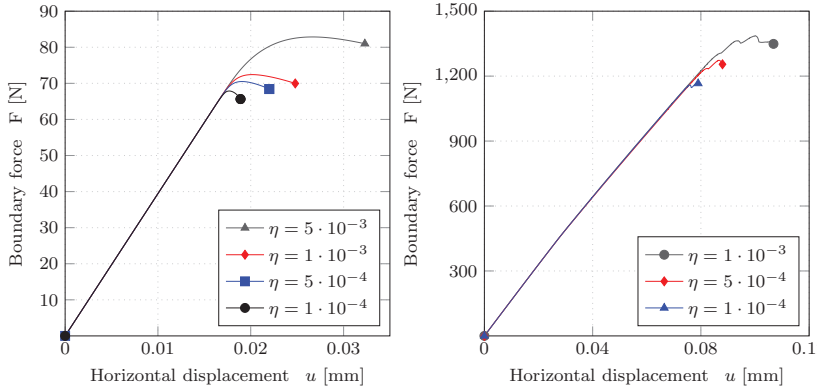

Figure 6.8: Viscous regularization - tension rod (left) and plate with open hole (right).

6.2.3 The IMPL-EX Scheme

This section focuses on the adaption and implementation of the IMPL-EX scheme from Oliver et al. [109, 110]. A comparison of the standard and the IMPL-EX schemes is of particular interest. The actual values and behavior of the damage model itself are discussed in greater detail later in this chapter. The IMPL-EX scheme is modified in such a way that it can be used for anisotropic damage models, using the equivalent displacement principle introduced in section 4.2.3. The theory behind the IMPL-EX scheme has been discussed in section 4.2. The upper left diagram in figure 6.9 shows three results from the tension rod model; the standard implicit scheme, the IMPL-EX scheme with automatic step size control, and the IMPL-EX scheme with a fixed step size. Two of them, standard implicit and IMPL-EX automatic step control, agree to each other. The IMPL-EX calculation is user aborted and had no issues delivering results deep in the degrading region. The third graph shows the results of a fixed and deliberately chosen large time increment. In this case, overprediction of the bearable maximum load occurs. The second example, a cantilever beam, is shown in the upper right graph. Again, a perfect agreement from both integration schemes can be observed if the time step used in the IMPL-EX scheme is sufficiently small. In the third example, a plate with open hole, the IMPL-EX scheme shows better numerical stability. The standard scheme aborts at a displacement of around 0.0067 mm, whereas the IMPL-EX scheme delivers results deep into the degraded region. This last example examines a tension rod with cyclic loading. The model is loaded, unloaded until the stress is zero, and then reloaded again. It is important to note the non-smooth transition where the reloading path meets the previous loading path. The jump at the transition point comes from the IMPL-EX scheme. This is because it uses information from the last two converged time steps to extrapolate the current one. In other words, it lags a step behind the actual time step. But after making the error, it corrects itself with further loading. Of course, the

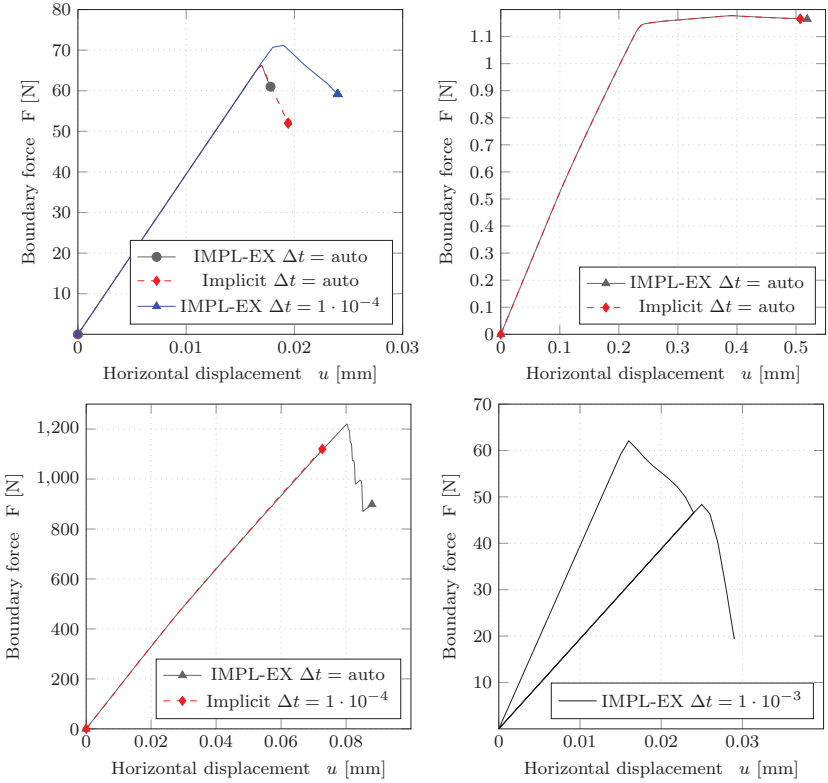

Figure 6.9: IMPL-EX scheme applied on: tension rod (upper left), cantilever beam (upper right), plate with open hole (bottom left); Reloading behavior (bottom right).

time step used for illustration is too large. It can be seen from in the discussed examples, that if the load increment is small enough, or if an automatic step control is used, the IMPL-EX scheme delivers reliable coincidence with the classical implicit integration scheme. Therefore, contrary to standard implicit schemes, a comparatively large number of load steps have to be performed. On the other hand, each load step converges in the first iteration step, so that the overall computation time is still reduced. This is due to the step linearity of the tangential material matrix. Additionally, the IMPL-EX scheme improves the numerical convergence to a large extent. For this reason, and because the standard implicit scheme has practical limitations due to its convergence issues, all following numerical examples are executed using the IMPL-EX scheme.

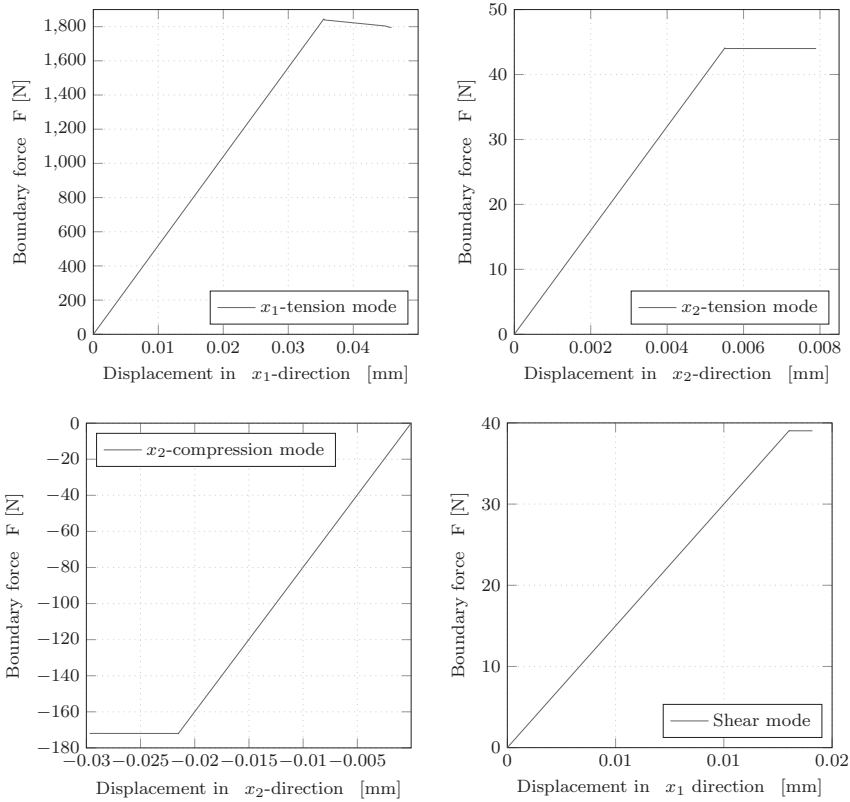

Figure 6.10: Pure single damage mode validation: D_1-tenison (upper left), D_2-tension (upper right), D_2-compression (bottom left); D_6-shear (bottom right).

6.2.4 Single Damage Mode Validation

The previous numerical examples were focused on a comparison of different stabilization procedures. In this section, as an initial plausibility assessment of the implemented damage model, the single damage modes are simulated on a unit cube with a discretization of 4x4x4 elements. Material number 2 from table 6.2, 6.3 and 6.4 is used.

In the upper left graph in figure 6.10, the pure D_1-tension damage mode (fiber failure) is simulated. The maximum bearable load is reached at $F = 1840$ N and matches perfectly the longitudinal tensional strength value $X_t = 1840$ N/mm^2. The same can be observed in the other three examples, where the matrix tension and matrix compression mode D_2, and the shear

damage mode D_6 are simulated. All single damage modes perfectly match their corresponding strength properties, which is a minimum requirement. This holds true regardless of whether strain or energy equivalence is employed.

6.2.5 Validation with Experimental Data - Multilayer Example

In this section, a numerical example is investigated to compare the results from the anisotropic damage model corresponding with experimental data . The system under investigation is a displacement suspended tension rod with a centered open hole, as shown in figure 6.11.

The length and width of the tension rod are $l = 203.2$ mm and $h = 25.4$ mm, the centered hole has a diameter of $d = 6.35$ mm, and one ply has a thickness of $t_p = 0.1308$ mm. In total, the model features 20 plies through the thickness in two different stacking orders, as declared in table 6.5. The material corresponds to material number 1 in table 6.1. Using symmetry conditions in thickness direction, only half of the system is modeled with a discretization of 80x10x10 elements. The experimental data is published in [130] and also used for verification in [86].

The two graphs in figure 6.12 show the results of two different layups investigated within the test model. In [130], only the maximum stress is declared, the comparison is shown in table 6.5. Table 6.5 shows that the predicted stress, corresponding to the maximum bearable load, agrees well with the experimental data. A small deviation of 3.22% or 4.25%, depending on the layup, can be observed. Additionally, the corresponding horizontal displacement has a relative deviation of about 5 and 3 percent, respective to the layup and compared to that published in [86]. In that study, the maximum bearable load is underestimated such that the corresponding strains would nearly match at the predicted stress state. Overall, an excellent agreement in maximum stress and displacement is achieved. Together with the examples examined in section 6.2.4, the model is sufficiently proved and assessed as good.

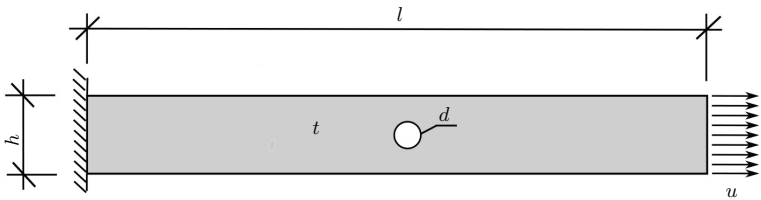

Figure 6.11: Geometry of a tension rod with a centered open hole.

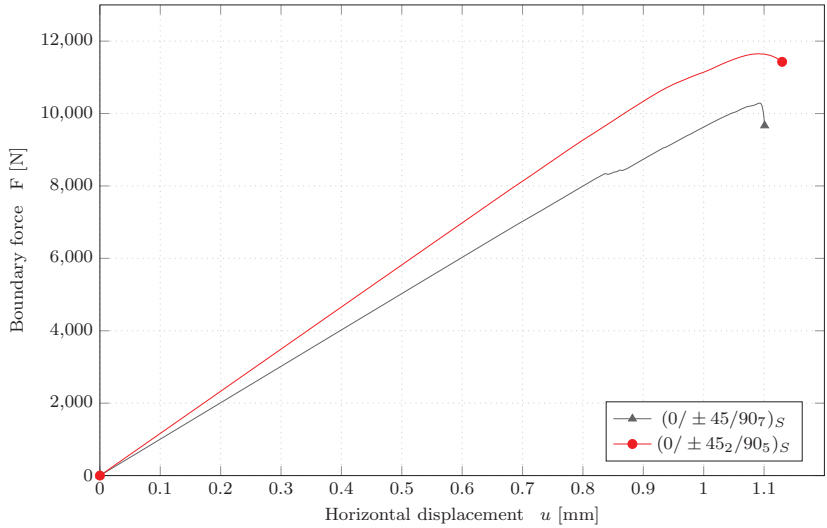

Figure 6.12: Tension rod with a centered open hole, discretization: 64x16x10 elements.

Table 6.5: Predicted and measured stress σ^{max} in [N/mm^2].

Layup	Predicted	Experiment	Deviation(%)
$[0^\circ/\pm 45^\circ/90^\circ_7]_S$	154.81	159.96	3.22
$[0^\circ/[\pm 45^\circ]_2/90^\circ_5]_S$	177.59	185.47	4.25

6.2.6 Effect of Different Damage Effect Tensors

In section 3.4.1 various approaches of the damage effect tensor $\mathbb{M}$ were introduced. In a simple manner, the different approaches are tested and contrasted with each other within the examples using a tension rod and a plate with an open hole using material number 2. It is evident in the tension rod example in figure 6.13, that all approaches are in good agreement. This is as expected because the damage is primarily driven by the damage variable D_1. The difference, with the exception of the $\mathbb{M}^3$ path, comes from the tapering of the cross section to create a predetermined breaking point. In the plate with an open hole in figure 6.13 (right), where a far more complex damage state is present, a difference in the maximum bearable load can be observed. The waved shape of the path corresponding to $\mathbb{M}^0$ is a result of the IMPL-EX scheme and can be reduced with a smaller step size. Overall, no general statement or suggestion as when to use each of the different effect tensors can be postulated without a deep understanding

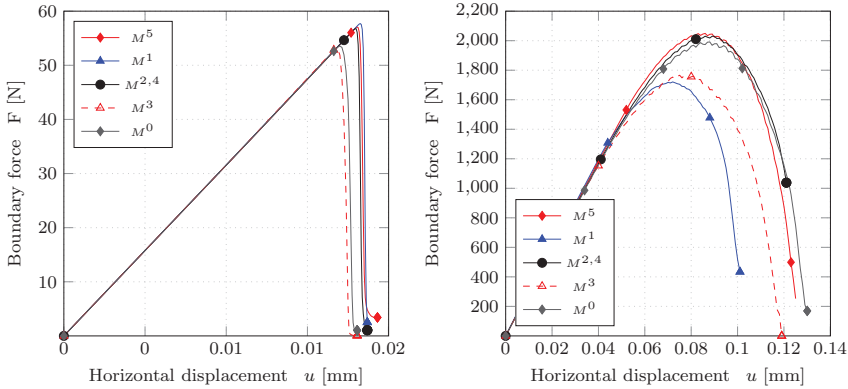

Figure 6.13: Damage effect tensor $\mathbb{M}^i$ applied on: a.) tension rod (left), b.) plate with open hole (right).

of fiber-reinforced composite behavior.

6.2.7 Effect of Different Equivalence Principles

In this numerical example, a compression rod is used to illustrate the effect of different equivalency principles. The geometry is the same as in the previous tension rod examples, the load is changed in its direction, and the material is number 2 from table 6.2. Figure 6.14 shows that for a strain equivalence (Eq0) Hashin's (H) and Cuntze's (C) failure mode criteria match, whereas for energy equivalence (Eq1), a difference is clearly visible. Furthermore, the difference of the maximum bearable load is, in energy equivalence, roughly 8% less than in strain equivalence. This can be explained by the fact that through the multiplication of $\mathbb{C}$ in energy modes, the damage variable is involved in quadratic order. Nevertheless, the maximum stress can never be higher than its strength property. The difference between the two equivalence principles becomes greater the more the system is able to distribute its loads. Finally, the effect of neglecting the damage terms beside the main diagonal is of interest. In the first four curves, the damage compliance tensor according to equation (3.38) is used, whereas in the first curve (Eq0-$\mathbb{M}^0$-C-s), the symmetrized compliance tensor according to equation (4.22) is used. Contrary to the claim made in [92], the effect of neglecting the damage entries apart from the main diagonal has a significant effect on the degrading behavior of the damaged material. The curve created with this neglect is much flatter than without it. However, the computation is more stable and the most important value is often the maximum bearable load, which is not affected thereby.

In the next sections, the local behavior of damage evolution is discussed together with specific user settings that can be performed.

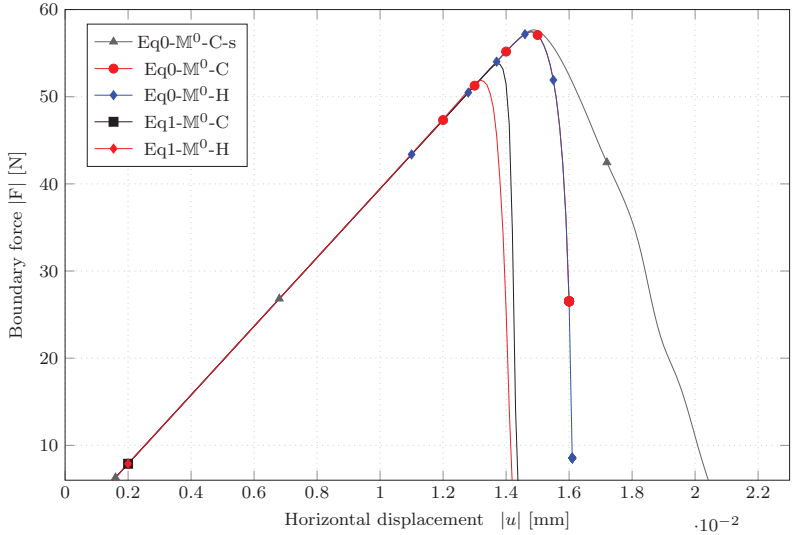

Figure 6.14: Strain vs. energy equivalence - Eq0=strain equivalence, Eq1=energy equivalence - C=Cuntze, H=Hashin.

6.2.8 Damage Investigation of a Tension Rod with One Layer

The previous examples successfully validate the default settings for further research. From this section on, the strain equivalence, Cuntze's FMC, and the corresponding damage effect tensor $\mathbb{M}^0$ are used unless otherwise stated. Having discussed general aspects and validated the material model, the current study now examines the example of the tension rod in greater detail with a focus on damage and stress evolution. In figure 6.15, the load displacement path of the tension rod example using material number 2 is illustrated. The horizontal displacement corresponds to any node on the right edge and the boundary force is the sum over all nodes facing the left edge. The calculation is displacement driven and symmetry conditions are used so that one-eighth model with a discretization of 30x6x6 element can be investigated. The short distance between damage initiation and maximum bearable load indicates that the system does not have a good ability for load redistribution (as expected). It is noteworthy that a converged solution is obtained until full damage is reached.

In the load displacement curve, three important points are marked, to which the figures 6.16, 6.17, and 6.18 correspond. The first point corresponds to the D_1 damage initiation. The damage arises at the maximum σ_{11} stress in the tapered upper right corner, as it should (figure 6.16). The profile can then bear a greater load until its maximum load state is reached and the model starts to degrade. The second point in the path is marked at $u = 0.0174$ mm. At this point,

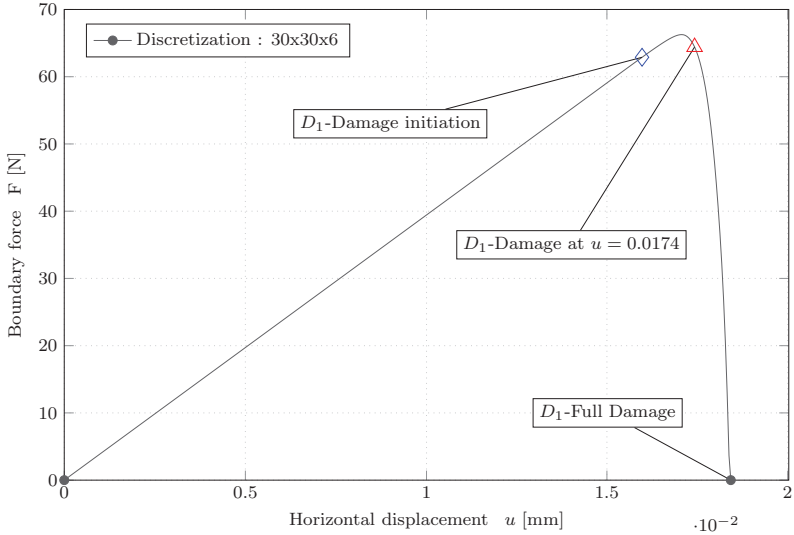

Figure 6.15: Tension rod discretized with 30x30x6 elements.

the damage has developed over the whole cross section and the upper right corner has already been damaged to 87%. It is evident that the upper right corner deprives the loading and load redistribution from the upper to the lower corner (figure 6.17). This develops to full damage ($D = 1$) of the area of the cross section of the hole, with corresponding stresses that are and must be zero (figure 6.18).

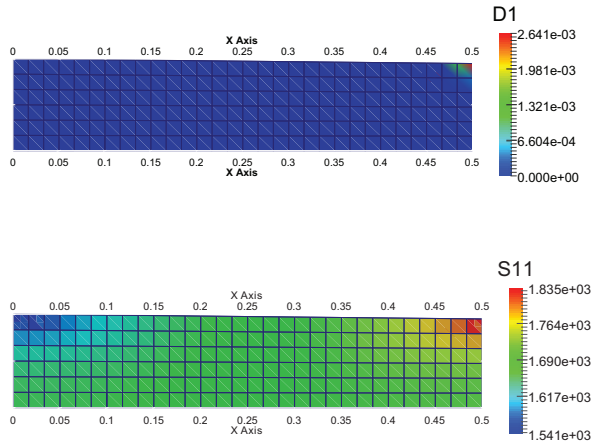

Figure 6.16: Damage variable D_1 and stress σ_{11} at damage initiation.

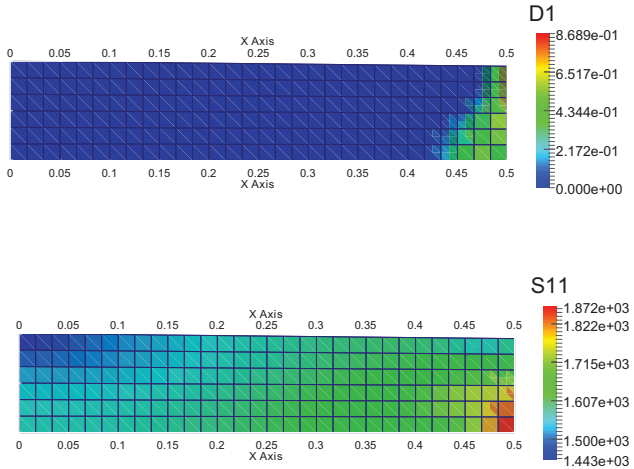

Figure 6.17: Damage variable D_1 and stress σ_{11} at $u = 0.0174$ mm.

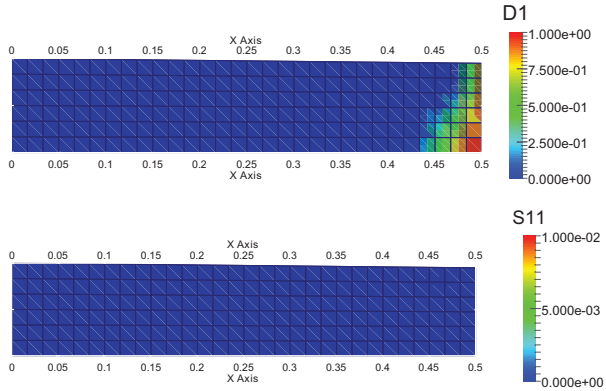

Figure 6.18: Damage variable D_1 and stress σ_{11} at full damage.

6.2.9 Damage Investigation of a Cantilever Beam - One Layer

This example shows the damage evolution of a cantilever beam with length $l = 2$ m, width $b = 0.1$ m, and height $h = 0.1$ m. The behavior is examined for a full model with a discretization of 50x6x6 elements. The beam is clamped on its left side, the vertical load acts on its right side and the vertical displacement is linked to the nodes on the bottom right edge of the profile. A displacement controlled calculation is executed using material number 4 from table 6.2. Because the overall stiffness of the profile during damage is reduced slower than in the tension rod example, the resulting path is flatter. Three important points, D_1-damage initiation caused by compression and tension, and D_6 shear damage are marked in the graph. The plots beneath the load displacement curve correspond to the marked endpoint of the path. The compression material strength is lower than the tensile strength and the elastic stress is equal at the bottom and top edges. As a result, the damage initiation first arises at the bottom edge with a negative σ_{11} stress. After damage is first initiated, the cross section can then bear almost twice the initiation load until tensile induced damage at the top edge arises. Then, the loss of stiffness

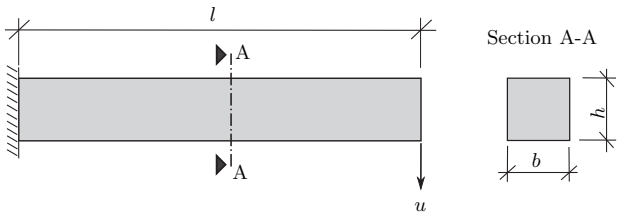

Figure 6.19: Geometry of a cantilever beam example.

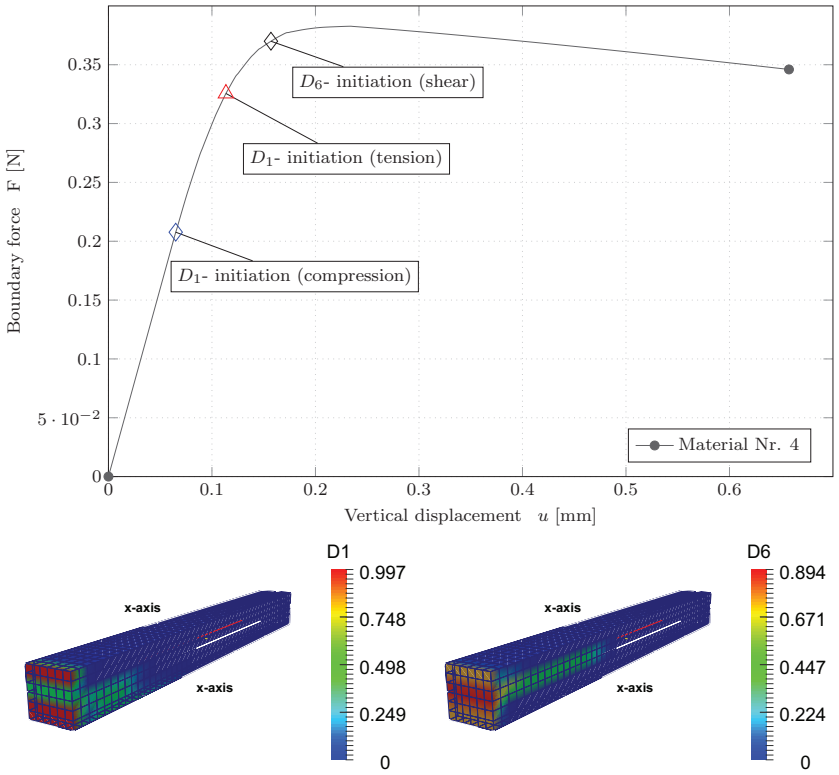

Figure 6.20: Cantilever beam: load displacement curve (top), damage variable $D1$ (middle) and damage variable $D6$ (bottom) at endpoint.

proceeds quickly and the path reaches its maximum bearable load and begins to decrease after passing the D_6-shear damage initiation. The evolution of damage is conclusive. This type of shear damage behavior is similarly seen, for example, in [55]. When the profile is further loaded, the shear damage proceeds to the right end of the cross section.

6.2.10 Damage Investigation of a Plate with Open Hole - One Layer

In this section, the behavior of the plate with an open hole, illustrated in figure 6.2 with material number 4 from table 6.2 is investigated. The numerical model utilizes symmetry conditions and one-eighth model with a discretization of 50x50x1 elements is calculated. It is remarkable that a converged solution exists up to nearly a full damage state on the load displacement path in figure 6.21. Particular attention should be paid to the difference between the load at damage

initiation and the maximum bearable load. The maximum bearable load is roughly 600% higher than the load present at D_2-damage initiation and 400% higher than the load corresponding to D_1-damage initiation. Two points besides the damage initiation on the load displacement path are marked for further use. The first point serves as a reference for a stress and a D_1-damage plot (figure 6.21) at displacement $u = 0.134$ mm. It is clearly visible in the upper right plot that the stress concentrates at the upper edge of the hole. The coloring of the damage variable D_1 is scaled and the area where $D_1 > 0.1$ is marked in red. The proportion in the present anisotropic case is similar to an isotropic case which would be three times greater and without the stress at the right edge of the hole. The damage initiates in the stress concentration point and develops along the symmetry edge, as can be seen in the lower left image. It is notable that the elements close to the concentration point are at this load step already fully damaged $D_1 = 0.98$. The second point corresponds to the displacement $u = 0.389$ mm, at which the cross section is fully damaged. Here, damage has evolved through the cross section of the hole in a nearly vertical direction on its symmetry edge. The upper right corner of the cross section is also damaged due to load redistribution. The corresponding D_2-damage variable is plotted in the bottom right picture.

To illustrate the local effect of an overly coarse discretization, the same problem is calculated with a mesh of 30x30x4 elements with both Hashin's and Cuntzes failure theory. In the left plot in figure 6.22, the damage leaves its path at a point, makes a curve, and finally returns to its symmetry edge. This local behavior only arises because of the mesh size, but causes only a small difference in the load displacement path. The results of using Hashin's criterion are illustrated in the right plot. As with Cuntze's FMC, the damage evolves along its expected path up to a point where it escapes to the right.

The previous examples show the sensitivity of numerical investigations of damaged materials. A fine mesh, illustrated on the left side in figure 6.21, is sufficient for obtaining a solution that is more expected than that in figure 6.22. On the other hand, if the mesh size is too small, convergence issues can arise. Generally, the simulation of damage in load suspended structures is challenging. In addition to a convergence study, critical reflection on the results, especially for the evolution of the damage variable, is necessary.

Another important observation can be made by examining, as before, the load displacement path in figure 6.21. From this, it can be seen that a difference of more than 600% lies between the first damage mode (D_2) and the maximum bearable load. Since in industrial dimensioning structures are related to the first ply failure (here D_2), an enormous oversizing of composite structures is present. On the other hand, due to load cycling and other influences on real structures, damage is not only driven through static loads. This means that other effects, such as fatigue and delamination, must also be considered in a simulation for an accurate and realistic prediction of damage. This task is completed in chapter 7.

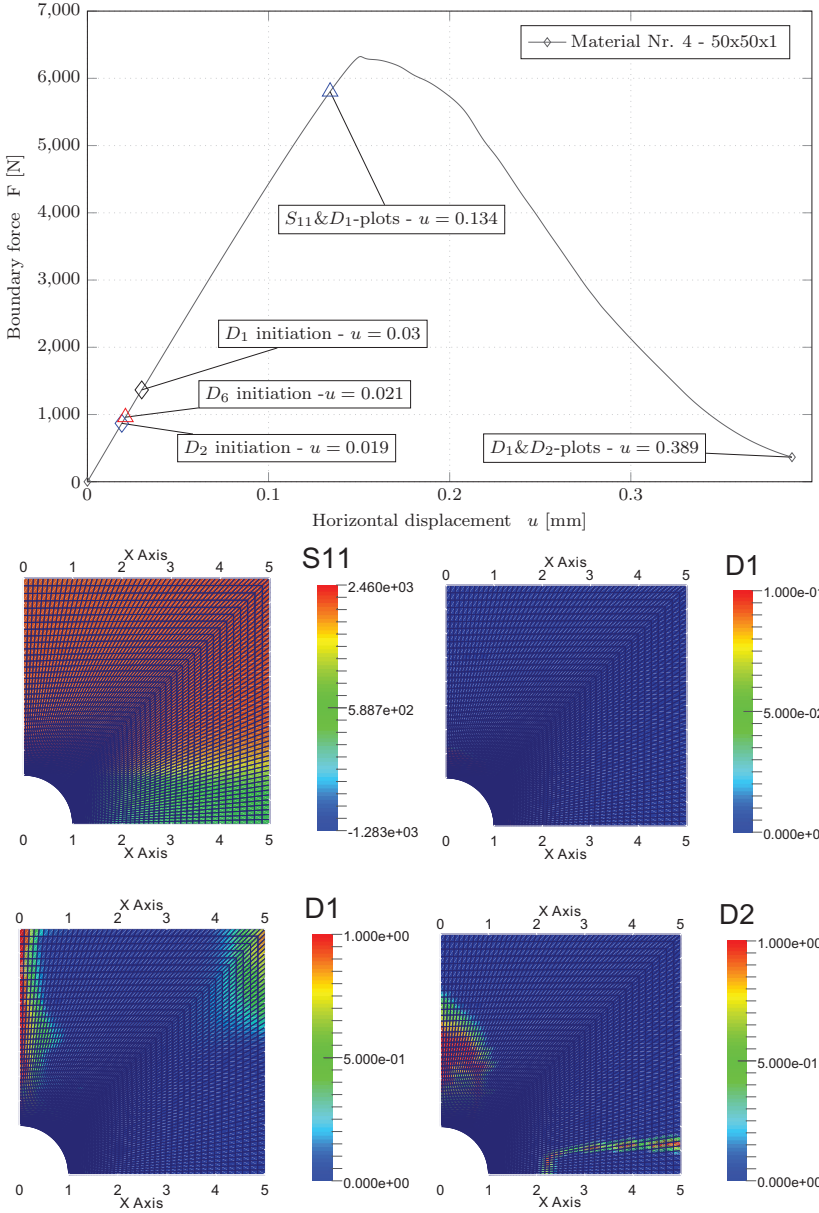

Figure 6.21: Plate with an open hole: load displacement graph (top), stress σ_1 (middle left) and damage variable D_1 (middle right) at $u = 0.134$ mm , damage variable D_1 (bottom left) and damage variable D_2 at $u = 0.389$ mm (bottom right).

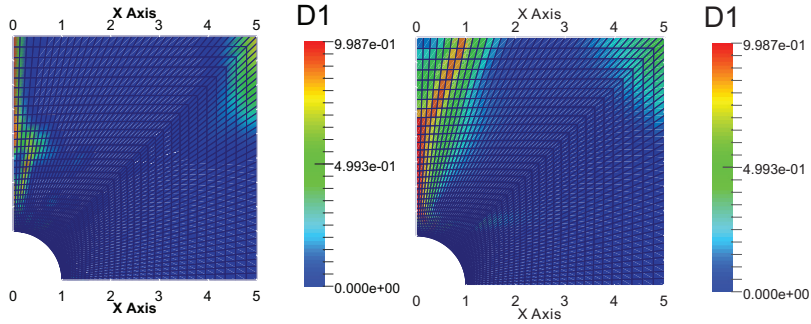

Figure 6.22: Plate with an open hole: Cuntze's FMC (left) and Hashin's damage criterion (right) with 30x30x4 elements.

Chapter 7

A Coupled Two-Scale Model for Damage Simulations

To capture the complex mechanism of damage in fiber reinforced composites, multiscale methods have been developed. In multiscale formulations, at least two different scales are used for the description of a problem. One global or macro scale and one local or micro scale. The global scale is used to discretize an arbitrary geometry of interest, whereas the local scale is used to capture the behavior of complex materials within a so called representative volume element (RVE). Within this study, both scales are discretized with finite elements and the RVE has a fixed scale, often determined within a convergence study. The basic concept of multiscale analysis is depicted in figure 7.1. The local or micro model is executed in each integration point of the global model. This can either be enabled by hard-coding the local FEM-routine into the material law of the integration point of the global system or by using a FE^2 approach [126] and [53], where the FE program is accessed a second time in the integration point. In both alternatives, the strain tensor of the integration point of the global model is imposed on the microscopic model via boundary conditions. The stresses and constitutive equations of the macroscale are then forwarded by the results of the microscale. The variables passed from the local to the global model are defined by volume averages over the local model. In a general nonlinear analysis, both scales have to be coupled within an iterative solution procedure in such a way that the local model is solved in each iteration of the global model.

The current chapter introduces a multiscale approach for damage models. The variational principle introduced in section 2.4 is first extended for use it in iterative, two-scale calculations. Second, the linearization of the variation and a general multiscale finite element formalism are introduced. Finally, global and local scales are discussed in terms of kinetic description and finite element adaption.

7.1 Variational Formulation of a Two-Scale Model

In this section, the formulation of the principle of virtual work (5.16) and its linearization (5.19) for the three dimensional continuum element are extended to incorporate the characterization of a local model. The formalism is established based on the work of [62].

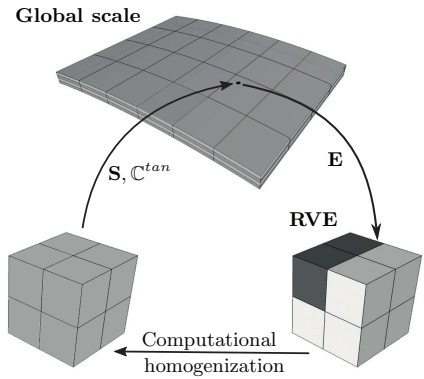

Figure 7.1: Depiction of a computational multiscale procedure.

As illustrated in figure 7.1, the local boundary model is accessed during the finite element calculation within each element in each integration point i of the global model. The connection from the global to the local model is established by passing in the global strains from integration point i to the local model where they are converted and act as displacement boundary conditions. Once the local equilibrium is found, the homogenized tangential material stiffness and averaged stress tensor are returned to the global model.

The equations are valid for all, but constructed for only one, arbitrarily chosen, global element. For a better distinction, the body of the local RVE is denoted with $\mathcal{B}_i$ and its boundaries with $\partial\mathcal{B}_i$. The continuum mechanical quantities of the local model can be established completely independent of that from the global model because the bodies $\mathcal{B}_i$ and $\mathcal{B}_0$ do not correlate. Indeed, in the scope of this work, kinetic equations such as displacements, stresses, and strains, derived in the previous chapters and used for the macroscopic description, are taken without modification for the description of the local model. From the independency it follows that the global model can be calculated geomeytrically nonlinear, whereas, at the same time, the local model is assumed to behave geometrically linearly.

The starting point for the derivation of the coupled model are the static field functions for the global and local model according to equations (2.54):

$$\begin{aligned} \operatorname{Div}\bar{\mathbf{P}} + \rho\mathbf{b}_0 &= \mathbf{0} \quad \text{in}\,\mathcal{B}_0 \quad , \\ \operatorname{Div}\boldsymbol{\sigma} + \rho\mathbf{b}_0 &= \mathbf{0} \quad \text{in}\,\mathcal{B}_i \quad . \end{aligned} \tag{7.1}$$

The first equation describes the global equilibrium, whereas the second describes the local equilibrium. In the following, the volume forces are neglected. As discussed, to fully describe the

boundary problem, static and geometric boundary conditions have to be introduced. For the local model, due to the absence of external loads, the following static boundary condition is obtained:

$$\boldsymbol{\sigma}\mathbf{N} = \mathbf{0} \quad \text{in } \partial\mathcal{B}_{i\sigma} \quad . \tag{7.2}$$

Additionally, as in chapter 5, the local geometric boundary condition $\mathbf{u}$ must be met on $\partial\mathcal{B}_{iu}$. In $\mathbf{u}$ the global-local coupling is performed. The local displacement boundaries are determined from strains of integration point i. The vector $\mathbf{u}$ is established in greater detail in equation (7.31).

Until the end of the current section, global quantities such as stresses $\bar{\mathbf{S}}$, strains $\bar{\mathbf{E}}$, and displacements $\bar{\mathbf{u}}$ acting in $\mathcal{B}_0$ are denoted with a bar, whereas local quantities in $\mathcal{B}_i$ are denoted without ($\boldsymbol{\sigma}$, $\boldsymbol{\varepsilon}$ and $\mathbf{u}$).

The coupled, global-local formulation is obtained by extending the principle of virtual work (2.81) with the variation of the local equilibrium given in equation (7.1). The variation is performed independently on the global and the local model. The test function can be summarized, containing both, as

$$\delta\boldsymbol{\theta} = [\delta\bar{\mathbf{u}}, \delta\mathbf{u}]^T \quad . \tag{7.3}$$

Following the same procedure as in section 2.4 yields

$$\begin{aligned} g(\boldsymbol{\theta}, \delta\boldsymbol{\theta}) := &\int_{\mathcal{B}_0} (\bar{\mathbf{S}} : \delta\bar{\mathbf{E}} - \mathbf{b}_0 \cdot \delta\bar{\mathbf{u}}) \, \mathrm{d}V - \int_{\partial\mathcal{B}_{0\sigma}} \mathbf{t}_0 \cdot \delta\bar{\mathbf{u}} \, \mathrm{d}A \\ &+ \sum_{e=1}^{nelem} \sum_{i=1}^{ngp} \frac{1}{V_i} \int_{\mathcal{B}_i} \boldsymbol{\sigma} : \delta\boldsymbol{\varepsilon} \, \mathrm{d}V = 0 \quad . \end{aligned} \tag{7.4}$$

Here, *nelem* denotes the total number of global elements, *ngp* the number of integration points per element, and V_i represents the volume of the RVE. As in section 2.4, for numerical implementation, the linearization

$$L[g(\boldsymbol{\theta}, \delta\boldsymbol{\theta}), \Delta\boldsymbol{\theta}] := g(\boldsymbol{\theta}, \delta\boldsymbol{\theta}) + \mathrm{D}\,[g(\boldsymbol{\theta}, \delta\boldsymbol{\theta}] \cdot \Delta\boldsymbol{\theta} \quad . \tag{7.5}$$

of the coupled model is needed. The first term is defined in equation (7.4), the second term is derived as

$$\begin{aligned} \mathrm{D}\,[g(\boldsymbol{\theta}, \delta\boldsymbol{\theta}] \cdot \Delta\boldsymbol{\theta} = &\int_{\mathcal{B}_0} \left(\bar{\mathbf{S}} : \Delta\delta\bar{\mathbf{E}} + \delta\bar{\mathbf{E}} : \bar{\mathbb{C}} : \Delta\bar{\mathbf{E}} \right) \mathrm{d}V \\ &+ \sum_{e=1}^{nelem} \sum_{e=1}^{ngp} \frac{1}{V_i} \int_{\mathcal{B}_i} \left(\boldsymbol{\sigma} : \Delta\delta\boldsymbol{\varepsilon} + \delta\boldsymbol{\varepsilon} : \mathbb{C} : \Delta\boldsymbol{\varepsilon} \right) \mathrm{d}V_i \quad . \end{aligned} \tag{7.6}$$

7.2 Finite Element Formulation of a Two-Scale Model

In the next step, the discretization of the local model is presented. For the local system, the same bilinear interpolation functions for the geometry and displacements as in the global system are used, which is in general unnecessary since both systems are independent of each other. The local system represents the microstructure of the global system by means of an RVE. The RVE returns the homogenized material stiffness $\bar{\mathbb{C}}$ and the averaged stress vector $\bar{\boldsymbol{\sigma}}$ to the global system. The actual size of the RVE must be determined within a convergence study.

Inserting the interpolation functions into the linearized weak form of equilibrium given in equation (7.5) and considering the definitions in equation (7.4) and (7.6) yields

$$
\begin{aligned}
&L\left[g(\boldsymbol{\theta}^h,\delta\boldsymbol{\theta}^h),\Delta\boldsymbol{\theta}^h\right] = \\
&\sum_{e=1}^{numel}
\begin{bmatrix} \delta\mathbf{v}^G \\ \delta\mathbf{V}_1 \\ \vdots \\ \delta\mathbf{V}_i \\ \vdots \\ \delta\mathbf{V}_{ngp} \end{bmatrix}_e^T
\left(
\begin{bmatrix}
\mathbf{k}^G(\bar{\mathbb{C}}_i) & & & & \dots & 0 \\
& \mathbf{K}_1^L & & & & \vdots \\
& & \ddots & & & \\
& & & \mathbf{K}_i^L & & \\
\vdots & & & & \ddots & \\
0 & \dots & & & & \mathbf{K}_{ngp}^L
\end{bmatrix}
\begin{bmatrix} \Delta\mathbf{v}^G \\ \Delta\mathbf{V}_1 \\ \vdots \\ \Delta\mathbf{V}_i \\ \vdots \\ \Delta\mathbf{V}_{ngp} \end{bmatrix}
+
\begin{bmatrix} \mathbf{f}^G(\bar{\boldsymbol{\sigma}}_i) \\ \mathbf{F}_1^L \\ \vdots \\ \mathbf{F}_i^L \\ \vdots \\ \mathbf{F}_{ngp}^L \end{bmatrix}
\right)_e .
\end{aligned}
\tag{7.7}
$$

Here, G and L identify the global and the local system, respectively. In equation (7.7), the matrices from the first row are obtained from the global part of the linearized weak form of equilibrium, equation (7.5). Furthermore e is the global element number and i is a specific integration point in e. The global element residual vector $\hat{\mathbf{f}}^G$ and the global tangential element stiffness matrix $\mathbf{k}^G$ have been derived in (5.18) and read

$$
\begin{aligned}
\mathbf{k}^G(\bar{\mathbb{C}}_i) &= \int_{\mathcal{B}_e} (\mathbf{B}^T\bar{\mathbb{C}}\mathbf{B} + \mathbf{G})\,\mathrm{d}V \\
\hat{\mathbf{f}}^G(\bar{\mathbf{S}}_i) &= \int_{\mathcal{B}_e} (\mathbf{B}^T\bar{\mathbf{S}} - \mathbf{N}^T\mathbf{b})\,\mathrm{d}V - \int_{\partial\mathcal{B}_{\sigma e}} \mathbf{N}^T\mathbf{t}_0\,\mathrm{d}A
\end{aligned}
\quad , \tag{7.8}
$$

where the superscript G identifies the global system unambiguously.

The matrices from the second to the last row in (7.7) refer each to the local boundary value problem at global integration point i of the system, where i runs from 1 to the total number of global integration points ngp in e.

The description of each local system of equation (7.7) is performed by

$$\delta \mathbf{V}_i^T (\mathbf{K}_i^L \Delta \mathbf{V}_i + \hat{\mathbf{F}}_i^L) = \frac{1}{V_i} \sum_{e=1}^{n} \delta \mathbf{v}_e^T (\mathbf{k}_e^L \Delta \mathbf{v}_e + \hat{\mathbf{f}}_e^L) \quad . \tag{7.9}$$

Here, e and n refer to the elements and the total element number from the discretization of the RVE. The local matrices are derived like before, leading to the element residual vector $\hat{\mathbf{f}}_e^L$ and the tangential element stiffness $\mathbf{k}_e^L$, given with

$$\begin{aligned} \mathbf{k}_e^L &= \int_{\mathcal{B}_i} (\mathbf{B}^T \mathbb{C} \mathbf{B} + \mathbf{G}) \, \mathrm{d}V \\ \hat{\mathbf{f}}_e^L &= \int_{\mathcal{B}_i} \mathbf{B}^T \boldsymbol{\sigma} \, \mathrm{d}V \end{aligned} \quad . \tag{7.10}$$

Note that the matrix $\mathbf{B}$ and the stresses $\boldsymbol{\sigma}$ and $\mathbf{S}$ in (7.8) and (7.10) are independent of each other and generally do not have to coincide.

For further calculation, the local element displacement vector in (7.9) is split into two parts. The first part $\mathbf{v}_a$ contains the displacements of inner nodes of the RVE, whereas the second part $\mathbf{v}_b$ holds the boundary displacements resulting from global strains at integration point i. The actual boundary displacements are discussed in greater detail in section 7.3.2. The inner displacements $\mathbf{v}_a$ are related to the displacements $\mathbf{V}_i$ via the standard assembly matrix $\mathbf{a}_e$. The boundary displacements $\mathbf{v}_b$ are related to the prescribed global strains at integration point i through a matrix $\mathbf{A}_e(x, y, z)$, specified in equation (7.32):

$$\mathbf{v}_e = \begin{bmatrix} \mathbf{v}_a \\ \mathbf{v}_b \end{bmatrix} = \begin{bmatrix} \mathbf{a}_e \mathbf{V}_i \\ \mathbf{A}_e \bar{\boldsymbol{\varepsilon}}_i \end{bmatrix} \quad . \tag{7.11}$$

As discussed, the variation and linearization of $\mathbf{v}$ are needed for finite element formulations. They are given with

$$\delta \mathbf{v}_e = \begin{bmatrix} \delta \mathbf{v}_a \\ \delta \mathbf{v}_b \end{bmatrix} = \begin{bmatrix} \mathbf{a}_e \delta \mathbf{V}_i \\ \mathbf{A}_e \delta \bar{\boldsymbol{\varepsilon}}_i \end{bmatrix}, \quad \Delta \mathbf{v}_e = \begin{bmatrix} \Delta \mathbf{v}_a \\ \Delta \mathbf{v}_b \end{bmatrix} = \begin{bmatrix} \mathbf{a}_e \Delta \mathbf{V}_i \\ \mathbf{A}_e \Delta \bar{\boldsymbol{\varepsilon}}_i \end{bmatrix} \quad . \tag{7.12}$$

According to the order of $\mathbf{v}_e$ in equation (7.11), the local submatrix $\mathbf{k}_e^L$ and the element residual vector $\hat{\mathbf{f}}_e^L$ are respectively rearranged:

$$\mathbf{k}_e^L = \begin{bmatrix} \mathbf{k}_{aa} & \mathbf{k}_{ab} \\ \mathbf{k}_{ba} & \mathbf{k}_{bb} \end{bmatrix}_e, \quad \hat{\mathbf{f}}_e^L = \begin{bmatrix} \mathbf{f}_a \\ \mathbf{f}_b \end{bmatrix}_e \quad . \tag{7.13}$$

Inserting definitions (7.12) and (7.13) into the local boundary value problem (7.9) yields

$$\begin{aligned}
&\delta\mathbf{V}_i^T(\mathbf{K}_i^L\Delta\mathbf{V}_i + \hat{\mathbf{F}}_i^L) \\
&\quad= \frac{1}{V_i}\sum_{e=1}^{n}\begin{bmatrix}\delta\mathbf{v}_a\\ \delta\mathbf{v}_b\end{bmatrix}_e^T\left\{\begin{bmatrix}\mathbf{k}_{aa} & \mathbf{k}_{ab}\\ \mathbf{k}_{ba} & \mathbf{k}_{bb}\end{bmatrix}\begin{bmatrix}\Delta\mathbf{v}_a\\ \Delta\mathbf{v}_b\end{bmatrix} + \begin{bmatrix}\mathbf{f}_a\\ \mathbf{f}_b\end{bmatrix}\right\}_e \quad . \\
&\quad= \frac{1}{V_i}\begin{bmatrix}\delta\mathbf{V}_i\\ \delta\bar{\boldsymbol{\varepsilon}}_i\end{bmatrix}_e^T\left\{\begin{bmatrix}\mathbf{a}_e^T\mathbf{k}_{aa}\mathbf{a}_e & \mathbf{a}_e^T\mathbf{k}_{ab}\mathbf{A}_e\\ \mathbf{A}_e^T\mathbf{k}_{ba}\mathbf{a}_e & \mathbf{A}_e^T\mathbf{k}_{bb}\mathbf{A}_e\end{bmatrix}\begin{bmatrix}\Delta\mathbf{V}_i\\ \Delta\bar{\boldsymbol{\varepsilon}}_i\end{bmatrix} + \begin{bmatrix}\mathbf{a}_e^T\mathbf{f}_a\\ \mathbf{A}_e^T\mathbf{f}_b\end{bmatrix}\right\}_e
\end{aligned} \tag{7.14}$$

The following definitions can be introduced for each integration point i

$$\begin{aligned}
\mathbf{K} &= \sum_{e=1}^{n}\mathbf{a}_e^T\mathbf{k}_{aa}\mathbf{a}_e \quad , \qquad \hat{\mathbf{F}}_a = \sum_{e=1}^{n}\mathbf{a}_e^T\mathbf{f}_a \quad , \\
\mathbf{L} &= \sum_{e=1}^{n}\mathbf{a}_e^T\mathbf{k}_{ab}\mathbf{A}_e \quad , \qquad \hat{\mathbf{F}}_b = \sum_{e=1}^{n}\mathbf{A}_e^T\mathbf{f}_b \quad , \\
\mathbf{M} &= \sum_{e=1}^{n}\mathbf{A}_e^T\mathbf{k}_{bb}\mathbf{A}_e \quad ,
\end{aligned} \tag{7.15}$$

with which a simplified shortened form of equation (7.14) is obtained:

$$\delta\mathbf{V}_i^T(\mathbf{K}_i^L\Delta\mathbf{V}_i + \hat{\mathbf{F}}_i^L) = \frac{1}{V_i}\begin{bmatrix}\delta\mathbf{V}_i\\ \delta\bar{\boldsymbol{\varepsilon}}_i\end{bmatrix}^T\left\{\begin{bmatrix}\mathbf{K} & \mathbf{L}\\ \mathbf{L}^T & \mathbf{M}\end{bmatrix}\begin{bmatrix}\Delta\mathbf{V}_i\\ \Delta\bar{\boldsymbol{\varepsilon}}_i\end{bmatrix} + \begin{bmatrix}\hat{\mathbf{F}}_a\\ \hat{\mathbf{F}}_b\end{bmatrix}\right\} \quad , \tag{7.16}$$

With an arbitrary variation $\delta\mathbf{V}_i \neq 0$, and considering that each row in matrix (7.7) must vanish, the relation

$$\mathbf{K}\Delta\mathbf{V}_i + \mathbf{L}\Delta\bar{\boldsymbol{\varepsilon}}_i + \hat{\mathbf{F}}_a = 0 \tag{7.17}$$

is obtained. The inner degrees of freedom $\Delta\mathbf{V}_i$ in equation (7.17) can be eliminated with static condensation by solving the first line in (7.16):

$$\Delta\mathbf{V}_i = -\mathbf{K}^{-1}(\mathbf{L}\Delta\bar{\boldsymbol{\varepsilon}}_i + \hat{\mathbf{F}}_a) \quad . \tag{7.18}$$

Here, $\mathbf{K}^{-1}$ exists as long as rigid body motions of the RVE are eliminated by boundary conditions. As we will see later in this study, additional boundary conditions to those given from the global integration point are necessary to fully eliminate rigid body motions.

Solving the second line in (7.16) by using equation (7.18) yields

$$\begin{aligned}
\delta\mathbf{V}_i^T(\mathbf{K}_i^L\Delta\mathbf{V}_i + \hat{\mathbf{F}}_i^L) &= \frac{1}{V_i}\delta\bar{\boldsymbol{\varepsilon}}_i^T\left[(\mathbf{M} - \mathbf{L}^T\mathbf{K}^{-1}\mathbf{L})\Delta\bar{\boldsymbol{\varepsilon}}_i + (\hat{\mathbf{F}}_b - \mathbf{L}^T\mathbf{K}^{-1}\hat{\mathbf{F}}_a)\right] \\
&= \delta\bar{\boldsymbol{\varepsilon}}_i^T(\bar{\mathbb{C}}_i\Delta\bar{\boldsymbol{\varepsilon}}_i + \bar{\boldsymbol{\sigma}}_i) \quad ,
\end{aligned} \tag{7.19}$$

where the discussed homogenized macro stresses $\bar{\boldsymbol{\sigma}}_i$ and the homogenized material tangent $\bar{\mathbb{C}}_i$

are defined by

$$\bar{\boldsymbol{\sigma}}_i = \frac{1}{V_i}(\hat{\mathbf{F}}_b - \mathbf{L}^T\mathbf{K}^{-1}\hat{\mathbf{F}}_a), \qquad \bar{\mathbb{C}}_i = \frac{1}{V_i}(\mathbf{M} - \mathbf{L}^T\mathbf{K}^{-1}\mathbf{L}) \quad . \tag{7.20}$$

Inserting this representation back into equation (7.7) leads to the following formulation:

$$L\left[g(\boldsymbol{\theta}^h, \delta\boldsymbol{\theta}^h), \Delta\boldsymbol{\theta}^h\right] =$$

$$\sum_{e=1}^{numel} \begin{bmatrix} \delta\mathbf{v}^G \\ \delta\bar{\boldsymbol{\varepsilon}}_1 \\ \vdots \\ \delta\bar{\boldsymbol{\varepsilon}}_i \\ \vdots \\ \delta\bar{\boldsymbol{\varepsilon}}_{ngp} \end{bmatrix}_e^T \left\{ \begin{bmatrix} \mathbf{k}^G(\bar{\mathbb{C}}_i) & & & \dots & 0 \\ & \bar{\mathbb{C}}_1 & & & \vdots \\ & & \ddots & & \\ & & & \bar{\mathbb{C}}_i & \\ \vdots & & & & \ddots \\ 0 & \dots & & & \bar{\mathbb{C}}_{ngp} \end{bmatrix} \begin{bmatrix} \Delta\mathbf{v}^G \\ \Delta\bar{\boldsymbol{\varepsilon}}_1 \\ \vdots \\ \Delta\bar{\boldsymbol{\varepsilon}}_i \\ \vdots \\ \Delta\bar{\boldsymbol{\varepsilon}}_{ngp} \end{bmatrix} + \begin{bmatrix} \mathbf{f}^G(\bar{\boldsymbol{\sigma}}_i) \\ \bar{\boldsymbol{\sigma}}_1 \\ \vdots \\ \bar{\boldsymbol{\sigma}}_i \\ \vdots \\ \bar{\boldsymbol{\sigma}}_{ngp} \end{bmatrix} \right\}_e \tag{7.21}$$

The previous equation shows coupling between the global and the local problem. The linearized global strains $\bar{\boldsymbol{\varepsilon}}$ enter in equation (7.11), whereas the homogenized macro stresses $\bar{\boldsymbol{\sigma}}_i$ and the homogenized material tangent $\bar{\mathbb{C}}$ of integration point i enter in the residual vector $\mathbf{f}^G(\bar{\boldsymbol{\sigma}})$ and the element stiffness matrix $\mathbf{k}^G(\bar{\mathbb{C}}_i)$. It is interesting to note that all local systems in each single global element are independent of each other. This is advantageous in parallel computing because the equation systems can be solved simultaneously. According to equation (7.21), equilibrium has to be reached in each single local system as well as in the global system. In cases of any nonlinearity in the local system, several iteration steps have to be performed until the final local equilibrium state is reached, leading to high calculation times. The authors of [62] have shown that the quadratic convergence rate of the global Newton iteration is also maintained with no more than a single iteration step within the local system. This has been used during most examples of this study. Indeed, for some of the examined damage examples, it was necessary to fully iterate the local system to debar convergence issues on the global model.

7.3 Micromechanics and Homogenization

In this section, a micromechanical model is introduced that is used in the coupled finite element simulation of damage in fiber reinforced composites. A short introduction of micromechanics and homogenization is given before equations of the underlying theory are derived. For a more elaborate overview of the development of micromechanics and homogenization, the reader is referred to [4, 59, 128, 142].

A composite structure is a body which is made up of two or more parts or materials. From a

macromechanical approach, the composite is observed as an anisotropic material without considering the underlying details of the composite. This is an approach that is widely used for linear elastic analysis, where it delivers reliable results. In nonlinear analysis, such as damage analysis, the macromechanical approach becomes problematic. Complex failures or damage mechanisms must be constructed in the various directions they can appear. Due to the fact that damage physically occurs on different constituents of the composite, a macromechanical description by means of an idealized effective anisotropic material will always have disadvantages. In contrast, micromechanical models consider the constituent materials in addition to accounting for the internal structure of a material. The individual internal phases (materials) of this composite are observed separately with their properties and geometrical arrangements, ordinarily described by means of continuum mechanics. From this, it is clear that micromechanical models capture the physics of complex behaviors at a more fundamental level. Thus, the key point of micromechanics is to predict the effective behavior of a heterogeneous material based on the different properties of the constituents. These effective properties characterize the macroscopic behavior and are obtained from the assembly of all constituents of the micro model through suitable averaging techniques, known as homogenization techniques. Quantities are determined on a sample which must reflect the statistical average of the whole. Hill [67] called this sample an RVE, a notation that has been used since then. One of the key points of micromechanics is to find an RVE that has enough information to replace the actual continuum properly, without letting the numerical effort become exorbitant, a suggestion that has already been made in a different context by Albert Einstein *'A model should be as simple as possible, but not simpler'*.

In the following section, the MOC is introduced in a comprehensive form. This method serves as a basis for the EMOC, used as the micro model in the implemented multiscale approach for damage simulations.

7.3.1 Method of Cells

In this section, the basic ideas of the MOC, referring to the textbook [4], are introduced in a comprehensive form. With respect to the finite element formulation of the MOC presented later in this chapter, a different notation to that introduced in [4] is used. The MOC was originally used for elastic behavior and is based on the assumption that the physical behavior of a composite can be approximated with a double periodic array, as illustrated in figure 7.2. Using this periodicity, one single RVE is then alternatively used for the micromechanical analysis of the whole composite material. The picture on the right in figure 7.2 shows the micro mechanical RVE, consisting of one fiber element and three matrix elements. The lengths h_1 and h_2 are calculated dependent on a user input parameter η that holds the fiber-matrix ratio. The elements within the RVE are identified through superscript numbers (β, γ) in brackets. The coordinate system is set up in such a way that the x_1-direction corresponds to the extension of the longitudinal fiber direction. In addition, a local coordinate system $\bar{x}_i$ is defined at the

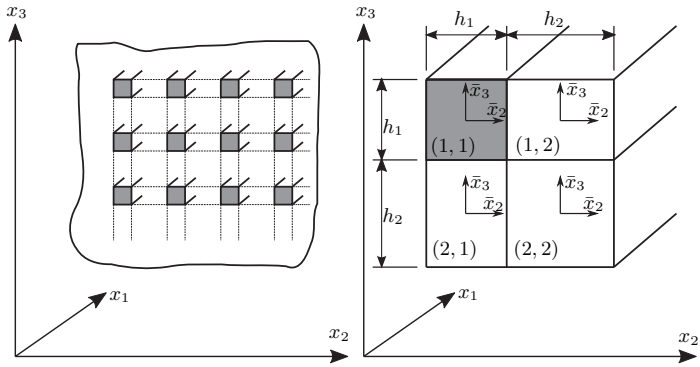

Figure 7.2: Double periodic arranged composite (left), one unit cell of the MOC (right).

center of each element, from which the displacements are interpolated linearly:

$$u_i^{\beta\gamma} = w_i^{(\beta\gamma)} + \bar{x}_2^{(\beta)}\,\phi_i^{(\beta\gamma)} + \bar{x}_3^{(\gamma)}\,\psi_i^{(\beta\gamma)} \quad . \tag{7.22}$$

Here, i runs from 1-3 and $w_i^{(\beta\gamma)}$ is the displacement at the center of the element. In this micromechanical model, linear elastic material behavior and small strains are assumed. Based on the displacement interpolation, equation (7.22), the pointwise strains in each element can be calculated according to equation (2.24) as

$$\varepsilon_{ij}^{(\beta\gamma)} = \frac{1}{2}\left(u_{i,j}^{(\beta\gamma)} + u_{j,i}^{(\beta\gamma)}\right) \quad . \tag{7.23}$$

Using the same ordering as in equation (2.125) yields the element strain vector

$$\boldsymbol{\varepsilon}^{(\beta\gamma)} = \left(\varepsilon_{11}^{(\beta\gamma)}, \varepsilon_{22}^{(\beta\gamma)}, \varepsilon_{33}^{(\beta\gamma)}, 2\varepsilon_{12}^{(\beta\gamma)}, 2\varepsilon_{13}^{(\beta\gamma)}, 2\varepsilon_{23}^{(\beta\gamma)}\right)^T \quad . \tag{7.24}$$

By neglecting thermal impact and assuming the previously mentioned linear theory, the pointwise stresses are given as

$$\boldsymbol{\sigma}^{(\beta\gamma)} = \mathbb{C}^{(\beta\gamma)}\,\boldsymbol{\varepsilon}^{(\beta\gamma)} \quad . \tag{7.25}$$

Because of the given linear displacement interpolation functions, strains, and therefore also stresses, remain constant within each element. Thus, the pointwise fields are identical to the averaged fields within each element:

$$\bar{\boldsymbol{\varepsilon}}_{ij}^{\beta\gamma} = \boldsymbol{\varepsilon}_{ij}^{\beta\gamma} \quad \text{and} \quad \bar{\boldsymbol{\sigma}}_{ij}^{\beta\gamma} = \boldsymbol{\sigma}_{ij}^{\beta\gamma} \quad . \tag{7.26}$$

Now that the kinetic description of each single element is known, it is necessary to calculate the resulting average stresses and material stiffness of the whole RVE. Additionally, continuity conditions at the interfaces between elements of the RVE must be introduced. Both aspects are discussed in the next section.

Homogenization and Continuity Conditions

The averaged stresses $\bar{\sigma}$ and material stiffness $\mathbf{K}^L$ of the RVE result from the homogenization procedure under consideration of continuity conditions which are themselves imposed in an averaged sense. In the framework of the method of cells, the homogenized stresses and strains of the RVE are computed from averaged quantities of each element:

$$\begin{aligned} \bar{\boldsymbol{\sigma}}_{ij} &= \frac{1}{V} \sum_{\beta,\gamma=1}^{2} v^{(\beta\gamma)}\, \bar{\boldsymbol{\sigma}}_{ij}^{(\beta\gamma)} \\ \bar{\boldsymbol{\varepsilon}}_{ij} &= \frac{1}{V} \sum_{\beta,\gamma=1}^{2} v^{(\beta\gamma)}\, \bar{\boldsymbol{\varepsilon}}_{ij}^{(\beta\gamma)} \quad . \end{aligned} \tag{7.27}$$

In equation (7.27), V is the volume of the RVE and $v^{(\beta\gamma)}$ the volume of the element $(\beta\gamma)$. The averaged strains in each element can be calculated with equations (7.22) and (7.23). Continuity conditions at the interfaces of the elements have to be used in conjunction with equilibrium conditions to fully describe the RVE. For linear elastic analysis, the traction continuity is given with

$$\begin{aligned} \bar{\sigma}_{2i}^{(\beta 1)} &= \bar{\sigma}_{2i}^{(\beta 2)} \\ \bar{\sigma}_{3i}^{(1\gamma)} &= \bar{\sigma}_{3i}^{(2\gamma)} \quad , \end{aligned} \tag{7.28}$$

and displacements continuities defined with

$$\begin{aligned} u_i^{(\beta 1)}\big|_{\bar{x}_2=\frac{h1}{2}} &= u_i^{(\beta 2)}\big|_{\bar{x}_2=-\frac{h2}{2}} \\ u_i^{(1\gamma)}\big|_{\bar{x}_3=-\frac{h1}{2}} &= u_i^{(2\gamma)}\big|_{\bar{x}_3=\frac{h1}{2}} \quad . \end{aligned} \tag{7.29}$$

A further derivation of the MOC's theory is consciously renounced. Instead, the introduced model is enhanced and the model is directly derived within the finite element formulation in the next section.

7.3.2 Enhanced Method of Cells (EMOC) and Finite Element Formulation

The MOC introduced in section 7.3.1 is extended to a third periodic $\mathbf{x}_1$-direction and enhanced with interface elements between adjacent elements, according to figure 7.3. The idea of enhancing the MOC with interface elements is introduced in [55]. The interface elements are used to capture damage process within the RVE. The damage modes in particular are given in table (7.1). With this idea, and contrary to the displacement conditions introduced in 7.3.1, relative displacements

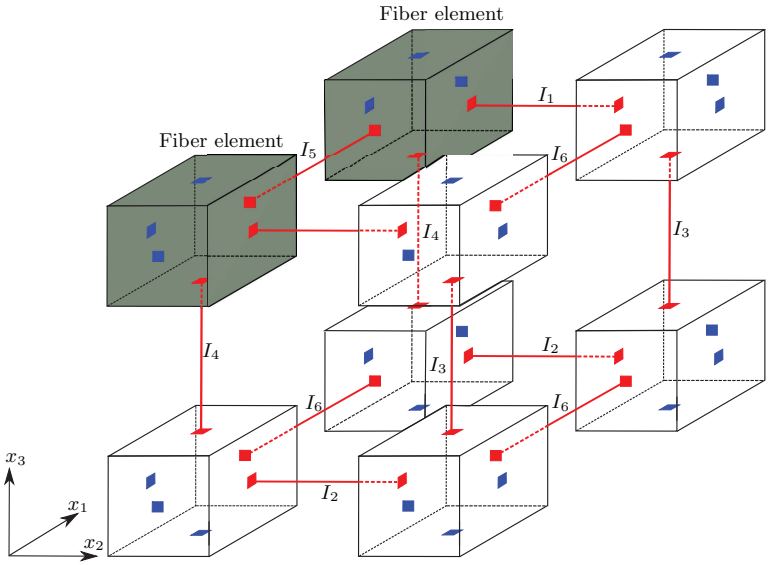

Figure 7.3: Schematic depiction of the EMOC: inner nodes (red), boundary nodes (blue), interface elements (red).

between adjacent elements are permitted. The consideration of nonlinear (damage) behavior of the RVE is solely described through the interface elements which allow the eight introduced subcell elements to remain linearly elastic. Consequently, the assumptions of constant strains $\bar{\boldsymbol{\varepsilon}}^{\beta\gamma}$ and stresses $\bar{\boldsymbol{\sigma}}^{\beta\gamma}$ within these eight elements remains valid. The EMOC is established as a nonlinear finite element routine for use within a finite element routine (multiscale). The EMOC routine is hard coded into the material law of a three-dimensional, eight-noded continuum element, introduced in chapter 5. As discussed, in multiscale analysis, this local RVE routine is called for each integration point of the global system. The local system expression is more general and, during this study, often used instead of the RVE expression. One single element is selected as a reference element, valid for all, on which the finite element description is performed, see figure 7.4, interface elements are discussed separately.

Boundary Conditions of the RVE

In figures 7.3 and 7.4, nodes marked in blue correspond to those that have displacement boundary conditions u_x, u_y, u_z from the global system, whereas red nodes are inner nodes. Inner displacements are obtained from an iteration procedure, using the converged displacements from the previous time step as a starting point. Within the theory of small strains ($\mathbf{E} = \boldsymbol{\varepsilon}$) and by using relation (7.23), the relation between the global strains $\bar{\boldsymbol{\varepsilon}}$ and the local boundary displacements

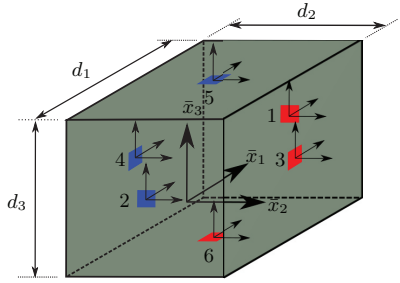

Figure 7.4: Schematic depiction of the EMOC reference element.

$\mathbf{u}$ can be directly written as

$$\begin{bmatrix} u_x \\ u_y \\ u_z \end{bmatrix} = \begin{bmatrix} x & 0 & 0 & \frac{1}{2}y & \frac{1}{2}z & 0 \\ 0 & y & 0 & \frac{1}{2}x & 0 & \frac{1}{2}z \\ 0 & 0 & z & 0 & \frac{1}{2}x & \frac{1}{2}y \end{bmatrix} \begin{bmatrix} \bar{\varepsilon}_{11} \\ \bar{\varepsilon}_{22} \\ \bar{\varepsilon}_{33} \\ 2\bar{\varepsilon}_{12} \\ 2\bar{\varepsilon}_{13} \\ 2\bar{\varepsilon}_{23} \end{bmatrix} \quad . \tag{7.30}$$

Equation (7.30) can be rewritten in a more general form:

$$\mathbf{u}_I = \mathbf{A}_I(x, y, z)\,\bar{\boldsymbol{\varepsilon}} \quad . \tag{7.31}$$

Here, I denotes the integration point of the global element e. The sum of all submatrices $\mathbf{A}_I$ then describes the matrix $\mathbf{A}_e$ introduced in equation (7.11)

$$\mathbf{A}_e = \begin{bmatrix} \delta_1 \mathbf{A}_1 \\ \vdots \\ \delta_I \mathbf{A}_I \\ \vdots \\ \delta_{nel} \mathbf{A}_{nel} \end{bmatrix} \quad \text{with} \quad \delta_I = \begin{cases} 1 & \text{if node } I \text{ has fixed DOFs} \\ 0 & \text{else} \end{cases} \quad , \tag{7.32}$$

where $nel = 6$ describes the number of nodes per local element in the local discretization.

Due to rigid body motions of the RVE, additional boundary conditions must be applied on specific inner nodes. The rigid body motions can be identified through its eigenvectors. The

constraint nodes can be chosen in such a way that the displacements of the inner nodes in one arbitrary direction are completely free. The free direction is chosen problem dependent, but the error of the additionally introduced boundary conditions of the other directions is small. The rigid body motions result from the simple structure of the RVE. Due to this limitation, the elements are restricted for use with linear elastic material behavior.

Formulation of the EMOC Reference Element

A six-noded, three dimensional element is chosen for the finite element formulation of one subcell element of the RVE. The nodes are placed in the center of the faces of the element, as illustrated in figure 7.4. Each node has three degrees of freedom (u_x, u_y, u_z) and a local coordinate system (x_1, x_2, x_3) in the center of the element. The relative dimension of the element is denoted with (d_1, d_2, d_3) and is dependent of the fiber-matrix ratio. Since homogenized (averaged) quantities are calculated, the absolute size of the RVE is irrelevant.

Using (7.23), and considering that the strains within the elements are constant, they can directly be calculated from the node displacements:

$$\begin{aligned}
\varepsilon_{11} &= \frac{(u_1^{(1)} - u_1^{(2)})}{d_1} \\
\varepsilon_{22} &= \frac{(u_2^{(3)} - u_2^{(4)})}{d_2} \\
\varepsilon_{33} &= \frac{(u_3^{(5)} - u_3^{(6)})}{d_3} \\
2\varepsilon_{12} &= \frac{(u_2^{(1)} - u_2^{(2)})}{d_1} + \frac{(u_1^{(3)} - u_1^{(4)})}{d_2} \\
2\varepsilon_{12} &= \frac{(u_3^{(1)} - u_3^{(2)})}{d_1} + \frac{(u_1^{(5)} - u_1^{(6)})}{d_3} \\
2\varepsilon_{12} &= \frac{(u_3^{(3)} - u_3^{(4)})}{d_2} + \frac{(u_2^{(5)} - u_2^{(6)})}{d_3} \quad .
\end{aligned} \tag{7.33}$$

Here, $u_j^{(i)}$ denotes the j^{th} degree of freedom of node i. For finite element implementation, equation (7.33) is rewritten as

$$\boldsymbol{\varepsilon} = \mathbf{B}\,\mathbf{u} \quad , \tag{7.34}$$

where $\boldsymbol{\varepsilon}$ and $\mathbf{u}$ are involved in the following order:

$$\begin{aligned}
\boldsymbol{\varepsilon} &= \{\varepsilon_{11}, \varepsilon_{22}, \varepsilon_{33}, \varepsilon_{12}, \varepsilon_{13}, \varepsilon_{23}\} \quad , \\
\mathbf{u} &= \{u_1^{(1)}, u_2^{(1)}, u_3^{(1)}, u_1^{(2)}, ..., u_1^{(6)}, u_2^{(6)}, u_3^{(6)}\} \quad .
\end{aligned} \tag{7.35}$$

From equations (7.33) and (7.34) the $\mathbf{B}$-matrix can be constructed in dependency on the element dimensions d_i. This matrix is explicitly described in [55] and not presented at this point. The $\mathbf{B}$-matrix is constant in each element. The local element stiffness matrix $\mathbf{k}_e^L$ and local element

residual vector $\hat{\mathbf{f}}_e^L$ of the elements can then be calculated with $\mathbf{B}$ as

$$\begin{aligned} \mathbf{k}_e^L &= (d_1\, d_2\, d_3)\, \mathbf{B}^T\, \mathbb{C}\, \mathbf{B} \quad , \\ \hat{\mathbf{f}}_e^L &= (d_1\, d_2\, d_3)\, \mathbf{B}^T\, \boldsymbol{\sigma} \quad , \end{aligned} \tag{7.36}$$

where e is the number of (micro) subcell elements and runs from 1-8.

Formulation of the Interface Element

The interface elements are used to model damage in the composite structure. Each interface element is connected through two adjacent inner nodes and each node features three degrees of freedom. All damage modes are defined by means of the universal binding energy relation introduced in section 3.6. The relative displacement between these nodes corresponds to the displacement u_i in equation (3.64). For each interface element, the components of the displacements $\mathbf{u}$ can be assigned to one normal (u_n) and two tangential directions (u_{t1}, u_{t2}). For a general description of the effective opening vector, a reformulation of equation (3.64) must be completed:

$$\delta = \sqrt{\gamma\; u_n^2 + \beta^2\,(u_{t1}^2 + u_{t2}^2)} \quad , \tag{7.37}$$

Here, β is a parameter that assigns different weights of the normal and tangential displacements, whereas γ depends on the actual damage mode.

According to figure 7.3, a distinction between three different major types of damage is performed:

- Fiber-fiber damage (FF)
- matrix-matrix damage (IFF)
- fiber-matrix damage (debonding) .

The entry parameters for the atomistic separation law, section 3.6, differ in each damage mode in terms of displacements $\delta(\mathbf{u})$, material strengths R, and critical displacement δ_c or critical fracture energy G_c. The major damage modes can be further subdivided into tension and compression cases and finally assigned, as shown in table 7.1: The strength force R and the fracture energy G are calculated by using the relative element dimensions d_i and the area of fracture A_i. The local element stiffness matrix $\mathbf{k}_e^L$ and the local element residual vector $\hat{\mathbf{f}}_e^L$ of the interface elements can be directly obtained either by the first and second derivative of ϕ or, when using the IMPL-EX scheme on the separation law, with

$$\begin{aligned} \mathbf{k}_e^L &= (1 - D_e)\mathbb{C}_e^0 \\ \mathbf{f}_e^L &= \mathbf{k}_e^L\, \mathbf{u}_e \quad . \end{aligned} \tag{7.38}$$

Here, e is the number of interface elements running from 1-12, D_e is the damage parameter defined in equation (3.70) and $\mathbb{C}_e^0$ s the undamaged corresponding stiffness matrix according to

Table 7.1: Overview of parameters required in the interface elements.

Damage Mode	Case	γ	Strength [N]	Energy [Nm]	Interface Nr.
Debonding	$u_n > 0$	1	$\mathrm{R^D}$	$\mathrm{G_D}$	I_1, I_4
	$u_n < 0$	0	$\mathrm{R^D}$	$\mathrm{G_D}$	I_1, I_4
FF	$u_n > 0$	1	$\mathrm{X^t}$	$\mathrm{G_{l+}}$	I_5
	$u_n < 0$	1	$\mathrm{X^c}$	$\mathrm{G_{l-}}$	I_5
IFF	$u_n > 0$	1	$\mathrm{Y^t}$	$\mathrm{G_{t+}}$	I_2, I_3, I_6
	$u_n < 0$	1	$\mathrm{Y^c}$	$\mathrm{G_{t-}}$	I_2, I_3, I_6

section 3.6. The implex scheme, defined in equation (4.16), is used with the opening displacements, equation (7.37), acting as the inner variable $\hat{r}_{n+1}$.

Assembly of Local Stiffness Matrix and Residual Vector

With the previous definitions, the assembled local stiffness matrix $\mathbf{K}_i^L$ of global integration point i and the corresponding local residual vector $\mathbf{F}_i^L$, needed in equation (7.7), can be assembled using the subcell element and the interface stiffness matrices $\mathbf{k}_e^L$ and $\mathbf{k}_e^L$. The previously defined stiffness matrices replace the matrix defined in equation (7.10) and the procedure shown in section 7.1 can be used from equation (7.11) on. With this definitions, the EMOC is fully described within a finite element formulation.

Chapter 8

Numerical Examples - Multiscale Model

In this section, the developed and implemented EMOC routine is validated with published test data. First, the routine is verified elastically and compared to results from the original MOC and the two-dimensional finite element implementation of the MOC presented in [55]. Second, the damage behavior of fiber-reinforced composites is investigated using the coupled multiscale approach introduced in chapter 7.

8.1 Linear Elastic Verification

For the elastic tests, the relative displacements between the adjacent cells, described by means of the interface elements, are numerically locked. For this purpose, a linear spring relation is used instead of the separation law, leading to a reformulation of equation (7.38) according to:

$$\mathbf{k}^j = \begin{bmatrix} k & 0 & 0 & -k & 0 & 0 \\ 0 & k & 0 & 0 & -k & 0 \\ 0 & 0 & k & 0 & 0 & -k \\ -k & 0 & 0 & k & 0 & 0 \\ 0 & -k & 0 & 0 & k & 0 \\ 0 & 0 & -k & 0 & 0 & k \end{bmatrix} . \tag{8.1}$$

By choosing a high value for k, set to $k = 5 \cdot 10^8$ GPa, the elements are numerical constrained to one another. The testing was performed on different material data sets. In the next section, the examples calculated in [55] are examined and the results are compared.

An eigenvalue analysis was used to identify eigenvalues and eigenvectors. Additional boundary conditions were found to be necessary to eliminate zero-energy modes of the EMOC. First, isotropic material behavior for the matrix, as well as the fiber cell, were applied.

Table 8.1: Micromechanical elastic properties for isotropic fiber and isotropic matrix in [GPa].

	E	G	ν[-]
Fiber	1000	416.67	0.2
Matrix	100	38.46	0.3

Table 8.2: Micromechanical elastic properties for transversely isotropic fiber and isotropic matrix in [GPa].

	E_{11}	E_{22}=E_{33}	G_{12}=G_{13}	G_{23}	$\nu_{12} = \nu_{13}$ [-]	ν_{23} [-]
Fiber	1000	500	300	200	0.20	0.25
Matrix	100	100	38.46	38.46	0.3	0.3

8.1.1 EMOC Compared to Analytical MOC

In this section, the elastic response of two different microscopic material set properties are verified with results given in [55]. The goal is to validate the developed EMOC with analytical results of the MOC. Thus, the tests aim to verify the enhancement of the three dimensional state and the implementation, but not the underlying theory itself. The theory supporting the EMOC is tested in the next section. In the first material set, both constituents, fiber and matrix, are assumed to be isotropic. The corresponding material data is given in table 8.1.

The second material set is assumed to be isotropic for the matrix and transversely isotropic for the fiber constituent, as shown in table 8.2. In both cases the spring-stiffness is set to $K = 5 \cdot 10^8$ GPa and the composites are composed of a fiber matrix ratio of $\eta = 0.5$. The effective stiffness matrix in a linear elastic calculation is directly obtained from the homogenization procedure. Because the material behavior is positionally and load state independent, it can be detached in any arbitrary integration point of the calculation. The results of the two homogenized effective material matrices $\mathbb{C}$ are summarized in tables 8.3 and 8.4. In both tables, the entries in the left column refer to results from an analytic calculation of the MOC, published in [55], whereas the entries in the right column are the results from the finite element calculation of the EMOC. In the first case, with isotropic fibers, a perfect agreement of the analytical and the numerical values can be seen. In the second case, with transversely isotropic fiber material, the results are also excellent, even though a small deviation can be seen between the analytical and numerical model. It should be noted that the effective material behavior is orthotropic and not transversely isotropic, otherwise the shear value would match the value given in equation (2.136).

Having verified the numerical implementation of the EMOC by contrasting it against analyt-

Table 8.3: Numerically obtained effective stiffness matrix for isotropic fiber material in [GPa].

	Method of Cells			Enhanced Method of Cells		
Effective Stiffness Matrix	594.38	90.30	90.30	594.38	90.30	90.30
	90.30	286.14	83.45	90.30	286.14	83.45
	90.30	83.45	286.14	90.30	83.45	286.14
Shear Modulus G_{12}.	87.20			87.20		
Shear Modulus G_{13}	87.20			87.20		
Shear Modulus G_{23}	70.42			70.42		

Table 8.4: Numerically obtained effective stiffness matrix for transversely isotropic fiber material in [GPa].

	Method of Cells			Enhanced Method of Cells		
Effective Stiffness Matrix	588.67	78.32	78.32	588.74	78.10	78.10
	78.32	241.58	77.69	78.10	241.44	79.21
	78.32	77.69	241.58	78.10	79.21	241.44
Shear Modulus G_{12}	82.17			82.17		
Shear Modulus G_{13}	82.17			82.17		
Shear Modulus G_{23}	64.52			64.51		

ical solutions, the next section aims to verify the numerical homogenization procedure with experimental test data.

8.1.2 EMOC Compared to WWFE and Unit Cell Methods

In a second step, the theory itself is tested against experimental data from the WWFE, published in [69] and [51]. Linear elastic material behavior is assumed and the relative displacements are numerically locked by applying a linear three dimensional spring law with a high stiffness coefficient ($K = 5 \cdot 10^8$ GPa) according to equation (8.1). Under investigation is a UD-composite made of epoxy resin RIM 135 with a fiber matrix ratio of $\eta = 0.6$, as given in [51]. The numerical results of the EMOC are compared to experimental results from the WWFE in table 8.6 and to results from coupled virtual tests methods with square and hexagonal unit cells, both given in [51]. The isotropic fiber and matrix input parameters are summarized in table 8.5. Because a linear elastic material behavior is assumed, the material matrix $\mathbb{C}$ can be directly obtained from the homogenization procedure. For the purpose of calculating the elastic properties of the homogenized material, the compliance matrix $\mathbb{S}$ is needed. It can be calculated by inverting $\mathbb{C}$,

Table 8.5: Elastic micromechanical properties for isotropic fiber and isotropic matrix in [N/mm^2].

	E	G	ν[-]
Fiber	74000	30800	0.2
Matrix	3350	1240	0.35

Table 8.6: Comparison of homogenized elastic properties in [N/mm^2].

	E_{11}	E_{22}=E_{33}	G_{12}=G_{13}	G_{23}	$\nu_{12} = \nu_{13}$ [-]	ν_{23} [-]
WWFE	45600	16200	5830	-	0.278	0.400
EMOC	45564	14078	4021	2923	0.252	0.272
Hex.	45700	11890	4270	4110	0.250	0.400
Square	45700	15060	4660	3300	0.250	0.262

yielding

$$\mathbb{S} = \begin{bmatrix} 2.1947 & -0.5536 & -0.5536 & 0 & 0 & 0 \\ -0.5536 & 7.1032 & -1.9341 & 0 & 0 & 0 \\ -0.5536 & -1.9341 & 7.1032 & 0 & 0 & 0 \\ 0 & 0 & 0 & 24.8680 & 0 & 0 \\ 0 & 0 & 0 & 0 & 24.8680 & 0 \\ 0 & 0 & 0 & 0 & 0 & 34.2126 \end{bmatrix} \cdot 10^{-5} \tag{8.2}$$

Using the relations in equation (2.130), the elastic properties of the homogenized material can easily be calculated from equation (8.2). The results are summarized in table 8.6: By comparing Poisson's ratio $\nu_{23} = 0.272$ from table 8.6 with the value for transversely isotropic materials $\nu_{23} = 1.408$ from equation (2.136), it is clear that an orthotropic and not a transversely isotropic material is present because in the latter case, both values would match. Table 8.6 shows that the Young's modulus E_{11} is in excellent agreement to the experiments and the other methods. However, E_{22} has a significant deviation but is still in an acceptable range, especially when compared to the hexagonal unit cell method. The same holds true for shear moduli G_{12} and G_{23}, and for the Poisson ratio ν_{12} and ν_{23}. Overall, the results of the EMOC are comparable to those obtained from the unit square method and are in relatively good agreement to experimental tests, particularly when allowing for the simplicity of the RVE of the EMOC.

Table 8.7: Single elastic constituent properties σ in [N/mm^2], δ in [%] and G_c in [N/mm].

	$Fiber_t$	$Fiber_c$	$Matrix_t$	$Matrix_c$	Shear	Debond
σ_c	2150	1450	69	120	55	40
δ_c	2.950	1.959	3.4	4.2	2.2	1.8
G_c	172.4	77.2	6.4	13.7	3.3	1.96

Having tested the elastic properties, the next section aims to verify the theory in nonlinear damage models.

8.2 Damage Investigations Using the EMOC Approach

In this section, the EMOC theory is tested and verified with experimental test data. First, plausibility tests on single damage modes are performed on a unit cube and the results compared to material data provided in [51]. Then, a specific composite is investigated and compared to other numerical and experimental data from the WWFE. Finally, the damage behavior of structures is discussed in greater detail, focusing on load displacement curves and damage evolution.

8.2.1 Isotropic Plausibility Tests

In this section, pure single damage modes are tested on a unit cube with displacement boundary conditions. An isotropic material is first simulated using quantities from concrete for fiber and matrix constituent input parameters. The critical strength σ_c, as well as the critical energy release rate G_c, are user input parameters necessary for the material routine. Using values given in section 6.1, namely $\sigma_c = 2.2$ N/mm^2 and $G_c = 0.085$ N/mm, the load displacement path must meet the maximum boundary force F= 2.2 N at critical displacement $u = 0.0145$ mm. Additionally, in the isotropic simulation, all curves from the damage modes investigated: tension and compression in $\mathbf{x}_1$-direction, tension in $\mathbf{x}_2$-direction, and tension in $\mathbf{x}_3$-direction must coincide, as shown in figure 8.1.

Second, the damage model is tested with the material data given in [51]. This material data has already been used in the elastic testing procedures in section 8.1. For the purpose of damage simulations, the elastic parameters from table 8.5 are used, in addition to the values summarized in table 8.6. The damage simulation of the single fiber and matrix constituents are compared to the values from [51] in terms of maximum stress and associated strain. The input parameters G_c are calculated, according to section 3.6, by $G_c = \delta_c \, e \, \sigma_c$, and summarized in table 8.7. The material parameters for debonding are chosen in a reasonable manner as they are not provided

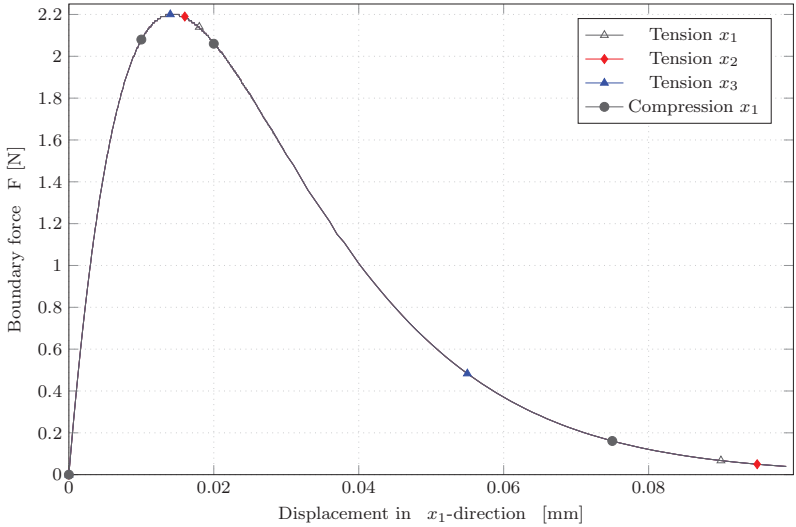

Figure 8.1: Simple damage modes of an isotropic concrete material.

in [51]. In contrast to the initial tests, isotropic material is applied for both fiber and matrix constituent. Of particular interest in this example is the proof that each damage mode matches the critical stress value σ_c at the associated critical strain value δ_c. Under investigation are the following damage modes:

- Fiber tension in $\mathbf{x}_1$-direction
- Fiber compression in in $\mathbf{x}_1$-direction
- Matrix tension in $\mathbf{x}_2$-direction
- Matrix compression $\mathbf{x}_2$-direction
- Shear in $\mathbf{x}_{12}$-direction
- Debonding in $\mathbf{x}_3$-direction

For the investigation of the single constituent damage modes matrix tension, matrix compression and shear, the debonding mode must be disabled. Otherwise, due to the lower strength value, this mode would become decisive. The impact of debonding during inter fiber failure is discussed in the composite example provided later in this section. In the following examples, the debonding mode in the $\mathbf{x}_2$-direction is exchanged with a matrix-matrix damage mode and the debonding mode in the $\mathbf{x}_3$-direction is disabled, when not stated otherwise. Before the resulting graphs of the different damage modes are discussed, one issue of the micro model is discussed. In figure

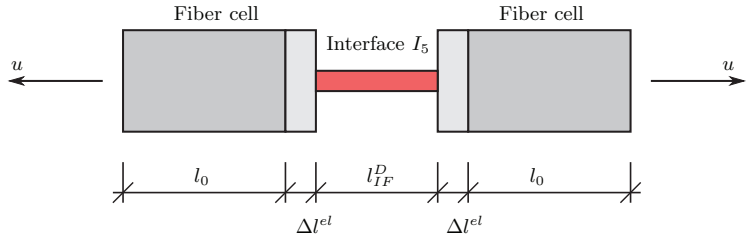

Figure 8.2: Depiction of strains in the micro model.

8.2 the fiber-fiber damage of the micro model is depicted. This figure shows that the overall strain in $\mathbf{x}_1$-direction is the sum of elastic strains in the cells ε^{el}, plus the strains allowed in the interface element ε_D^{IF}. Considering that the cells behave in a linear elastic manner and damage is described solely through the interface element, then the micro model indeed returns the correct damage stress σ_c, but not the correct corresponding strain value δ_c. To overcome this issue, the overall strains must be reassessed from the elastic cell strains.

Figure 8.3 illustrates the resulting load displacement curves from the single damage calculations of unit cubes. The blue graphs correspond to results including the discussed elastic micro strains, whereas black graphs correspond to results where the elastic strains have been rectified.

In the following, the rectified results are discussed in greater detail. The single fiber constituent failure is simulated using a fiber-matrix ratio of $\eta = 99.9\%$, and damage is solely admitted in the interface elements. The resulting graph is smooth exponential function with a maximum stress state of $\sigma_c^{ft} = 2147.9$ N/mm^2 at the associated strain state $\varepsilon_c^{ft} = 0.0296$. By comparing the results with the input parameters, summarized in table 8.7, an almost perfect coincidence can be seen. The same is observed in the graphs of fiber $\sigma_c^{fc} = 1448.6$ N/mm^2 at $\varepsilon_c^{ft} = 0.0194$, matrix tension $\sigma_c^{mt} = 68.99$ N/mm^2 at $\varepsilon_c^{mt} = 0.0176$, and matrix compression $\sigma_c^{mt} = 120.0$ N/mm^2 at $\varepsilon_c^{mt} = 0.0417$. The final, remaining tests are debonding and shear damage. The debonding mode is activated and a displacement controlled simulation in the x_3-direction is performed. The maximum stress state is perfectly matched, $\sigma_c^{mc} = 40.0$ N/mm^2, and the associated strain value is slightly higher, with $\varepsilon_c^{mc} = 0.018$, but without relevance for numerical simulations. The same holds true for the shear damage values $\sigma_c^{mc} = 55.0$ N/mm^2 and $\varepsilon_c^{mc} = 0.0223$.

By comparing the two resulting graphs of the rectified and non-rectified strain states, given in figure 8.3, it can be seen that the deviation of strains in fiber damage cases are significant and have maximum values at the maximum stress states. From there on, due to the increasing loss of stiffness in the interface element, the deviation of both results decreases until both paths coincide, as illustrated in figure 8.6. This behavior can be explained by comparing the relative stiffness of micro cells during the damage process. At the beginning of the calculation, the interface element stiffness is higher than the stiffness of the elastic cells. Thus, the deformation

in the micro model is mainly described by the elastic cells. In contrast, when damage has progressed further, the interface stiffness has a lower stiffness than the elastic parts and the deformation is mainly described by the interface element.

In bearing load calculations of structures, the maximum stress state is the most important value and the corresponding strain deviation can be accepted, especially when considering that strains values match each other in a more progressed damage state. Otherwise, as shown earlier, the strains must be rectified in the micromodel. Additionally, the effect of over predicted strains reduces in damage simulations of more complex structures.

The preceding simulations were performed to verify the implemented model with the parameters presented in [51]. Input parameters are the maximum stress state σ_c and the fracture energy, dependent on the failure strain ε_c. All single constituent damage modes have been shown to return the correct maximum stress at the associated strain value. The actual paths of the load displacement curves in figure 8.3 are discussed in greater detail later in this chapter. In the next section, a composite layup is investigated in terms of homogenized effective quantities.

8.2.2 Composite Strength Parameter Test

In this section, the numerical results of a composite using the EMOC are compared to experimental results from the WWFE and to results from a virtual unique square method, given in [51]. The material input parameters are the same as in the previous sections, summarized in tables 8.5 and 8.7. The composite is composed of a fiber-matrix ratio of $\eta = 0.6$ and the tests are simulated on a unique square model with displacement boundary conditions. Since the debonding failure mode affects the matrix-matrix and shear modes, reasonable values were chosen. According to explanations provided by the previous section, the critical fracture energy G_c can be calculated from the critical failure stress σ_c and the critical associated failure strain ε_c. With the values from the WWFE, given in [51], the following values were adjusted. The matrix damage modes are performed by applying displacement boundary conditions in $\mathbf{x}_2$-direction. The related stress and energy release rates for debonding are set to $\sigma_c = 55$ N/mm^2 and $G_c = 0,3438$ N/mm in matrix tension mode IFF1, and $\sigma_c = 165$ N/mm^2 and $G_c = 5.38$ N/mm in matrix compression mode IFF2. The load displacement graphs of the simulations are given in figure 8.5.

The corresponding maximum stress and strain values are summarized and compared to experimental and analytical data, as shown in table 8.8. By observing the results, a good agreement in fiber tension mode FF1, and an acceptable agreement in fiber compression mode FF2 in terms of σ_c and ε_c, can be seen. The inter fiber modes IFF1 and IFF2 are also in good agreement to the experimental data from the WWFE, and much better than those from the virtual square method. The shear damage mode IFF3 shows a clear deviation to the WWFE but is still closer than the virtual square method. This has also been observed within the elastic tests of the previous section, where the shear values were not in such a good agreement as the other values.

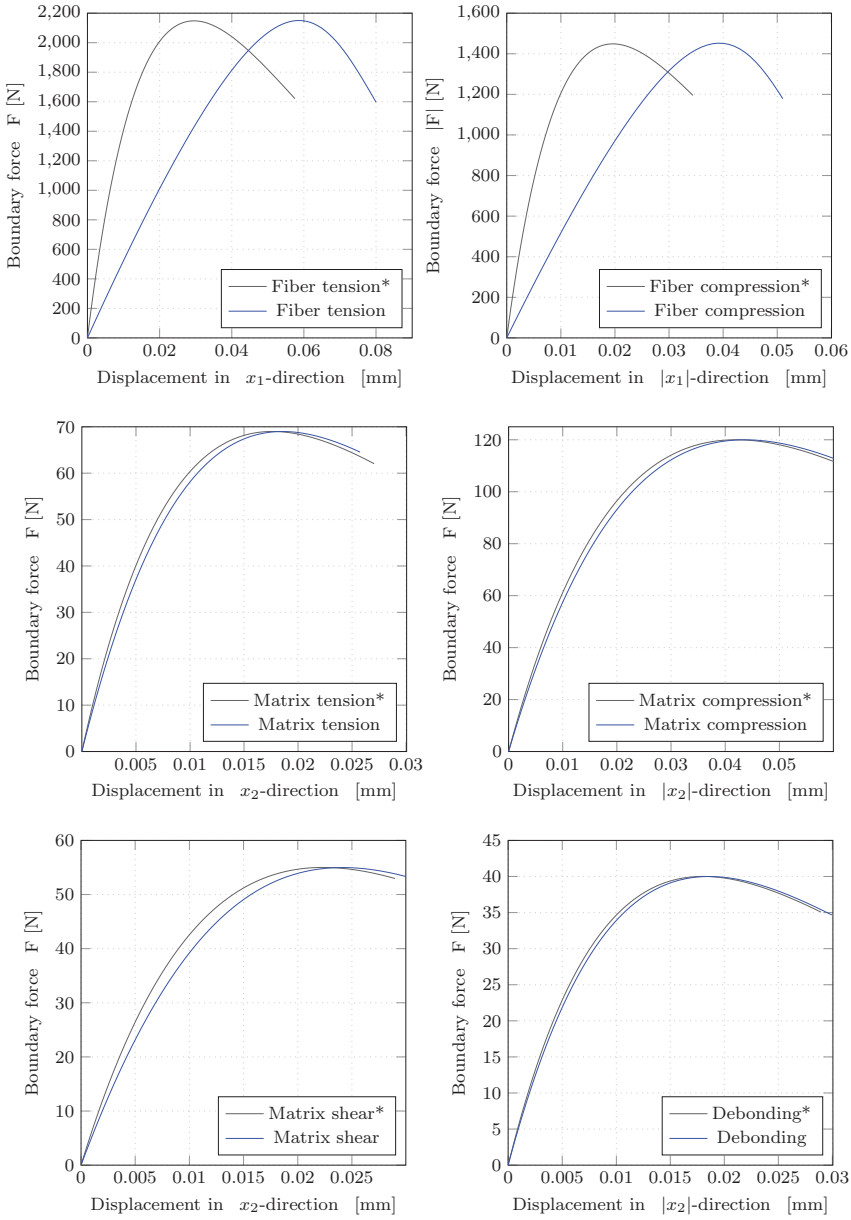

Figure 8.3: Pure single damage modes of constituents: fiber tension (upper left), fiber compression (upper right), matrix tension (middle left), matrix compression (middle right), matrix shear (bottom left), debonding (bottom right).

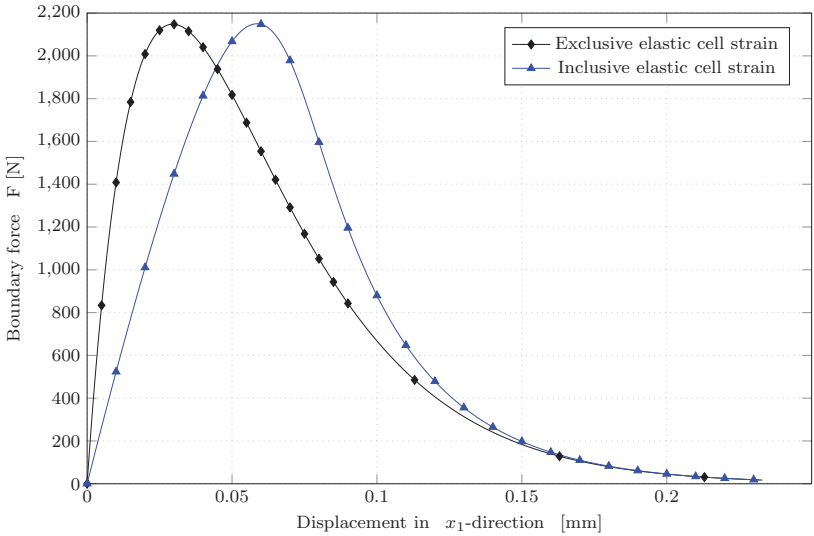

Figure 8.4: Exponential cohesive law vs. linear-exponential cohesive law.

Table 8.8: Composite strength parameters - σ in [N/mm^2] and ε in [%].

Source		FF1	FF2	IFF1	IFF2	IFF3
EMOC	σ_c	1317	908	45.3	144	58.9
	ε_c	2.930	2.000	0.246	1.300	2.920
WWFE	σ_c	1280	800	45.0	145	73
	ε_c	2.807	1.750	0.250	1.200	4.000
Square	σ_c	1308	870	38.3	149.5	51.7
	ε_c	2.905	1.960	0.300	1.050	3.420

It is clear that in IFF1 mode, the maximum stress value is governed by debonding since the composite stiffness is lower than the single constituent stiffness of the used epoxy material.

A side effect of using the cohesive law with rectified strains, discussed in the previous section, is that the initial stiffness in damage simulations becomes higher than the effective elastic stiffness in section 8.1. This is due to the fact that the maximum stress is enforced by an exponential function to its associated strain value. An over prediction of the initial stiffness is a result of the theory and present from the beginning of the calculation. But, the implemented model is optimized in terms of numerical robustness and to return the correct maximum stress state

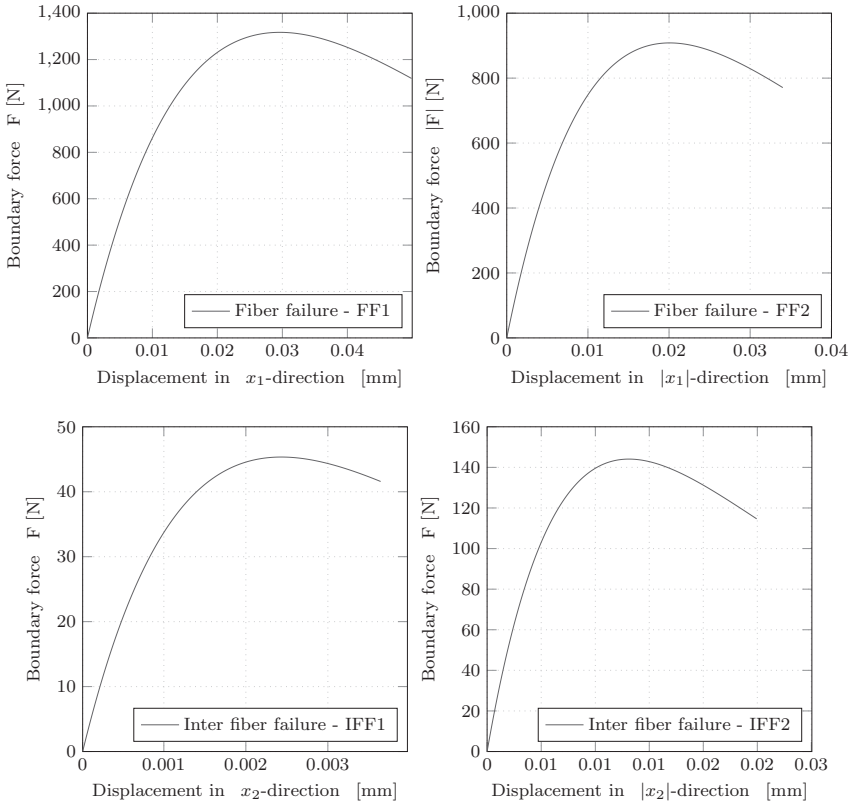

Figure 8.5: Pure single damage modes of constituents: fiber tension (upper left), fiber compression (upper right), matrix tension (bottom left), matrix compression (bottom right).

at associated strain state. For the calculation of maximum bearing loads, the initial regime is not on interest. If the correct elastic values are of interest, the elastic model can be used. Additionally, there is a simple alternative to acquire the correct elastic stress-strain values in the beginning of the simulation. By simply adding an elastic regime in the material law, where the stiffness is constant and the damage parameter is $d = 0$, as long as its critical strain state ε_c is reached, a correct stiffness is returned as long as damage is absence. This is shown in figure 8.6, where a comparison of the standard rectified exponential damage law and a linear-exponential damage law are shown for the fiber damage mode FF1. Using the linear-exponential damage law, the correct stress-strain state is returned up to the critical strain value. Then, it follows the same path as the exponential cohesive law, which results in a slight miscalculation of the fracture energy. But, this model is not as robust as the exponential model because of the kink

where it switches from the elastic to the damage regime, and is therefore not further discussed in the current study. Again, this cohesive material degradation law is implemented because of its numerical robustness and optimized for calculations of maximum bearing loads of structures.

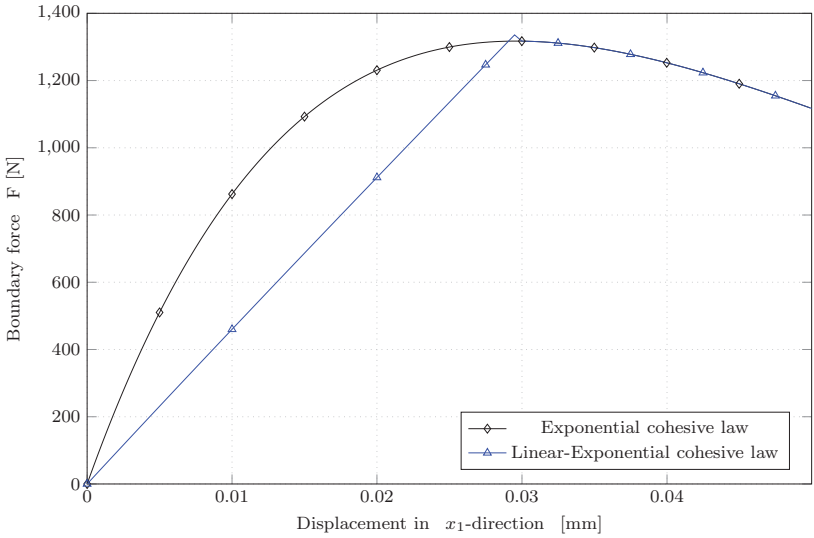

Figure 8.6: Exponential cohesive law vs. linear-exponential cohesive law.

8.2.3 Independency of Mesh Geometry

This example shows an immense advantage of using the coupled multiscale approach instead of a macroscopic approach for damage simulations. A unit cube with displacement boundary conditions is investigated using the concrete material previously discussed. Three different discretization of the cube are calculated. The left picture in figure 8.7 shows the results of the EMOC approach, whereas the right picture shows the results using the isotropic damage law, discussed in section 4.1. This example is cautiously chosen because of its homogeneous stress state because, in that case, a damage localization is debarred. The graphs on the right in figure 8.7 show that the isotropic damage model does not show any convergence. The calculated dissipated energy is wrong and the results depend highly on the discretization of the cube. However, not only the element size influences the qualities of the results, but also the shape of the elements, due to the simple approach for the characteristic element length as the cubic root of the Gauss point volume, discussed in section 4.1. On the other hand, the multiscale model is completely independent of the mesh size, explained by the fixed element size of the micro model. In this case, the crack area is independent of the size and shape from the global

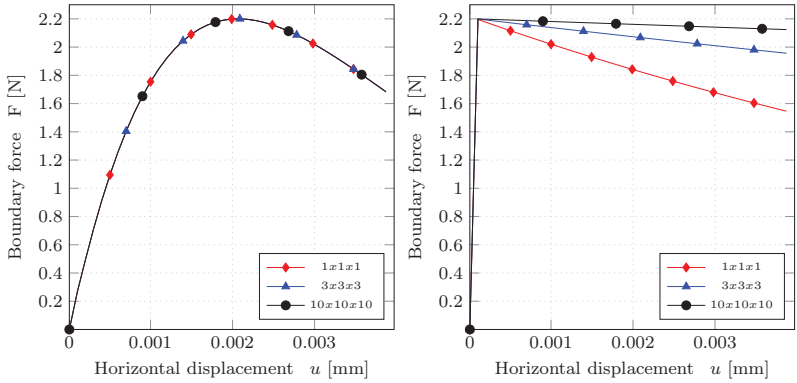

Figure 8.7: Net convergence test using the multiscale approach (left) and the macrospic approach (right).

elements, ensuring a correct calculation of the dissipated energy.

8.2.4 Delamination

In this section, the delamination damage mode is verified through a comparison with results obtained from an existing cohesive law model. Therefore, a unit cube is modeled twice, once as a homogeneous cube using the EMOC routine, and once with two elastic parts and a centered, thin cohesive zone, illustrated in figure 8.8. Choosing the same, very stiff value for the elastic parts in both models ensures that the deformation is described solely through the interface element. The applied cohesive zone model is presented in [61] and uses the same atomistic binding energy as the EMOC as introduced in equation (3.62). The cohesive zone model had already been implemented in the finite element software Feap and has been exhaustively validated with experimental test data. The critical energy release rate for debonding or delamination modes has to be thoughtfully chosen. A valuable overview of how to predict such values is given in[129]. The input parameters of the model are summarized in table 8.7.

The results of the calculations are shown by figure 8.9. The perfect coincidence of both theories can be seen, yet another proof of the implemented EMOC theory. Sections 8.2.5 and 8.2.6 revisit delamination modes and investigate the evolution of the delamination damage variable in greater detail.

8.2.5 Damage Investigation of a Tension Rod

In this section, a tension rod example is investigated in greater detail with a focus on damage evolution and load displacement behavior. The geometry of the rod is given in 6.1. The elastic,

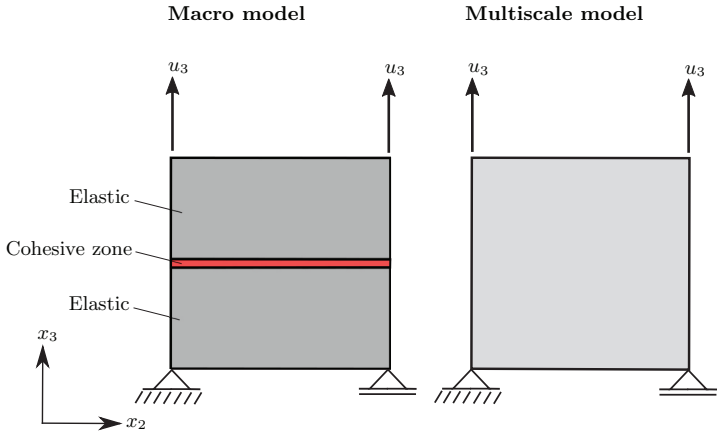

Figure 8.8: Cross section of the investigated debonding models.

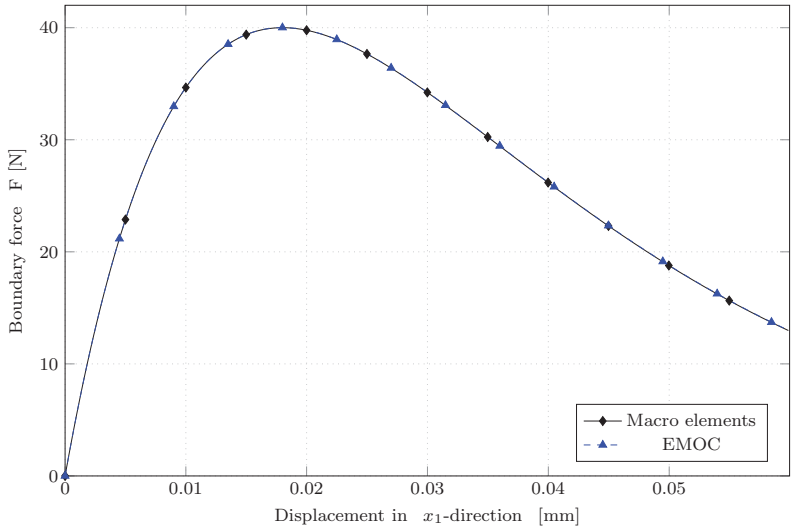

Figure 8.9: Delamination modeled with cohesive macro and EMOC multiscale elements.

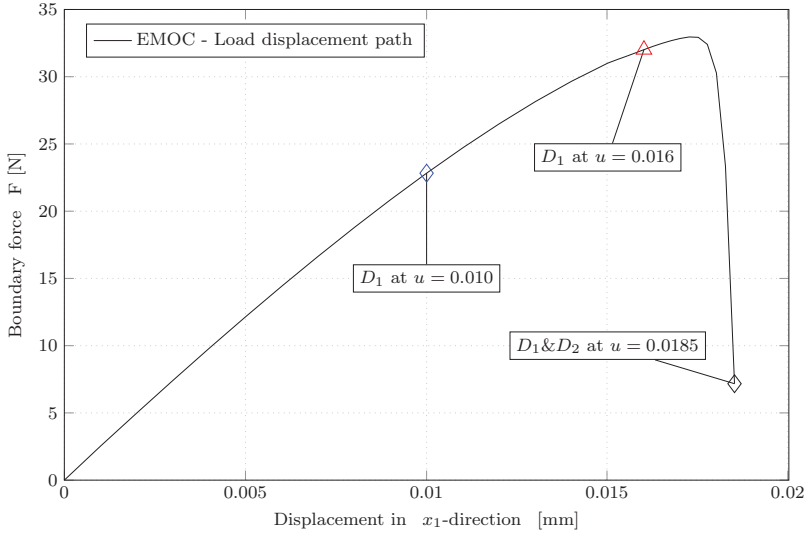

Figure 8.10: Load displacement path of the tension rod example using the multiscale approach.

micromechanical material data is summarized in 8.5 and used together with damage properties shown in table 8.7. The calculation is displacement driven and symmetry conditions are utilized such that a one-eighth model with a discretization of 20x2x2 elements is investigated.

The load displacement path of the tension rod example is illustrated in figure 8.10. The horizontal displacement corresponds to any node on the right edge and the plotted boundary force is the sum over all nodes facing the left edge. The load displacement path shows a behavior similar to that of the macroscopic anisotropic damage model depicted in figure 6.15. However, unlike that model, here, damage is present from the beginning of the calculation, a result of the cohesive law that was used. In figure 8.10, three points are marked at positions $u = 0.01$ mm, $u = 0.016$ mm and $u = 0.0185$ mm, where the damage variable D_1, representing fiber damage, is investigated in greater detail. Additionally, at the last position of the load displacement path, the damage variable D_{2-1}, representing matrix damage in the x_1-direction, is depicted.

The first picture in figure 8.11 at $u = 0.01$ mm shows that fiber damage begins in the upper corner where the cross section is tapered. At this point, a damage value of $D_1 = 0.35$ is observed. In the second picture, at position $u = 0.016$ mm, the damage variable already has a value of $D_1 = 0.605$, but is still concentrated at the tapered edge. After passing this point, damage grows exponentially and the maximum bearable load is reached at $F \approx 33$ N. From this maximum point, damage distributes over the entire cross section and the bearable load sharply falls. At the same position, the matrix damage in the $\mathbf{x}_1$ direction has also grown to full damage

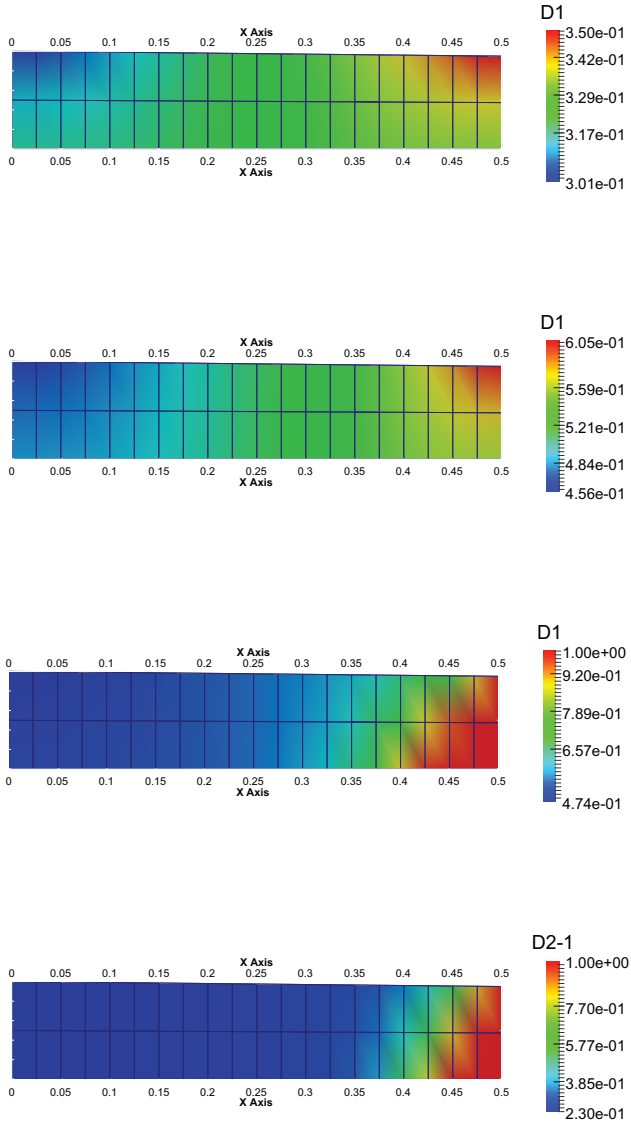

Figure 8.11: Tension rod example - top to bottom: Damage variable D_1 at $u = 0.01$ mm, damage variable D_1 at $u = 0.016$ mm , damage variable D_1 and damage variable D_{2-1} at $u = 0.0185$ mm.

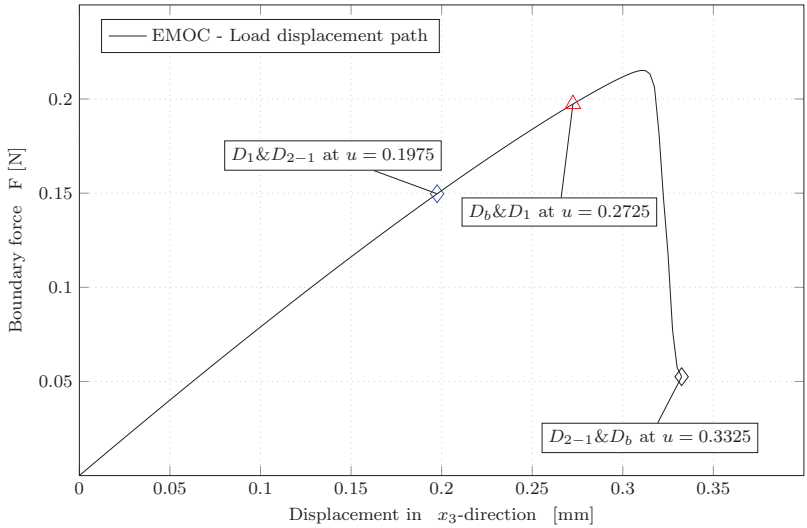

Figure 8.12: Load displacement path of a cantilever beam using the EMOC multiscale approach.

$D_2 = 1.0$. Both can be seen in the two lower pictures of figure 8.11.

8.2.6 Damage Investigation of a Cantilever Beam

The current example details damage evolution in a cantilever beam. The geometry is described in chapter 6 and depicted in figure 6.19. The beam is clamped on its left side and displacement boundary conditions are applied on the bottom right edge in a vertical direction. The material parameters from table 8.5 and 8.7 are used for the simulation. Figure 8.12 depicts the load displacement path of the simulation. As in the previous examples, specific points of interest are marked where the damage state is notable. The load displacement path shows a similar behavior to that of the macroscopic damage model, depicted in figure 6.20, from the beginning of the calculation until the maximum bearable load is reached. For the first marked point of the graph in figure 8.12, at position $u = 0.1975$ mm, the matrix damage initiation D_{2-1} in x_1-direction is plotted in the upper left picture of figure 8.13. This is meaningful behavior because the area of the upper cross section stands, due to its loading, under tension stress; and the tension strength value of the matrix is lower than the compression strength value. The second position marked is at a displacement value of $u = 0.2725$ mm. At this point, fiber damage D_1 and debonding damage D_b are depicted in the upper right and middle left pictures of figure 8.13, respectively. Considering the lower fiber strength, fiber damage must first occur at the bottom edge of the cross section, which it does. Interestingly, at this position, the debonding variable

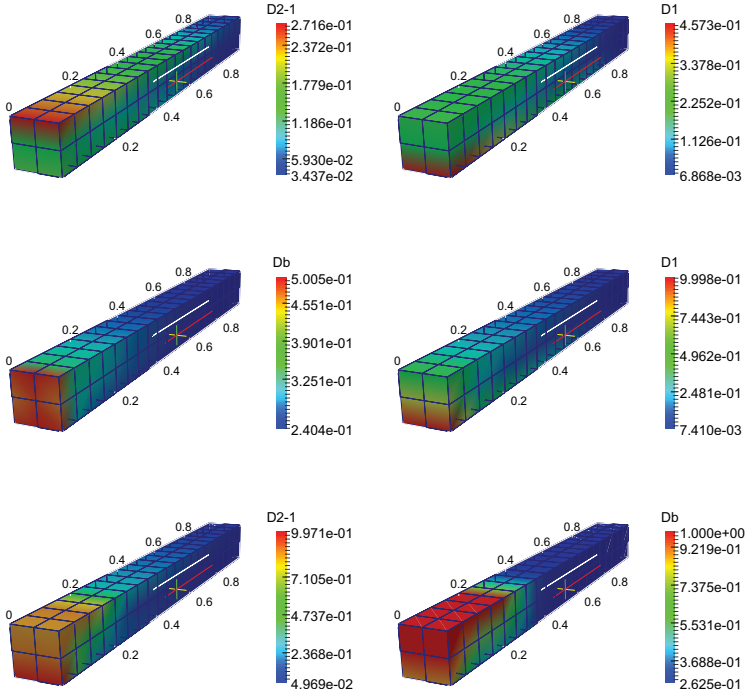

Figure 8.13: Tension rod: Damage variable D_{2-1} (top left) and damage variable D_1 at $u = 0.1975$ mm (top right); debonding D_b and damage variable D_1 at $u = 0.2725$ mm; damage variable $D_2 - 1$ and damage variable D_b at $u = 0.3325$ mm.

already exhibits a value of $D_b = 0.5$ close to its clamped face on the right side of the beam. The last three pictures, fiber damage D_1, matrix damage D_{2-1} and debonding D_b are depicted in the middle right, bottom left, and bottom right picture at position $u = 0.3325$ mm, respectively. After passing the maximum bearing load ($F \approx 0.21519$ N), the cantilever beam shows a different behavior than its macroscopic counterpart, illustrated in figure 6.20. The stiffness degrease of the cantilever beam is much higher in the multiscale model. Observing the discussed damage states at the last position, the fiber damage variable has a value of $D_1 = 0.999$, indicating full damage at the bottom part of the beam. On the other hand, the matrix damage variable D_{2-1} displays a maximum also at the bottom side, in contrast to its initiation region at the top side of the beam. This can be attributed to debonding. The debonding strength of the beam is lower than the matrix strength and the cantilever beam has already lost stiffness due to debonding damage, shown in the bottom right picture. Debonding grows in the entire upper region up to a value of $D_b = 1$. This is also the reason for the steep degradation of the overall stiffness of the cross section, observed in the load displacement path in figure 8.12

Chapter 9

Conclusions and Future Perspectives

This thesis contributes to numerical simulations of damage in fiber reinforced composite structures, focusing on the finite element implementation of macroscopic and multiscale damage models. First, an isotropic damage model was borrowed and implemented for the investigation of concrete material. Several examples were used to test this routine and generate a deeper comprehension of how damage models work and where difficulties can arise when simulating damage in complex structures. Furthermore, this isotropic damage model was frequently used for comparisons. The results from the developed anisotropic damage models were first generally tested with isotropic material data. An implicit-explicit integration scheme was used to stabilize the numerical calculation. This integration scheme was developed 16 years after the damage model was proposed by the same author.

A macroscopic damage model was developed and implemented with the purpose of simulating damage in transversely isotropic materials, such as fiber-reinforced composites. In a first attempt, several different, existing anisotropic damage models were implemented. All had convergence issues within the Newton iteration during the calculation. Thus, a new and more numerically robust macroscopic anisotropic damage model was developed and implemented in the finite element software Feap. This model combined the benefits of several existing models. First, the damage model was based on the concept of equivalent displacements, a theory originally applied in delamination models in conjunction with Hashin's failure criteria or Cuntze's failure mode concept. The latter was applied because of its outstanding agreement with experimental test data, shown in the WWFE. To reduce mesh dependent solutions, the crack band theory was incorporated into the equivalent displacements using a characteristic element length. Besides strain equivalence and strain energy equivalence principles, the evolution of damage is described by a linear softening law, separately in each failure mode, based on energy dissipation during damage progress. The constitutive equations were derived from a Gibbs energy function with four to six different damage modes, depending on whether Hashin's failure criteria or Cuntze's failure mode concept was used. The lack of numerical robustness was considerably improved by adapting the implicit-explicit integration scheme from the isotropic damage model. Applying this integration scheme leads to so-called step linear problems where the algorithmic tangent operator becomes constant in each load step of the calculation. This yields from the fact that the damage describing inner variable is exclusively dependent on values from the last two

converged load steps. When using this integration scheme, small load steps must be chosen in comparison to the standard implicit scheme. In return, due to the aforementioned linear step's, the Newton iteration converges at the first iteration step, which finally leads to an overall saving in computational effort.

The anisotropic macroscopic damage model was used in conjunction with a general, nonlinearly defined finite element description of an eight-noded continuum element with linear interpolation functions. Several numerical examples with different geometries and material data sets were examined to verify the developed damage model. In an initial example, results of calculations, without stabilization schemes, from different implemented damage models were compared with each other. Studying the resulting load displacement paths showed that stabilization procedures are inevitable when dealing with such complex damage simulations. Therefore, the effect of using viscous regularization procedures was highlighted before the benefits of using the IMPL-EX scheme were shown. The damage model was further compared to experimental test data of a displacement suspended tension rod with a centered open hole. The rod featured 20 plies through the thickness in two different stacking orders. The deviation between the results of the simulation and experimental test data was roughly 3% and 4%, respective to the investigated stacking order. With these excellent results, the damage model is proven to correctly approximately describe the complex physical behavior of anisotropic damage models. After having shown the accuracy of the model, further examples were examined with a focus on determining the maximum bearing loads of structures and the corresponding evolution of damage itself.

A second approach to capture the complex mechanism of damage in fiber-reinforced composites was provided by a coupled multiscale damage model. Multiscale models have advantages in the description of damage because they capture the damage process on the micro scale on which it actually occurs. Using this approach for the description of damage, the use of complex failure modes, such as Cuntze's failure mode concept, is redundant. Instead, isotropic failure modes for each constituent can be applied on the microscale, greatly simplifying the mechanical description. Additionally, when using a microscale approach, far fewer material parameters are required, simplifying the model considerably since they are difficult to obtain or measure. The microscale model is hard-coded into the material point of the macroscale model which saves calculation time compared to the FE^2 method. Both scales are described by means of finite elements. Therefore, the formulation of the principle of virtual work and its linearizations for a three dimensional continuum element were extended to incorporate the characterization of the local model. The connection between both scales was established via displacement boundary conditions. One of the key points of multiscale models is to predict the resulting effective properties of a representative volume element. These effective properties characterize the macroscopic behavior and can be obtained from the assembly of all constituents of the micro model through suitable homogenization techniques. The implemented micromechanical model was labeled the EMOC, in reference to the MOC which served as a basis for the development. The MOC was extended to a third, periodic direction and enhanced with nonlinear interface elements between adjacent elements. The interface elements were solely used for the description of damage and

other elements assumed to behave linear elastic. Using this approach, a more detailed description of single damage modes was provided. This model differs from fiber damage, debonding, and matrix damage in each of the three spatial directions. Each damage mode was described through a universal, atomistic relationship between the binding energies of materials. This atomistic relationship has often been used in the context of interface elements for analysis of delamination and has proven to be highly robust in numerical calculations because of its smooth exponential nature, especially when used together with the aforementioned IMPL-EX scheme. The implementation focused on numerical robustness and provided a general framework for a coupled multiscale damage model which can easily be modified, especially in terms of the applied degradation law.

The thesis concluded with a verification of the coupled multiscale approach with numerical examples. First, the interface elements were numerically locked and the EMOC routine compared to analytical values of the MOC. Here, perfect coincidence of both approaches was observed. After the proof of correct implementation, the EMOC routine was contrasted with elastic experimental results from the WWFE and results from another unite cell method. The resulting homogenized elastic properties were in good agreement with the experimental results and comparatively better than results from the other summarized approaches. After having tested the elastic model, further examples focused on the verification of damage states. During single plausibility tests, excellent agreement with experimental test data from the WWFE was observed in terms of maximum bearing load and associated failure strain. Due to the fixed size of the micro model, the results were completely independent of the shape of the global elements, implying that the energy released is in any case correctly calculated. In the examples that followed, delamination and the load displacement behavior were discussed in greater detail with a focus on damage evolution.

Overall, both the macroscopic and the multiscale damage model have proven to deliver reliable results. Though, there may be space for further research and development. One such task would be the improvement of degradation laws used in the macroscopic, as well as in the multiscale model. The bilinear damage law, used in each damage mode of the macro model, was implemented because of its simple nature. A more accurate approach would be to adjust the shape of the damage law according to the present damage mode. Fiber damage, for example, is often described through a bilinear degradation law, whereas matrix damage is often assumed to behave exponentially. The decision on when to use which damage law should be based on experimental tests, a task which is not realized in our institute, where the focus is on developing finite element routines. On the contrary, the implemented damage law of the multiscale model was chosen because of its outstanding numerical robustness. Using this exponential damage law, together with the series connection of elements in the micro model, leads to issues when the stress strain states are of particular interest. The strains in the micro model must be rectified from the elastic strains in the cells in connection to the interface elements, a task which is not always be as simple as it sounds. However, in the scope of bearing load calculations, the focus is on the prediction of maximum stress states so this issue is consciously accepted to improve

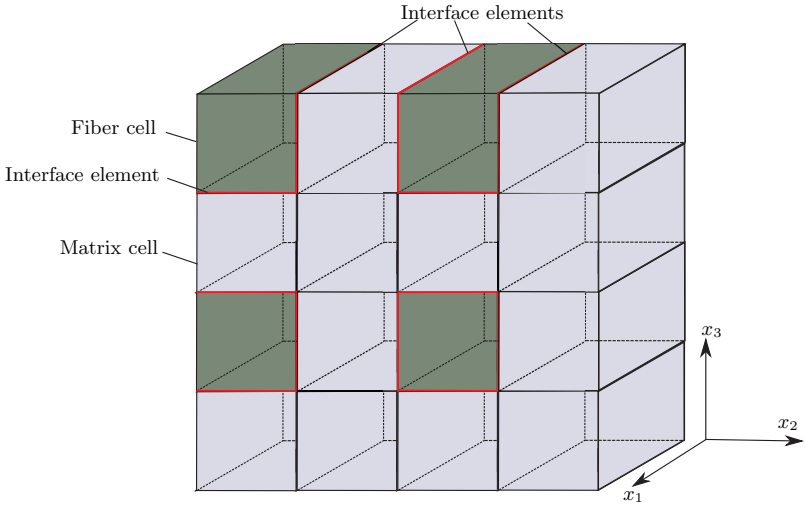

Figure 9.1: Visualization of a finer cell method for use in FE^2 Method

the Newton convergence in complex calculations.

Another improvement would be expected by using a more finely scaled micro system, as depicted in figure 9.1, a modification of the introduced EMOC model. One key point is that the original, four subcell elements can be used in multiples in $\mathbf{x}_2$ and $\mathbf{x}_3$ directions such, that the actual size of the RVE is adjusted problem dependent in a convergence study. Therefore, the micro model must be able to be used flexible in its size, a fact that promotes its use for the FE^2 method. When using the FE^2 approach, the elastic, six-noded EMOC elements could be replaced by eight-noded or even twenty-noded continuum elements with higher order interpolation functions to reduce locking effects. Another benefit of using standard continuum elements is that damage does not have to be described solely through interface elements. Instead, fiber and matrix damage can be allowed in the corresponding micro elements. When applying additional degradation laws with a linear elastic region, as for laws introduced in the macroscopic damage models, the issue of over predicted strains vanishes and the model returns the correct elastic response. Furthermore, to capture debonding damage modes between the fiber and matrix elements, cohesive interface elements are introduced, as can be seen in figure 9.1.

Bibliography

[1] J. Aboudi. Micromechanical analysis of composites by the method of cells. *Applied Mechanics Reviews* 42 (7), pp. 193–221, 1989.

[2] J. Aboudi. Micromechanical analysis of composites by the method of cells-update. *Applied Mechanics Reviews* 49 (10S), S83–S91, 1996.

[3] J. Aboudi. The generalized method of cells and high-fidelity generalized method of cells micromechanical models-A review. *Mechanics of Advanced Materials and Structures* 11 (4-5), pp. 329–366, 2004.

[4] J. Aboudi, S. M. Arnold, and B. A. Bednarcyk. *Micromechanics of composite materials: a generalized multiscale analysis approach*. Butterworth-Heinemann, 2012.

[5] G Alfano and MA Crisfield. Finite element interface models for the delamination analysis of laminated composites: mechanical and computational issues. *International journal for numerical methods in engineering* 50 (7), pp. 1701–1736, 2001.

[6] H. Altenbach. *Kontinuumsmechanik*. Springer, 2012.

[7] H. Altenbach, A. Bolchoun, and V.A. Kolupaev. Phenomenological yield and failure criteria. *Plasticity of Pressure-Sensitive Materials*. Springer, 2014, pp. 49–152.

[8] H. Altenbach and V.A. Kolupaev. Classical and non-classical failure criteria. *Failure and Damage Analysis of Advanced Materials*. Springer, 2015, pp. 1–66.

[9] E.J. Barbero. *Finite Element Analysis Of Composite Materials*. Taylor and Francis Group, 2008.

[10] G. I. Barenblatt. The mathematical theory of equilibrium cracks in brittle fracture. *Advances in applied mechanics* 7, pp. 55–129, 1962.

[11] K.-J. Bathe. *Finite-Elemente-Methoden*. Springer, 2002.

[12] Z. P. Bazant. Can multiscale-multiphysics methods predict softening damage and structural failure? *International Journal for Multiscale Computational Engineering* 8 (1) 2010.

[13] Z.P. Bazant and B.H. Oh. Crack band theory for fracture of concrete. *Materiaux et construction* 16 (3), pp. 155–177, 1983.

[14] P.W.R. Beaumont, R.A. Dimant, and H.R. Shercliff. Failure processes in composite materials: getting physical. *Journal of materials science* 41 (20), pp. 6526–6546, 2006.

[15] E. Becker and W. Bürger. *Kontinuumsmechanik*. B. G. Teubner, 1975.

[16] W. Becker and D. Gross. *Mechanik elastischer Körper und Strukturen*. Springer, 2002.

[17] T. Belytschko, W. K. Liu, B. Moran, and K. Elkhodary. *Nonlinear finite elements for continua and structures*. John Wiley & Sons, 2013.

[18] M.L. Benzeggagh and M. Kenane. Measurement of mixed-mode delamination fracture toughness of unidirectional glass/epoxy composites with mixed-mode bending apparatus. *Composites science and technology* 56 (4), pp. 439–449, 1996.

[19] J. Besson, G. Cailletaud, J.L. Chaboche, and S. Forest. *Non-linear mechanics of materials*. Vol. 167. Springer Science & Business Media, 2009.

[20] J. Betten. Applications of tensor functions to the formulation of constitutive equations involving damage and initial anisotropy. *Engineering Fracture Mechanics* 25 (5), pp. 573–584, 1986.

[21] G. T. Camacho and M. Ortiz. Computational modelling of impact damage in brittle materials. *International Journal of solids and structures* 33 (20), pp. 2899–2938, 1996.

[22] P.P. Camanho and C.G. Davila. *Mixed-Mode Decohesion Finite Elements for the Simulation of Delamination in Composite Materials*. Tech. rep. NASA/TM-2002-211737. 2002.

[23] L. A. Carlsson, D. F. Adams, and R. B. Pipes. *Experimental characterization of advanced composite materials*. CRC press, 2014.

[24] J.L. Chaboche. Sur l'utilisation des variables d'etat interne pour la description du comportement viscoplastique et de la rupture par endommagement. *Proceedings of French-Polish symposium*. 1977.

[25] J.L. Chaboche. The concept of efective strain applied to elasticity and viscoelasticity in the presence of anisotropic damage. *Colloque International surle Comportement Mecanique des Solides Anisotropes* 1979-77 (1) 1979.

[26] J.L. Chaboche. Continuous damage mechanics - a tool to describe phenomena before crack initiation. *Nuclear Engineering and Design* 64 (2), pp. 233–247, 1981.

[27] J.L. Chaboche. Continuum damage mechanics: Part I - General Concepts. *Journal of applied mechanics* 55 (1), pp. 59–64, 1988.

[28] J.L. Chaboche. Continuum damage mechanics: Part II - Damage growth, crack initiation, and crack growth. *Journal of applied mechanics* 55 (1), pp. 65–72, 1988.

[29] J.L. Chaboche. Development of continuum damage mechanics for elastic solids sustaining anisotropic and unilateral damage. *Internal Journal of Damage Mechanics* 2 (1), pp. 311–329, 1993.

[30] J.L. Chaboche, P.M. Lesne, and J.F. Maire. Continuum damage mechanics, anisotropy and damage deactivation for brittle materials like concrete and ceramic composites 1995.

[31] P. Chadwick. *Continuum Mechanics: Concise Theory and Problems*. Dover Publications, 1998.

[32] N. Charalambakis. Homogenization techniques and micromechanics. A survey and perspectives. *Applied Mechanics Reviews* 63 (3), p. 030803, 2010.

[33] M. Chatiri and A. Matzenmiller. A Damage-Mode Based Three Dimensional Constitutive Model for Fibre-Reinforced Composites. *CMC: Computers, Materials & Continua* 35 (3), pp. 255–283, 2013.

[34] X.F. Chen and C.L. Chow. On damage strain energy release rate Y. *International Journal of Damage Mechanics* 4 (3), pp. 251–263, 1995.

[35] C.L. Chow and T.J. Lu. A normative representation of stress and strain for continuum damage mechanics. *Theoretical and applied fracture mechanics* 12 (2), pp. 161–187, 1989.

[36] C.L. Chow and T.J. Lu. On evolution laws of anisotropic damage. *Engineering Fracture Mechanics* 34 (3), pp. 679–701, 1989.

[37] C.L. Chow and J. Wang. An anisotropic theory of continuum damage mechanics for ductile fracture. *Engineering Fracture Mechanics* 27 (5), pp. 547–558, 1987.

[38] R. M. Christensen. *Mechanics of composite materials*. Courier Corporation, 2012.

[39] R.M. Christensen. A critical evaluation for a class of micro-mechanics models. *Inelastic Deformation of Composite Materials*. Springer, 1991, pp. 275–282.

[40] R.M. Christensen and K.H. Lo. Solutions for effective shear properties in three phase sphere and cylinder models. *Journal of the Mechanics and Physics of Solids* 27 (4), pp. 315–330, 1979.

[41] J. P. Cordebois and F. Sidoroff. Endommagement anisotrope en elasticite et plasticite. *Journal de Mecanique Theorique et Appliquee Numero Special* 1 (1), pp. 45–60, 1982.

[42] J.P. Cordebois and F. Sidoroff. Damage induced elastic anisotropy. *Mechanical Behavior of Anisotropic Solids/Comportment Mechanique des Solides Anisotropes*. Springer, 1982, pp. 761–774.

[43] R. G. Cuntze. SM98-018/313 The FAILURE MODE CONCEPT-a New Comprehensive 3D-Strength Analysis Concept for Any Brittle and Ductile Behaving Material. *Spacecraft Structures, Materials and Mechanical Testing*. Vol. 428. 1999, p. 269.

[44] R.G. Cuntze. The predictive capability of failure mode concept-based strength criteria for multi-directional laminates-part B. *Composites Science and Technology* 64 (3), pp. 487–516, 2004.

[45] R.G. Cuntze and A. Freund. The predictive capability of failure mode concept-based strength criteria for multidirectional laminates. *Composites Science and Technology* 64 (3), pp. 343–377, 2004.

[46] R. De Borst, M. A. Crisfield, J. J. Remmers, and C. V. Verhoosel. *Nonlinear finite element analysis of solids and structures*. John Wiley & Sons, 2012.

[47] M. V. Donadon, S. F. M. De Almeida, M. A. Arbelo, and A. R. de Faria. A three-dimensional ply failure model for composite structures. *International Journal of Aerospace Engineering* 2009 2009.

[48] M.V. Donadon, S.F.M. Almeida, M.A. Arbelo, and A.R. Faria. A Three-Dimensional Ply Failure Model for Composite Structures. *Internal Journal of Aerospace Enginieering* 2009 (486063), pp. 1–22, 2009.

[49] A. Düster, H.-G. Sehlhorst, and E. Rank. Numerical homogenization of heterogeneous and cellular materials utilizing the finite cell method. *Computational Mechanics* 50 (4), pp. 413–431, 2012.

[50] J. Echaabi, F. Trochu, and R. Gauvin. Review of failure criteria of fibrous composite materials. *Polymer Composites* 17 (6), pp. 786–798, 1996.

[51] G. Ernst, M. Vogler, C. Hühne, and R. Rolfes. Multiscale progressive failure analysis of textile composites. *Composites Science and Technology* 70 (1), pp. 61–72, 2010.

[52] J. D. Eshelby. The determination of the elastic field of an ellipsoidal inclusion, and related problems. *Proceedings of the Royal Society of London A: Mathematical, Physical and Engineering Sciences*. Vol. 241. 1226. The Royal Society. 1957, pp. 376–396.

[53] F. Feyel and J.-L. Chaboche. FE 2 multiscale approach for modelling the elastoviscoplastic behaviour of long fibre SiC/Ti composite materials. *Computer methods in applied mechanics and engineering* 183 (3), pp. 309–330, 2000.

[54] U. Galvanetto and M. F. Aliabadi. *Multiscale modeling in solid mechanics: computational approaches*. Vol. 3. World Scientific, 2009.

[55] J.P Gardner. "Micromechanical Modeling of Composite Materials in Finite Element Analysis Using an Embedded Cell Approch". MA thesis. Cambridge, MA, USA: Massachusetts Institute of Technology, 1994.

[56] M.G.D. Geers, V.G. Kouznetsova, and W.A.M. Brekelmans. Multi-scale computational homogenization: Trends and challenges. *Journal of computational and applied mathematics* 234 (7), pp. 2175–2182, 2010.

[57] S. Ghosh, K. Lee, and S. Moorthy. Two scale analysis of heterogeneous elastic-plastic materials with asymptotic homogenization and Voronoi cell finite element model. *Computer Methods in Applied Mechanics and Engineering* 132 (1–2), pp. 63–116, 1996.

[58] S. Ghosh, K. Lee, and P. Raghavan. A multi-level computational model for multi-scale damage analysis in composite and porous materials. *International Journal of Solids and Structures* 38, pp. 2335–2385, 2001.

[59] D. Gross and T. Seelig. *Bruchmechanik - Mit einer Einführung in die Mikromechanik*. Springer, 2006.

[60] D. Gross, H. Werner, and P. Wriggers. *Technische Mechanik 4*. Springer, 2009.

[61] F. Gruttmann and V.D. Pham. A finite element model for the analysis of buckling driven delaminations of thin films on rigid substrates. *Computational Mechanics* 41 (3), pp. 361–370, 2008.

[62] F. Gruttmann and W. Wagner. A coupled two-scale shell model with applications to layered structures. *International Journal for Numerical Methods in Engineering* 94, pp. 1233–1254, 2013.

[63] F. Guo-dong, L. Jun, and W. Bao-lai. Progressive damage and nonlinear analysis of 3D four-directional braided composites under unidirectional tension. *Composite Structures* 89 (1), pp. 126–133, 2009.

[64] Z. Hashin. The elastic moduli of heterogeneous materials. *Journal of Applied Mechanics* 29 (1), pp. 143–150, 1962.

[65] Z. Hashin. Failure criteria for unidirectional fiber composites. *Journal of applied mechanics* 47 (2), pp. 329–334, 1980.

[66] D. Heller. *A nonlinear multiscale finite element model for comb-like sandwich panels*. Vol. 40. Forschungsberichte des Instituts für Mechanik der Technischen Universität Darmstadt, 2016.

[67] R. Hill. Elastic properties of reinforced solids: some theoretical principles. *Journal of the Mechanics and Physics of Solids* 11, pp. 357–372, 1963.

[68] R. Hill. A self-consistent mechanics of composite materials. *Journal of the Mechanics and Physics of Solids* 13 (4), pp. 213–222, 1965.

[69] M. J. Hinton, A. S. Kaddour, and P. D. Soden. *Failure criteria in fibre reinforced polymer composites: the world-wide failure exercise*. Elsevier, 2004.

[70] G.A. Holzapfel. *Nonlinear Solid Mechanics: A Continuum Approach for Engineering*. John Wiley and Sons, 2000.

[71] T.J.R. Hughes. *The Finite Element Method: Linear Static and Dynamic Finite Element Analysis*. Dover Civil and Mechanical Engineering, 2000.

[72] F. Irgens. *Continuum Mechanics*. Springer, 2008.

[73] L.M. Kachanov. On the Time Rupture under Creep Conditions. *Otd. Tech. Nauk* 8 (1), pp. 26–31, 1958.

[74] V.G. Kouznetsova, M.G.D. Geers, and W.A.M. Brekelmans. Multi-scale constitutive modelling of heterogeneous materials with a gradient-enhanced computational homogenization scheme. *International Journal for Numerical Methods in Engineering* 54 (8), pp. 1235–1260, 2002.

[75] V.G. Kouznetsova, M.G.D. Geers, and W.A.M. Brekelmans. Multi-scale second-order computational homogenization of multi-phase materials: a nested finite element solution strategy. *Computer Methods in Applied Mechanics and Engineering* 193 (48–51), pp. 5525–5550, 2004.

[76] D. Krajcinovic. *Damage mechanics*. Vol. 41. Elsevier, 1996.

[77] Y. W. Kwon, D. H. Allen, and R. Talreja. *Multiscale modeling and simulation of composite materials and structures*. Vol. 47. Springer, 2008.

[78] M. Lai, E. Krempl, and D. Ruben. *Introduction To Continuum Mechanics*. Elsevier Butterworth-Heinemann, 2010.

[79] I. Lapczyk and J.A. Hurtado. Progressive damage modeling in fiber-reinforced materials. *Composites Part A: Applied Science and Manufacturing* 38 (11), pp. 2333–2341, 2007.

[80] J. Lemaitre. Evaluation of dissipation and damage in metals submitted to dynamic loading. *Proceedings of the ICM-1*. 1971.

[81] J. Lemaitre. *A Course on Damage Mechanics*. Springer, 1992.

[82] P. Linde and H. de Boer. Modelling of inter-rivet buckling of hybrid composites. *Composite structures* 73 (2), pp. 221–228, 2006.

[83] Y. Liu, B. Zwingmann, and M. Schlaich. Nonlinear Progressive Damage Analysis of Notched or Bolted Fibre-Reinforced Polymer (FRP) Laminates Based on a Three-Dimensional Strain Failure Criterion. *Polymers* 6 (4), p. 949, 2014.

[84] G. Maass and F. Gruttmann. A three-dimensional progressive damage model for fiber reinforced composites with an implicit-explicit integration scheme. *Proceedings in Applied Mathematics and Mechanics* 15, pp. 139–140.

[85] P. Maimi, J.A. Mayugo, and P.P. Camanho. A three-dimensional damage model for transversely isotropic composite laminates. *Journal of Composite Materials* 42 (25), pp. 2717–2745, 2008.

[86] P. Maimi, P.P. Camanho, J.A. Mayugo, and C.G. Davila. *A Thermodynamically Consistent Damage Model for Advanced Composites*. Tech. rep. NASA/TM-2006-214282. NASA Langley Research Center, 2006.

[87] P. Maimi, P.P. Camanho, J.A. Mayugo, and C.G. Davila. A continuum damage model for composite laminates: Part I–Constitutive model. *Mechanics of Materials* 39 (10), pp. 897–908, 2007.

[88] P. Maimi, P. P. Camanho, J.A. Mayugo, and C.G. Davila. A continuum damage model for composite laminates: Part II–Computational implementation and validation. *Mechanics of Materials* 39 (10), pp. 909–919, 2007.

[89] P Maimı, PP Camanho, JA Mayugo, and A Turon. Matrix cracking and delamination in laminated composites. Part I: Ply constitutive law, first ply failure and onset of delamination. *Mechanics of materials* 43 (4), pp. 169–185, 2011.

[90] P. Maimi, P.P. Camanho, J.A. Mayugo, and A. Turon. Matrix cracking and delamination in laminated composites. Part II: Evolution of crack density and delamination. *Mechanics of Materials* 43 (4), pp. 194–211, 2011.

[91] L.E. Malvern. *Introduction to the Mechanics of a Continuous Medium*. Prentice Hall, 1977.

[92] A. Matzenmiller, J. Lubliner, and R.L. Taylor. A constitutive model for anisotropic damage in fiber-composites. *Mechanics of materials* 20 (2), pp. 125–152, 1995.

[93] R. McLaughlin. A study of the differential scheme for composite materials. *International Journal of Engineering Science* 15 (4), pp. 237–244, 1977.

[94] F.P. Van der Meer, L.J. Sluys, S.R. Hallett, and M.R. Wisnom. Computational modeling of complex failure mechanisms in laminates. *Journal of Composite Materials* 2011.

[95] C. Miehe, J. Schröder, and J. Schotte. Computational homogenization analysis in finite plasticity simulation of texture development in polycrystalline materials. *Computer Methods in Applied Mechanics and Engineering* 171, pp. 387–418, 1999.

[96] T. Mori and K. Tanaka. Average stress in matrix and average elastic energy of materials with missing inclusions. *Acta Metallurgica* 21 (5), pp. 571–574, 1973.

[97] S. Murakami. Creep damage analysis in thin-walled tubes. *Inelastic Behavior of Pressure Vessel and Piping Components* PVP-PB-028 (1), pp. 55–69, 1978.

[98] S. Murakami. Effect of cavity distribution in constitutive equations of creep and creep damage. *EUROMECH Colloquium-147 on Damage Mechanics*. 1981.

[99] S. Murakami. Mechanical modeling of material damage. *Journal of Applied Mechanics* 55 (2), pp. 280–286, 1988.

[100] S. Murakami. *Continuum Damage Mechanics*. Springer, 2012.

[101] S. Murakami and N. Ohno. A continuum theory of creep and creep damage. *Creep in structures*. Springer, 1981, pp. 422–444.

[102] A. Needleman. A continuum model for void nucleation by inclusion debonding. *Journal of applied mechanics* 54 (3), pp. 525–531, 1987.

[103] A. Needleman. An analysis of tensile decohesion along an interface. *Journal of the Mechanics and Physics of Solids* 38 (3), pp. 289–324, 1990.

[104] S. Nemat-Nasser, N. Yu, and M. Hori. Bounds and estimates of overall moduli of composites with periodic microstructure. *Mechanics of materials* 15 (3), pp. 163–181, 1993.

[105] R. J. Nuismer. Predicting the performance and failure of multidirectional polymeric matrix composite laminates- A combined micro-macro approach. *Advances in composite materials*, pp. 436–452, 1980.

[106] J. T. Oden and J. N. Reddy. *An introduction to the mathematical theory of finite elements*. Courier Corporation, 2012.

[107] J. Oliver. A consistent characteristic length for smeared cracking models. *International Journal for Numerical Methods in Engineering* 28 (2), pp. 461–474, 1989. ISSN: 1097-0207. DOI: 10.1002/nme.1620280214. URL: http://dx.doi.org/10.1002/nme.1620280214.

[108] J. Oliver, M. Cervera, and S. Oller. Isotropic damage models and smeared crack analysis of concrete. *Proceedings of SCI-C 1990*. 1990.

[109] J. Oliver, A.E. Huespe, and J.C. Cante. An implicit/explicit integration scheme to increase computability of non-linear material and contact/friction problems. *Computer Methods in Applied Mechanics and Engineering* 197 (21), pp. 1865–1889, 2008.

[110] J. Oliver, A.E. Huespe, S. Blanco, and D.L. Linero. Stability and robustness issues in numerical modeling of material failure with the strong discontinuity approach. *Computer Methods in Applied Mechanics and Engineering* 195 (52), pp. 7093–7114, 2006.

[111] M. Ortiz. Microcrack coalescence and macroscopic crack growth initiation in brittle solids. *International Journal of Solids and Structures* 24 (3), pp. 231–250, 1988.

[112] M. Ortiz and A. Pandolfi. Finite-deformation irreversible cohesive elements for three-dimensional crack-propagation analysis. *International Journal for Numerical Methods in Engineering* 44 (9), pp. 1267–1282, 1999.

[113] M. Paley and J. Aboudi. Micromechanical analysis of composites by the generalized cells model. *Mechanics of materials* 14 (2), pp. 127–139, 1992.

[114] Yi Pan and Assimina A Pelegri. Progressive damage analysis of random chopped fiber composite using finite elements. *Journal of Engineering Materials and Technology* 133 (1), p. 011018, 2011.

[115] A. Puck and H. Schuermann. Failure analysis of FRP laminates by means of physically based phenomenological models. *Composites Science and Technology* 62 (12), pp. 1633–1662, 2002.

[116] J. N. Reddy. *An Introduction to Nonlinear Finite Element Analysis: with applications to heat transfer, fluid mechanics, and solid mechanics*. OUP Oxford, 2014.

[117] Y.N. Robotnov. Creep rupture in applied mechanics. *Proceedings of the 12th International Congress on Applied Mechanics*. 1968.

[118] J. H. Rose, J. Ferrante, and J. R. Smith. Universal binding energy curves for metals and bimetallic interfaces. *Physical Review Letters* 47 (9), p. 675, 1981.

[119] J.C.J. Schellekens and R. De Borst. A non-linear finite element approach for the analysis of mode-I free edge delamination in composites. *International Journal of Solids and Structures* 30 (9), pp. 1239–1253, 1993.

[120] J.C.J. Schellekens and R. De Borst. On the numerical integration of interface elements. *International Journal for Numerical Methods in Engineering* 36 (1), pp. 43–66, 1993.

[121] J. Schröder. A numerical two-scale homogenization scheme: the FE2-method. *Plasticity and Beyond*. Springer, 2014, pp. 1–64.

[122] J.C. Simo and T.J.R. Hughes. *Computational Inelasticity*. Springer, 2000.

[123] J.C. Simo and J. Ju. On continuum damage-elastoplasticity at finite strains. *Computational Mechanics* 5 (5), pp. 375–400, 1989.

[124] J.C. Simo, J. Ju, and R.L. Taylor. Strain- and stress-based continuum damage models: II. computational aspects. *Internal Journal Solids Structures* 23 (7), pp. 841–869, 1987.

[125] J.C. Simo and J.W. Ju. Strain-and stress-based continuum damage models: I. Formulation. *International journal of solids and structures* 23 (7), pp. 821–840, 1987.

[126] R.J.M. Smit, W.A.M. Brekelmans, and H.E.H. Meijer. Prediction of the mechanical behavior of nonlinear heterogeneous systems by multi-level finite element modeling. *Computer Methods in Applied Mechanics and Engineering* 155 (1), pp. 181–192, 1998.

[127] I. M. Smith and D. V. Griffiths. *Programming the finite element method*. John Wiley & Sons, 2005.

[128] J. Spahn. *An Efficient Multiscale Method for Modeling Progressive Damage in Composite Materials*. Forschungsbericht des Lehrstuhls für Technische Mechanik der Technischen Universität Kaiserslautern, 2015.

[129] H Sun, S Rajendran, and DQ Song. Finite Element Analysis on Delamination Fracture Toughness of Composite Specimens. *Proceedings of 2nd Asian ANSYS User Conference*. Vol. 2. 1998, pp. 1–8.

[130] S. C. Tan. A progressive failure model for composite laminates containing openings. *Journal of Composite Materials* 25 (5), pp. 556–577, 1991.

[131] V. Tvergaard and J. W. Hutchinson. The relation between crack growth resistance and fracture process parameters in elastic-plastic solids. *Journal of the Mechanics and Physics of Solids* 40 (6), pp. 1377–1397, 1992.

[132] V. Tvergaard and J. W. Hutchinson. The influence of plasticity on mixed mode interface toughness. *Journal of the Mechanics and Physics of Solids* 41 (6), pp. 1119–1135, 1993.

[133] Jörg F Unger and Stefan Eckardt. Multiscale modeling of concrete. *Archives of Computational Methods in Engineering* 18 (3), pp. 341–393, 2011.

[134] W. Wagner and C. Balzani. Simulation of delamination in stringer stiffened fiber-reinforced composite shells. *Computers & Structures* 86 (9), pp. 930–939, 2008.

[135] W. Wagner, F. Gruttmann, and W. Sprenger. A finite element formulation for the simulation of propagating delaminations in layered composite structures. *International Journal for Numerical Methods in Engineering* 51 (11), pp. 1337–1359, 2001.

[136] Y.Q. Wang, M.B. Tong, and S.H. Zhu. Three dimensional continuum damage mechanics model of progressive failure analysis in fibre-reinforced composite laminates. *50th AIAA Structures, Structural Dynamics, and Materials Conference. California: American Institute of Aeronautics and Astronautics*. 2009.

[137] P. Wriggers. *Nonlinear Finite Element Methods*. Springer, 2008.

[138] W. Zhang and Y. Cai. *Continuum Damage Mechanics*. Springer, 2010.

[139] Q.S. Zheng and J. Betten. On damage effective stress and equivalence hypothesis. *International Journal of Damage Mechanics* 5 (3), pp. 219–240, 1996.

[140] O.C. Zienkiewicz, R.L. Taylor, and D.F. Fox. *The Finite Element Method for Solid and Structural Mechanics*. Elsevier Butterworth-Heinemann, 2013.

[141] O.C. Zienkiewicz, R.L. Taylor, and J.Z. Zhu. *The Finite Element Method: Its Basis and Fundamentals*. Elsevier Butterworth-Heinemann, 2013.

[142] T.I. Zohdi and P. Wriggers. *An introduction to computational micromechanics*. Springer Science & Business Media, 2008.

Bisher sind in dieser Reihe erschienen

Band 1
Zur mikrorissinduzierten Schädigung spröder Materialien
B. Lauterbach, Dissertation 2001, ISBN 3-935868-01-4

Band 2
3D-Simulation der Mikrostrukturentwicklung in Zwei-Phasen-Materialien
R. Müller, Dissertation 2001, ISBN 3-935868-02-2

Band 3
Zur numerischen Simulation von Morphologieänderungen in mikroheterogenen Materialien
S. Kolling, Dissertation 2001, ISBN 3-935868-03-0

Band 4
Theoretische und numerische Untersuchung von Versagensmechanismen in Metall-Keramik-Verbundwerkstoffen
T. Emmel, Dissertation 2002, ISBN 3-935868-04-9

Band 5
On microcrack dominated problems in dynamics and statics of brittle fracture: a numerical study by boundary element techniques
S. Rafiee, Dissertation 2002, ISBN 3-935868-05-7

Band 6
Kontinuumsmechanik anisotroper Festkörper und Fluide
H. Ehrentraut, Habilitationsschrift 2002, ISBN 3-935868-06-5

Band 7
Plane unsteady inviscid incompressible hydrodynamics of a thin elastic profile
N. Blinkova, Dissertation 2002, ISBN 3-935868-07-3

Band 8
Anmerkungen zur Simulation von entfestigendem Materialverhalten
H. Baaser, Habilitationsschrift 2004, ISBN 3-935868-08-1

Band 9
Orts- und zeitadaptive DAE-Methoden zur Beschreibung elastisch-plastischen Materialverhaltens innerhalb der FEM
S. Eckert, Dissertation 2005, ISBN 3-935868-09-X

Band 10
Simulations of the Flow of the Ross Ice Shelf, Antarctica: Parameter Sensitivity Tests and Temperature-Dependent Rate Factor
A. Humbert, Dissertation 2005, ISBN 3-935868-10-3

Band 11
A Thermo-mechanical Continuum Theory with Internal Length of Cohesionless Granular Materials
Chung Fang, Dissertation 2006, ISBN 3-935868-11-1

Band 12
Modeling Dry Granular Avalanches past Different Obstructions: Numerical Simulation and Laboratory Analyses
Chiou Min-Ching, Dissertation 2006, ISBN 3-935868-12-X

Band 13
Configurational forces in defect mechanics and in computational methods
R. Müller, Habilitationsschrift 2005, ISBN 3-935868-13-8

Band 14
Hyperelastic dynamics in physical and material space
S. Kolling, Habilitationsschrift 2007, ISBN 978-3-935868-14-3

Band 15
Phenomenological modeling of ferroelectric material behavior
V. Mehling, Dissertation 2007, ISBN 978-3-935868-15-0

Band 16
Ein mischungsbasiertes Materialmodell zum Knochenumbau
R.-R. Kühn, Dissertation 2006, ISBN 978-3-935868-16-7

Band 17
Einige Erweiterungen der Rand-Finite-Elemente-Methode und deren Anwendung auf Randeffekte in ebenen Laminaten
J. Artel, Dissertation 2007, ISBN 978-3-935868-17-4

Band 18
Spannungskonzentrations-Effekte an Verstärkungspflaster-Ecken
H. Wigger, Dissertation 2008, ISBN 978-3-935868-18-1

Band 19
Rotationseffekte in der Kristallplastizität
C. Bröse, Dissertation 2007, ISBN 978-3-935868-19-8

Band 20
Finite-Element-Modelle zur Simulation von Delaminationen dünner Filme auf Substraten
V. D. Pham, Dissertation 2010, ISBN 978-3-935868-20-4

Band 21
Asymptotische Nahfeldanalysen ebener Multi-Materialverbindungsstellen mit der Methode komplexer Potentiale
C. Sator, Dissertation 2010, ISBN 978-3-935868-21-1

Band 22
Modellierung spröder Rissbildung an Spannungskonzentrationen mit der Bruchmechanik finiter Risse
J. Hebel, Dissertation 2010, ISBN 978-3-935868-22-8

Band 23
Some Contributions to the Homogenization of Macroscopically Isotropic Composites
V. Salit, Dissertation 2011, ISBN 978-3-935868-23-5

Band 24
Asymptotic Analysis of the Load Transfer on Double-Lap Bolted Joints
J. Kratochvíl, Dissertation 2012, ISBN 978-3-935868-24-2

Band 25
Spannungssingularitätsordnungen in linear-elastischen und piezoelektrischen Multimaterialkonfigurationen mit der Rand-Finite-Elemente-Methode
W. Mayland, Dissertation 2012, ISBN 978-3-935868-25-9

Band 26
Plastizität und Skaleneffekte sowie Deformations- und Versagensmodellierung dünner metallischer Schichten bei Nanoindentation
A. Trondl, Dissertation 2012, ISBN 978-3-935868-26-6

Band 27
Theoretical modeling and parallel programming of a nonlinear composite finite shell element based on a mixed global-local variational principle
M. Schürg, Dissertation 2012, ISBN 978-3-935868-27-3

Band 28
Strukturmechanische Modellierung und Analyse des Tragverhaltens von dünnwandigen hochbelasteten Composite-Biege- und Querkraftträgern
A. M. Kroker, Dissertation 2013, ISBN 978-3-935868-28-0

Band 30
Der Laminatrandeffekt und seine Analyse, insbesondere mit der Rand-Finite-Elemente-Methode
J. Lindemann, Dissertation 2013, ISBN 978-3-935868-30-3

Band 31
Avoidance of brake squeal by a separation of the brake disc's eigenfrequencies: A structural optimization problem
A. Wagner, Dissertation 2013, ISBN 978-3-935868-31-0

Band 32
Ultrasonic Generators for Energy Harvesting Applications: Self-Excitation and Mechanical Frequency Transformation
E. Heffel, Dissertation 2013, ISBN 978-3-935868-32-7

Band 33
Neue Ansätze zur Analyse der Lastübertragung und Initiierung finiter Risse in Klebverbindungen
P. Weißgraeber, Dissertation 2014, ISBN 978-3-935868-33-4

Band 34
Instabilities and Wear Propagation in Calenders: Interactions with Structural Dynamics and Contact Kinematics
M. Eckstein, Dissertation 2014, ISBN 978-3-935868-34-1

Band 35
Adaptive Camber Airfoil for Load Alleviation in Horizontal Axis Wind Turbines: Analytical and Numerical Study
H. Spiegelberg, Dissertation 2014, ISBN 978-3-935868-35-8

Band 36
Erweiterungen der Rand-Finite-Elemente-Methode zur Analyse von Platten und Laminaten mit besonderem Fokus auf der Ermittlung von Singularitätsordnungen an Rissen und Kerben
R. Dieringer, Dissertation 2015, ISBN 978-3-935868-36-5

Band 37
Entwicklung und Analyse mikromechanischer Modelle zur Beschreibung des Effektivverhaltens von geschlossenzelligen Polymerschäumen
N.-C. Fahlbusch, Dissertation 2015, ISBN 978-3-935868-37-2

Band 38
Reduktion niederfrequenter Schwingungen von Windenergieanlagen durch Tilgersysteme
S. Katz, Dissertation 2015, ISBN 978-3-935868-38-9

Band 39
Multistable Structures for Broad Bandwidth Vibration-based Energy Harvesters: An Analytical Design Investigation
M. Heymanns, Dissertation 2015, ISBN 978-3-935868-39-6

Band 40
A nonlinear multiscale finite element model for comb-like sandwich panels
D. Heller, Dissertation 2016, ISBN 978-3-935868-40-2

Band 41
Rückwirkung des Gleitlagermoments auf die Drehbewegung des Rotors
P. Felscher, Dissertation 2016, ISBN 978-3-935868-41-9